

A Thesis Submitted for the Degree of PhD at the University of Warwick

Permanent WRAP URL:

<http://wrap.warwick.ac.uk/147207>

Copyright and reuse:

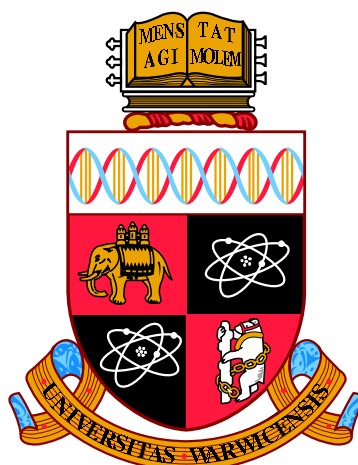
This thesis is made available online and is protected by original copyright.

Please scroll down to view the document itself.

Please refer to the repository record for this item for information to help you to cite it.

Our policy information is available from the repository home page.

For more information, please contact the WRAP Team at: wrap@warwick.ac.uk



**Nanoscale Materials Characterisation:
Nanoelectrode Fabrication for Topographic and
Electrochemical Mapping**

by

James Foden Edmondson

Thesis

Submitted to the University of Warwick

for the degree of Analytical Science

Doctor of Philosophy

Molecular Analytical Science Centre for Doctoral Training

October 2019

Contents

List of Tables	v
List of Figures	vi
Declarations	xi
Abstract	xii
Abbreviations	xiii
Chapter 1 Introduction	1
1.1 Thesis Summary	1
1.2 Scanning Tunnelling Microscopy	2
1.2.1 Operational Theory	3
1.2.2 Tip Positional Control	4
1.2.3 The STM Tip	6
1.2.4 In-situ and Electrochemical STM Studies	7
1.3 AFM	9
1.4 SEPM	10
1.4.1 SECM	10
1.4.2 SICM	19
1.4.3 SECCM	21
1.5 Hybrid SEPM Techniques	22
1.5.1 AFM-SECM	22
1.5.2 AFM-SICM	23
1.5.3 STM-SECM	24
1.5.4 SICM-SECM	25
1.6 Nanoelectrodes	26
1.6.1 Fabrication	26

1.6.2	Characterisation	28
1.7	Aims and Objectives	29
1.8	References	32
Chapter 2	Carbon Fiber based Platinum Nanoelectrodes	44
2.1	Introduction	44
2.1.1	Carbon Nanoelectrodes	44
2.1.2	Platinum Nanoelectrodes	49
2.2	Methodology	50
2.2.1	Carbon Nanoelectrodes	50
2.2.2	Platinum Electrodeposition on Carbon Nanoelectrodes	53
2.2.3	CV Peak Integration	55
2.2.4	Instrumentation	55
2.3	Results	56
2.3.1	Carbon Nanoelectrodes	56
2.3.2	Platinum Electrodeposition on Carbon Nanoelectrodes	60
2.4	Conclusions	65
2.5	References	67
Chapter 3	Synchronous Conductance - Scanning Electrochemical Microscopy (C-SECM) Measurements	70
3.1	Introduction	71
3.2	Methodology	73
3.2.1	PtNE Fabrication	73
3.2.2	2D Au Nanocrystals and AuNPs	75
3.2.3	SPM Instrumentation	77
3.2.4	C-SECM Measurements	78
3.3	Results and Discussion	79
3.3.1	Piezoelectric Actuators Stability	79
3.3.2	Ambient Measurements	82
3.3.3	C-SECM in Electrolyte Solution	85
3.3.4	Future C-SECM and STM-SECM	92
3.4	Conclusions	94
3.5	Acknowledgements	94
3.6	References	95

Chapter 4 Bipolar Nanoelectrodes: Fabrication and Characterisation	100
4.1 Introduction	100
4.1.1 Fabrication	100
4.1.2 Characterisation	102
4.2 Methodology	104
4.3 Results	106
4.4 Conclusions	115
4.5 Acknowledgements	115
4.6 References	116
 Chapter 5 Bipolar Nanoelectrodes: Applications in Scanning Electrochemical Probe Microscopy	 117
5.1 Introduction	117
5.2 Methodology	119
5.3 Results	122
5.3.1 In-situ STM	122
5.3.2 Nanoscale SECM	125
5.3.3 Future Possibilities	128
5.4 Conclusions	130
5.5 Acknowledgements	130
5.6 References	131
 Chapter 6 Characterisation of Benzotriazole Adsorption on the Cu(110) Surface	 132
6.1 Introduction	133
6.1.1 Benzotriazole (BTAH)	133
6.1.2 BTAH on Cu(111)	134
6.1.3 BTAH on Cu(100)	136
6.1.4 BTAH on Cu(110)	136
6.1.5 High Resolution Electron Energy Loss Spectroscopy	137
6.2 Methodology	138
6.3 Results	142
6.3.1 Low Coverage	142
6.3.2 Monolayer Coverage	142
6.3.3 Multilayer Coverage	144
6.3.4 HREELS	148
6.3.5 Oxygen Reconstructed Cu(110)	149

6.4	Conclusions	150
6.5	Acknowledgements	151
6.6	References	152
Chapter 7	Summary and Outlook	155

List of Tables

1.1	Constants for conical electrodes with an insulating sheath.	17
2.1	Summary of coil heating parameters for CNE fabrication.	60

List of Figures

1.1	SEM images of mechanically cut and electrochemically etched STM tips.	3
1.2	Schematic of a piezoelectric tube scanner.	5
1.3	Constant height and constant current imaging mode schematics for STM.	6
1.4	AFM operation schematic and a typical force-distance curve.	9
1.5	Feedback mode SECM operation diagram for catalytically active and inert substrates with approximate approach curves.	12
1.6	Scanning modes of SECM	13
1.7	Illustrative diagram of a CV with CVs of UMEs with different scan rates.	16
1.8	Schematic of different UME geometries with dimensions.	17
1.9	Illustration of SICM operation.	19
1.10	Illustration of SECCM operation.	21
1.11	Schematic of a cavity electrode with experimental CV.	30
2.1	Compared microscopy and voltammetry for different carbon electrode geometries.	47
2.2	STEM image of a 30 nm quartz nanopipette and TEM image of a Pt filled CNE.	51
2.3	Parameters during pulling cycle of a P2000 laser puller.	51
2.4	Diagram and image of torch heating CNE fabrication method.	52
2.5	Diagram and image of coil heating CNE fabrication method.	53
2.6	Details of background removal for CV peak integration.	55
2.7	Sigmoidal CVs of CNEs fabricated with the torch method.	56
2.8	Peaked shape CV of a CNE fabricated with the torch method.	57
2.9	STEM images and CVs for three example CNEs fabricated with the coil method.	59

2.10	CVs of CNEs before and after Pt deposition with Pt deposition trace.	61
2.11	Cyclic method of Pt deposition on a FIB milled CNE.	62
2.12	Au deposition using pulse method on CNEs.	63
2.13	TEM of an almost ideal AuNE formed with the pulse method on a CNE.	64
2.14	Galvanostatic deposition of Pt on a CNE.	66
3.1	Voltammograms of PtNE before and after Pt deposition, with deposition voltammogram.	75
3.2	STEM image of a good and poor PtNE geometry with voltammetry for the poor example.	76
3.3	CV of GC substrate used in C-SECM experiments.	77
3.4	Fast Fourier transforms of tip currents with purposefully generated noise.	78
3.5	Schematic of electrode setup and hopping pulse scheme used for C-SECM.	80
3.6	Measured piezoelectric noise and drift for two actuators using a capacitive sensor.	81
3.7	Ambient tunnelling approach curve with 2 nm s^{-1} approach rate.	83
3.8	Ambient topographic scans using hopping mode in an SECM instrument.	84
3.9	Approach curve from ambient topographic scan and piezoelectric overshoot data.	86
3.10	Tip current measured throughout a C-SECM scan.	87
3.11	C-SECM scans of a Au nanocrystal with HER.	88
3.12	Typical approach curve in C-SECM scans with histograms and plots relating to approach overshoot magnitude and frequency.	89
3.13	Pixel current trace comparison during SECM pulses	90
3.14	C-SECM scans with very short retract rate showing increased contact pixels.	91
3.15	SEM of a Au nanocrystal before and after C-SECM experiments.	92
3.16	Dependence of approach rate and short retract distance on the number of tip-substrate contact pixel frequency.	93
4.1	Schematic for deposition stages of BPNE fabrication.	101
4.2	Schematic of a closed bipolar electrochemical cell.	103
4.3	Comparison of current trace changes to BPNE quality.	106

4.4	BPNE geometry from STEM converted to a two dimensional geometry for COMSOL simulations.	107
4.5	Current trace of BPNE formation with STEM image of an electrode.	108
4.6	Elemental analysis of a BPNE.	109
4.7	CVs of UMEs to determine formal potentials in a BPNE.	110
4.8	STEM images of BPNEs with measured and simulated CVs.	111
4.9	BPNE CVs with varied internal and external concentrations with summary of expected and measured data.	112
4.10	STEM images of BPNEs formed with Pt.	113
4.11	Electropolymerisation of aniline in a meniscus cell and inside a BPNE.	114
5.1	CVs taken before and after breaking of a BPNE for STM.	120
5.2	Schematic representation of a BPNE used as an STM tip.	123
5.3	In-situ STM with a BPNE as the tip with accompanying STM line profile and STEM of BPNE.	124
5.4	Negative feedback SECM approach with COMSOL simulated approach and CV.	126
5.5	Positive feedback SECM approach curve with STEM image of electrode and corresponding CVs.	127
5.6	STEM image and electrochemical response of BPNE during and after SECM scans.	129
6.1	BTAH structure and Cu(BTA) ₂ dimeric structure.	133
6.2	Upright and flat configurations for BTAH adsorption on Cu from DFT calculations.	134
6.3	Schematic representation of dipole effects and measurement angle for HREELS.	138
6.4	Apparatus used for BTAH deposition in vacuum.	139
6.5	STM image of clean and oxygen reconstructed Cu(110) used for calibration and confirming crystallographic orientations.	141
6.6	STM images of lowest coverage of BTAH on Cu(110) studied.	143
6.7	STM images of slightly greater than a monolayer BTAH coverage on Cu(110).	144
6.8	Highest coverage studied as deposited and after annealing.	145
6.9	Large ridge and small chain structures observed with higher coverages upon annealing. Line profile and structural model also presented.	146
6.10	Experimental and simulated HREELS structure for various BTAH configurations.	147

6.11 BTAH deposited on partially oxygen reconstructed Cu(110), large scale, molecular scale and molecular model.	149
---	-----

Acknowledgements

Firstly I would like to thank my supervisors Prof. Giovanni Costantini and Prof. Patrick R. Unwin for their continued advice and support throughout my research.

I would like to thank the EPSRC for a PhD studentship through the EPSRC Centre for Doctoral Training in Molecular Analytical Science, grant number EP/L015307/1.

I would also like to acknowledge all members of the Costantini group, the Warwick Electrochemistry and Interfaces Group and the Molecular Analytical Science Centre for Doctoral Training for many discussions and collaborations in both research and social aspects of my PhD. Special thanks go to Dr. Gabriel Meloni, Dr. Cameron Bentley and Dr. Minkyung Kang for initial training and continued support in experimental and theoretical aspects of electrochemical imaging.

Most importantly I would like to acknowledge my family for supporting my education both financially and emotionally, always encouraging throughout the ups and downs of my studies at school, undergraduate and postgraduate level. All of my academic, sporting and personal achievements to date could not have been accomplished without them.

Declarations

The work presented in this thesis is entirely my own, except where acknowledged otherwise. This thesis is submitted to the University of Warwick in support of my application for the degree of Doctor of Philosophy. It has been composed by myself and has not been submitted in any previous application for any degree apart from some of the data presented in Chapter 6 which was previously submitted for my MSc in Molecular Analytical Science, however, all data analysis and interpretation was carried out during my PhD studies.

The work presented (including data generated and data analysis) was carried out by the author except in the cases outlined below:

The data in Figure 6.10 were collected by Dr. Federico Grillo from the University of St. Andrews, however, the interpretation and incorporation with the rest of the data in Chapter 6 has been carried out by myself.

I have contributed to the following publications that are not included in this thesis:

Nanoscale Electrochemical Mapping

Cameron L. Bentley, **James Edmondson**, Gabriel N. Meloni, David Perry, Viacheslav Shkirskiy, and Patrick R. Unwin, *Anal. Chem.*, **2019**, 91, 84-108.

The following publication has been submitted to *ChemElectroChem*:

Synchronous Conductance - Scanning Electrochemical Microscopy (C-SECM) Measurements

James F. Edmondson, Gabriel Meloni, Giovanni Costantini and Patrick R. Unwin
Paper which is in preparation to be published:

Benzotriazole Adsorption on the Cu(110) Surface

Marco Turano, **James Edmondson**, Federico Grillo and Giovanni Costantini

Abstract

Historical electrochemical methods of materials characterisation typically examine the macroscale response of a system of interest. This provides some information, but makes it difficult to elucidate the fundamental relationship between structure and functionality of a material. For this reason there has been a large push towards studying structure-activity relationships at the nanoscale or single entity level, with electrochemical imaging techniques coming to the fore. These techniques typically use a mobile electrode probe to investigate the system, and the probe that is used (a “nanoelectrode”) is key. A previous method of nanoelectrode fabrication involving the electrodeposition of platinum on pyrolysis formed carbon nanoelectrodes has been reported and investigated in terms of reproducibility and most effective methods of characterisation (Chapter 2). New methods for fabrication are still being pursued and a recent approach utilising chemical reduction at a nanopipette-solution interface is investigated for its application in electrochemical imaging techniques (Chapters 4 & 5).

There is a myriad of analytical techniques for surface materials characterisation and several fall within the category of scanning electrochemical probe microscopy (SEPM). Within SEPM, hybrid techniques are popular, combining the advantages of individual techniques. The combination of scanning tunnelling microscopy (STM) with scanning electrochemical microscopy (SECM) has shown promise in previous studies, but has not been widely adopted due to the challenges associated with probe fabrication and instrument operation. These challenges have been addressed with the assessment of SEPM systems for conductance and/or tunnelling - SECM measurements using a novel scanning protocol (Chapter 3). If truly molecular topographical resolution is the goal, then STM has proven itself to be an extremely successful technique. To demonstrate, molecules of benzotriazole were deposited on a Cu(110) surface to elucidate fundamental structural information, this system is one where STM-SECM or conducting-SECM could potentially be applied in the future (Chapter 6).

Abbreviations

AC	Alternating Current
AFM	Atomic Force Microscopy
AFM-SECM	Atomic Force Microscopy - Scanning Electrochemical Microscopy
AFM-SICM	Atomic Force Microscopy - Scanning Ion Conductance Microscopy
BPNE	Bipolar Nanoelectrode
BTAH	Benzotriazole
C-SECM	Conductance - Scanning Electrochemical Microscopy
CNE	Carbon Nanoelectrode
CV	Cyclic Voltammetry
CVD	Chemical Vapor Deposition
DC	Direct Current
DFT	Density Functional Theory
EC-STM	Electrochemical - Scanning Tunnelling Microscopy
EDX	Energy-Dispersive X-ray Spectroscopy
FEM	Finite Element Method
FIB	Focused Ion Beam
FluidFM	Fluidic Force Microscopy
FWHM	Full Width Half Maximum
G/C	Generation / Collection

GC	Glassy Carbon
HOPG	Highly Ordered Pyrolytic Graphite
HER	Hydrogen Evolution Reaction
HREELS	High Resolution Electron Energy Loss Spectroscopy
NE	Nanoelectrode
NMR	Nuclear Magnetic Resonance
NP	Nanoparticle
QRCE	Quasi-Reference Counter Electrode
RHE	Reversible Hydrogen Electrode
SCE	Saturated Calomel Electrode
SECCM	Scanning Electrochemical Cell Microscopy
SECM	Scanning Electrochemical Microscopy
SEM	Scanning Electron Microscopy
SEPM	Scanning Electrochemical Probe Microscopy
SICM	Scanning Ion Conductance Microscopy
SICM-SECM	Scanning Ion Conductance Microscopy - Scanning Electrochemical Microscopy
SG/TC	Substrate Generation / Tip Collection
SPM	Scanning Probe Microscopy
STM	Scanning Tunnelling Microscopy
STM-SECM	Scanning Tunnelling Microscopy - Scanning Electrochemical Microscopy
STEM	Scanning Transmission Electron Microscopy
TEM	Transmission Electron Microscopy
TG/SC	Tip Generation / Substrate Collection

UHV	Ultra-High Vacuum
UME	Ultramicroelectrode
UPS	Ultraviolet Photoelectron Spectroscopy
XPS	X-ray Photoelectron Spectroscopy

Chapter 1

Introduction

1.1 Thesis Summary

Nanoelectrodes are a pre-requisite for several nanoscale electrochemical experiments, despite this requirement, their fabrication and characterisation are far from trivial. This thesis addresses one previous method of nanoelectrode fabrication and also applies this method to a specific hybrid nanoscale imaging technique termed conductance - scanning electrochemical microscopy (C-SECM). This thesis then goes on to introduce and study a more recently reported method for nanoelectrode fabrication and characterisation before the application of these electrodes for nanoscale scanning electrochemical probe microscopy. The final chapter focusses on the adsorption of a molecule (benzotriazole) on a metal (Cu(110)) surface in an ideal system (ultra-high vacuum) for a demonstration of the capability of scanning tunnelling microscopy (STM).

Chapter 2 studies the fabrication and characterisation of carbon nanoelectrodes, previously described in the literature. Purely electrochemical methods of nanoelectrode characterisation can provide misleading conclusions if proper interpretation is not carried out, characterisation with both voltammetry and microscopy of carbon nanoelectrodes is carried out in this chapter. These carbon nanoelectrodes were then used as a substrate for Pt electrodeposition to form Pt nanoelectrodes using several different experimental procedures. Once again the use of electrochemical methods of characterisation are presented, along with electron microscopy studies to show the advantages and limitations of each approach.

In Chapter 3 the Pt nanoelectrodes fabricated in Chapter 2 were used in a state of the art electrochemical imaging instrument to carry out a C-SECM study of an exemplar system of the hydrogen evolution reaction (HER) on Au nanocrystals.

The method of C-SECM operation is different to previous STM-SECM attempts, utilising a hopping mode to simultaneously map topography and electrochemical activity. The lateral resolution achieved is also greater than that of previous electrochemical imaging studies using nanoscale electrode probes. The specific instrumentation setup presents certain limitations to the presented method as is discussed, but the study highlights the future use of C-SECM for nanoscale materials characterisation.

Due to the issues presented in Chapter 2 a newer method for Au nanoelectrode fabrication is described and studied in Chapter 4. Characterisation of these electrodes is then carried out using electron microscopy and a non-trivial electrochemical approach. These electrodes present a very simple and extremely reproducible method of fabricating Au nanoelectrodes with a good geometry, especially when compared to the methods described in Chapter 2. However their electrochemical characterisation presents some challenges with regards to predictability.

The electrodes studied in Chapter 4 are tested for their suitability as nanoscale electrochemical probes in Chapter 5, with a specific emphasis on in-situ STM and SECM, with ideal future applications being in STM-SECM studies. Whilst the electrodes show promise for these applications, there are some drawbacks and challenges to be overcome before they become a staple fabrication method in the field of electrochemical imaging.

As the previous chapters have discussed, nanoscale electrochemical imaging and electrode fabrication can be extremely challenging and there are many issues to be addressed. To demonstrate the capability of STM itself, Chapter 6 describes a study carried out using an ultra-high vacuum (UHV) STM to investigate the adsorption of a corrosion inhibitor, benzotriazole on a single crystal Cu(110) surface.

1.2 Scanning Tunnelling Microscopy

Scanning tunnelling microscopy (STM) was the first scanning probe microscopy (SPM) technique, developed in 1981.¹ Since then STM has demonstrated an exceptional ability to study the topography and electronic structure of conducting surfaces at the atomic level.² STM is often used in ultra-high vacuum (UHV) and/or at low temperatures (liquid nitrogen or liquid helium).³⁻⁵ STM can also be operated in a variety of methodologies in addition to pure topographical measurements such as scanning tunnelling spectroscopy,⁶ single molecule conductance measurements^{7,8} and many others. Here the introduction will be limited mostly to the use of STM for topography and electrochemical measurements in ambient and in-situ

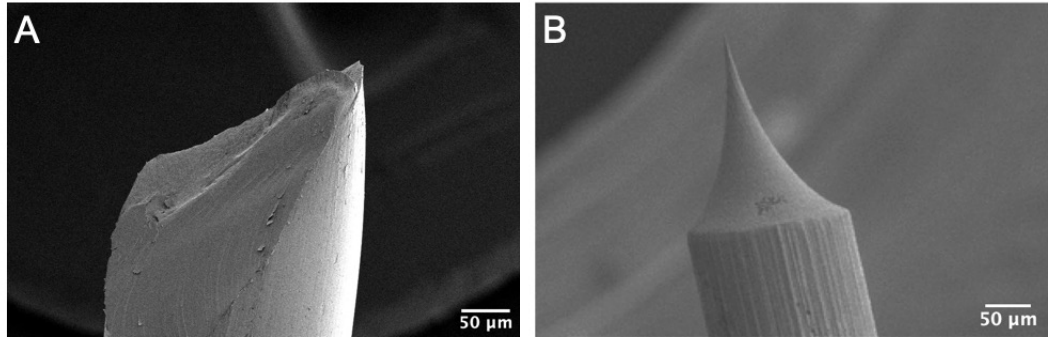


Figure 1.1: Scanning electron microscopy (SEM) images of mechanically cut Pt/Ir (A) and electrochemically etched W (B) wires used as STM tips. (B) Reproduced from Wüthrich, *et al.*, *J. Micromechanics Microengineering*, 15, **2005**.¹⁰ Copyright (2005) Institute of Physics.

environments.

1.2.1 Operational Theory

STM utilises the phenomenon of quantum tunnelling, a subatomic particle can pass through a potential barrier that it could not do under the laws of classical mechanics. In the case of STM, the subatomic particle is the electron and the barrier is the physical gap between the STM tip and the surface of interest. STM tips are typically made from Pt/Ir or W wires that have been mechanically cut (Figure 1.1A) or electrochemically etched (Figure 1.1B).⁹ At some point the tip will be atomically sharp at the end and when the tip is brought in a sufficiently close proximity (≈ 4 nm) the tunnelling probability between the tip and surface becomes non-negligible.⁶ Generally the tip and surface will have different work functions and at equilibrium the two will have a common Fermi level. This creates an electric field in the gap between them. The typical work functions of metals is several eV which is generally much higher than the thermal energy of electrons, therefore there is a barrier for the electrons between the tip and surface. This barrier is impassible classically, however, in reality electrons have a delocalised wave function meaning there is a non-zero probability of electrons tunnelling across the gap and creating a tunnelling current which can be measured. Once a potential difference is applied, the Fermi level of the sample is shifted by $-eV$ (where e is the electron charge and V is the applied potential), creating a net tunnelling current.⁶

The overall tunnelling current can be derived using the approach developed by Bardeen.^{11,12} The approach starts with the stationary Schrödinger equations:

$$(\hat{T} + \hat{U}_S)\psi_\mu = E_\mu\psi_\mu \quad (1.1)$$

$$(\hat{T} + \hat{U}_T)\chi_\nu = E_\nu\chi_\nu \quad (1.2)$$

where \hat{T} and \hat{U} are the kinetic and potential energy operators respectively, S and T refer to the sample and tip respectively, ψ_μ and χ_ν are the unperturbed wavefunctions and E is the energy.⁶ The Bardeen approach continues derivation from here with many steps and approximations to give the final result for the overall tunnelling current I given by:

$$I = \frac{4\pi e}{\hbar} \int_0^{eV} \rho_T(E_F^T - eV + \epsilon) \rho_S(E_F^S + \epsilon) e^{-2ks} d\epsilon \quad (1.3)$$

with

$$k \approx \frac{\sqrt{m(\phi_T + \phi_S)}}{\hbar} \quad (1.4)$$

e is the electron charge, \hbar is the reduced Planck constant, V is the applied potential, ρ is the density of states, E_F is the Fermi energy, ϵ is the energy to integrate, s is the sample to tip separation, m is the electron mass and ϕ is the work function.⁶ This equation has several terms and variables, however, the most important to note is the tunnelling current (I) is exponentially dependent on the tip to sample separation (s). This is the primary reason that STM has such incredible resolution, a change of height on the atomic scale results in an exponential change in the measured tunnelling current. The lateral resolution of STM has also been approximated as $((2 \text{ \AA})(R + s))^{\frac{1}{2}}$ assuming the end of the tip is spherical with radius R and with all values in \AA .¹³

1.2.2 Tip Positional Control

To operate an STM, the movement of the tip has to be controlled in an extremely precise fashion. To achieve atomic resolution the position of the tip needs to be controlled on the Ångström scale. This motion is realised with the use of piezoelectric ceramic actuators. Piezoelectrics can expand or contract with an applied voltage, this also works in the opposite regime where expanding or contracting the piezoelectric will create a voltage; to a good approximation the response is linear with a proportionality constant.¹⁴ The required properties for a piezoelectric scanner are: high mechanical resonance frequencies, high scan speeds, high spatial resolution, independent three-dimensional control, low creep and minimal thermal drift.⁶ Many forms of scanners have been used for STM, however, a single piezoelectric tube is

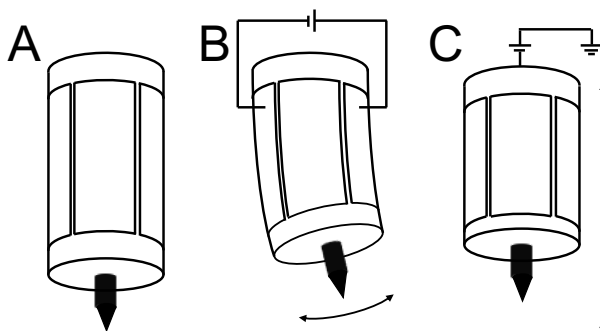


Figure 1.2: (A) Schematic of a piezoelectric tube scanner with a mounted tip and four external electrodes. (B) Applying a bias on the external electrodes allows for lateral motion of the STM tip. Applying a bias to the internal electrode (C) or external electrodes in unison allows for vertical motion.⁶

the most common. This consists of a piezoelectric material tube with four electrode sections around the outside and optionally an electrode inside. Applying opposing voltages to these outer electrodes will move the tip in the lateral directions, while vertical motion is realised by polarizing either all the external electrodes in unison or by polarising an inner electrode relative to the outer ones (Figure 1.2).^{6,15} Whilst these exist in a wide range of sizes and materials, STM tube scanners will typically have a lateral range of a few microns and a vertical range of around one micron.^{16,17}

Creating an STM image involves moving the tip across the surface of interest and measuring the tunnelling current at each location. Two modes are generally used for imaging; constant height mode (Figure 1.3A) and constant current mode (Figure 1.3B). As the name would suggest, in constant height mode the vertical displacement of the tip is kept constant and the change in tunnelling current across the surface is the feature of interest. If there is a dip in the surface, a reduced tunnelling current is observed, and vice versa for a bump. This mode is only used over a small area on very flat surfaces otherwise the tip could crash into the surface. Resolution is also lost in any features that are below the imaging plane and thermal drift during the length of the scan could cause the tip to contact the sample.⁶ Constant current mode adjusts the vertical displacement of the tip to keep the tunnelling current constant using a computer controlled feedback mechanism and records the voltage applied to the vertical adjustment piezoelectric. This mode is the most commonly used as it can be applied to a greater range of surface topographies. Repeating either of these modes in a raster pattern will generate an STM image of the surface.⁶

A notable issue is presented for surfaces covered with adsorbates as constant current imaging is only an accurate topographical representation if the local density

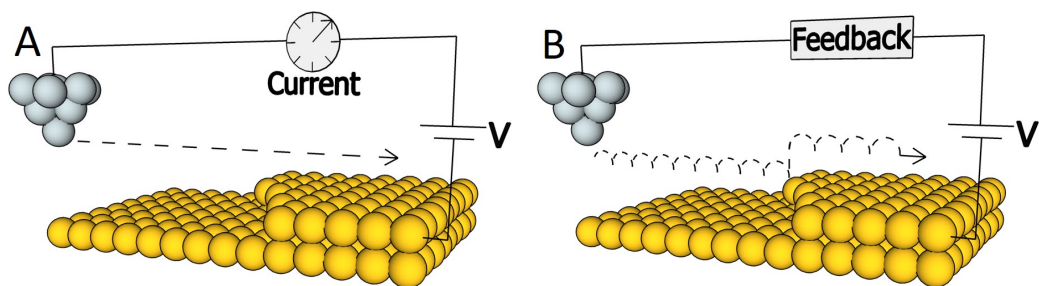


Figure 1.3: (A) Constant height mode, where the height of the tip is kept constant and the change in tunnelling current is measured. (B) Constant current mode, where the tunnelling current is kept constant using a feedback loop to adjust the tip to surface separation, whilst recording the piezoelectric extension.

of states is constant (see equation 1.3). In STM imaging electronegative atoms adsorbed on metal surfaces appear as depressions, this is due to a charge transfer that takes place between the substrate and the adsorbed atom which screens the metals conduction electrons.^{6,18}

1.2.3 The STM Tip

The first major criteria for an STM tip is that it is conductive to allow electrons to tunnel and current to flow. The atomic scale structure of the tip is also extremely important for STM imaging: ideally the tip should be terminated by a single atom if atomic resolution is the goal. If tunnelling occurs at more than one atom (double tip), image artefacts will be produced. The purity of the tip is also an important factor, oxide layers can have a very high resistance, causing the tip to physically touch the sample before a tunnelling current is observed, therefore a chemically inert metal is the most suitable material for an STM tip. For these reasons, generally materials like Pt/Ir or W wires are used.^{6,19}

Whilst these wires alone will suffice in ambient or UHV conditions, in-situ or electrochemical conditions require modification to these wires. Specifically if the solution is conductive then the tip will simply short the circuit resulting in saturated currents. In order to operate STM in conductive solutions the tips are insulated so that only a small area is exposed at the end. Doing this limits the currents measured from Faradaic processes and as long as the tunnelling current is greater than these processes then STM measurements can still be obtained.^{20,21}

There have been several methods used to insulate tips for in-situ STM measurements, a few more commonly used methods are summarised below. One method

is insulating using melted wax, the tip is moved into molten Apiezon wax using a fine manipulator until a thermal equilibrium is met, the tip is then moved up and out of the wax. The precise temperature of the wax makes a large difference to the quality and coverage of the insulation.^{22–24} Another method is coating in varnish where the wire is left tip upwards with varnish on the end and then cured to expose the very tip.^{21,25,26} Electrophoretic paint can also be used to insulate STM tips. The tip is submerged in an electrophoretic paint (Clearclad, Glassophor, etc.), a potential is applied between the tip and a Pt electrode to create the coating and then the tip is cured to harden the coating and expose the apex. The specific deposition and curing conditions depend greatly on the exact paint used.^{21,27–29}

1.2.4 In-situ and Electrochemical STM Studies

The first STM study, carried out in UHV, demonstrated the monoatomic steps of, and surface reconstructions associated with, CaIrSn_4 and Au surfaces.¹ Shortly thereafter, the 7×7 reconstruction on Si(111) was imaged in real space directly for the first time.³⁰ Atomic resolution studies of graphite surfaces in air and water first demonstrated the possibility of using STM as a tool for in-situ surface characterisation,^{31,32} once this had been carried out, it did not take long before STM measurements in an electrochemical environment were reported, termed electrochemical (EC)-STM. Some of the earliest work in this area involved imaging a graphite surface before and after Au electrodeposition without removing the sample from the electroplating solution.²⁰ The first study to use a three-electrode setup (i.e., with the tip, substrate and a reference electrode) demonstrated the electrochemical deposition and dissolution of Ag under potentiostatic conditions, this was followed shortly thereafter by the publication of a full design specification for an EC-STM.³³

Over the years many EC-STM studies have been carried out, so for the sake of this thesis some more interesting studies in the last few years will be highlighted to show what is at the forefront of EC-STM.

One key capability of EC-STM is to map surface topography whilst carrying out voltammetry on the substrate. Several recent studies highlight this, for example anion intercalation in highly ordered polycrystalline graphite (HOPG) with 4 different electrolytes (HCl , HClO_4 , H_2SO_4 and H_3PO_4) has been studied. The group cycled the potential of the substrate between EC-STM scans to show that in HClO_4 and H_2SO_4 anion intercalation resulted in “blister” formation not seen with the other electrolytes. The first stages of the intercalation process were also outlined.³⁴ Another study described the potential dependence of germanene growth

on the Au(111) surface, showing that the initial deposition occurs at defects in the Au(111) herringbone reconstruction. Subsequently growth in troughs of the surface relaxes the structure, further growth was shown to occur via a second layer of weakly bound islands.³⁵

EC-STM also has significant applications within the field of energy materials, a recent study looked at the ability of iron-pthalocyanine layers adsorbed on Au(111) to catalyse the oxygen reduction reaction.³⁶ Electrochemical roughening of Pt(111) in HClO₄ has been studied recently with EC-STM, this was achieved by cycling the potential of the system (between 0.05 and 1.35 V vs a reversible hydrogen electrode, RHE) and taking EC-STM scans with the potential held in the double layer region (0.4 V vs RHE) building up a series of images showing the roughening as a function of cycle number.³⁷

Generally speaking the limiting factor for the speed of acquisition for STM images is the feedback required for constant current mode imaging. As mentioned previously (Section 1.2.2), constant height STM is limited in the topography possible to study, and any resolution is lost for a substrate which is not directly in the imaging plane, however, it can be operated much faster than the constant current mode.^{38,39} A recent study investigated the surface dynamics of Au(111) crystals in different ionic liquids, with STM images obtained in only ≈ 100 ms per frame. This acquisition rate allows the system to be investigated on the electrochemical timescale.³⁸ The same group also studied Bi electrodeposition on Au(111) and Au(100), the time resolution achieved allowed for real time videos of atomic movement, showing the influence of Bi-Bi covalent bonds on the morphology of the electrodeposition.³⁹

A rather novel approach to EC-STM was conducted recently where noise in the tunnelling current was used to investigate electrochemical phenomena. As mentioned earlier (Section 1.2.3) EC-STM tips are insulated to try and minimise the contribution of Faradaic currents to maximise the signal to noise ratio. This study took a conventional EC-STM instrument with a Pt(111) crystal and analysed the Faradaic noise during the scanning procedure. They showed that when the substrate potential was appropriate for the hydrogen evolution reaction (HER), the noise was increased over surface features like step edges. This increase is attributed to a greater catalytic activity which changes the local composition of the solution and hence the tunnelling barrier. The same study also investigated Pd islands on Au(111), an increase in noise was recorded over the Pd islands and an even greater increase is seen over the first few atoms of the Pd/Au boundary. This technique is not currently fully quantitative, however it does show how conventional EC-STM can be sensitive to catalytic properties.⁴⁰

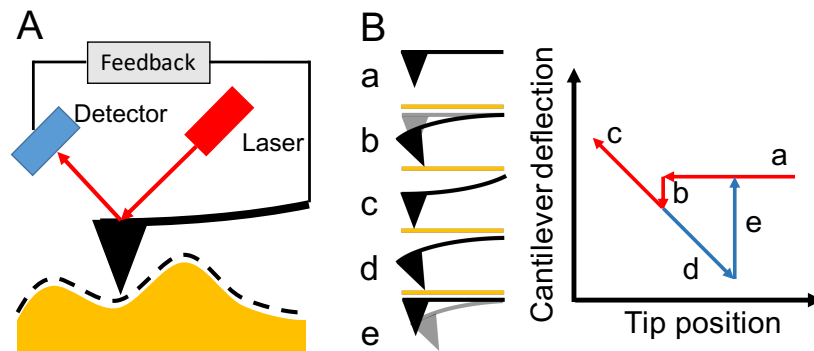


Figure 1.4: (A) Schematic of an AFM tip tracing surface topography with a detector used to monitor the change in laser and hence cantilever position. (B) Phases of a force-distance curve. In (a) the tip is approached towards the surface, (b) an adhesive force between tip and sample reduces force on the cantilever, (c) the force increases as the tip is driven into the surface, (d) the adhesive force of the surface keeps the tip on the surface, (e) the tip detaches from the surface.

1.3 AFM

The atomic force microscope (AFM) was developed very shortly after STM,⁴¹ and AFM and STM are by far the most utilised SPMs. An in depth review of AFM use in electrochemical environments is beyond the scope of this thesis, but AFM has been used with other scanning electrochemical probe microscopy (SEPM) techniques in a hybrid setting (see Section 1.5) and therefore a brief overview of operational principles will be described here.

AFM involves measuring the force between a sharp tip and the sample on the atomic scale. Typically the tip will be mounted on a cantilever and the deflection of this cantilever is used to measure the force, the deflection is recorded by reflecting a laser off the cantilever and onto a detector (Figure 1.4A). The force (F) in the most basic case is given by Hooke's law: $F = -kz$ where k is the stiffness and z is the deflection of the cantilever.⁴² A force-distance curve typically observed in AFM is described in Figure 1.4B, however, depending on the surface, tip and environment these curves can look quite different.⁴²

There are several modes of operating an AFM and this determines what probe motion and feedback is used, the most common are described below. Feedback in contact mode is carried out by setting a desired force on the cantilever, the feedback loop will then adjust the tip to sample separation to keep this force constant. This contact however, can damage the surface as the tip is essentially dragged across it.^{43,44} This leads into non-contact mode AFM, in this case the tip

is kept a set distance ($30 - 150 \text{ \AA}$) above the surface and the Van der Waals forces are detected. As would be expected the forces measured here are much weaker than in contact mode, so the cantilever is oscillated near its resonant frequency which allows for small deviations in this vibration due to the forces to be monitored.^{44,45} The forces here are over a very short distance and generally the surface will have a fluid contaminant layer which is thicker than the operating distance required and therefore the tip can become trapped in the layer or moves too far from the surface to measure these forces. Finally, tapping mode AFM is similar to contact mode in that the cantilever is oscillated near its resonant frequency, however, in this mode the tip contacts and then detaches from the surface with each oscillation. This mode eliminates the lateral forces found in contact mode but the impact force can often be larger, which can blunt the AFM tip.^{44,46}

Critically, as AFM measures force it can be applied to conductors and insulators (unlike STM), it has also been utilised in air, solution and vacuum.⁴⁷

1.4 SEPM

Following the success of STM, many other types of SPM have followed suit for the investigation of surfaces at high resolution. Depending on the type of probe used, and operational method, a plethora of different information can be obtained about a surface. This has led to many different types of SPM. Specifically of interest to this thesis is the category of scanning electrochemical probe microscopy (SEPM), where local electrochemistry is the information of key interest. Below, the focus will be on scanning electrochemical microscopy (SECM) as the most relevant technique to the thesis, but details of the other key and most commonly used SEPM techniques are also briefly described and have been covered in recent reviews.^{48–50}

1.4.1 SECM

Scanning electrochemical microscopy (SECM), first described in the late 1980s, is the most widely adopted form of SEPM and has proven to be extremely effective at determining local electrochemistry at a surface.^{51–54} Historically, the resolution of SECM has been limited to the micrometer scale due to the probes used being ultramicroelectrodes (UMEs), however more recently the achievable resolution has moved into the nanoscale due to new fabrication methods for nanoelectrodes (NEs).

1.4.1.1 Operational Principles

SECM operates by measuring the current on a UME or NE as it is scanned in close proximity to a substrate in solution. SECM can determine surface topography and electrochemical activity, although not normally at the same time. There are several different ways of operating an SECM in terms of the potentials used, the currents measured and the pattern of motion for scanning.⁵¹

One class of operation for SECM is in generation/collection (G/C) modes. The two types of G/C mode used are substrate generation/tip collection (SG/TC) and tip generation/substrate collection (TG/SC). During G/C modes both the substrate current (i_S) and tip current (i_T) are measured and the potential for both is controlled.^{55,56}

In TG/SC mode a product is generated at the tip and the substrate is used to collect it. As an example the oxidised form of a species (O) could be reduced at the tip to the product (R) following $O + ne^- \rightarrow R$, then the substrate would have a suitable potential to collect R via the opposite process ($R - ne^- \rightarrow O$). Collection efficiency is given by i_S/i_T . Since the substrate is generally much larger than the tip, and if the tip is sufficiently close to the surface (within a couple of tip radii), then this tends towards 1 (100 %). However if R reacts in solution whilst traversing between the tip and substrate, then this efficiency will be decreased. The collection efficiency can be measured to find the rate constant for the homogeneous reaction.^{57,58} TG/SC can be used to screen electrocatalysts,⁵⁹ generating a species at the tip (with constant current) and then measuring the change in substrate current as the potential of the substrate is controlled.^{60,61} SG/TC essentially operates in the opposite fashion to TG/SC where the substrate generates the product and the tip collects it. As the species (O) diffuses away from the substrate, having been electrolysed (from R) a fraction of O will be converted back to R at the tip. The time dependent current response at the tip is sensitive to the diffusion coefficient ratio of the O/R couple. Additionally, in steady state conditions the tip current can be combined with the current value for electrolysis of R in bulk to measure differences in the diffusion coefficient for the reduced and oxidised form of the couple.^{62,63} Approaching the tip to the substrate results in a concentration gradient and scanning across the surface can highlight active regions of the substrate.^{55,56}

Another operational mode very similar to TG/SC is called feedback mode. This is the most frequently used mode, where only i_T is monitored.^{55,58} Whilst the tip is sufficiently far from the surface the measured i_T is governed by diffusion of species to the tip (Figure 1.5A). When the probe is approached to a catalytically active substrate at a suitable potential (Figure 1.5B), the substrate can regener-

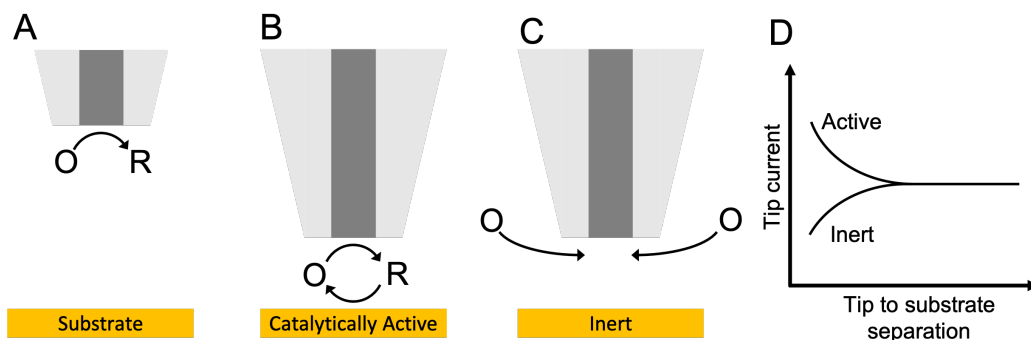


Figure 1.5: (A) Oxidised form of species reduced at the SECM tip when far from surface. (B) A catalytically active substrate can re-oxidise the reduced form creating an increase in current. (C) An inert substrate hinders diffusion of species towards the tip resulting in a reduced current. (D) Approximate expected approach curve to a catalytically active or inert substrate.

ate the species and therefore an increase in current is observed (positive feedback). For an inert substrate (Figure 1.5C) the diffusion of electroactive species towards the probe will be hindered and therefore a diminished current at the probe is observed (negative feedback). Due to these processes, approaching an SECM tip to different substrates will result in a different approach curve (Figure 1.5D). These approach curves are typically plotted in normalised quantities as $i_T/i_{T,\infty}$ ($i_{T,\infty}$ is the tip current far from the surface) against $L = d/a$ where d is the tip to substrate separation and a is the probe radius. Given these are both dimensionless variables, the approach curve does not contain any information about species concentration or diffusion coefficients. The approach curves can therefore be used to determine d from measured i_T .^{51,54} However, the approach curve for an insulator also depends on the radius of the insulating sheath around the conductive part of the probe, as this also limits the diffusion of species to the tip.⁶⁴⁻⁶⁷

SECM mostly involves measurements of steady state currents. The advantage being that double-layer charging and adsorption do not effect the measured current.^{68,69} Transient mode SECM, however, measures i_T as a function of time and can be used for a system that has a time dependence or for determining diffusion coefficients.^{64,70} Techniques such as cyclic voltammetry (CV) can also be used at the tip during SECM operation. Fast scan CV has been used to allow for chemical imaging without feedback interactions and reaction intermediates have also been studied using typical slower CV studies during SECM operation.^{71,72}

SECM has been operated in several scanning methodologies, to list the most

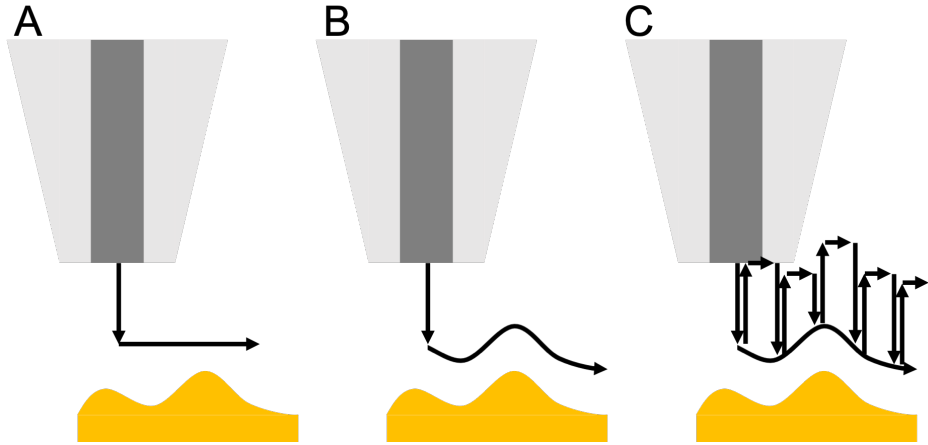


Figure 1.6: (A) Constant height mode where the probe height is kept constant and the change in current is measured. (B) Constant current mode, where the current is kept constant by adjusting and monitoring the height of the tip. (C) Hopping mode where the probe is approached to a set current at each pixel before retracting back a set distance and approaching the next, monitoring the final position in each approach.

utilised; constant height (Figure 1.6A), constant current (Figure 1.6B) and hopping mode (Figure 1.6C).^{73,74} Constant height, and current, operate very similarly to analogous techniques in STM where the height is kept constant and current monitored, or the current is kept constant by varying the height of the probe respectively. Similar to STM, constant height mode is only useful for flat substrates as otherwise the tip could make contact with the surface, whereas constant current mode is slower but can be applied to a greater variety of topographies. Hopping mode scanning was first introduced in scanning ion conductance microscopy (SICM) where the probe is approached to the surface at each pixel until the set threshold for current is reached, the probe is then retracted back a set distance and re-approached at the next pixel.^{75,76} The resulting image in hopping mode should closely resemble a constant current image as the current set point before retracting is constant. Whilst this method is slower than the other methods it can be applied to any surface topography if an appropriate retract distance is set. Hopping also allows approach curves to be recorded for every pixel which can elucidate additional information.⁷⁴

1.4.1.2 Instrumentation

Similarly to STM, fine probe positioning is required for effective experiments. However, as mentioned previously (Section 1.2.2), the lateral range of traditional STM piezoelectric tube scanners is on the several micron scale.^{16,17} Given that originally

the size of probes used for SECM was also on the several micron scale, this range is not particularly useful. Hence SECM instruments have typically used positioning systems that have a much larger scan range with a greatly reduced resolution.⁵¹ Several different approaches to this have been taken including, but not limited to, electric stepper motors and stacked piezoelectric transducers.^{51,77} Typical stacked piezoelectric transducers have a range somewhere between 10 – 300 μm with the best possible resolution being around 0.1 nm. Stacked systems also tend to have poorer overall stability and rigidity than tube scanners, however, for electrochemical imaging they allow for a greater range of motion and usually easier mounting of probes, due to their larger overall size and mounting points.^{78,79}

Other components of SEPM instruments are very similar to STM ones. Generally instrumentation is housed inside a Faraday cage of some description to limit electronic noise from equipment and external sources.⁸⁰ Currents are measured using electrometers and potentiostats, the specifics of which depend on the absolute current measured and precision required.⁸⁰ It should be noted that SEPM currents can be much lower than tunnelling currents (especially with nanoscale SEPM).^{80–82}

1.4.1.3 Probes

Originally, SECM was carried out using UMEs.^{51–54} UMEs are widely used in electrochemistry due to having small diffusion layers and overall currents, which allows for steady state conditions and very high scan rates with minimal distortion.^{83,84} In essence a UME is simply an electrode where the electroactive area is on the scale of a few microns. Typically these are fabricated by taking a wire of electroactive metal (e.g. Au, Pt etc.) with a diameter between $\approx 1 - 30 \mu\text{m}$ and insulating it in a glass sheath.^{85,86} UMEs are then usually characterised by microscopy and voltammetry.⁸⁶

CVs are used widely in electrochemistry for characterising electrodes. During a potential sweep, the current measured will increase as the electrolysis begins. However, as the potential is swept further the electrolysis at the electrode surface reduces the local concentration of the species and the electrolysis rate becomes much greater than the diffusion rate of new material to the electrode. An example of the reversible reduction of Ferrocenium ($\text{Fc}^+ + \text{e}^- \rightleftharpoons \text{Fc}$) is shown in Figure 1.7A. As the potential is scanned negatively from A to D, Fc^+ is reduced to Fc at the electrode surface, resulting in depletion of Fc^+ near the electrode. At the peak cathodic current (C), diffusion of further Fc^+ from the bulk solution to the electrode surface becomes the limiting process. As the scan continues, the depletion layer of Fc^+ at the electrode surface (diffusion layer) continues to grow, slowing the mass transport of further Fc^+ to the electrode surface and hence reducing the measured current

(C→D).^{83,87} When the potential sweep direction is reversed (D→G), the concentration of Fc^+ at the surface is depleted but the concentration of Fc is increased. The Fc at the surface is oxidised back to Fc^+ as the potential is swept anodically.^{83,87}

The Nernst equation describes the relationship between the potential of the electrode (E) to the relative activities of the oxidised (Ox) and reduced form of a species (Red) at equilibrium:

$$E = E^0 + \frac{RT}{nF} \ln \frac{(\text{Ox})}{(\text{Red})} \quad (1.5)$$

where E^0 is the standard potential of the species, R is the gas constant, T is the temperature in Kelvin, n is the number of electrons transferred in the process and F is the Faraday constant.^{83,87} Applying this equation to the example above, E^0 is replaced by the formal potential ($E^{0'}$), which is dependent on specific experimental conditions, n is set to 1 and the activities of the oxidised and reduced form are replaced with the concentrations $[\text{Fc}^+]$ and $[\text{Fc}]$ respectively, such that:

$$E = E^{0'} + \frac{RT}{F} \ln \frac{[\text{Fc}^+]}{[\text{Fc}]} \quad (1.6)$$

The formal potential is given by the point at which the surface concentrations of Fc^+ and Fc are equal (Figure 1.7A, B and E). This can also be measured as the average potential of points C and F.^{83,87}

When carrying out CV experiments with UMEs and NEs, a sigmoidal response is observed, compared to macroscale electrodes where the characteristic peak shaped CV shape is seen (Figure 1.7A).^{83,87} In reality the shape of the CV is due to effects of both size and scan rate, for instance a UME or NE scanned quickly enough will also display the peaks. For a UME or NE, however, radial diffusion to the edges of the electrode becomes important and increases the diffusion rate to the electrode, meaning that steady state CVs can be obtained at much quicker scan rates than macro electrodes (see Figure 1.7B).^{83,87}

Two example CVs of a 10 μm diameter Au UME with different scan rates are shown in Figure 1.7C. It can be seen that at faster scan rates the CV deviates from the ideal steady state sigmoidal response and tends more towards a peak shaped CV such as Figure 1.7A. This transition can be described by the dimensionless scan rate:⁸⁸

$$\sigma = \left(\frac{F}{RT} \right) \left(\frac{\nu a^2}{D} \right) \quad (1.7)$$

where F is the Faraday constant, R is the gas constant, T is the temperature in Kelvin, ν is the scan rate in V s^{-1} , a is the electrode radius and D is the diffusion

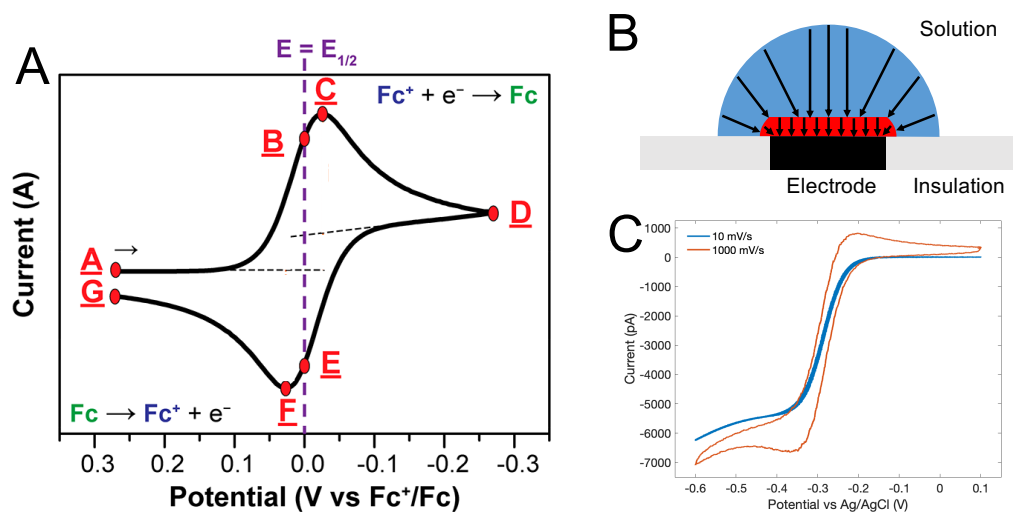


Figure 1.7: (A) Illustrative CV of reversible reduction for Fc^+ to Fc . Adapted from Elgrishi, *et al.*, *J. Chem. Educ.*, 95(2), **2018**.⁸⁷. (B) Diffusion profile of species to a microelectrode surface for a short time scale/ fast scan rate (red) and for a longer time scale/ slower scan rate (blue). (C) CVs of a 10 μm diameter Au UME in 5.5 mM $[\text{Ru}(\text{NH}_3)_6]^{3+}$ and 0.1 M KNO_3 with 10 mV s^{-1} (blue trace) and 1000 mV s^{-1} (orange trace) scan rates. Peaks in the CV are observed with faster scan rates for the same electrode.

coefficient. At $\sigma = 10^{-3}$ a sigmoidal response is measured, at $\sigma = 1$ peaks start to form and at $\sigma = 10^3$ a peak shaped response is observed.⁸⁸ In Figure 1.7C, σ is given by 0.0124 and 1.238 for 10 mV s^{-1} and 1000 mV s^{-1} respectively.

For UMEs with an infinite insulating sheath the steady state current measured at the UME can be determined from equation 1.8 for a disc shaped electrode (Figure 1.8A) and equation 1.9 for a hemispherical electrode (Figure 1.8B), where i_{ss} is the steady state limiting current, n is the number of electrons transferred in the redox process, F is the Faraday constant, D is the diffusion coefficient of the redox species, c is the concentration of the redox species and a is the radius of the UME.^{89,90} However, how large the insulating sheath has to be to be considered infinite is not trivial, it has been shown that deviations from the above can be up to 1.2 % for an electrode with an $RG = 10$, with decreasing deviations for increasing RG values (where RG is the ratio of insulating sheath radius to electrode radius, r_g/a).⁶⁷ Etched electrodes typically take the shape of a finite cone (Figure 1.8C) and follow equation 1.10 for the steady state current, where h is the length of the electrode exposed from the sheath, $q = 0.3661$, $p = 1.14466$ and $H = h/a$.⁹¹ The effect of an insulating sheath on conical electrodes has also been studied and follows

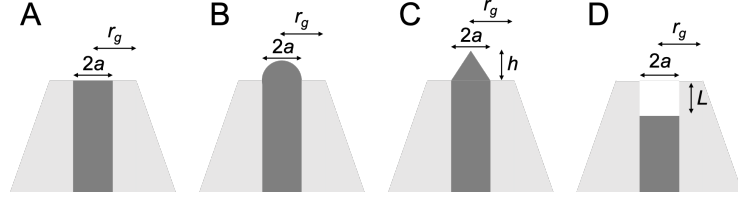


Figure 1.8: Example UME geometries with radius a , sheath radius r_g , height h and recession depth L labelled. Disc shaped (A), hemispherical (B), conical (C) and recessed (D) geometries for UMEs.

Table 1.1: Approximate numerical values for constants A, B, C & D with dependence on H for use with equation 1.11.⁹¹

	$H = 0$	$H = 0.5$	$H = 1$	$H = 2$	$H = 3$
A	1.0000	1.1270	1.2979	1.6769	2.0585
B	0.1380	0.1972	0.2795	0.5240	0.8910
C	0.6723	0.5667	0.4506	0.1794	-0.1900
D	-0.8686	-0.9025	-0.9436	-0.9857	-1.0288

equation 1.11, the values for A, B, C & D are dependent on H for which approximate analytical solutions give the values in Table 1.1.⁶⁵ If the electrode is recessed within the insulating sheath (Figure 1.8D), then the steady state current is reduced and given by equation 1.12, where L is the recession depth.⁹⁰

$$i_{ss}^{\text{disc}} = 4nFDca \quad (1.8)$$

$$i_{ss}^{\text{hemisphere}} = 2\pi nFDca \quad (1.9)$$

$$i_{ss}^{\text{cone}} = (1 + qH^P) 4nFDca \quad (1.10)$$

$$i_{ss}^{\text{cone}} = i_{ss}^{\text{disc}} (A + B(RG - C)^D) \quad (1.11)$$

$$i_{ss}^{\text{recess}} = \frac{4\pi nFDca^2}{4L + \pi a} \quad (1.12)$$

In more recent years the size of electrodes used has decreased dramatically (i.e. NEs) in an effort to increase the resolution of electrochemical studies and take electrochemistry to the nanoscale. Whilst much of UME theory and characterisation is compatible with NEs, NE fabrication and characterisation is a lot less trivial than

for UMEs and will be discussed later (Section 1.6).

1.4.1.4 Nanoscale SECM

The ultimate resolution of SECM is limited by two main factors: (i) the size of electrode used and (ii) diffusion of species to that electrode.⁴⁹ Hence reducing the size of the electrode increases the possible resolution of SECM (addressed in Section 1.6). A few reviews have covered recent nanoscale SECM studies and so some recent articles will be briefly summarised here.^{80,92,93} In one study the homogeneity of thiophenol diazonium films on HOPG has been addressed at the 10 s of nm scale, with 14 nm Pd nanocubes also being studied.⁹⁴ The hydrogen oxidation reaction on Pt nanoparticles (NPs) with a few 10s to 100 nm radius, with a focused ion beam (FIB) milled 90 nm radius PtNE, was also realised by one group.⁹⁵ 10 – 20 nm radius PtNEs have been used to study single NPs, with radii down to 10 nm being resolvable.⁹⁶ The same group has also demonstrated the investigation of HER on Au NPs with ≈ 6 nm spatial resolution using an ≈ 3 nm radius PtNE.⁹⁷ Another recent study also set out a method to create PtNEs without a laser puller and used a hopping mode approach to SECM as mentioned previously (section 1.4.1.1). However, whilst the electrodes were on the 100s of nm scale the SECM resolution was still on the micron scale.⁷⁴

Due to SECM being a non-contact technique it has also seen application in biological systems, with nanoscale SECM single biological samples have been investigated. SECM approach curves and amperometry have been applied to individual neurons at the 100 s of nm scale to elucidate the cellular permeability and the release of acetylcholine in response to high concentration K^+ stimulation.⁹⁸ Topographic images of human breast epithelial cell, have been obtained with a spatial resolution of ≈ 100 nm, this was achieved using negative feedback with $[Ru(NH_3)_6]^{3+}$ as the redox mediator.⁹⁹ A 300 nm PtNE has been used to measure the flux of FcMeOH across the cell membrane of epithelial cells.¹⁰⁰ NEs can also be inserted through the membrane of biological cells without affecting the activity of the cell. Species such as reactive oxygen and nitrogen species can then be measured.^{101,102} SECM has also been applied to membrane protein distribution on individual cells at the same time as obtaining topographic information.^{103,104}

In addition to the instrumentation requirements set out in Section 1.4.1.2, for effective nanoscale SECM imaging, even more attention is required to minimise vibrational and electronic noise in addition to minimising thermal drift. Minimising drift is especially important for constant height experiments.⁸⁰ A recent report detailed a nanoscale SECM instrument with specific focus on LabVIEW code for

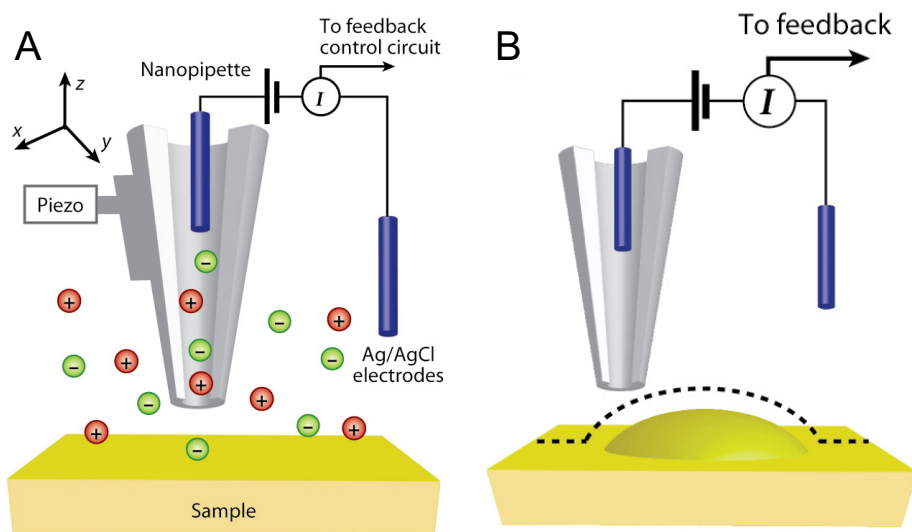


Figure 1.9: (A) SICM operational illustration, the nanopipette is filled with electrolyte, one electrode is inserted into the nanopipette and another into the bulk solution. A bias is applied between the electrodes to create an ion current, which can be used with a feedback loop to map topography (B). The nanopipette and/ or substrate is mounted on piezoelectric positioners to control the motion and separation of both. Posted with permission from the Annual Review of Analytical Chemistry, Volume 5(1), **2012**, © by Annual Reviews, <http://www.annualreviews.org>.¹⁰⁹

synchronous electrochemical and positional control, an isothermal chamber to minimise thermal drift, a bipotentiostat for electrochemical response and the SECM stage itself. These factors are all extremely important for effective operation of SECM at the nanoscale.⁸⁰

1.4.2 SICM

SICM is a form of SEPM that utilises the flow of ions between two quasi-reference counter electrodes (QRCEs), one inside a micro or nanopipette (tip) and the other in bulk solution, with a bias between them (Figure 1.9A). A QRCE is a simple electrode (such as a Ag/AgCl wire) which replaces the use of a standard reference and counter electrode, this is justifiable if the currents measured are small and the surface area of the QRCE is large in comparison to the working electrode.¹⁰⁵ As the pipette gets close to the surface (within a tip diameter), the flow of ions into or out of the pipette is hindered.^{106,107} Using this phenomena, SICM can be used to map topography of samples in solution (Figure 1.9B). SICM has been popular in imaging of soft samples such as biological systems due to its non-contact nature and the ability to operate in physiological solutions.^{107,108}

More recently SICM has also been used to gather much more information than just topography by adjusting the biases and probe motion throughout the scanning procedure. Functional information such as surface charge has also been obtained simultaneously with topographic information.^{110–113} This has been achieved using a hopping mode approach (see Section 1.4.1.1) where the probe is approached to a desired threshold and retracted at each predefined pixel whilst monitoring the probe position.^{75,76} However, a few different operational methods have been used with this mode. The first involves oscillating the probe with high frequency over a short range (288 Hz at 10 nm peak-to-peak in this study) during the approach, the ion alternating current (AC) and direct current (DC) response is measured along with the phase of the measured ionic current. The AC amplitude is used for the approach threshold, the last recorded approach location is used to map topography and the phase change is used to map surface charge.¹¹² Another SICM methodology involves oscillates the probe bias rather than probe position. The AC component of the current is sensitive to surface topography even with zero bias difference between the electrodes in bulk and in the nanopipette, when the potential difference is non-zero the current becomes sensitive to surface charge.¹¹⁰ In this case, the probe is approached with zero potential difference until a phase change threshold is reached (used to map topography). Then a CV is carried out at this position to sense surface charge, the probe is retracted and another CV is obtained to use for background correction.¹¹⁰ Increased speed and reduced complexity has been achieved by removing any AC components and approaching more traditionally with a small bias (+20 mV here) until a threshold change in DC current is obtained, this point is used to map topography. The significant speed improvement is made by then pulsing the bias to the most sensitive value for surface charge (−400 mV) rather than running a whole CV.¹¹³

In addition, one study using 30 nm diameter nanopipettes was able to simultaneously map topography and electrochemical reactivity with SICM.¹¹⁴ A hopping mode scanning protocol was employed where the probe is approached using a DC feedback first to measure topography, before a short retract (typically 20 nm). The retract step minimises the impact of the tip on mass transport at the substrate and avoids double layer effects on the current response. The substrate is then pulsed from a potential where no electrochemical reaction occurs to an active one for a short period (typically 20 ms). The response during the pulse phase is then used to map electrochemical reactivity, before the probe is retracted and moved to the next pixel.¹¹⁴

SICM has proven itself as an extremely effective technique in the SEPM

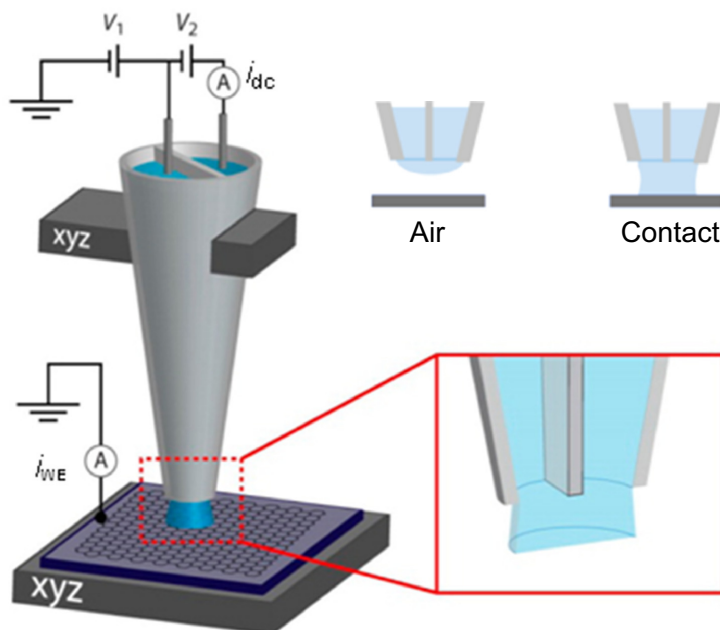


Figure 1.10: Illustration of double barrelled SECCM operation, where electrodes and electrolyte are used in both barrels to approach the probe into meniscus contact with the substrate. Reprinted from Bentley *et al.*, 6(1), **2017**, Copyright (2017), with permission from Elsevier.¹²⁰

field. However, the ultimate topographic resolution is limited by the size of the probe used; the resolution is on the order of three times the pipette radius.^{115–117} The smallest probes that have been used for SICM have been on the 10 – 20 nm diameter scale, giving a resolution around 20 nm.^{118,119} This resolution is impressive and much greater than typically possible with SECM but still short of STM and AFM.

1.4.3 SECCM

Scanning electrochemical cell microscopy (SECCM) uses a droplet at the end of a pipette to make local electrochemical measurements on a surface.¹²¹ A nanopipette is filled with electrolyte and a QRCE is inserted, the electrolyte will form a droplet/meniscus at the end of the pipette. The probe is approached to the substrate until contact is made by the meniscus to the surface (the pipette itself does not touch the surface), this creates a local electrochemical cell with a size similar to that of the probe diameter. Measurements are then made by applying a potential between the QRCE and the substrate. With contact made, the probe can then be scanned across the surface to generate a map of electrochemical activity. SECCM

can be used in this format with a single barrel pipette on conductive samples.^{122–124} However, SECCM can also be applied to insulating substrates, using a dual barrel pipette, by monitoring the current between the two barrels which gives information about deformation of the meniscus (Figure 1.10).^{121,123,125} Original studies with droplets studied corrosion on the surface of macroscopic electrodes on the scale of $1 - 1000 \mu\text{m}$.¹²⁶ SECCM operates on much smaller scales, using a hopping mode and applying traditional electrochemical measurements (i.e. CV, chronoamperometry) at each approach.^{123,124,127–129} The highest resolution examples recently used nanopipettes with a diameter of 30 nm to map homogeneous catalytic activity on 2D Au nanocrystals¹²⁴ and heterogeneous activity on Au NPs.¹²³

Whilst this resolution may increase slightly further with smaller nanopipettes, the resolution of SECCM, similarly to SICM, will always be limited by the size of the pipette used. However, as with SICM, this resolution is better than has been achieved with SECM but not at the scale of STM and AFM.

1.5 Hybrid SEPM Techniques

Hybrid SEPM techniques involve the combination of other SPM techniques to utilise the strengths of each technique and overcome some of the limitations of each. Below, some of the most common are described, with a focus on STM-SECM. Recent advancements have also been covered in several recent reviews.^{48–50}

1.5.1 AFM-SECM

The atomic force microscope - scanning electrochemical microscope (AFM-SECM) allows for simultaneous mapping of topography (AFM) and electrochemical activity (SECM).^{130–134} The key to AFM-SECM, like most hybrid techniques, is the choice of probe.^{130,131} The first AFM-SECM study used flattened and etched Pt microwires insulated with electrophoretic paint, to simultaneously map the topography and electrochemical activity of etched polycarbonate ultrafiltration membranes, and performing etching studies of crystals.¹³⁰ The flattened section serves as the cantilever and the insulation means that only the very end of the wire is exposed, creating a microelectrode. A following study converted a typical AFM cantilever, to a AFM-SECM probe by sputtering Au onto a silicon nitride AFM cantilever before insulating with a thin layer of silicon nitride by plasma enhanced chemical vapour deposition. Finally the Au was re-exposed using FIB. This AFM-SECM system was then applied to map an Au grating on a GaAs substrate.¹³¹

More recently, one study used a conical nanoscale electrode on the end of

an AFM tip, fabricated similarly to above with sputtering and chemical vapour deposition. However, Pt/C was then deposited onto the exposed Au using ion-beam induced deposition and sharpened using FIB. The end result was a probe with a diameter of ≈ 20 nm. The probes were then used to map topography and diffusion within arrays of nanopores.¹³⁵ A second recent study mapped topography and electrochemical activity of a calibration standard of Pt on SiO₂ using AFM-SECM with a 50 nm radius Pt probe. The probe was fabricated by mounting a nanoprobe onto a quartz cantilever in a FIB/SEM using adhesive hardened by the electron beam.¹³⁶ There is a small trade-off in ultimate SECM resolution here compared to the highest resolution achieved in purely SECM studies.⁹⁷ However, one of the clear advantages of AFM-SECM is that it solves the problem of topography/activity convolution (mentioned earlier Section 1.4.1). In addition, the AFM allows for a greater range of topography to be probed than with constant height SECM.⁴⁴ Now AFM-SECM instrumentation and probes are commercially available.^{133,137,138}

1.5.2 AFM-SICM

Atomic force microscopy - scanning ion conductance microscopy (AFM-SICM) has not been as widely adopted as AFM-SECM, likely because both AFM and SICM serve primarily as topographic techniques. A quantitative comparison of AFM and SICM as topographic techniques, in terms of contact point during approach and scanning, has been completed. Both techniques were applied to a calibration grid and a network of neurites on a Petri dish.¹³⁹ However, more interest has been in using the AFM component as a force sensor whilst the SICM like fluid channel can be used to deliver soluble molecules, often referred to as FluidFM (fluidic force microscopy).¹⁴⁰ The first study to do this created a hollow channel through an AFM cantilever with a hole at the end of the probe with diameter from 1 μ m to 100 nm to dispense solution.¹⁴⁰ The AFM feedback was used to position the probe and dyes were introduced into individual living cells.¹⁴⁰ Since then FluidFM has been applied in molecular and cellular biology in several studies.¹⁴¹

In addition to biological systems, FluidFM has been applied to electrochemical patterning.¹⁴² Here the AFM force feedback allowed for a soft approach to the electrode surface and for maintaining soft contact with the surface during topographical mapping and lithography processes. Copper was electroplated onto Cu by reduction of aryldiazonium salts from the fluid channel at the electrode surface.¹⁴² High speed charge mapping has also been realised with FluidFM; topography was mapped using the force feedback from AFM, whilst the ionic current was measured through the fluid channel to detect surface charge information.¹⁴³ This methodology

increases scan speed for charge mapping compared to other current SICM methods and allows charge mapping of “hard” materials. A recent study used cantilevers with a < 20 nm diameter opening for the fluid channel, representing the highest resolution FluidFM study to date (65 nm surface features). However, SICM topography was distorted due to effects from the probe opening angle and wall thickness, specifically local current enhancements at step edges. These distortions should be considered for future high resolution studies with SICM probes where there are larger wall thicknesses.¹⁴⁴ Similar to AFM-SECM, FluidFM is now commercially available, including the probes and full instruments.^{145,146}

1.5.3 STM-SECM

The basis of scanning tunnelling microscopy - scanning electrochemical microscopy (STM-SECM) is to make high resolution topographic maps (STM) simultaneously with electrochemical maps (SECM). The first attempt at STM-SECM mapped the topography of PdNPs on an Au(111) surface, retracted the tip away, generated H_2 at the surface by pulsing the potential, which was then amperometrically collected at the tip (SG/TC mode of SECM).¹⁴⁷ Another study used a similar approach, where a topographic map was made of an Au electrode, the tip coordinates were then traced with a small offset away from the surface (“lift-mode”) with the substrate at a suitable potential to drive reduction of $[\text{Ru}(\text{NH}_3)_6]^{3+}$ which was collected as $[\text{Ru}(\text{NH}_3)_6]^{2+}$ at the tip.¹⁴⁸ Both of these approaches acquired electrochemical information about the surfaces, however, in the first case the tip was much larger than the PdNPs studied and in the second, the exact NE geometry was difficult to determine and therefore effective modelling of the SECM data was not possible.

STM-SECM has seen a resurgence in the literature recently, mostly due to newer, easier methods for fabrication of NEs (see Section. 1.6). 14 nm Pd nanocubes were studied with a 10 nm Pt SECM tip, the observed resolution was much greater than would be possible with SECM due to diffusional broadening and further investigation suggested that the measured response was actually from electron tunnelling between the particle and a very sharp small point on the tip.¹⁴⁹ Subsequent studies from the same group investigated AuNPs on an insulating surface. Whilst the tip was $\gtrsim 4$ nm from the AuNP a positive feedback was recorded as FeMeOH oxidised at the tip was regenerated at the AuNP. Once the probe was brought closer then a tunnelling regime was reached between the tip and the NP, in this situation the particle then essentially acts as part of the tip. To show this, CVs were recorded in the SECM and in the tunnelling regime, showing an increased steady state current in $[\text{Ru}(\text{NH}_3)_6]^{3+}$ due to the increased size of the NP compared to the tip. The same

was done with HClO_4 , which showed a delayed onset for HER due to the difference in overpotential for Pt and Au.^{150,151}

NE fabrication is key to nanoscale electrochemistry. One group recently fabricated Au NEs using a bipolar electroless plating method (described in detail in Section 1.6). These probes were then approached to a surface using tunnelling feedback to investigate AuNPs on this surface with SECM in a constant height mode.¹⁵²

1.5.4 SICM-SECM

The most common probe for scanning ion conductance microscopy - scanning electrochemical microscopy (SICM-SECM) is a dual barrelled micro or nanopipette. One channel of the probe is left open to be used as an SICM probe for topographic mapping and positioning, whilst the other is filled with a solid electrode material for SECM electrochemical mapping.¹⁵³ Much like standard SICM, this technique has been very effective in mapping various biological systems such as *Zea mays* root hair cells. In this specific study the SICM channel was used to both map topography and deliver $[\text{Ru}(\text{NH}_3)_6]^{3+}$, uptake of the $[\text{Ru}(\text{NH}_3)_6]^{3+}$ was simultaneously monitored by the SECM channel. A key development in this study was updating both channels in bulk solution at each pixel, this allows any drift or deterioration during the scan to be monitored.¹⁵⁴ Another dual barrelled experiment (probes between 100 nm to 1 μm total diameter) has been carried out, where the carbon barrel was sensitised via the electrodeposition of PtNPs. The PtNPs increase the measured response from the ORR and enabled mapping of the electrocatalytic process on Pt nanospheres, where the smallest case measured was spheres with 150 nm diameter.¹⁵⁵ A different approach to SICM-SECM has been demonstrated where a nanopipette/ nanoring electrode was fabricated.¹⁵⁶ This was done by coating a glass nanopipette with Ti/Pt or Ti/Au via sputtering, followed by electrophoretic paint insulation. The final fabrication step was to FIB mill the end of the electrode. The result is a probe which has an empty channel at the centre for SICM, surrounded by a glass wall, further surrounded by a ring electrode for SECM, finally encapsulated by electrophoretic paint. The final probes had an SICM channel diameter of 220 nm, the ring electrode had an inner and outer diameter of 330 nm and 550 nm respectively.¹⁵⁶ These probes were then applied to simultaneous mapping of topography and electrochemistry for enzymes and single live cells.¹⁵⁶

SICM-SECM once again overcomes the topography/ activity convolution that is encountered with traditional SECM. SICM-SECM, however, faces the same issues as its individual techniques in terms of the achievable resolution; the probe

size is the limiting factor and making dual barrel pipettes down to sub 100 nm is even more challenging than for single channel probes.

1.6 Nanoelectrodes

NEs have many uses in electrochemistry,^{48,50,157–159} specific to this thesis is their use for nanoscale electrochemical mapping. The first type of nanoelectrodes were nanobands as they are easier to produce than disc type electrodes,^{160–162} however nanobands are not typically suitable for electrochemical mapping¹⁶² and hence the rest of the following will primarily address disc and conical type electrodes. The main goals of NE fabrication are to make reproducible, cheap and robust probes. Characterisation of NEs is also non-trivial, various electrochemical and microscopy techniques have been used to elucidate information such as geometry and overall electroactive area.^{55,163,164}

1.6.1 Fabrication

As mentioned previously (Section 1.2.3), EC-STM generally limits Faradaic currents by insulating a Pt/Ir or W wire. However, the size and geometry of these electrodes are not typically suitable for nanoscale electrochemical mapping, because although the leakage current for these probes is, by definition, small enough to still observe the tunnelling current, nanoscale electrochemical currents can be orders of magnitude smaller.^{81,82,165} However, this is not always the case; one study used etched Pt wire insulated with electrophoretic paint to produce electrodes with radii between 1 μm and 10 nm, and measured electrochemical currents down to 100 pA with their smallest electrodes.¹⁶⁶ Other groups have also used this method for electrochemical studies, increasing the detection limits possible.^{167,168} However, in addition to the overall area, electrode geometry plays a large role in the electrochemical response of probes and in general these methods have a poorly defined geometry. Therefore, different methods are typically used to make NEs for electrochemical imaging.^{48,55,163,164}

One slightly different approach with electrophoretic paint was reported, where a glass capillary was laser pulled and then externally coated in AuNPs, the Au tip was then insulated with electrophoretic paint as mentioned in section 1.2.3.¹⁶⁹ This method improves upon the geometry issue of wires but would still face challenges with the insulating stage.

PtNEs have been fabricated by laser pulling Pt wire inside a glass capillary. In short, a Pt wire is inserted inside a glass capillary and a vacuum is applied to each

end of the capillary prior to the laser pulling process. The laser pulling program is then split into two phases, the first phase starts the quartz melting and sealing around the Pt, the second phase then pulls the capillary into two parts as normal.¹⁷⁰ Tuning the exact parameters for these NEs proves challenging, plus parameters are not transferable between different laser pulling instruments, even of the same model.

Another method for fabricating NEs involves the pyrolysis of hydrocarbons inside a quartz nanopipette to form a carbon nanoelectrode (CNE). Typically this has been done by laser pulling a quartz capillary to a small diameter (nanopipette), flowing butane through the back of the nanopipette, flowing Ar over the end using a larger capillary, before heating the system with a butane torch (or similar).¹⁷¹ Whilst this method is quick, cheap and easy, it often results in electrodes which are recessed or damaged with misleading voltammetric results.¹⁷² Recently one group has taken a more analytical approach to the same method by strictly controlling the parameters involved. Butane and Ar flow/ pressure is controlled and the torch is replaced by an electrically heated coil which also has fine motor control. The whole fabrication instrument is also kept in a controlled atmosphere.¹⁷² This methodology is discussed thoroughly in Chapter 2.

The carbon burning method has also been used to fabricate dual barrel NEs for use in SICM-SECM, by plugging one barrel of a theta pipette during the burning, one channel is left open for SICM measurements while the other is filled with carbon for SECM measurements.^{173,174}

Another method for CNE fabrication is similar to traditional EC-STM tips where a carbon fiber is electrochemically etched using a 50 Hz square wave voltage (4 – 5.5 V) in 10 mM NaOH solution. The tip is then insulated with electrophoretic paint (Clearclad HSR, LVH Coating Ltd, U.K.) by applying a 5 – 7 V bias for 60 – 90 s, curing (~ 195 °C for ~ 30 mins) and then depositing again for 20 – 40 s before another final cure. In contrast to EC-STM tips made with Pt/Ir wire, this method has produced CNEs with a reported radius of 1 nm.^{175,176}

The same group (Chen & Kucernak)^{175,176} studied the electrochemical deposition of Pt on carbon using these carbon fibre NEs. Electrodeposition was performed by submerging the electrode in 1 mM H_2PtCl_6 with 100 mM H_2SO_4 , 0.8 V is applied (vs saturated calomel electrode, SCE) before deposition and then the potential was stepped to the deposition potential. A variety of potentials were tested to gather information about the Pt deposition process.¹⁷⁷ Another group carried out similar experiments to fabricate single Pt nanocrystals on carbon burnt NEs.¹⁷⁸ Both reports were primarily concerned with the deposition process itself, however, the methodologies could suggest a new way to create PtNEs as will be discussed

later (Chapter 2).

A recently reported method used a bipolar electrodeposition method to fabricate AuNEs of 30 nm diameter. In short a quartz capillary is laser pulled to a 30 nm opening and filled with a Au deposition solution (10 mM HAuCl_4 and 10 mM KCl in deionised water) and a Ag/AgCl reference electrode is inserted. The pipette is then submerged into a solution of 10 mM NaBH_4 in ethanol with a 0.3 V bias applied between the reference in the pipette and one in the NaBH_4 solution. A chemical reduction creates a Au plug at the end of the pipette, this results in a closed bipolar electrode from which Au is then electrochemically reduced at the inner face of the Au plug causing further growth of the plug back up the pipette.¹⁷⁹ This method is quick ($\approx 5 - 10$ minutes) and creates a very reproducible AuNE that can be operated in a bipolar fashion (see Chapter 4).

Another group (Zhang *et. al.*)^{180,181} demonstrated electroplating of laser pulled capillaries by filling with any of Ag, Au, Cu and Pt deposition solutions and immersing the capillary in a gallium/indium electrode. FIB milling is then used to create the final disc shaped electrode with sizes ranging from 30 – 350 nm in diameter.¹⁸⁰ Another report demonstrated a similar approach using Ag, Au and Pt solutions inside and an organic phase outside the pipette. Electrodes were made with diameters from 50 – 5000 nm.¹⁸¹

The final stages of NE fabrication often includes FIB milling as this can create a very well controlled final size for electrodes and potentially remove any damage or inconsistencies at the very end, it also creates a well defined disc shape ideal for SECM studies. Unfortunately FIB instruments are expensive and not widely available, also FIB milling electrodes accurately below 100 nm proves very challenging.^{173,182} Despite these limitations FIB milling is becoming more widely used in the literature.^{48,164}

1.6.2 Characterisation

The main two ways of characterising NEs are by microscopy and electrochemistry techniques. Typically microscopy will be in the form of transmission electron microscopy (TEM) as this gives the best resolution and, due to the transmission, in some cases can elucidate information about the internal structure of the NE.^{163,170} Care must be taken however with high electron energies used in TEM as these can damage or alter NE structure and geometry.^{163,170} In addition, often NEs have to be broken at some point to fit them onto a TEM grid or holder, meaning that TEM must be carried out after the probe has been used.^{163,170} Electrochemical methods generally involve running steady state voltammetry in a redox mediator. Whilst

this often allows for characterisation in-situ and does not necessarily require expensive equipment, voltammetric results can be very misleading without accompanied microscopy techniques.^{172,183,184}

Similar to UMEs discussed in section 1.4.1.3, CV is the most common way of electrochemically characterising NEs. Equations 1.8–1.12 still apply to NEs, however, determining specific values for geometric dimensions can be more difficult.¹⁵⁹ UMEs are often made from a wire of fixed diameter and therefore the radius parameter is well defined. In the case of NEs this value may not be trivial to determine, in addition features such as recession and leakage are more commonly observed in NEs than with larger scale electrodes.^{81,170,184} One way to determine if there is leakage is to compare CVs with different scan rates. With significant leakage, peak like features can be observed with fast scan rates ($\gtrsim 10 \text{ V s}^{-1}$) due to the electroactive species being present inside the insulation, these peaks will have an area proportional to the scan rate.⁹⁶

Another geometry observed which is less common with larger electrodes is the “nanosampler” or cavity electrode. This is when a CNE is formed similar to a recessed geometry but with carbon deposited along the walls and a more conical geometry inside the electrode (Figure 1.11A).¹⁸³ In this case, under CV, instead of a sigmoidal steady state response, a peaked response more similar to a macroscale electrode CV is observed (Figure 1.11B). This is because the redox material inside the cavity becomes depleted quickly. However, past the peak a steady state limiting current is reached which is only dependent on the diameter of the aperture at the end of the capillary.¹⁸³ The area under the peak is proportional to the scan rate and to the volume of the cavity, such that the volume is given by:

$$V = \frac{Q}{cF} \quad (1.13)$$

where Q is the total charge given by the area under the peak, F is the Faraday constant and c is the redox species concentration. In addition to these features, if the area under the peak increases with subsequent sweeps, then this indicates a hollow electrode as the solution makes its way further and further along the capillary.¹⁸³

1.7 Aims and Objectives

As mentioned above, electrochemical imaging techniques are limited in their lateral topographic resolution by both the size of the probe used and the diffusion of redox species to that probe. STM-SECM (Section 1.5.3) is one potential avenue to

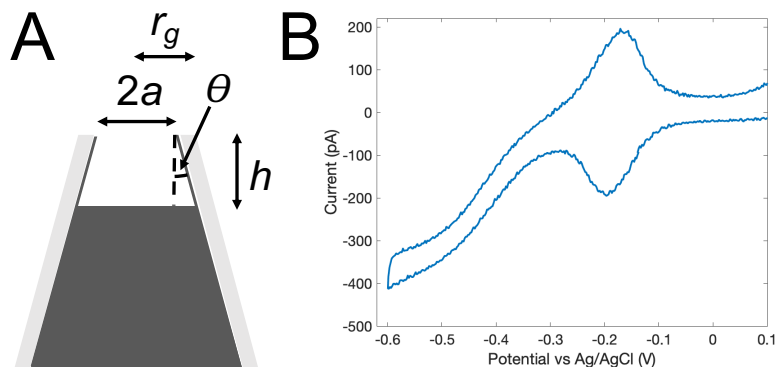


Figure 1.11: (A) Schematic of cavity electrode geometry. Carbon fills partially up the nanopipette and along the walls to the end. (B) CV of a CNE exhibiting features expected for a cavity electrode, both peaks and a steady state response are observed. 5 mM $[\text{Ru}(\text{NH}_3)_6]^{3+}$ in 0.1 M KCl with a 0.2 V s^{-1} scan rate. Data collected personally.

overcome this limitation. One key challenge to STM-SECM is the methodology of probe motion and the differing length scales typically studied with STM and SECM. The goal of Chapter 3 is to assess the suitability of a state of the art electrochemical imaging instrument for tunnelling type studies and C-SECM measurements. A hopping style approach to C-SECM was carried out with an exemplar system of Au nanocrystals on a GC support. Lateral topographic resolution much better than previous SEPM work is demonstrated, but the instrumentation configuration does have its limitations and will be compared to other recent studies with similar methodologies.

The second key challenge of STM-SECM is the choice, fabrication and characterisation of NEs. This is a challenge in various areas of nanoscale electrochemistry, not only for STM-SECM, and so Chapter 2 aims to fabricate CNEs with a previously documented method before electrodeposition of Pt onto these electrodes in order to create ideal NEs for STM-SECM studies. Due to the limitations and difficulties discussed in Chapter 2, a newer method for fabrication and characterisation is investigated in Chapter 4 with the goal of improving upon the reliability and reproducibility of electrodes from Chapter 2. Whilst this method shows great promise in terms of NE geometry studied with electron microscopy, the electrochemical response does present some challenges.

Chapter 5 of this thesis attempts to assess the suitability of the electrodes fabricated in Chapter 4 for in-situ STM and SECM, which, in future, could lead to their use in STM-SECM experiments and other nanoscale electrochemical experi-

ments.

Efforts to understand the mechanism of benzotriazole adsorption on copper are taken in Chapter 6. Much debate and relatively few studies exist in regards to the adsorption of benzotriazole on copper at the molecular level. Here the goal was to make some progress towards a full adsorption model utilising STM in an ideal system of a Cu(110) surface in UHV, which also demonstrates the information attainable at the molecular level with STM. High resolution electron energy loss spectroscopy (HREELS) data was also acquired to aid in STM analysis and the role of oxygen in the adsorption process was also briefly investigated.

1.8 References

- [1] Binning, G., Rohrer, H., Gerber, C. & Weibel, E. *Phys. Rev. Lett.*, 49(1), 57–61, **1982**.
- [2] Ramachandra Rao, M. S. & Margaritondo, G. *J. Phys. D: Appl. Phys.*, 44(46), 460301, **2011**.
- [3] Eigler, D. M. & Schweizer, E. K. *Nature*, 344(6266), 524–526, **1990**.
- [4] Eigler, D. M., Weiss, P. S., Schweizer, E. K. & Lang, N. D. *Phys. Rev. Lett.*, 66(9), 1189–1192, **1991**.
- [5] Ferris, J. H., Kushmerick, J. G., Johnson, J. A., Yoshikawa Youngquist, M. G., Kessinger, R. B., Kingsbury, H. F. & Weiss, P. S. *Rev. Sci. Instrum.*, 69(7), 2691–2695, **1998**.
- [6] Della Pia, A. & Costantini, G. In G. Bracco & B. Holst, editors, *Surf. Sci. Tech.*, Wiley-VCH, Berlin, Heidelberg, pages 565–597. **2013**.
- [7] Nichols, R. J. & Higgins, S. J. *Acc. Chem. Res.*, 49(11), 2640–2648, **2016**.
- [8] Nazmutdinov, R. R., Zinkicheva, T. T., Shermukhamedov, S. A., Zhang, J. & Ulstrup, J. *Curr. Opin. Electrochem.*, 7, 179–187, **2018**.
- [9] Mironov, V. L. *Fundamentals of Scanning Probe Microscopy*. Wiley-VCH, **2004**.
- [10] Wüthrich, R., Hof, L., Lal, A., Fujisaki, K., Bleuler, H., Mandin, P. & Picard, G. *J. Micromechanics Microengineering*, 15, S268–S275, **2005**.
- [11] Bardeen, J. *Phys. Rev. Lett.*, 6(2), 57–59, **1961**.
- [12] Gottlieb, A. D. & Wesoloski, L. *Nanotechnology*, 17(8), R57–R65, **2006**.
- [13] Tersoff, J. & Hamann, D. R. *Phys. Rev. B*, 31(2), 805–813, **1985**.
- [14] Qin, Q.-H. In *Adv. Mech. Piezoelectricity*, Wiley-VCH, Berlin, Heidelberg, pages 1–19. **2013**.
- [15] Chen, C. J. & Smith, W. F. *Introduction to Scanning Tunneling Microscopy*, volume 62. Wiley-VCH, 2nd edition, **1994**.
- [16] Kalkan, F., Zaum, C. & Morgenstern, K. *Rev. Sci. Instrum.*, 83(10), 103903, **2012**.

- [17] Petersen, L., Schunack, M., Schaefer, B., Linderoth, T. R., Rasmussen, P. B., Sprunger, P. T., Laegsgaard, E., Stensgaard, I. & Besenbacher, F. *Rev. Sci. Instrum.*, 72(2), 1438–1444, **2001**.
- [18] Wintterlin, J., Zambelli, T., Barth, J. V. & Ertl, G. *Nature*, 390(6659), 495–497, **1997**.
- [19] Bai, C. *Scanning Tunneling Microscopy and Its Application*. Wiley-VCH, **2000**.
- [20] Drake, B., Sonnenfeld, R., Schneir, J. & Hansma, P. K. *Surf. Sci.*, 181(1-2), 92–97, **1987**.
- [21] Bach, C. E., Nichols, R. J., Meyer, H. & Besenhard, J. O. *Surf. Coat. Technol.*, 67(3), 139–144, **1994**.
- [22] Nagahara, L. A., Thundat, T. & Lindsay, S. M. *Rev. Sci. Instrum.*, 60(10), 3128–3130, **1989**.
- [23] Sattler, K. D. *Handbook of Nanophysics: Principles and Methods*. Wiley-VCH, 1st edition, **2017**.
- [24] Wiechers, J., Twomey, T., Kolb, D. M. & Behm, R. J. *J. Electroanal. Chem.*, 248(2), 451–460, **1988**.
- [25] Green, M. P., Hanson, K. J., Scherson, D. A., Xing, X., Richter, M., Ross, P. N., Carr, R. & Lindau, I. *J. Phys. Chem.*, 93(6), 2181–2184, **1989**.
- [26] Vitus, C. M., Chang, S. C., Schardt, B. C. & Weaver, M. J. *J. Phys. Chem.*, 95(20), 7559–7563, **1991**.
- [27] Thorgaard, S. N. & Buhlmann, P. *Anal. Chem.*, 79(23), 9224–9228, **2007**.
- [28] Bach, C. E., Nichols, R. J., Beckmann, W. & Meyer, H. *J. Electrochem. Soc.*, 140(5), 1281, **1993**.
- [29] Schulte, A. *Proc. SPIE*, 3512, 353–357, **1998**.
- [30] Binnig, G., Rohrer, H., Gerber, C. & Weibel, E. *Phys. Rev. Lett.*, 50(2), 120–123, **1983**.
- [31] Schneir, J., Sonnenfeld, R., Hansma, P. K. & Tersoff, J. *Phys. Rev. B*, 34(8), 4979–4984, **1986**.

- [32] Sonnenfeld, R. & Hansma, P. K. *Science*, 232(4747), 211–213, **1986**.
- [33] Dovek, M. M., Heben, M. J., Lang, C. A., Lewis, N. S. & Quate, C. F. *Rev. Sci. Instrum.*, 59(11), 2333–2336, **1988**.
- [34] Bussetti, G., Yivlialin, R., Alliata, D., Li Bassi, A., Castiglioni, C., Tomasini, M., Casari, C. S., Passoni, M., Biagioni, P., Ciccacci, F. & Duò, L. *J. Phys. Chem. C*, 120(11), 6088–6093, **2016**.
- [35] Bui, N. N., Ledina, M., Reber, T. J., Jung, J. & Stickney, J. L. *ACS Nano*, 11(9), 9481–9489, **2017**.
- [36] Gu, J. Y., Cai, Z. F., Wang, D. & Wan, L. J. *ACS Nano*, 10(9), 8746–8750, **2016**.
- [37] Jacobse, L., Huang, Y. F., Koper, M. T. & Rost, M. J. *Nat. Mater.*, 17(3), 277–282, **2018**.
- [38] Wen, R., Rahn, B. & Magnussen, O. M. *J. Phys. Chem. C*, 120(29), 15765–15771, **2016**.
- [39] Matsushima, H., Lin, S. W., Morin, S. & Magnussen, O. M. *Faraday Discuss.*, 193(0), 171–185, **2016**.
- [40] Pfisterer, J. H., Liang, Y., Schneider, O. & Bandarenka, A. S. *Nature*, 549(7670), 74–77, **2017**.
- [41] Binnig, G. K. *Method and atomic force microscope for imaging faces with atomic resolution*. US4724318A, **1990**.
- [42] Bhushan, B. *Handbook of Micro/Nano Tribology*. Wiley-VCH, 2nd edition, **1998**.
- [43] Goldie, I. & Wetterqvist, H. *Acta Orthop. Belgica*, 40(3), 285–293, **1974**.
- [44] Haugstad, G. *Atomic force microscopy : understanding basic modes and advanced applications*. Wiley-VCH, **2012**.
- [45] Martin, Y., Williams, C. C. & Wickramasinghe, H. K. *J. Appl. Phys.*, 61(10), 4723–4729, **1987**.
- [46] Zhong, Q., Inniss, D., Kjoller, K. & Elings, V. B. *Surf. Sci.*, 290(1-2), L688–L692, **1993**.

- [47] Seo, Y. & Jhe, W. *Reports Prog. Phys.*, 71(1), 16101, **2007**.
- [48] Bentley, C. L., Edmondson, J., Meloni, G. N., Perry, D., Shkirskiy, V. & Unwin, P. R. *Anal. Chem.*, 91(1), 84–108, **2019**.
- [49] O’Connell, M. A. & Wain, A. J. *Anal. Methods*, 7(17), 6983–6999, **2015**.
- [50] Takahashi, Y., Kumatani, A., Shiku, H. & Matsue, T. *Anal. Chem.*, 89(1), 342–357, **2017**.
- [51] Bard, A. J., Fan, F. R. F., Kwak, J. & Lev, O. *Anal. Chem.*, 61(2), 132–138, **1989**.
- [52] Engstrom, R. C., Weber, M., Wunder, D. J., Burgess, R. & Winquist, S. *Anal. Chem.*, 58(4), 844–848, **1986**.
- [53] Kwak, J. & Bard, A. J. *Anal. Chem.*, 61(17), 1794–1799, **1989**.
- [54] Kwak, J. & Bard, A. J. *Anal. Chem.*, 61(11), 1221–1227, **1989**.
- [55] Zoski, C. G. *J. Electrochem. Soc.*, 163(4), H3088–H3100, **2016**.
- [56] Barker, A. L., Gonsalves, M., MacPherson, J. V., Slevin, C. J. & Unwin, P. R. *Anal. Chim. Acta*, 385(1-3), 223–240, **1999**.
- [57] Unwin, P. R. & Bard, A. J. *J. Phys. Chem.*, 95(20), 7814–7824, **1991**.
- [58] Denuault, G., Frank, M. H. T. & Nugues, S. In A. A. Gewirth & H. Siegenthaler, editors, *Nanoscale Probes of the Solid/Liquid Interface*, Springer Netherlands, Dordrecht, pages 69–82. **1995**.
- [59] Bard, A. J. & Mirkin, M. V. *Scanning Electrochemical Microscopy*. Wiley-VCH, 2nd edition, **2012**.
- [60] Fernández, J. L. & Bard, A. J. *Anal. Chem.*, 75(13), 2967–2974, **2003**.
- [61] Fernández, J. L., Walsh, D. A. & Bard, A. J. *J. Am. Chem. Soc.*, 127(1), 357–365, **2005**.
- [62] Martin, R. D. & Unwin, P. R. *J. Electroanal. Chem.*, 439(1), 123–136, **1997**.
- [63] Martin, R. D. & Unwin, P. R. *Anal. Chem.*, 70(2), 276–284, **1998**.
- [64] Bard, A. J., Denuault, G., Friesner, R. A., Dornblaser, B. C. & Tuckerman, L. S. *Anal. Chem.*, 63(13), 1282–1288, **1991**.

- [65] Zoski, C. G. & Mirkin, M. V. *Anal. Chem.*, 74(9), 1986–1992, **2002**.
- [66] Zoski, C. G., Liu, B. & Bard, A. J. *Anal. Chem.*, 76(13), 3646–3654, **2004**.
- [67] Amphlett, J. L. & Denuault, G. *J. Phys. Chem. B*, 102(49), 9946–9951, **1998**.
- [68] Ekanayake, C. B., Wijesinghe, M. B. & Zoski, C. G. *Anal. Chem.*, 85(8), 4022–4029, **2013**.
- [69] Mirkin, M. V., Richards, T. C. & Bard, A. J. *J. Phys. Chem.*, 97(29), 7672–7677, **1993**.
- [70] Denuault, G., Mirkin, M. V. & Bard, A. J. *J. Electroanal. Chem.*, 308(1-2), 27–38, **1991**.
- [71] Rodríguez-López, J., Alpuche-Avilés, M. A. & Bard, A. J. *J. Am. Chem. Soc.*, 130(50), 16985–16995, **2008**.
- [72] Schrock, D. S., Wipf, D. O. & Baur, J. E. *Anal. Chem.*, 79(13), 4931–4941, **2007**.
- [73] Wipf, D. O., Bard, A. J. & Tallman, D. E. *Anal. Chem.*, 65(10), 1373–1377, **1993**.
- [74] Jedraszko, J., Michalak, M., Jönsson-Niedziolka, M. & Nogala, W. *J. Electroanal. Chem.*, 815, 231–237, **2018**.
- [75] Novak, P., Li, C., Shevchuk, A. I., Stepanyan, R., Caldwell, M., Hughes, S., Smart, T. G., Gorelik, J., Ostanin, V. P., Lab, M. J., Moss, G. W., Frolenkov, G. I., Klenerman, D. & Korchev, Y. E. *Nat. Methods*, 6(4), 279–281, **2009**.
- [76] Takahashi, Y., Murakami, Y., Nagamine, K., Shiku, H., Aoyagi, S., Yasukawa, T., Kanzaki, M. & Matsue, T. *Phys. Chem. Chem. Phys.*, 12(34), 10012–10017, **2010**.
- [77] Luo, H., Dong, C., Gao, S., Du, C., Xiao, K. & Li, X. *RSC Adv.*, 4(100), 56582–56595, **2014**.
- [78] Zhang, P. In *Adv. Ind. Control Technol.*, Wiley-VCH, Oxford, chapter 3, pages 73–116. **2010**.
- [79] Physik Instrumente LTD UK. *PICA Piezoelectric Stack Actuators*, www.physikinstrumente.co.uk/en/products/piezoelectric-transducers-actuators/stack-actuators/, **2019**.

- [80] Kim, J., Renault, C., Nioradze, N., Arroyo, N., Leonard, K. C. & Bard, A. J. *Anal. Chem.*, 88(20), 10284–10289, **2016**.
- [81] Sun, P. & Mirkin, M. V. *Anal. Chem.*, 78(18), 6526–6534, **2006**.
- [82] Zhang, B., Galusha, J., Shiozawa, P. G., Wang, G., Bergren, A. J., Jones, R. M., White, R. J., Ervin, E. N., Cauley, C. C. & White, H. S. *Anal. Chem.*, 79(13), 4778–4787, **2007**.
- [83] Wightman, R. M. *Anal. Chem.*, 53(9), 1125A–1134A, **1981**.
- [84] Heinze, J. *Angew. Chemie Int. Ed. English*, 32(9), 1268–1288, **1993**.
- [85] Sur, U. K., Dhason, A. & Lakshminarayanan, V. *J. Chem. Educ.*, 89(1), 168–172, **2012**.
- [86] Danis, L., Polcari, D., Kwan, A., Gateman, S. M. & Mauzeroll, J. *Anal. Chem.*, 87(5), 2565–2569, **2015**.
- [87] Elgrishi, N., Rountree, K. J., McCarthy, B. D., Rountree, E. S., Eisenhart, T. T. & Dempsey, J. L. *J. Chem. Educ.*, 95(2), 197–206, **2018**.
- [88] Compton, R. G. & Banks, C. E. *Understanding Voltammetry*. Wiley-VCH, 2nd edition, **2011**.
- [89] Bond, A. M., Oldham, K. B. & Zoski, C. G. *J. Electroanal. Chem. Interfacial Electrochem.*, 245(1), 71–104, **1988**.
- [90] Bond, A. M., Luscombe, D., Oldham, K. B. & Zoski, C. G. *J. Electroanal. Chem. Interfacial Electrochem.*, 249(1), 1–14, **1988**.
- [91] Zoski, C. *Electroanalysis*, 14(1516), 1041–1051, **2002**.
- [92] Kai, T., Zoski, C. G. & Bard, A. J. *Chem. Commun.*, 54(16), 1934–1947, **2018**.
- [93] Izquierdo, J., Knittel, P. & Kranz, C. *Anal. Bioanal. Chem.*, 410(2), 307–324, **2018**.
- [94] Blanchard, P.-Y., Sun, T., Yu, Y., Wei, Z., Matsui, H. & Mirkin, M. V. *Langmuir*, 32(10), 2500–2508, **2016**.
- [95] Kim, J., Renault, C., Nioradze, N., Arroyo-Currás, N., Leonard, K. C. & Bard, A. J. *J. Am. Chem. Soc.*, 138(27), 8560–8568, **2016**.

- [96] Yu, Y., Sun, T. & Mirkin, M. V. *Anal. Chem.*, 87(14), 7446–7453, **2015**.
- [97] Sun, T., Yu, Y., Zacher, B. J. & Mirkin, M. V. *Angew. Chemie - Int. Ed.*, 53(51), 14120–14123, **2014**.
- [98] Welle, T., Alanis, K., Colombo, M. L., Sweedler, J. V. & Shen, M. *Chem. Sci.*, 9(22), 4937–4941, **2018**.
- [99] Sun, P., Laforge, F. O., Abeyweera, T. P., Rotenberg, S. A., Carpino, J. & Mirkin, M. V. *Proc. Natl. Acad. Sci.*, 105(2), 443 LP – 448, **2008**.
- [100] Bergner, S., Wegener, J. & Matysik, F.-M. *Anal. Methods*, 4(3), 623–629, **2012**.
- [101] Wang, Y., Noël, J.-M., Velmurugan, J., Nogala, W., Mirkin, M. V., Lu, C., Guille Collignon, M., Lemaître, F. & Amatore, C. *Proc. Natl. Acad. Sci.*, 109(29), 11534 LP – 11539, **2012**.
- [102] Li, Y., Hu, K., Yu, Y., Rotenberg, S. A., Amatore, C. & Mirkin, M. V. *J. Am. Chem. Soc.*, 139(37), 13055–13062, **2017**.
- [103] Takahashi, Y., Miyamoto, T., Shiku, H., Asano, R., Yasukawa, T., Kumagai, I. & Matsue, T. *Anal. Chem.*, 81(7), 2785–2790, **2009**.
- [104] Takahashi, Y., Shevchuk, A. I., Novak, P., Babakinejad, B., Macpherson, J., Unwin, P. R., Shiku, H., Gorelik, J., Klenerman, D., Korchev, Y. E. & Matsue, T. *Proc. Natl. Acad. Sci.*, 109(29), 11540 LP – 11545, **2012**.
- [105] Perera, R. T. & Rosenstein, J. K. *Sci. Reports*, 8(1), 1965, **2018**.
- [106] Wilkins, S. J. & Finlan, M. F. In *Handb. Phys. Med. Biol.*, Wiley-VCH, volume 243, chapter 35. **2010**.
- [107] Siegel, S. *Zeitschrift fur Kunstgeschichte*, 79(2), 159–163, **2016**.
- [108] Korchev, Y. E., Bashford, C. L., Milovanovic, M., Vodyanoy, I. & Lab, M. J. *Biophys. J.*, 73(2), 653–658, **1997**.
- [109] Chen, C.-C., Zhou, Y. & Baker, L. A. *Annu. Rev. Anal. Chem.*, 5(1), 207–228, **2012**.
- [110] Perry, D., Al Botros, R., Momotenko, D., Kinnear, S. L. & Unwin, P. R. *ACS Nano*, 9(7), 7266–7276, **2015**.

- [111] Sa, N., Lan, W. J., Shi, W. & Baker, L. A. *ACS Nano*, 7(12), 11272–11282, **2013**.
- [112] McKelvey, K., Kinnear, S. L., Perry, D., Momotenko, D. & Unwin, P. R. *J. Am. Chem. Soc.*, 136(39), 13735–13744, **2014**.
- [113] Page, A., Perry, D., Young, P., Mitchell, D., Frenguelli, B. G. & Unwin, P. R. *Anal. Chem.*, 88(22), 10854–10859, **2016**.
- [114] Kang, M., Perry, D., Bentley, C. L., West, G., Page, A. & Unwin, P. R. *ACS Nano*, 11(9), 9525–9535, **2017**.
- [115] Edwards, M. A., Williams, C. G., Whitworth, A. L. & Unwin, P. R. *Anal. Chem.*, 81(11), 4482–4492, **2009**.
- [116] Weber, A. E. & Baker, L. A. *J. Electrochem. Soc.*, 161(14), H924–H929, **2014**.
- [117] Rheinlaender, J. & Schäffer, T. E. *J. Appl. Phys.*, 105(9), 94905, **2009**.
- [118] Shevchuk, A. I., Frolenkov, G. I., Sánchez, D., James, P. S., Freedman, N., Lab, M. J., Jones, R., Klenerman, D. & Korchev, Y. E. *Angew. Chemie - Int. Ed.*, 45(14), 2212–2216, **2006**.
- [119] Takahashi, Y. *Electrochemistry*, 82(5), 331–334, **2014**.
- [120] Bentley, C. L., Kang, M. & Unwin, P. R. *Curr. Opin. Electrochem.*, 6(1), 23–30, **2017**.
- [121] Ebejer, N., Güell, A. G., Lai, S. C., McKelvey, K., Snowden, M. E. & Unwin, P. R. *Annu. Rev. Anal. Chem.*, 6(1), 329–351, **2013**.
- [122] Tao, B., Yule, L. C., Daviddi, E., Bentley, C. L. & Unwin, P. R. *Angew. Chemie Int. Ed.*, 58(14), 4606–4611, **2019**.
- [123] Bentley, C. L., Kang, M. & Unwin, P. R. *J. Am. Chem. Soc.*, 139(46), 16813–16821, **2017**.
- [124] Bentley, C. L. & Unwin, P. R. *Faraday Discuss.*, 210, 365–379, **2018**.
- [125] Aaronson, B. D., Güell, A. G., McKelvey, K., Momotenko, D. & Unwin, P. R. In *Nanoelectrochemistry*, Wiley-VCH, pages 655–693. **2015**.
- [126] Suter, T. & Böhni, H. *Electrochim. Acta*, 42(20-22), 3275–3280, **1997**.

- [127] Unwin, P. R., Güell, A. G. & Zhang, G. *Acc. Chem. Res.*, 49(9), 2041–2048, **2016**.
- [128] Bentley, C. L., Kang, M., Maddar, F. M., Li, F., Walker, M., Zhang, J. & Unwin, P. R. *Chem. Sci.*, 8(9), 6583–6593, **2017**.
- [129] Daviddi, E., Gonos, K. L., Colburn, A. W., Bentley, C. L. & Unwin, P. R. *Anal. Chem.*, 91(14), 9229–9237, **2019**.
- [130] Macpherson, J. V. & Unwin, P. R. *Anal. Chem.*, 72(2), 276–285, **2000**.
- [131] Kranz, C., Friedbacher, G., Mizaikoff, B., Lugstein, A., Smoliner, J. & Bertagnolli, E. *Anal. Chem.*, 73(11), 2491–2500, **2001**.
- [132] Knittel, P., Mizaikoff, B. & Kranz, C. *Anal. Chem.*, 88(12), 6174–6178, **2016**.
- [133] Huang, Z., De Wolf, P., Poddar, R., Li, C., Mark, A., Nellist, M. R., Chen, Y., Jiang, J., Papastavrou, G., Boettcher, S. W., Xiang, C. & Brunschwig, B. S. *Microsc. Today*, 24(06), 18–25, **2016**.
- [134] Knittel, P., Bibikova, O. & Kranz, C. *Faraday Discuss.*, 193(0), 353–369, **2016**.
- [135] Liu, Y., Holzinger, A., Knittel, P., Poltorak, L., Gamero-Quijano, A., Rickard, W. D., Walcarius, A., Herzog, G., Kranz, C. & Arrigan, D. W. *Anal. Chem.*, 88(13), 6689–6695, **2016**.
- [136] Velmurugan, J., Agrawal, A., An, S., Choudhary, E. & Szalai, V. A. *Anal. Chem.*, 89(5), 2687–2691, **2017**.
- [137] Bruker. *PeakForce SECM*, www.bruker.com/products/surface-and-dimensional-analysis/atomic-force-microscopes/modes/modes/imaging-modes/peakforce-secm/overview.html, **2019**.
- [138] Nellist, M. R., Chen, Y., Mark, A., Gödrich, S., Stelling, C., Jiang, J., Poddar, R., Li, C., Kumar, R., Papastavrou, G., Retsch, M., Brunschwig, B. S., Huang, Z., Xiang, C. & Boettcher, S. W. *Nanotechnology*, 28(9), 95711, **2017**.
- [139] Ossola, D., Dorwling-Carter, L., Dermutz, H., Behr, P., Vörös, J. & Zambelli, T. *Phys. Rev. Lett.*, 115(23), 238103, **2015**.
- [140] Meister, A., Gabi, M., Behr, P., Studer, P., Vörös, J., Niedermann, P., Bitterli, J., Polesel-Maris, J., Liley, M., Heinzelmann, H. & Zambelli, T. *Nano Lett.*, 9(6), 2501–2507, **2009**.

- [141] Amarouch, M. Y., El Hilaly, J. & Mazouzi, D. *Scanning*, 2018, 7801274, **2018**.
- [142] Hirt, L., Grüter, R. R., Berthelot, T., Cornut, R., Vörös, J. & Zambelli, T. *RSC Adv.*, 5(103), 84517–84522, **2015**.
- [143] Dorwling-Carter, L., Aramesh, M., Han, H., Zambelli, T. & Momotenko, D. *Anal. Chem.*, 90(19), 11453–11460, **2018**.
- [144] Dorwling-Carter, L., Aramesh, M., Forró, C., Tiefenauer, R. F., Shorubalko, I., Vörös, J. & Zambelli, T. *J. Appl. Phys.*, 124(17), 174902, **2018**.
- [145] Nanosurf. *FluidFM probe microscopy*, www.nanosurf.com/en/products/flex-fpm-flexafm-with-fluidfm-functionality, **2019**.
- [146] Cytosurge. *FluidFM Technology*, www.cytosurge.com/page/technology, **2019**.
- [147] Meier, J., Friedrich, K. A. & Stimming, U. *Faraday Discuss.*, pages 365–372; discussion 441–462, **2002**.
- [148] Treutler, T. H. & Wittstock, G. *Electrochim. Acta*, 48(20-22), 2923–2932, **2003**.
- [149] Mirkin, M. V., Sun, T., Yu, Y. & Zhou, M. *Acc. Chem. Res.*, 49(10), 2328–2335, **2016**.
- [150] Sun, T., Wang, D. & Mirkin, M. V. *Angew. Chemie - Int. Ed.*, 57(25), 7463–7467, **2018**.
- [151] Sun, T., Wang, D. & Mirkin, M. V. *Faraday Discuss.*, 210, 173–188, **2018**.
- [152] Wang, F. F., Wang, W., He, X., Han, L., Zhou, J. Z., Tian, Z. Q., Tian, Z. W. & Zhan, D. *Sci. China Chem.*, 60(5), 649–655, **2017**.
- [153] Takahashi, Y., Shevchuk, A. I., Novak, P., Zhang, Y., Ebejer, N., Macpherson, J. V., Unwin, P. R., Pollard, A. J., Roy, D., Clifford, C. A., Shiku, H., Matsue, T., Klenerman, D. & Korchev, Y. E. *Angew. Chemie - Int. Ed.*, 50(41), 9638–9642, **2011**.
- [154] Page, A., Perry, D. & Unwin, P. R. *Proc. R. Soc. A Math. Phys. Eng. Sci.*, 473(2200), **2017**.
- [155] O’Connell, M. A. & Wain, A. J. *Anal. Chem.*, 86(24), 12100–12107, **2014**.
- [156] Takahashi, Y., Shevchuk, A. I., Novak, P., Murakami, Y., Shiku, H., Korchev, Y. E. & Matsue, T. *J. Am. Chem. Soc.*, 132(29), 10118–10126, **2010**.

- [157] Mirkin, M. V. & Amemiya, S. *Nanoelectrochemistry*. Wiley-VCH, **2015**.
- [158] Oja, S. M., Fan, Y., Armstrong, C. M., Defnet, P. & Zhang, B. *Anal. Chem.*, 88(1), 414–430, **2016**.
- [159] Clausmeyer, J. & Schuhmann, W. *TrAC Trends Anal. Chem.*, 79, 46–59, **2016**.
- [160] Morris, R. B., Franta, D. J. & White, H. S. *J. Phys. Chem.*, 91(13), 3559–3564, **1987**.
- [161] Seddon, B. J., Eddowes, M. J., Firth, A., Owen, A. E. & Girault, H. H. J. *Electrochim. Acta*, 36(5), 763–771, **1991**.
- [162] Arrigan, D. W. M. *Analyst*, 129(12), 1157–1165, **2004**.
- [163] Cox, J. T. & Zhang, B. *Annu. Rev. Anal. Chem.*, 5(1), 253–272, **2012**.
- [164] Kranz, C. *Analyst*, 139(2), 336–352, **2013**.
- [165] Itaya, K. & Tomita, E. *Surf. Sci.*, 201(3), L507 – L512, **1988**.
- [166] Slevin, C. J., Gray, N. J., Macpherson, J. V., Webb, M. A. & Unwin, P. R. *Electrochem. Commun.*, 1(7), 282–288, **1999**.
- [167] Conyers, J. L. & White, H. S. *Anal. Chem.*, 72(18), 4441–4446, **2000**.
- [168] Sun, P., Zhang, Z., Guo, J. & Shao, Y. *Anal. Chem.*, 73(21), 5346–5351, **2001**.
- [169] Sripirom, J., Kuhn, S., Jung, U., Magnussen, O. & Schulte, A. *Anal. Chem.*, 85(2), 837–842, **2013**.
- [170] Ying, Y. L., Ding, Z., Zhan, D. & Long, Y. T. *Chem. Sci.*, 8(5), 3338–3348, **2017**.
- [171] Sen, M., Takahashi, Y., Matsumae, Y., Horiguchi, Y., Kumatani, A., Ino, K., Shiku, H. & Matsue, T. *Anal. Chem.*, 87(6), 3484–3489, **2015**.
- [172] Wilde, P., Quast, T., Aiyappa, H. B., Chen, Y. T., Botz, A., Tarnev, T., Marquitan, M., Feldhege, S., Lindner, A., Andronescu, C. & Schuhmann, W. *ChemElectroChem*, 5(20), 3083–3088, **2018**.
- [173] Thakar, R., Weber, A. E., Morris, C. A. & Baker, L. A. *Analyst*, 138(20), 5973–5982, **2013**.

- [174] McKelvey, K., Nadappuram, B. P., Actis, P., Takahashi, Y., Korchev, Y. E., Matsue, T., Robinson, C. & Unwin, P. R. *Anal. Chem.*, 85(15), 7519–7526, **2013**.
- [175] Chen, S. & Kucernak, A. *Electrochem. Commun.*, 4(1), 80–85, **2002**.
- [176] Chen, S. & Kucernak, A. *J. Phys. Chem. B*, 106(36), 9396–9404, **2002**.
- [177] Chen, S. & Kucernak, A. *J. Phys. Chem. B*, 107(33), 8392–8402, **2003**.
- [178] Huang, K., Clausmeyer, J., Luo, L., Jarvis, K. & Crooks, R. M. *Faraday Discuss.*, 210, 267–280, **2018**.
- [179] Gao, R., Ying, Y. L., Li, Y. J., Hu, Y. X., Yu, R. J., Lin, Y. & Long, Y. T. *Angew. Chemie - Int. Ed.*, 57(4), 1011–1015, **2018**.
- [180] Hao, R. & Zhang, B. *Anal. Chem.*, 88(1), 614–620, **2016**.
- [181] Zhu, X., Qiao, Y., Zhang, X., Zhang, S., Yin, X., Gu, J., Chen, Y., Zhu, Z., Li, M. & Shao, Y. *Anal. Chem.*, 86(14), 7001–7008, **2014**.
- [182] Chen, R., Hu, K., Yu, Y., Mirkin, M. V. & Amemiya, S. *J. Electrochem. Soc.*, 163(4), H3032–H3037, **2016**.
- [183] Yu, Y., Noël, J. M., Mirkin, M. V., Gao, Y., Mashtalir, O., Friedman, G. & Gogotsi, Y. *Anal. Chem.*, 86(7), 3365–3372, **2014**.
- [184] Sun, P. & Mirkin, M. V. *Anal. Chem.*, 79(15), 5809–5816, **2007**.

Chapter 2

Carbon Fiber based Platinum Nanoelectrodes

Carbon nanoelectrodes (CNEs) and platinum nanoelectrodes (PtNEs) are widely used in the field of nanoscale electrochemistry for both scanning electrochemical probe microscopy (SEPM) and other studies such as single molecule or particle detection and analysis. Many fabrication methods have been presented through the years with varying levels of success and reproducibility. This chapter firstly focusses on two pyrolytic methods for fabricating CNEs before investigating three different methods of Pt electrodeposition on CNEs to form PtNEs. The advantages and disadvantages of these methods are discussed, highlighting the need for proper fabrication and characterisation protocols which are often overlooked in the literature.

2.1 Introduction

Nanoelectrodes (NEs) are electrodes that have geometry in the sub 100s of nm range and are an essential component for carrying out electrochemical experiments at the nanoscale.¹⁻³ The small scale of the exposed electrode allows for localisation of electrochemistry and the resolution of the experiment is generally governed by the size of the NE.⁴ However, fabrication of NEs provides many challenges; robustness, ease of fabrication, reproducibility, geometry and cost are just a few factors that prove technically difficult in this field.^{3,5}

2.1.1 Carbon Nanoelectrodes

CNEs have seen wide application within SEPM due to their low cost, large potential scan window, resistance to biofouling, ease of surface modification and well

understood surface chemistry.⁶⁻⁸ Several methods for fabricating CNEs have been reported over the years. The three most commonly seen involve etched carbon microfibres, carbon pyrolysis and chemical vapor deposition (CVD).^{1,2,9,10}

Conical CNEs can be formed by sealing carbon fibers inside of glass capillaries. Some older methods aspirated a carbon fiber inside of a capillary which was then pulled down to the size of the fiber using a pipette puller.^{11,12} A slightly more recent method starts by attaching a carbon fiber to a Cu wire using conductive paint, the carbon fiber is then inserted into a glass capillary leaving ≈ 1 cm of carbon fiber exposed at the end. The fiber is then moved into the inner region of a gas lamp flame (≈ 350 °C) which results in a slow etching of the fiber, this is then sealed to the capillary using epoxy.¹³ Whilst these probes had an apex with radii of 100 – 300 nm, the exposed length of carbon was ≈ 200 μm due to the way that the sealing step is carried out. It would also be extremely difficult to regulate the amount of carbon fiber exposed using this approach. However one way around this is to further etch away the carbon fiber using a microforge. This can result in an exposed carbon fiber that has a base radii of 100 nm and length of less than a micron. This method also has a reported success rate of over 75 % with an excellent seal between the glass and fiber.¹⁴ These electrodes are a great improvement to the method and showed good results for their designed purpose (being inserted into small biological systems). However, for truly nanoscale SEPM the total exposed area needs to be on the nanoscale not the microscale.

The above studies with etched carbon fibers have developed carbon electrodes with nanometre sized radii but not overall length. One study has used insulation of etched carbon fibers to create electrodes with exposed radii down to 1 nm.¹⁵ A carbon fiber (3.5 μm diameter) is attached to a copper wire using colloidal graphite. The carbon fiber is then etched using an AC voltage in 0.01 M NaOH against a GC rod. To insulate the etched fiber, cathodic electrophoretic paint is deposited (similar to that used in traditional EC-STM tips, see Section 1.2.3) before curing at ≈ 195 °C. The deposition and curing steps were repeated to form smaller CNEs. The copper-carbon assembly is then sealed with epoxy inside a glass capillary, leaving only the insulated carbon fiber exposed.¹⁵ One issue with electrophoretic coatings is that if the coating is too thick then no electrode will be exposed upon curing, if it is too thin then pores and holes in the coating can be formed. To overcome this, the carbon fiber is moved so that it protrudes vertically from the deposition solution and remains in contact only by a thin meniscus. Using this method, electrodes with radii on the 10s of nm scale were achievable and a 1 nm radii electrode was also presented. However the SEM in this study was not able to distinguish between

the carbon and the coating at the tip due to the instrument resolution, making characterisation of exact geometry impossible.¹⁵ These electrodes were also further characterised by voltammetry in a variety of redox mediators with a range of formal potentials, kinetic rate constants and charge. It was shown that no deviation from expected CV behaviour is seen until electrodes are smaller than ≈ 20 nm, at which point the CV becomes “spread out” with the half wave potential shifting to more negative values.¹⁶

Another method for fabricating conical CNEs involves CVD of carbon inside a quartz nanopipette.¹⁷ A quartz capillary is filled with a catalyst solution of ferric nitrate in isopropyl alcohol, followed by laser pulling of the capillary. Carbon is then deposited via CVD on the catalyst covered surface using Ar and methane, the length of CVD time controls the thickness of the carbon layer deposited. Wet etching (buffered hydrofluoric acid) is used to remove the quartz at the very tip and expose the remaining carbon, the exposed area is controlled by the temperature and the length of time for the wet etch. The exposed carbon can also be further reduced using plasma oxidation which leaves a diameter of 10 – 100s of nm.¹⁷ Similar to the previously described method, the micron length scale of the exposed carbon would be the limiting factor for use in SEPM rather than probing biological systems. Another report reduced the diameter to 10 – 30 nm, however, the length exposed was still too long for use in nanoscale SEPM applications.¹⁸

A common method for fabrication of carbon electrodes has been pyrolysis of hydrocarbons inside of capillaries.^{5,19} An older study demonstrated this by pulling quartz capillaries to an opening of 1 – 4 μm before flowing methane inside and heating with a Bunsen burner. To avoid damage to the tip the pulled capillary was inserted into a larger quartz capillary for protection during the burning process. In this case the carbon filled capillary was then cut by scalpel with the aid of a microscope.²⁰ As time has passed, electrodes fabricated using pyrolysis have decreased in size. Another study using pyrolysis of acetylene in a nitrogen atmosphere produced carbon electrodes with diameters between 500 nm to 2 μm .²¹

The same pyrolysis method has also been applied to dual barrel pipettes where one barrel is blocked so the gas only fills one channel, resulting in a dual barrel electrode with one carbon channel and one empty. These electrodes have been demonstrated down to a total size of 100 nm (i.e. two 50 nm channels) and are usually used as a multifunctional probe where the carbon channel is used for SECM and the open channel for SICM.^{22–24}

One recent study has taken the pyrolysis method of CNE fabrication to new levels, controlling several of the important factors in an attempt to improve

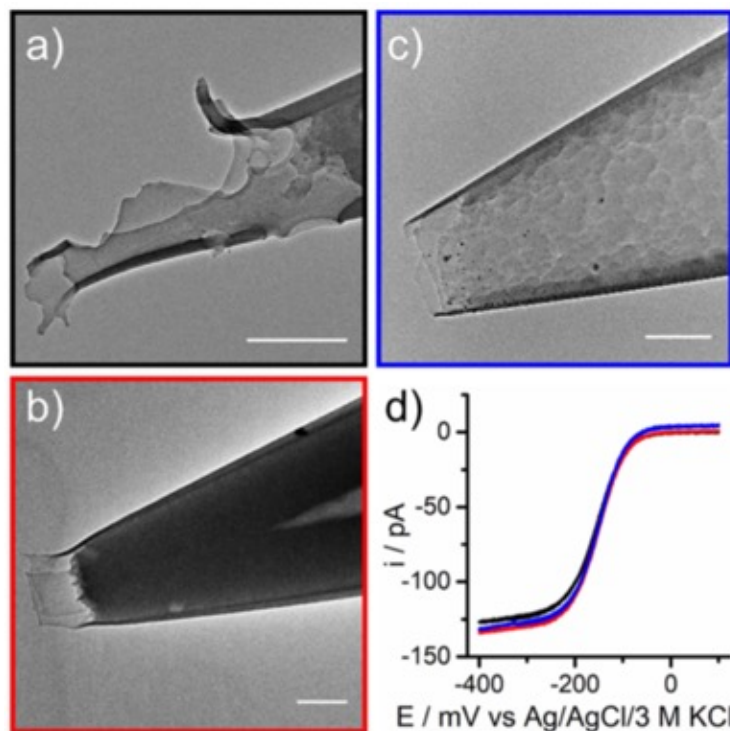


Figure 2.1: Different CNE geometries, (a) disfigured, (b) recessed, (c) hollow, shown with TEM images. (d) Corresponding CVs in 5 mM $[\text{Ru}(\text{NH}_3)_6]^{3+/2+}$ and 0.1 M KCl, with a 25 mV s^{-1} scan rate. Very similar CV responses are seen despite the varied electrode geometry. Figure reproduced from Wilde, *et al.*⁵ with permission from John Wiley and Sons.

the reproducibility.⁵ The study starts by highlighting the current issues with CNE fabrication and the limitations of using voltammetry as the sole characterisation technique. As an example three CNEs with distinct structural geometries are highlighted with the use of TEM; disfigured, recessed and hollow (Figure 2.1a,b,c). The corresponding CVs in 5 mM $[\text{Ru}(\text{NH}_3)_6]^{3+/2+}$ and 0.1 M KCl show extremely similar responses (Figure 2.1d). This reinforces the fact that the proper characterisation of NEs requires both the use of microscopy and voltammetry. The study also investigated a recessed CNE with another redox mediator (FcDiMeOH) and the effects of varied scan rates ($25 - 1000 \text{ mV s}^{-1}$) to see if there was a dependence due to the electrode geometry. However, it was found that the CV response was again very similar between the conditions.⁵

Despite the quick and cheap nature of the handheld torch method of gas pyrolysis, the major limitation is the lack of control for the flame temperature, movement and length of time.⁵ Disfigured electrodes can result from temperatures

which are too high or with too lengthy exposure times, the resulting electrode geometry is also very sensitive to the differences in these parameters.⁵ To attempt to overcome these limitations the above study took a more technically engineered setup to control the key parameters: instead of a gas torch an electrically heated coil was used, for which the temperature was tuned by adjusting the electrical current flowing through it. Temperature profiles for the fabrication procedure were also recorded by replacing the nanopipette with a thermocouple. The coil was mounted on an electric stepper motor which, along with the coil temperature was controlled via computer. Both the butane capillary and Ar capillary were mounted on micrometers to allow for fine alignment of the pipette in two dimensions, whilst the Ar was flowed through an Al_2O_3 capillary and controlled by a needle valve and pressure regulator. Propane and butane were mixed in a three way valve with both gases controlled via pressure regulators. One reported issue is the limited lifetime of the coil itself, which therefore requires adjustment and recalibration of the heating current, also the exact length of nanopipette inserted into the Ar capillary varies on the scale of hundreds of micrometres.⁵

Using this instrument with different parameters allowed for different types of CNE to be fabricated. The first type presented are CNEs which have a thin layer of carbon on the inside wall but leave a hollow channel through the centre (Figure 2.1c). This was achieved using a quick heating (35 s) up to 960 °C holding and then cooling over ≈ 2 minutes. Increasing the temperature to 1020 °C closes the channel and leaves a cone shaped recess. To fully fill the recess and leave a disc electrode, a second heating step up to 700 °C is used. Temperature variations in this second heating stage make a large difference to the final electrode geometry, too low and carbon overflows, too high and the electrode will be disfigured (Figure 2.1a).⁵

One widely used way of making sure that CNEs have a well defined geometry is to use FIB milling to cut the electrode at the end to the desired dimensions. This method is extremely appealing due to the controllability of the geometry and any disfigured portions of electrode can simply be removed.^{8,25} Unfortunately there are limitations, firstly it requires an instrument capable of doing FIB milling, which may not be widely available and also adds to the cost of each probe. Producing reliable electrodes below 100 nm diameter is often not possible due to the resolution of the instrument and the fact that electron charging of the capillary will often result in drift during the milling procedure.²⁵

2.1.2 Platinum Nanoelectrodes

Pt is often used as a material for electrodes in electrochemistry as it is fairly robust, chemically inert and an extremely active catalyst,^{26,27} hence here Pt was electrodeposited onto the CNE for use in nanoscale topographical and electrochemical mapping (Chapter 3). The Pt serves to sensitise the electrode to catalytic processes and ensures that electrode material protrudes from the quartz for tunnelling type measurements. Many methods of fabricating PtNEs have been reported with varying success, some are covered briefly here before the description of the method that was used in our studies.

A common method of PtNE fabrication in the literature utilises a laser based pipette puller to seal Pt wire inside of quartz glass.^{28–30} Pt microwires are inserted into a borosilicate capillary, then a vacuum is applied to both ends of the capillary before pulling in a laser puller. With the parameters that were used by these groups, the result was the Pt being completely covered in the borosilicate. In order to expose the Pt, either etching (with 40 % HF) or mechanical polishing was carried out. The extremely fine polishing is achieved using a micropipette beveller equipped with a micromanipulator and microscope.³¹ This method has been repeated in a similar fashion several times since, with varied pulling parameters and polishing solutions.^{28–30} Whilst many previous studies relied on the use of a laser based pipette puller, one study recently showed a method of using much cheaper coil based heaters to insulate Pt wire with borosilicate before polishing to create PtNEs.²⁶ The outstanding issues with these methods for PtNE fabrication is that differing laser pullers require different pulling parameters even with the same materials and instrument model. In addition varying the Pt or capillary specifics will also change the parameters needed and, as will be described below (Section 2.2.1), there are many free parameters to be tuned, making the pulling conditions very hard to elucidate. In addition, polishing mechanically to the nanoscale presents issues with reproducibility and accuracy.

A few previous studies have investigated the electrodeposition of Pt onto CNEs, either to study the electrodeposition process itself or to form PtNEs.^{19,32,33} In some ways, CNEs act as an ideal substrate for electrodeposition as reducing the electroactive area reduces the number of possible nucleation sites. An electroactive area on the few nanometre radii scale will result in just one nucleation site.³³ Pt electrodeposition is typically carried out using a Pt containing acid such as H_2PtCl_6 or K_2PtCl_6 , proceeding via reduction of Pt^{4+} to Pt^0 from the 4 electron process: $\text{PtCl}_6^{2-} + 4\text{e}^- \rightarrow \text{Pt} + 6\text{Cl}^-$.^{34–36} Pt electrodeposition in a macroscale system is shown to result in three reduction phases and has been reported on carbon fiber

bundles, HOPG and GC.^{37–39} The first wave is attributed to reduction following $\text{Pt}^{4+} + 2\text{e}^- \rightarrow \text{Pt}^{2+}$, the second is associated with $\text{Pt}^{2+} + 2\text{e}^- \rightarrow \text{Pt}^0$ and the third is due to electrodeposition of H on already deposited Pt particles.³⁷ Sweeping to potentials in the first wave does not result in Pt deposition, whereas sweeping to the second wave does.³³ In the case of microelectrodes, two reduction waves are observed before the deposition process starts, whereas on NEs only one reduction wave is observed before the main deposition peak. In the case of NEs it has been suggested that the observation of only a single reduction peak is because the first peak becomes very irreversible and overlaps with the second.³³

2.2 Methodology

2.2.1 Carbon Nanoelectrodes

CNEs were fabricated in two separate fashions. Both methods start with ≈ 50 nm nanopipettes fabricated from quartz capillaries (QF100-50-10, Sutter Instrument Co.) using a P-2000 laser based pipette puller (Sutter Instrument Co.). This method of nanopipette fabrication is widely used in SEPM as it is extremely reproducible and also the pulling results in two nearly identical pipettes so that one can be used for experiments whilst the other is kept as a clean reference which can be analysed with microscopy (Figure 2.2A).^{1,2,9,10} A laser puller works by clamping two ends of a capillary and applying a laser to the centre. The clamps have pulleys attached which apply a tension to each end. The laser starts to melt the centre and as it does so, the capillary is then pulled apart to form two nearly identical nanopipettes. The instrument has several tunable parameters: *heat*, *filament*, *velocity*, *delay* and *pull*. Additionally multiple lines can be added to the program allowing further tuning of the process. *Heat* determines the laser power and is scaled 0–999 with values usually in the range of 700–900 for quartz. *Filament* specifies the scanning pattern for the laser, higher values scan the laser in a wider pattern along the capillary with settings of 0–6 corresponding to 1–8 mm pattern width. *Velocity* gives a way of accurately measuring the glass temperature and determines the point at which the “hard pull” starts, the scale used is 10–100 with higher values used for micro/nanopipettes. *Delay* controls the time between when the *heat* is turned off and the “hard pull” starts. The higher the *delay* the cooler the glass for the “hard pull”, higher *delay* values correspond to shorter tapers and range from 0–255. A *delay* value of 128 corresponds to the “hard pull” starting at the same time as laser deactivation. *Pull* ranges from 0–250 and controls the force used in the “hard pull”. Higher *pull* values result in smaller tip diameter and longer tapers. A schematic summarising

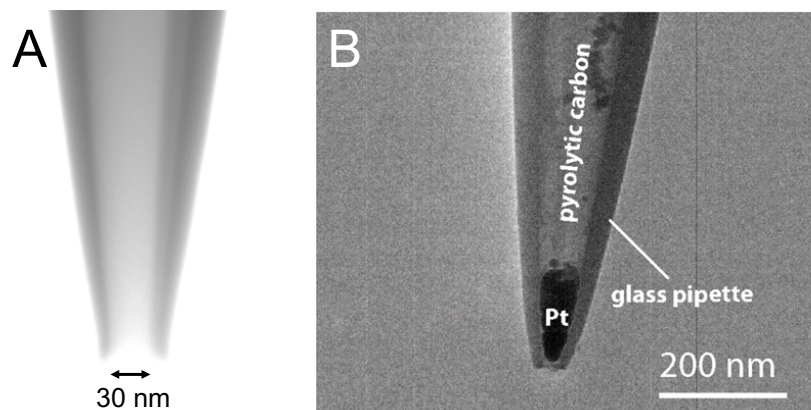


Figure 2.2: STEM image of a 30 nm diameter laser pulled quartz nanopipette. (B) TEM image of an ideal Pt filled CNE. Adapted with permission from Kang, M., *et al.*, *Langmuir*, 32(32), **2016**.¹⁰ Copyright (2016) American Chemical Society.

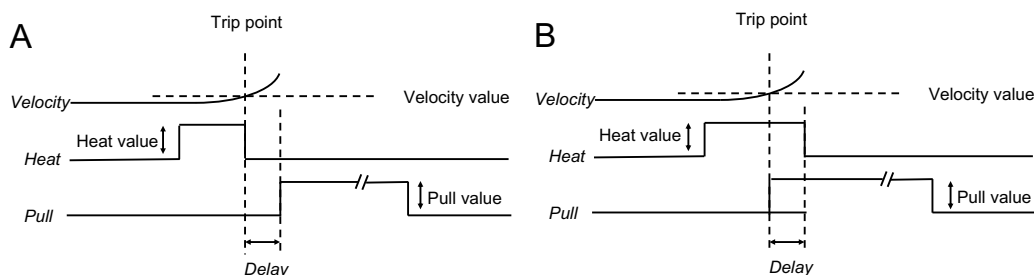


Figure 2.3: Pull cycle of a P2000 laser pipette puller. With *delay* > 128 (A), “hard pull” starts following a pause after the *velocity* trip point and *heat* is switched off. When *delay* < 128 (B) the “hard pull” is started before the *heat* is turned off. Figures reproduced from Sutter Instrument Company.⁴⁰

the laser pulling procedure and parameters is shown in Figure 2.3.⁴⁰ For the ≈ 50 nm diameter pipettes here a two line program was used for pulling with the following parameters: 1. *Heat* = 750, *Filament* = 4, *Velocity* = 30, *Delay* = 150, *Pull* = 80, 2. *Heat* = 650, *Filament* = 3, *Velocity* = 40, *Delay* = 135, *Pull* = 150.

It should be noted that laser pullers can produce extremely reproducible nanopipettes, however, the parameters are not generally transferable between instruments. In addition, physical dimensions of the pulled pipettes can drift slightly over time, especially as contaminants build up on the mirrors. Hence pulling times for pipettes should be monitored and mirrors should be cleaned regularly.⁴⁰

CNEs were then fabricated from these nanopipettes. This is performed using the pyrolysis of hydrocarbons (Butane and Propane 600 ml, RS PRO) inside the nanopipette to pyrolytically deposit carbon. The nanopipette is filled with the

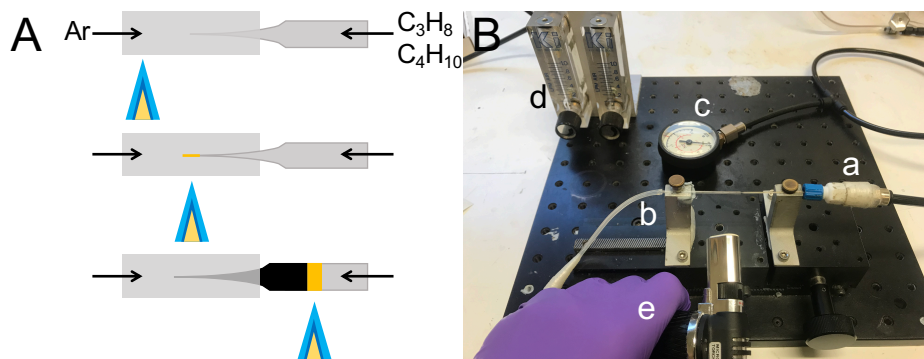


Figure 2.4: Torch heating method of CNE fabrication. (A) Schematic representation of hydrocarbon pyrolysis. The hydrocarbons inside the nanopipette is pyrolysed using a handheld torch. The heat is moved slowly along the length until the very tip shines brightly. The heat is then quickly moved along to form a glossy black coating. (B) Image of instrumentation used for torch heating. (a) Nanopipette is filled with the hydrocarbon mixture using Omnifit connectors and pressure gauge (c). Ar flow is through a larger capillary (b) and controlled with flow gauge (d). Heating is realised using a handheld torch (e).

hydrocarbon mixture and the pressure P_b is measured using a pressure gauge. The pulled tip is also surrounded with Ar ($\geq 99.998\%$, Sigma-Aldrich) creating an oxygen deficient environment to promote combustion to solid carbon rather than CO and/or CO₂. The inert environment is created by flowing Ar through a larger diameter capillary (QF120-90-10, Sutter Instrument Co.) with the pulled end of the nanopipette inserted inside. The Ar flow rate F_{Ar} is also recorded using a flow gauge (Key Instruments).

How the hydrocarbons are heated is where the two CNE fabrication methods differ. The first uses a simple propane and butane fuelled torch (gas blow torch, RS PRO) whilst the other uses a modified glass micropipette puller with electronic control. The torch is set to its hottest setting and held on the Ar capillary away from the nanopipette. After a few seconds of heating the torch is moved until the flame is just away from the nanopipette. Once the end of the nanopipette is observed to glow white, the torch is quickly but smoothly moved along the nanopipette, with a total heating time in the region of 10 – 20 seconds. A glossy black finish should be observed along the length (Figure 2.4). Nanoelectrodes have been shown to be easily damaged by electrostatic discharge due to the large potentials that can be generated and the small area of the nanoelectrode.⁴¹ Hence, in an attempt to reduce this an anti-static ankle bracelet was worn during handling of electrodes.

In an attempt to improve reproducibility of the pyrolysis method, similar

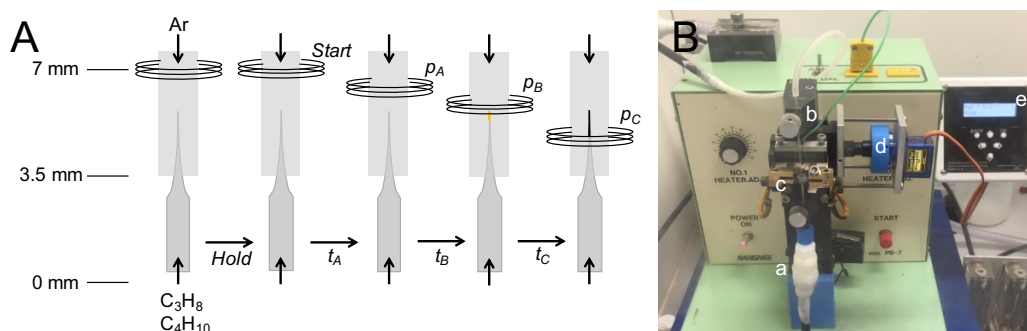


Figure 2.5: (A) Coil heating method of CNE fabrication. The coil temperature is set digitally, four positions are set: *Start*, p_A , p_B and p_C , with 7 mm representing the top and 0 mm at the bottom. The time taken to reach each of these positions after the previous is set as t_A , t_B and t_C . (B) Image of system. (a) Hydrocarbon mixture flowed through tubing with Omniflow connector, (b) Ar flow through larger diameter capillary, (c) electrically heated coil, (d) electric stepper motor for coil, (e) electronic control unit.

to a previous study, an electronically controlled system was constructed⁵ from a micropipette puller. A glass micropipette puller consists of an electrically heated coil and the pulling is achieved by a clamp with a weight. As the coil heats up the glass starts to melt and the weight will pull the two halves apart. Here the puller (Narishige PB-7) was modified to exclude the pulling weight and electronic control of the coil was added. The temperature of the coil, T_{coil} can be set before heating and the position of the coil in time can be programmed. The motion of the coil was programmed such that four coil positions and three propagation times are used. The total range of motion for the coil is 7 mm with a resolution of 0.1 mm. The four positions programmed are *Start*, p_A , p_B and p_C . The time parameters t_A , t_B and t_C set how long it takes the coil to move from the previous set position with *Hold* being the length of time before the coil moves to p_A . This is summarised in Figure 2.5.

2.2.2 Platinum Electrodeposition on Carbon Nanoelectrodes

The final step of the probe fabrication involves electrodeposition of Pt onto the CNE. This was attempted using three separate electrochemical methods all involving a CNE in a Pt deposition solution. The first method used a limited number of potential sweeps, the second used a timed pulse and current threshold, the third took a galvanostatic deposition approach. The ideal result from these processes would look similar to the electrode shown in Figure 2.2B, where the Pt is confined

within the end of the CNE, is in good contact with the carbon, and seals the end so no carbon is exposed. For our purposes, ideally the Pt would be slightly protruding from the quartz to allow for Pt to create tunnelling contact before the glass contacts the surface as these probes were intended for use in STM-SECM type experiments (Chapter 3).

All approaches here use the same solution for Pt deposition which comprised of 1 mM $\text{H}_2\text{PtCl}_6 \cdot 6\text{H}_2\text{O}$ (37.5 % Pt basis, Sigma-Aldrich) with 0.1 M HClO_4 (70 %, Sigma-Aldrich), with potentials measured against a Ag/AgCl reference electrode formed by anodising Ag wire (0.125 mm annealed, 99.99 %, Sigma-Aldrich) in a saturated KCl (> 99 %, Sigma-Aldrich) solution.

The cyclic method works by starting the electrode potential sufficiently positive (0.3 V) to have no electrochemical activity and then cycling the potential sufficiently negative (−0.2 V) to reduce the Pt acid to form solid Pt on the CNE. With each potential sweep an increase in the current response is observed, as more Pt is deposited there is more area for the next sweep of Pt deposition to occur upon and therefore a greater current response.

The pulse method also starts with the CNE potential sufficiently positive so that no electrochemical activity is present. The potential is then instantaneously switched to a potential to reduce the Pt, the potential is held there until the measured deposition current reaches a set threshold value, where the potential is then reverted back to the starting value to avoid further deposition.

The galvanostatic method involves setting a desired deposition current, the galvanostat will then shift the applied potential to give this value, the length of time for this process is then controlled to limit the amount of Pt deposition. The length of time required can also be estimated for a recessed CNE using equation 1.12. Steady state voltammograms were performed and combining the measured i_{ss} with the expected radius (a), the recession depth (L) could be calculated. It is assumed that the recess is short and that this essentially forms an empty cylinder at the end of the pipette, therefore the mass of Pt required to fill this cylinder is easily calculable. Using the density of Pt (ρ), the volume of the cylinder ($\pi a^2 L$) and Faraday's law for total charge (Q):

$$Q = nFN \quad (2.1)$$

the time required to fill the recess, t is given by:

$$t = \frac{nF\rho\pi a^2 L}{Mi} \quad (2.2)$$

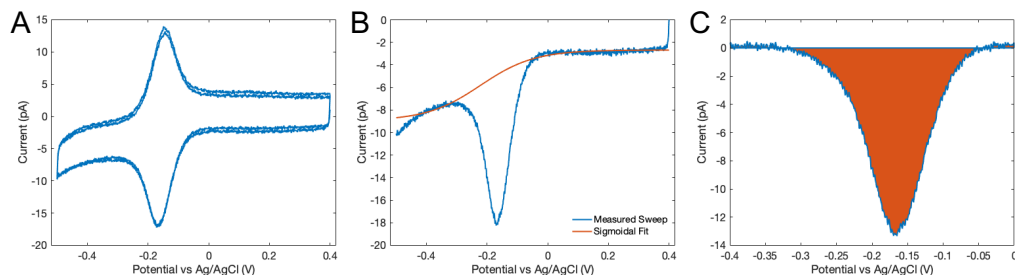


Figure 2.6: (A) Example CV with two cycles of a CNE for the reduction of 1.4 mM $[\text{Ru}(\text{NH}_3)_6]^{3+}$ and 0.1 M KCl at a sweep rate of 0.1 V s^{-1} . (B) The first sweep is isolated and a sigmoidal background is plotted to simulate the steady state response. (C) Background removed peak with shaded area showing integrated region. Values calculated for data shown: $a = 17 \text{ nm}$, $h = 1 \text{ }\mu\text{m}$.

where n is the number of electrons in the deposition process, F is the Faraday constant, N is the number of moles of Pt, M is the molecular weight of Pt and i is the set current for the galvanostat.

2.2.3 CV Peak Integration

As mentioned in Chapter 1, the area under peaks in a CV is a useful quantity to be measured, as in Section 1.6 where the area under a peak is proportional to the volume of a cavity electrode assuming that the steady state response is subtracted. The integration method used here is illustrated in Figure 2.6. First the sweep of interest is selected, second the potential range of the peak is selected, then a sigmoidal plot is used to fit the steady state response of the electrode, this is then subtracted from the sweep to allow for the integration of the region.

2.2.4 Instrumentation

All scanning transmission electron microscopy (STEM) images in the results section were obtained using a Zeiss Gemini SEM, using 30 kV accelerating voltage in a STEM mode with electrodes mounted on a multi-TEM sample holder. Electrochemical measurements were carried out in a two electrode setup with the CNE or PtNE used as the working electrode and a Ag/AgCl QRCE formed by anodising a Ag wire (0.125 mm annealed, 99.99 %, Sigma-Aldrich) in a saturated KCl ($\geq 99 \%$, Sigma-Aldrich) solution. Potentials were applied and currents measured using in house constructed electrometers and controlled using an FPGA card (PCIe-7825R, National Instruments) with home designed LabVIEW software (WEC-SPM).⁴² The electrodes, connections and solutions were all held inside a sealed Faraday cage dur-

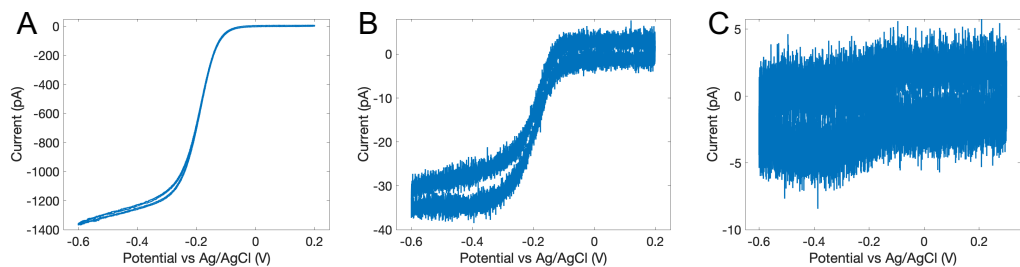


Figure 2.7: CVs of three separate CNEs for the reduction of 2 mM $[\text{Ru}(\text{NH}_3)_6]^{3+}$ in 0.1 M KCl fabricated using the torch method. All electrodes have the same conditions but differing steady state limiting currents. Sweep rate: 0.1 V s^{-1} . The largest response is seen in (A), then (B) and finally (C).

ing the experiments to reduce electronic noise.

2.3 Results

2.3.1 Carbon Nanoelectrodes

2.3.1.1 Torch Heating

The torch method of fabricating CNEs has been widely used but not always thoroughly investigated in previous research.^{2,20,21} Parameters such as the P_b value and F_{Ar} are controlled but the temperature and length of time heating is difficult to control precisely (and have a greater effect on the final electrode). Using the torch method generally results in one of three different responses when characterised using CV. One response is the ideal sigmoidal shape expected for a diffusion limited electrode (Figure 2.7). The sigmoidal shape with low charging currents would suggest an ideal geometry for the electrodes. However, as can be seen comparing Figure 2.7A,B,C the magnitude of the limiting current is vastly different despite the use of the same redox mediator (2 mM $[\text{Ru}(\text{NH}_3)_6]^{3+}$), the same initial nanopipettes and the same pulling program. There are several possible explanations for this discrepancy; one is that the electrode with a larger response has been damaged by the heat such that more electrode area is accessible to the solution. Another explanation is the electrode with the smaller response is highly recessed leading to a smaller steady state current. For an ideal disc shaped electrode with a diameter of 50 nm in a 2 mM $[\text{Ru}(\text{NH}_3)_6]^{3+}$ solution, the expected steady state current (given by equation 1.8) would be 15 pA. So for the electrode in Figure 2.7A with a $\approx 1300 \text{ pA}$ response, it is likely that damage has occurred. For the electrode in Figure 2.7B this value ($\approx 32 \text{ pA}$) is much closer to the expected but there may still be a small amount of

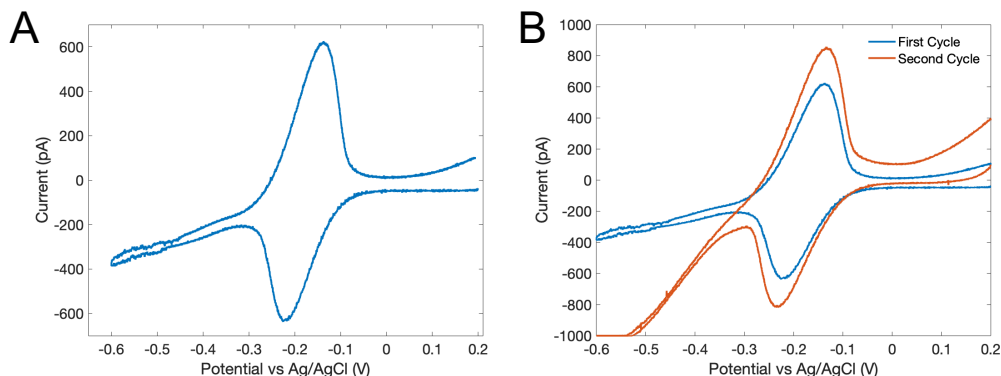


Figure 2.8: (A) CV of CNE for the reduction of 2 mM $[\text{Ru}(\text{NH}_3)_6]^{3+}$ in 0.1 M KCl, fabricated using the torch method. A peak shape similar to what would be expected for a cavity electrode is observed rather than the ideal sigmoidal steady state response. Sweep rate: 0.1 V s^{-1} . (B) Same electrode as in (A) showing the second cycle over the same potential range (orange).

damage or the carbon could have overflowed slightly, for instance if a hemispherical shape is used (equation 1.9) then the expected steady state current would be 25 pA, much closer to the observed response. Figure 2.7C displays an electrode where the observed current is lower than expected (1.5 pA vs 15 pA). In this case the limiting current is barely noticeable over the background noise and is likely due to a highly recessed electrode geometry. Using equation 1.12 it can be shown that the expected recess for this limiting current would be 180 nm.

The second type of response often observed with CNEs fabricated with a torch is displayed in Figure 2.8A, where instead of seeing a steady state sigmoidal shape a peaked shape is observed. If the electrode is damaged enough then a macroscale type of response would make sense. However, these peaked shaped CVs are often obtained even with low overall measured currents. This pattern is generally attributed to a cavity electrode (see Section 1.6.2).⁴³ As mentioned previously (Section 1.6), the area under the peak is proportional to the scan rate and the volume of the cavity. The magnitude of the steady state response can be used with equation 1.8 for a flat geometry to find a value for a , then using equation 1.13 and taking an idealised geometry as in Figure 1.11A, the estimated depth of recession can be calculated. In this case the steady state current of $\approx 300 \text{ pA}$ gives an approximate value for the radius a of 440 nm, which leads to a depth of approximately $40 \mu\text{m}$. This obviously a very large value given the expected radius, however, subsequent sweeps actually showed an increase in peak area (Figure 2.8B). which suggests that this electrode is actually a hollow cavity with carbon deposited along the walls,

where the increasing current is due to the solution propagating further down the pipette.

The final type of response observed is where no observable electrochemical signal is measured. This could be due to either extremely recessed electrodes such that the response is lower than the detection limit of the instrument, or there could be small gaps in the carbon coating which would mean that no electrical connection is made between the end of the electrode and the copper wire.

2.3.1.2 Coil Heating

The use of an electrically heated and electronically controlled coil for carbon deposition allows for a much greater degree of control than possible with the torch method. A large range of parameters were tested with the coil method.

Following fabrication of CNEs using the coil, CVs were carried out using $[\text{Ru}(\text{NH}_3)_6]^{3+}$ with KCl, this was followed by microscopy via TEM or STEM. It was generally found that very small or no change to the heating parameters could make a significant difference between different CNE geometries. Four electrodes are shown in Figure 2.9. The heating parameters for these four electrodes are summarised in Table 2.1. Figure 2.9A is a disfigured electrode which generally was the result of higher temperatures and/or longer heating times, in this case three heating cycles were used which caused the damage seen. Even with the damage presented, similar to Figure 2.1 a sigmoidal CV (Figure 2.9B) is observed and with a current (≈ 15 pA) which would be expected for a disc electrode with a diameter of ≈ 70 nm. The CNE shown in Figure 2.9C appears to be a well filled CNE with no gaps in filling. Using equation 1.8 yields an expected response of 6 pA which we would expect to be just visible over the background noise but is not observed (Figure 2.9D). It is possible that the filling was not as complete further along the electrode so no electrical connection is made with the inserted wire, unfortunately the STEM cannot image further up the pipette due to the thickness of the glass wall. Reduced noise was achieved (through improved instrument grounding) for the CNE in Figure 2.9F and the CV (Figure 2.9G) shows a sigmoidal response. However, there is a great degree of charging observed (separation between sweeps) and the steady state current of 3.5 pA matches fairly well if a disc shaped geometry is assumed (4.3 pA) but using the STEM image makes it seem as though the carbon is recessed by a rather large length (≈ 950 nm) which would lead to an expected response of 0.03 pA. There are two possibilities considered for this response. The first is that the contrast in the image is simply showing a greater carbon density further down the pipette but the tip is still filled to the end, the second is the possibility of damage further

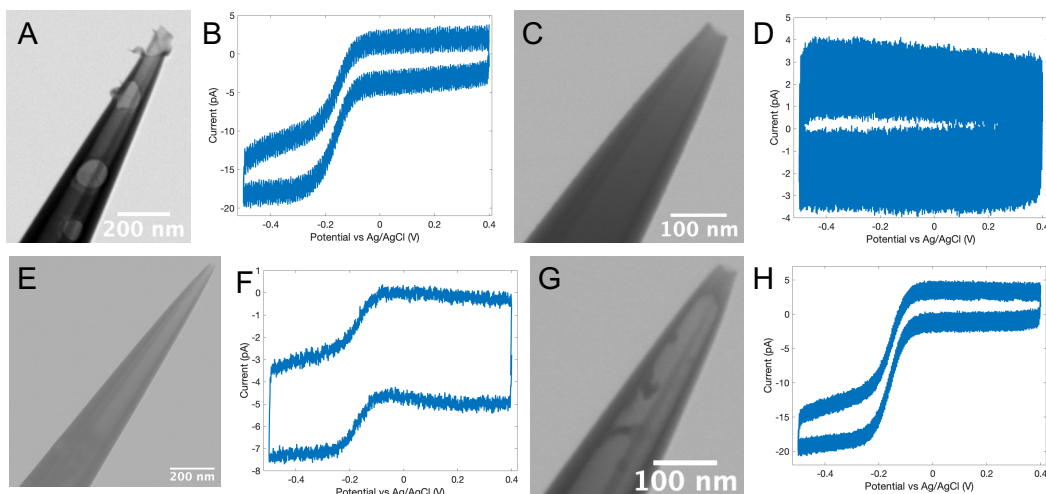


Figure 2.9: Examples of four CNEs fabricated with the coil method. Bright field STEM images (A,C,E,G) correspond to CVs (B,D,F,H). CVs for the reduction of 1.4 mM $[\text{Ru}(\text{NH}_3)_6]^{3+}$ with 0.1 M KCl at 0.2 V s^{-1} .

along the pipette which is not visible in the STEM. The final CNE demonstrated in Figure 2.9G exhibits another geometry where the end of the electrode is filled but behind this is only coated down the walls. This, however, should not be an issue for application unless the very end was damaged, exposing the cavity. The CV response (Figure 2.9H) gives a steady state current of $\approx 17 \text{ pA}$ which is greater than the expected 6 pA for a 30 nm disc, therefore the carbon plug at the end of the electrode may not be as perfect as the STEM would suggest. The above highlights the importance of care being taken with analysing electrodes via STEM images and voltammetry. STEM can be misleading due to only being a 2D image and the contrast is tunable and only relative, meaning that even if an area appears empty there is the possibility that it is just not as densely filled as another visible area.

Despite the extra degrees of control, the overall process is still quite irreproducible. One of the issues is that the coil used for heating oxidises and wears out very quickly, meaning that the exact temperature parameters used have to be adjusted for each electrode and very quickly the coil has to be replaced to keep temperatures high enough. When changing coils, the position of the two capillaries and the coil itself have to be realigned and no two coils give exactly the same response. Even with the use of a thermocouple to measure the temperature, it is difficult to say that the temperature at the actual end of the pipette is the same each time as the thermocouple is not located at the tip of the pipette. There could be possible improvements by integrating a temperature feedback loop, so that the current flow-

Table 2.1: Summary of coil heating parameters for the electrodes shown in Figure 2.9. Positions are in mm and times are in seconds. CNE A and G had more than one heating cycle labelled by A-1, A-2, etc.

CNE	<i>Start</i>	p_A	p_B	p_C	<i>Hold</i>	t_A	t_B	t_C	T_{coil} ($^{\circ}\text{C}$)	P_b (bar)
A-1	6.5	4	0	0	30	31	31	0	800	1.5
A-2	6.5	4	0	0	0	31	31	0	800	1.5
A-3	6.5	4	0	0	0	31	31	0	800	1.5
C	6.5	4	2	0	100	20	21	21	750	1.5
E-1	6.5	4	2	0	60	31	31	0	720	0.5
E-2	6.5	4	2	0	0	10	20	20	720	0.5
G	6.5	4	2	0	200	20	21	21	750	0.5

ing through the coil is adjusted using the thermocouple as a guide, unfortunately this is also quite difficult with the quick nature of wear to the coils and the delay in temperature change when the heating current is changed.

2.3.2 Platinum Electrodeposition on Carbon Nanoelectrodes

2.3.2.1 Cyclic Voltammetry Deposition

The first method of Pt electrodeposition investigated was the use of a sweeping voltage in a Pt deposition solution, stopping when the current was above a certain value on the negative sweep. This method has the advantage of an obvious response as the current increases to show Pt depositing. In addition the gradual sweep of potential means there is no sudden drastic change in potential that could potentially cause issues (Section 2.3.2.2). One obvious disadvantage to this method is that during a specific sweep the current could greatly exceed the desired threshold leading to a larger amount of Pt than desired.

Figure 2.10 shows two examples of Pt deposition on CNEs using the cycling method. Taking Figure 2.10A, the CNE has a steady state current of ≈ 53 pA, if a disc shaped geometry is assumed then this gives an electrode size of ≈ 172 nm. If an electrode of this diameter had a hemispherical geometry then the expected steady state current would be ≈ 83 pA. For this example 86 pA is observed after deposition which suggests that the Pt has deposited on the end of the CNE in an almost ideal hemispherical fashion. In contrast the example in Figure 2.10C shows an electrode which is expected to be ≈ 60 nm in diameter if modelled as a disc (from the ≈ 18 pA steady state current). For a hemispherical Pt deposition an expected steady state current of 30 pA would be observed after deposition, in this case the steady state current is 94 pA suggesting that more Pt than required for

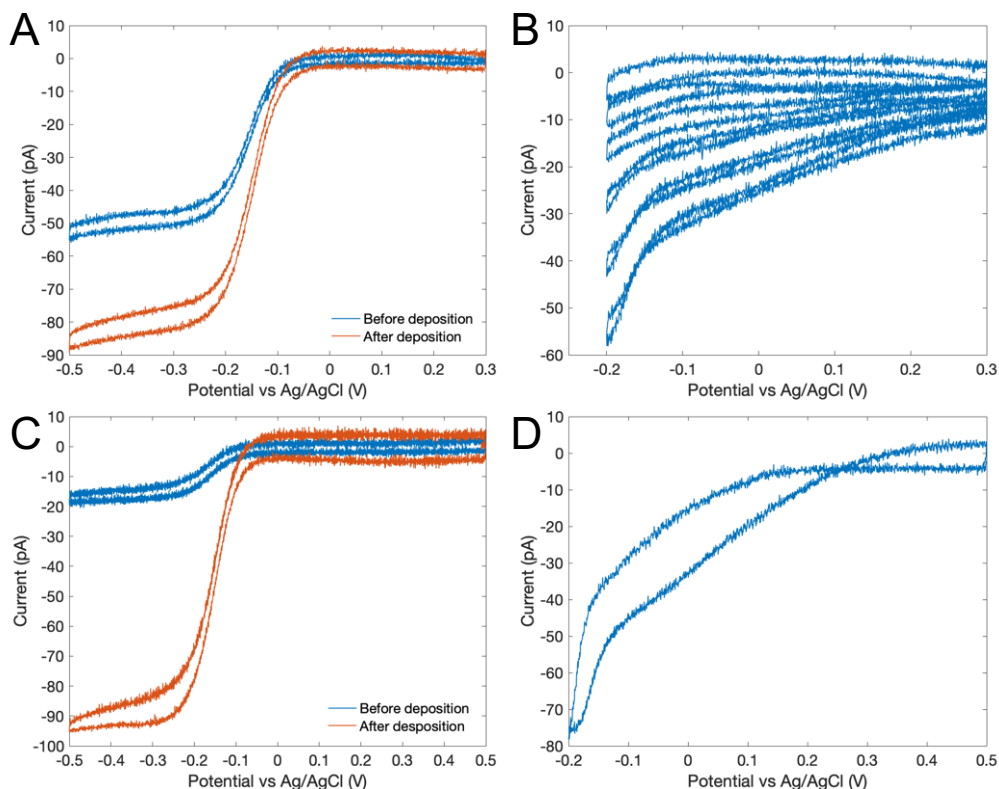


Figure 2.10: (A,C) CVs of CNEs before (blue trace) and after (orange trace) Pt deposition shown in (B,D). An increase in the steady state current is observed after the Pt deposition attributed to the larger area of Pt over carbon. The Pt depositions over the same potential range show differing traces. (A,C) demonstrate the reduction of 2 mM $[\text{Ru}(\text{NH}_3)_6]^{3+}$ and 0.1 M KCl. Pt deposition (B,D) carried out in 1 mM $\text{H}_2\text{PtCl}_6 \cdot 6\text{H}_2\text{O}$ and 0.1 M HClO_4 , targeted threshold current was 50 pA, sweep rate for all CVs was 0.2 V s^{-1} .

a hemispherical electrode has been deposited. In this case the Pt deposition only used one sweep (Figure 2.10D), and in that time too much Pt was deposited despite the same potential range as Figure 2.10B being used where 6 sweeps were required to result in a hemispherical response, highlighting one issue with this method of deposition. This discrepancy is likely due to the initial nucleation, which can vary dramatically.

To have a more ideal substrate for Pt deposition, some electrodes were cut using FIB milling to remove any damaged regions of the CNE at the expense of electrode size. One example of this is shown in Figure 2.11. This electrode started as a 30 nm diameter CNE with some damage further up the electrode, it was then FIB milled to a diameter of 400 nm. The CV after FIB milling shows a steady

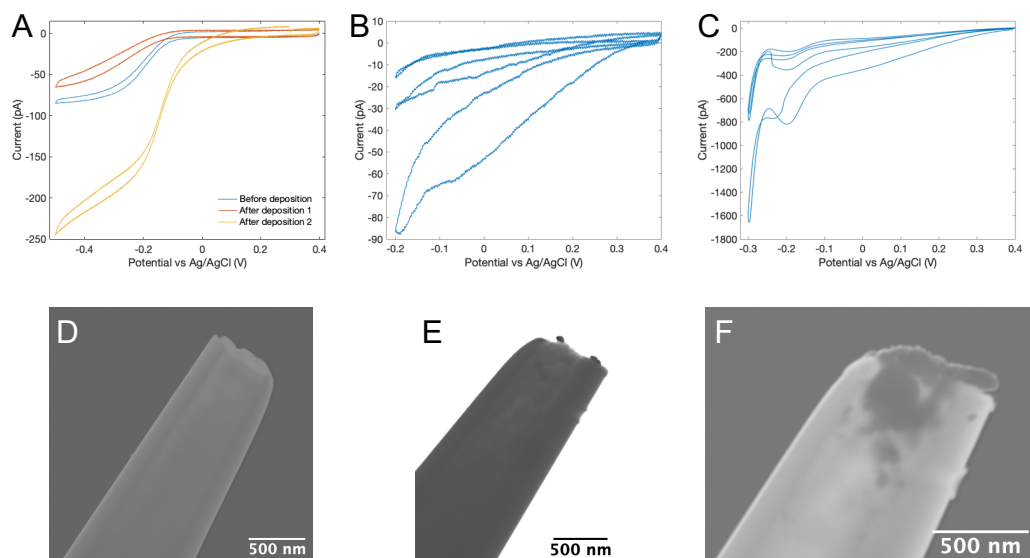


Figure 2.11: PtNE fabrication using the coil method for the CNE, followed by FIB milling and Pt deposition using cycling. (A) CV of the electrode after FIB milling (blue), after the first Pt deposition (orange) and after the final Pt deposition (yellow), demonstrating the reduction of 2 mM $[\text{Ru}(\text{NH}_3)_6]^{3+}$ and 0.1 M KCl. Traces during first (B) and second (C) Pt deposition in 1 mM $\text{H}_2\text{PtCl}_6 \cdot 6\text{H}_2\text{O}$ and 0.1 M HClO_4 . The sweep rate for (A,B,C) is 0.2 V s^{-1} . STEM images after FIB milling (D, bright field with darkened background), after the first (E, bright field) and second (F, bright field with darkened background) Pt deposition.

state current of $\approx 80 \text{ pA}$ (Figure 2.11A), which is less than the expected $\approx 120 \text{ pA}$ for a disc of this size. The STEM also shows that the CNE does not appear to be fully filled with carbon (Figure 2.11D), although this is difficult to see due to the thickness of the glass at this diameter and the electron energy in the STEM is only 30 keV (limiting transmission). The first Pt deposition takes the expected form with an increase in current observed in each sweep, although the currents observed are similar to that of the smaller electrodes (Figure 2.10). The STEM (Figure 2.11E) agrees with this, showing only small deposits of Pt, much less than completely full. In addition there appears to be several locations where Pt has nucleated which would be expected due to the larger geometry than previous CNEs.³³ The CV after this first deposition (Figure 2.11A, orange trace) actually shows a reduction in the steady state current, which could be attributed to some of the Pt blocking solution flow to some of the carbon further down the electrode, hence reducing the overall electroactive area. To attempt further Pt deposition, a second sweeping phase was performed using more negative potential (Figure 2.11C), the resulting deposition currents are much higher (up to 1600 pA vs 80 pA in the first) and of a different

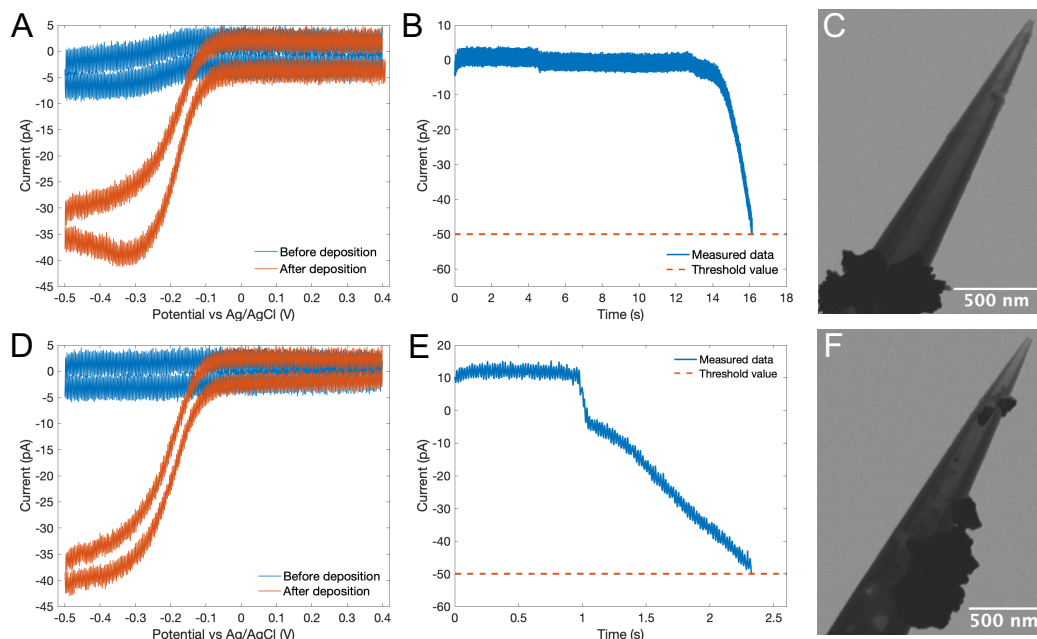


Figure 2.12: Two examples of Au deposition with the pulse methodology on CNEs. CVs of electrodes before (blue) and after (orange) Au deposition (A,D) with corresponding deposition traces at 0.4 V (B,E). The threshold current is set at 50 pA (orange dashed line) before the potential is reset. STEM images of electrodes after Au deposition (C,F), showing the non ideal geometry, where the Au has deposited much further up the length of the pipette and protrudes from the sides significantly. CVs acquired in 1 mM $[\text{Ru}(\text{NH}_3)_6]^{3+}$ and 0.1 M KCl at 0.2 V s^{-1} . Electrodepositions carried out in 1 mM AuCl_3 , 50 mM KCl and 50 mM HClO_4 .

shape, the STEM (Figure 2.11F) shows that the end of electrode is now filled with Pt, and the CV (Figure 2.11A, yellow trace) now shows a greatly increased response of 240 pA which is in approximate agreement with the STEM image if a geometry between a disc and hemisphere is assumed for the $\approx 630 \text{ nm}$ diameter. The different shape and lack of Pt deposition in the first scan suggests that this scan is mostly in the first reduction wave as discussed at the end of Section 2.1, hence minimal Pt is deposited, whereas the second deposition attempt to a more negative potential enters the second reduction wave and deposits a great deal more Pt on the CNE.

2.3.2.2 Chronoamperometric Deposition

In addition to the Pt studies, the pulse methodology was also used with Au on CNEs (Figure 2.12). For these experiments the deposition solution consisted of 1 mM AuCl_3 (99 %, Sigma-Aldrich), 50 mM KCl and 50 mM HClO_4 . The potential was held at 1 V before and after deposition and then switched to 0.4 V until the

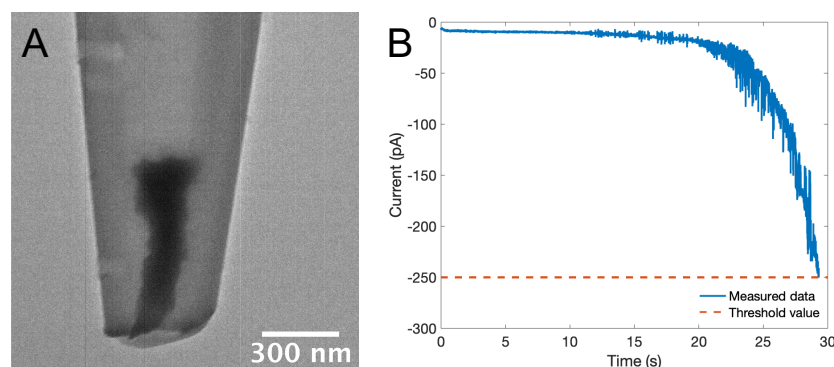


Figure 2.13: (A) TEM image of AuNE formed with the pulse method of electrodeposition the trace for which is shown in (B). Carried out in 1 mM AuCl_3 , 50 mM KCl and 50 mM HClO_4 , with 0.35 V applied to the CNE.

threshold of 50 pA was reached. The depositions in Figure 2.12B,E both show a similar response of no activity for some time before a very sudden nucleation and growth. The voltammetry before (blue trace) and after (orange trace) deposition (Figure 2.12A,D) also show a very promising voltammetric profile in terms of an increase in steady state current whilst maintaining the typical sigmoidal profile of a NE. Unfortunately, as can be seen from the STEM images (Figure 2.12C,F), the final electrode geometries are far from ideal. For these electrodes it appears as though the initial CNE was damaged and hence the Au has then deposited at several locations along the tip rather than at the end. This once again highlights the necessity for full characterisation of NEs with both CV and microscopy before and after deposition.

Similar to the FIB example, for the cyclic method in Figure 2.11, here a ≈ 50 nm diameter CNE with damage at the tip was FIB milled to 400 nm diameter to remove the damage and give a more ideal deposition surface. The same pulse methodology was applied as above with a Au deposition solution, however, the current threshold was increased (to 250 pA) to account for the larger size of the electrode (Figure 2.13B). In this case the Au deposits in an almost ideal fashion (see Figure 2.13A), confined to the end of the electrode, almost flush with the FIB milled surface. Ideally for our studies in Chapter 3 the Au would protrude slightly from the end of the quartz, but this represents a good disc electrode. As eluded to with the cyclic method, this result also shows how metal electrodeposition experiments are more easily performed on larger electrodes. This is a likely reason for much fewer nanoscale studies with SECM compared with larger scale studies.

2.3.2.3 Galvanostatic Deposition

Attempts at galvanostatic deposition of Pt were limited. Some attempts, however, did produce promising results. Figure 2.14A shows the CV before and after Pt deposition on a CNE. The steady state current of 20 pA for the pure CNE was used to calculate an approximate recession depth of 18 nm using equation 1.12. Equation 2.2 was then used to calculate the approximate deposition time required. The minimum set current possible with our instrument is 0.1 pA, hence this was used to allow for the best control of time. With these parameters it was estimated that a time of ≈ 15 seconds would fill the recess with Pt and so the deposition was carried out for slightly longer than this to attempt to get the Pt to protrude from the end of the electrode. Figure 2.14B shows how the potential changes during the deposition to attempt to keep the deposition current constant. It can be seen that a fairly high overpotential is required at the start, then the potential required drops very quickly after the deposition process starts. After the deposition process, the CV steady state current in $[\text{Ru}(\text{NH}_3)_6]^{3+}$ has risen to ≈ 80 pA which is greater than the expected 60 pA for a hemisphere; using equation 1.11 for a cone with an insulating sheath would suggest a protrusion of ≈ 25 nm. Unfortunately this sort of response was in the minority, generally it was found that far too much Pt was deposited. There are a few possibilities for this result, one is similar to above where the CNE was damaged in the pyrolysis process which leads to several possible nucleation points along the electrodes. Another specific to this method is that, as mentioned, initially a high overpotential is required to create nucleation of the Pt, but then further deposition is much quicker and as shown in Figure 2.14B there is a finite time for the potential to adjust and lots of Pt can be deposited in this period. Additionally the minimum current useable was 0.1 pA; the noise at this current makes maintaining this current precisely difficult, however, using higher currents requires much shorter times, which would then require much finer time control.

2.4 Conclusions

Whilst some advancements have been made towards making CNE fabrication more reproducible, there are many challenges to CNE production, especially when using pyrolysis type methods. The heating process is extremely difficult to reproduce over the course of several electrodes due to the number of parameters involved and degradation of heating elements which cause these parameters to shift. The torch based method will always be very irreproducible as the variances in human operation are inherently large, however, it does have the advantage that it is very quick, so

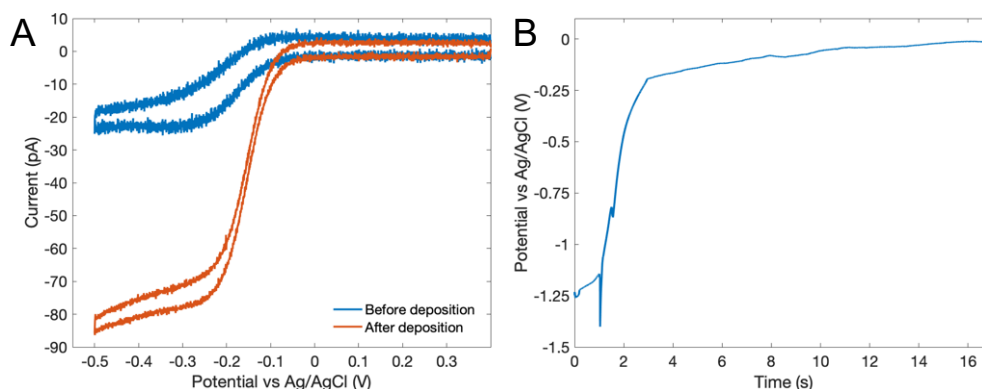


Figure 2.14: (A) CV of CNE before and after Pt deposition using the galvanostatic method. An increase in steady state current is seen after. 5 mM $[\text{Ru}(\text{NH}_3)_6]^{3+}$ and 0.1 M KCl, 0.2 V s^{-1} . (B) Monitor of potential during galvanostatic deposition. 1 mM $\text{H}_2\text{PtCl}_6 \cdot 6\text{H}_2\text{O}$ and 0.1 M HClO_4 , current set point: 0.1 pA.

many can be fabricated in a short space of time. However, as shown here, quickly characterising electrodes with CV is not a reliable method of determining electrode geometry. Methods which use high heat to form carbon will always have some chance of damaging the electrodes when very small nanopipettes are used.

Electrodeposition of Pt on CNEs was investigated with mixed results. Pt deposition is a statistical phenomenon, meaning that it is very hard to predict. This problem becomes enhanced when the substrates used (CNEs) are not ideal in geometry and composition. Each of the three methods described here have shown some merit, with the cyclic method giving the most promising results. This is possibly because it does not require a high starting overpotential which tends to create a runaway deposition shortly after.

One crucial factor enforced here is the need for thorough characterisation of NEs regardless of the fabrication procedure, often in the literature electrodes are under characterised with just a CV without the accompaniment of microscopy techniques. It has been shown here and by others that CVs of NEs do give some useful information about the electroactive surface area but can be very misleading when it comes to precise geometry and how an electrode will perform when used for other experiments due to the mass transport differences to the electrode.

2.5 References

- [1] Oja, S. M., Fan, Y., Armstrong, C. M., Defnet, P. & Zhang, B. *Anal. Chem.*, 88(1), 414–430, **2016**.
- [2] Bentley, C. L., Edmondson, J., Meloni, G. N., Perry, D., Shkirskiy, V. & Unwin, P. R. *Anal. Chem.*, 91(1), 84–108, **2019**.
- [3] Clausmeyer, J. & Schuhmann, W. *TrAC Trends Anal. Chem.*, 79, 46–59, **2016**.
- [4] Bard, A. J. & Mirkin, M. V. *Scanning Electrochemical Microscopy*. Wiley-VCH, 2nd edition, **2012**.
- [5] Wilde, P., Quast, T., Aiyappa, H. B., Chen, Y. T., Botz, A., Tarnev, T., Marquitan, M., Feldhege, S., Lindner, A., Andronescu, C. & Schuhmann, W. *ChemElectroChem*, 5(20), 3083–3088, **2018**.
- [6] Chen, P. & McCreery, R. L. *Anal. Chem.*, 68(22), 3958–3965, **1996**.
- [7] McCreery, R. L. *Chem. Rev.*, 108(7), 2646–2687, **2008**.
- [8] Thakar, R., Weber, A. E., Morris, C. A. & Baker, L. A. *Analyst*, 138(20), 5973–5982, **2013**.
- [9] Kranz, C. *Analyst*, 139(2), 336–352, **2013**.
- [10] Kang, M., Momotenko, D., Page, A., Perry, D. & Unwin, P. R. *Langmuir*, 32(32), 7993–8008, **2016**.
- [11] Chen, G., Ye, J. N. & Cheng, J. S. *Chromatographia*, 52(3), 137–141, **2000**.
- [12] Chen, T.-L., Luo, G.-p. & Ewing, A. G. *Anal. Chem.*, 66 19, 3031–3035, **1994**.
- [13] Huang, W.-H., Pang, D.-W., Tong, H., Wang, Z.-L. & Cheng, J.-K. *Anal. Chem.*, 73(5), 1048–1052, **2001**.
- [14] Li, Y.-T., Zhang, S.-H., Wang, L., Xiao, R.-R., Liu, W., Zhang, X.-W., Zhou, Z., Amatore, C. & Huang, W.-H. *Angew. Chemie Int. Ed.*, 53(46), 12456–12460, **2014**.
- [15] Chen, S. & Kucernak, A. *Electrochem. Commun.*, 4(1), 80–85, **2002**.
- [16] Chen, S. & Kucernak, A. *J. Phys. Chem. B*, 106(36), 9396–9404, **2002**.

- [17] Schrlau, M. G., Falls, E. M., Ziober, B. L. & Bau, H. H. *Nanotechnology*, 19(1), 15101, **2007**.
- [18] Singhal, R., Bhattacharyya, S., Orynbayeva, Z., Vitol, E., Friedman, G. & Gogotsi, Y. *Nanotechnology*, 21(1), 15304, **2009**.
- [19] Sen, M., Takahashi, Y., Matsumae, Y., Horiguchi, Y., Kumatani, A., Ino, K., Shiku, H. & Matsue, T. *Anal. Chem.*, 87(6), 3484–3489, **2015**.
- [20] Kim, Y. T., Scarnulis, D. M. & Ewing, A. G. *Anal. Chem.*, 58(8), 1782–1786, **1986**.
- [21] McNally, M. & Wong, D. K. Y. *Anal. Chem.*, 73(20), 4793–4800, **2001**.
- [22] Takahashi, Y., Shevchuk, A. I., Novak, P., Zhang, Y., Ebejer, N., Macpherson, J. V., Unwin, P. R., Pollard, A. J., Roy, D., Clifford, C. A., Shiku, H., Matsue, T., Klenerman, D. & Korchev, Y. E. *Angew. Chemie - Int. Ed.*, 50(41), 9638–9642, **2011**.
- [23] Page, A., Kang, M., Armitstead, A., Perry, D. & Unwin, P. R. *Anal. Chem.*, 89(5), 3021–3028, **2017**.
- [24] Nadappuram, B. P., McKelvey, K., Al Botros, R., Colburn, A. W. & Unwin, P. R. *Anal. Chem.*, 85(17), 8070–8074, **2013**.
- [25] Chen, R., Hu, K., Yu, Y., Mirkin, M. V. & Amemiya, S. *J. Electrochem. Soc.*, 163(4), H3032–H3037, **2016**.
- [26] Jedraszko, J., Michalak, M., Jönsson-Niedziolka, M. & Nogala, W. *J. Electroanal. Chem.*, 815, 231–237, **2018**.
- [27] Jacobse, L., Raaijman, S. J. & Koper, M. T. M. *Phys. Chem. Chem. Phys.*, 18(41), 28451–28457, **2016**.
- [28] Yu, Y., Sun, T. & Mirkin, M. V. *Anal. Chem.*, 87(14), 7446–7453, **2015**.
- [29] Katemann, B. & Schuhmann, W. *Electroanalysis*, 14(1), 22–28, **2002**.
- [30] Ying, Y. L., Ding, Z., Zhan, D. & Long, Y. T. *Chem. Sci.*, 8(5), 3338–3348, **2017**.
- [31] Shao, Y., Mirkin, M. V., Fish, G., Kokotov, S., Palanker, D. & Lewis, A. *Anal. Chem.*, 69(8), 1627–1634, **1997**.

- [32] Huang, K., Clausmeyer, J., Luo, L., Jarvis, K. & Crooks, R. M. *Faraday Discuss.*, 210, 267–280, **2018**.
- [33] Chen, S. & Kucernak, A. *J. Phys. Chem. B*, 107(33), 8392–8402, **2003**.
- [34] Zhao, Y., Fan, L., Zhong, H. & Li, Y. *Microchim. Acta*, 158(3), 327–334, **2007**.
- [35] Lee, I., Chan, K. Y. & Phillips, D. L. *Appl. Surf. Sci.*, 136(4), 321–330, **1998**.
- [36] Domínguez-Domínguez, S., Arias-Pardilla, J., Berenguer-Murcia, Á., Morallón, E. & Cazorla-Amorós, D. *J. Appl. Electrochem.*, 38(2), 259–268, **2008**.
- [37] Georgolios, N., Jannakoudakis, D. & Karabinas, P. *J. Electroanal. Chem. Interfacial Electrochem.*, 264(1), 235–245, **1989**.
- [38] Zubimendi, J. L., Vazquez, L., Ocon, P., Vara, J. M., Triaca, W. E., Salvarezza, R. C. & Arvia, A. J. *J. Phys. Chem.*, 97(19), 5095–5102, **1993**.
- [39] Shimazu, K., Weisshaar, D. & Kuwana, T. *J. Electroanal. Chem. Interfacial Electrochem.*, 223(1), 223–234, **1987**.
- [40] Sutter Instrument Company. *P-2000 Laser-Based Micropipette Puller System Operation Manual*, neurophysics.ucsd.edu/Manuals/Sutter%20Instruments/P-2000_Operation%20Manual.pdf, **2016**.
- [41] Nioradze, N., Chen, R., Kim, J., Shen, M., Santhosh, P. & Amemiya, S. *Anal. Chem.*, 85(13), 6198–6202, **2013**.
- [42] <https://warwick.ac.uk/fac/sci/chemistry/research/unwin/electrochemistry/wec-spm/> Warwick Electrochemistry and Interfaces Group. *WEC-SPM*, **2019**.
- [43] Yu, Y., Noël, J. M., Mirkin, M. V., Gao, Y., Mashtalir, O., Friedman, G. & Gogotsi, Y. *Anal. Chem.*, 86(7), 3365–3372, **2014**.

Chapter 3

Synchronous Conductance - Scanning Electrochemical Microscopy (C-SECM) Measurements

Many improvements in recent years have taken electrochemical imaging techniques to increasingly higher resolution, with greater amounts of functional information. But electrochemical imaging techniques are often still limited in their lateral topographical resolution by either diffusion or by the size of the probe being used. Separating topographical and electrochemical signals is also a long standing limitation in electrochemical imaging and generally forming hybrid scanning techniques has been a solution. Despite some success, previous studies utilising electron tunnelling have been limited and rely on specific instrumentation. Here we demonstrate the conversion of a high-end scanning electrochemical microscope (SECM) to perform conductance - scanning electrochemical microscopy (C-SECM) and tunnelling measurements, with the challenges and limitations associated. Pt nanoelectrodes (PtNEs) formed by electrodeposition on carbon nanoelectrodes (CNEs) were used as the C-SECM tip. An exemplar system of the hydrogen evolution reaction (HER) on 2D Au nanocrystals was used to demonstrate the technique, making use of conductance topography and SECM to map the electrochemical activity.

3.1 Introduction

There has been a surge of SEPM techniques, especially in recent years that aim to simultaneously acquire highly localised topographical, electrochemical and activity based information,¹⁻³ the first of which was SECM.⁴ SECM makes use of a probe with a very small electroactive area so that the electrochemical activity can be measured locally. With the positioning of the probe realised by a nanopositioning system, the activity can be mapped with a resolution similar to the size of the probe. Originally this was carried out using UMEs⁴⁻⁶ on the scale of microns and since then many methods have been used to create much smaller electrodes taking the resolution of SECM into the nanoscale (see Section 1.4.1).^{1,7-10} Other electrochemical scanning probe techniques have also been demonstrated, such as SICM and SECCM, both of which have made vast improvements to the resolution and functional information obtainable in recent years.¹¹⁻¹⁵

Whilst these techniques have proven themselves as extremely useful tools, they do have their limitations. The resolution of SECM is limited by diffusion of the active species to the electrode surface, and the size of the probe; the signal obtained is also a convolution of the probe to surface separation and the electrochemical activity, meaning that often modelling and other techniques are required.^{16,17} SICM faces similar issues, with a diffusion limited response, and determining the surface to probe separation is non-trivial (Section 1.4.2).¹⁸ Whilst SECCM can determine an absolute topography measurement, the resolution is still limited by the probe size and also leaves “footprints” where the probe lands on the surface and therefore alters it (Section 1.4.3).¹³

To try and overcome some of the issues surrounding SEPMs, groups have turned to creating combined multi-technique SPMs (see Section 1.5).^{19,20} SICM-SECM is one such example, where a double barrelled probe is used, one barrel is used as an SICM probe whilst the other is used as an SECM probe. This allows for SICM to map topography whilst SECM maps electrochemistry (Section 1.5.4).²¹ Another very successful combined technique is AFM-SECM, so much so that a commercial instrument has been employed recently.^{22,23} In this case AFM is used to map topography and SECM to map electrochemical activity (Section 1.5.1).²⁴⁻²⁶ Like most SEPM techniques, the major limitation is the choice, fabrication and characterisation of the probes used. Having two barrels in a probe limits the minimum size that an SICM-SECM probe can be and for AFM-SECM creating a probe with a small enough electroactive area and whilst being robust enough to make repeated contact with the surface presents challenges.²⁷

One of the first combined SPMs was STM-SECM (see Section 1.5.3) where insulated Pt/Ir wires were used as probes.²⁸ If the Faradaic leakage current is less than that of the tunnelling current then these probes can be used for in-situ STM. This has been achieved in a few different ways previously.^{29–31} The key for STM-SECM is that the leakage current also has to be smaller than the currents that are to be measured electrochemically.^{4,5,32,33} The key advantages of STM-SECM are that it is non-contact so the sample and probe should not be damaged and that the topographic STM resolution is limited by the geometry of the probe and not the overall electroactive area.³⁴ Combining this fact with the exponential nature of tunnelling current with tip to sample separation, leads to the ability of STM to map topography at the atomic scale.^{35,36} The STM also provides an absolute sample to probe separation, hence deconvolving topography and electrochemistry in SECM measurements.^{29,30} Previous STM-SECM studies have acquired STM (topography) and SECM (electrochemical activity) data asynchronously.^{28,37} In these approaches constant current STM scans were used to map the surface topography, the topographic coordinates are then retraced at a greater sample to tip separation in an SECM fashion (also known as “lift mode”).³⁷ Another similar study used the topographic map to then pick specific points to go back to for electrochemical measurements (NP sites).²⁸ Both of these studies utilised typical STM instrumentation (tube piezoelectric actuators, see Section 1.2.2), however, the Faradaic leakage currents were too high for many electrochemically interesting systems, the probe geometry was hard to elucidate and between acquisition of topographic and electrochemical data there is the possibility of sample and tip drift due to thermal effects and drift of the holders and piezoelectric actuators. These drifts are more concerning with more recent studies which use SEPM instrumentation. Observations of tunnelling currents during an SECM experiment were presented with an analysis of approach curves moving from an SECM to tunnelling regime, using piezoelectric actuators which have an overall travel range of 100 μm and a greatly reduced stability (≈ 1 nm) compared to typical STM instrumentation.^{7,38–40} Tests to prove that these types of SEPM instrumentation are capable of consistent tunnelling experiments have not been demonstrated and this is addressed throughout the following chapter.

Here, we demonstrate the conversion of a high end SEPM instrument to a C-SECM instrument in order to simultaneously map topography and electrochemical activity, overcoming some of the drawbacks of SECM, such as the topographic resolution and the convolution of activity and tip-sample separation in current measurements. The limitations of such an approach are addressed and compared to

recent studies involving similar regimes. Pt electrodeposited on CNEs (as in Chapter 2) was used as the probe, with a “hopping pulse” methodology similar to a previous SICM¹¹ and SECM⁴¹ study to carry out the topography and SECM scans simultaneously, avoiding drift between the two.

The experiment chosen here to demonstrate the C-SECM methodology is a study of the HER for Au 2D nanocrystals on a glassy carbon (GC) support, which has recently had topography-activity measurements made at the nanoscale using SECCM.⁴² This system was chosen as the sharp well defined shapes of the crystals make for ideal demonstrations of the resolution achievable. This system also allows for a stark contrast electrochemically as the GC support requires a very high overpotential to generate hydrogen, whereas hydrogen is generated more readily on Au.^{43,44} In air conductance measurements were also made to investigate key factors for consideration when attempting to make conductance or tunnelling based measurements on a SEPM platform.

3.2 Methodology

3.2.1 PtNE Fabrication

Parasitic currents in coated wire tips are a well known issue in previous liquid-phase STM reports.^{45,46} Hence, here nanoscale SECM probes consisting of Pt sensitised CNEs were used as the C-SECM tip. The method of PtNE fabrication is set out in Chapter 2 and follows the coil heating (Section 2.2.1) and cyclic method of Pt deposition (Section 2.2.2). The specifics for the electrodes in this chapter are as follows: firstly, quartz capillaries (QF100-50-10, Sutter Instrument Co.) were pulled to a 50 nm aperture using a P-2000 laser based pipette puller (Sutter Instrument Co.). A two line program was used for pulling: 1. *Heat* = 750, *Filament* = 4, *Velocity* = 30, *Delay* = 150, *Pull* = 80, 2. *Heat* = 650, *Filament* = 3, *Velocity* = 40, *Delay* = 135, *Pull* = 150. Pyrolytic carbon was then deposited on the inner walls of the capillary in a similar fashion to reported previously.^{47,48} In short, a hydrocarbon mixture (butane and propane 600 ml gas torch refill, RS PRO) was flowed into the rear of the capillary from the non-pulled end (up to a pressure of 1.2 bar), whilst Ar ($\geq 99.998\%$, Sigma-Aldrich) was continuously flowed over the end of the capillary using a larger diameter capillary (QF120-90-10, Sutter Instrument Co.), with a flow rate of 0.2 L min^{-1} . Whilst the gasses were flowing, an electrically heated coil was propagated along the length of the capillaries. The coil temperature was held steady around $750\text{ }^{\circ}\text{C}$ whilst the motion of the coil was realised using an electric stepper motor controlled by in-house constructed electronics. The program for coil

propagation was optimised to give a glossy black finish to the probes, an electrical connection was then made by inserting a copper (or similar) wire into the back of the capillary so that it makes a physical contact with the carbon.

The final step of fabrication involves potentiodynamic electrodeposition of Pt onto the CNE, expanding on a previously reported method.¹⁹ The electrodeposition of Pt sensitises the tip to electrocatalytic processes and ensures that the metal protrudes from the end of the quartz pipette, required for conductance and tunnelling measurements. This was carried out using a two electrode setup with the CNE as the working electrode and an Ag/AgCl QRCE formed by anodising 0.125 mm annealed Ag wire, (99.99 %, Sigma-Aldrich) in a saturated KCl (> 99 %, Sigma-Aldrich) solution. An electrometer (built in house) was used to apply the potential and measure the current simultaneously. The deposition solution consisted of 1 mM $\text{H}_2\text{PtCl}_6 \cdot 6\text{H}_2\text{O}$ (≥ 99.9 %, Sigma-Aldrich) and 0.1 M HClO_4 (70 %, Sigma-Aldrich). The deposition was carried out by cycling the potential at the electrode from 0.3 V to -0.2 V, whilst monitoring the current increase with each sweep until the current surpassed 50 pA (Figure 3.1a). Figure 3.1b displays CVs taken before (blue) and after (orange) Pt deposition which display an increase in the magnitude of the steady state current by a factor of $\pi/2$ which would be expected from a transition from a disc shaped to a hemispherical geometry (see equation 1.8 & 1.9), whilst the sigmoidal shape associated with a diffusion limited reaction was maintained.⁴⁹ STEM was used for further characterisation of these electrodes, an example is shown in Figure 3.2a. As mentioned previously (Section 2.2.1), an anti-static ankle bracelet was worn whilst handling nanoelectrodes in an attempt to reduce the risk of electrostatic damage to electrodes.

If it is assumed that the electroactive area of the electrode is hemispherical and the reaction is limited by diffusion, the electroactive area can be estimated using equation 1.9 ($i_{\text{ss}} = 2\pi nFDca$) for the steady state limiting current, where n is the number of electrons in the redox process, F is the Faraday constant (96485.33 sAmol⁻¹), a is the radius of the hemi-sphere and D and c are the diffusion coefficient and concentration of the electroactive species respectively.⁴⁹ For the example in Figure 3.1b, the value of a is determined to be approximately 30 nm giving an electrode area of 0.006 μm^2 in reasonable agreement with the STEM images (Figure 3.2a). This does not, however, take into account back diffusion to the electrode surface which would increase the expected steady state current.

Due to the nature of the Pt deposition, each NE does not have exactly the same electroactive area, hence each NE is characterised with a CV in $[\text{Ru}(\text{NH}_3)_6]^{3+}$ (hexaamineruthenium(III) chloride, 98 %, Sigma-Aldrich) and KCl (> 99 %, Sigma-

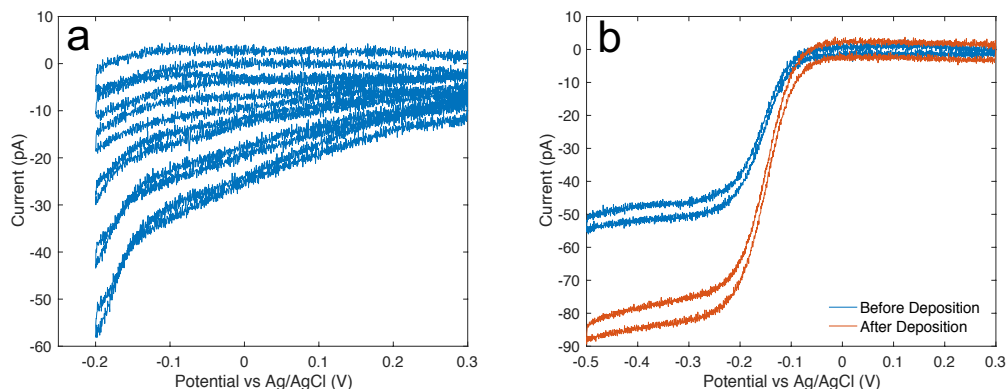


Figure 3.1: (a) Voltage sweeps recorded in Pt deposition solution (1 mM $\text{H}_2\text{PtCl}_6 \cdot 6\text{H}_2\text{O}$ and 0.1 M HClO_4); the increase in current at negative potentials with each sweep is monitored. The sweep rate is 0.2 V s^{-1} . (b) CV of CNE before (blue trace) and after (orange trace) Pt deposition in (a), recorded in 5 mM $\text{Ru}(\text{NH}_3)_6^{3+}$ and 0.1 M KCl, with a 0.2 V s^{-1} sweep rate.

Aldrich) as in Figure 3.1b. The calculated electroactive radius generally ranged from 15 nm to 100 nm. The tip used in C-SECM studies presented here was $\approx 80 \text{ nm}$ in electroactive radius (Figure 3.1b).

As discussed in Chapter 2, this methodology does have limitations. Some information relating to the quality of NEs can be inferred from CV, however, estimating the total electroactive area entirely from the mass transport limited current may not be completely accurate. Recent work showed examples of several CNEs that displayed good sigmoidal voltammograms but when imaged in TEM were shown to have varying geometries, not all of which were ideal (see Figure 2.1).⁴⁸ Here we have also observed similar results, additionally we have found that electrodes may even be hollow with only a thin lining of carbon down the interior walls of the capillary. Damage to the pipette during the carbon deposition process is also possible, this can then cause Pt deposition to occur in other locations than the end of the probe (Figure 3.2b) whilst still showing the expected sigmoidal voltammetry afterwards (Figure 3.2c). A combination of high resolution microscopy techniques and voltammetric analysis appear to be the only way to ensure proper probe characterisation (see Chapter 2).²

3.2.2 2D Au Nanocrystals and AuNPs

2D Au nanocrystals were fabricated similarly to previous literature.^{42,50,51} 50 g lemongrass (*Cymbopogon flexuosus*) was finely cut and boiled in 250 mL deionised water for 5 minutes. This was then left to cool to room temperature and 5 mL was

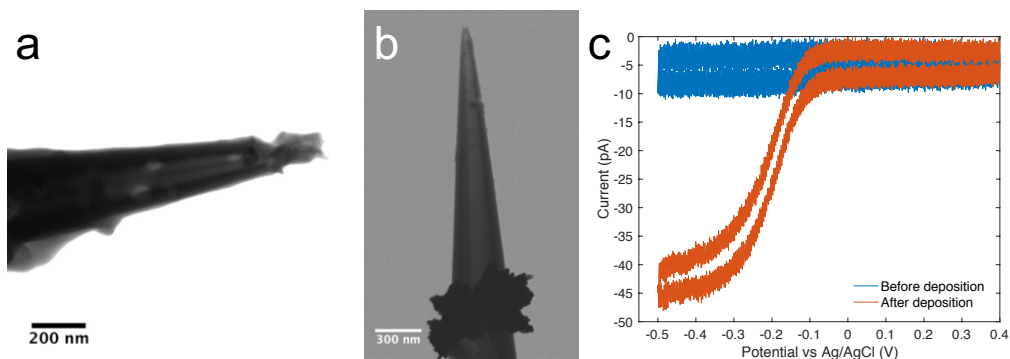


Figure 3.2: (a) STEM image of Pt deposited on a CNE. It can be seen that the Pt protrudes from the end of the electrode in a confined area. (b) STEM image of Pt deposited on a damaged CNE. (c) CVs before (blue) and after (orange) Pt deposition for NE in (b). 1 mM $\text{Ru}(\text{NH}_3)_6^{3+}$ in 0.1 M KCl, 0.2 V s^{-1} . Poor electrode geometry is observed despite the expected voltammetric response.

added to 45 mL of 1 mM HAuCl_4 (99.99 %, Sigma-Aldrich). The solution was then purified by three centrifuge cycles at 3000 g and resuspended in 50 mL deionised water. 2 μL of this solution was then drop cast on a GC substrate (glassy carbon plate, 3 mm thick, type 1, 25 x 25 mm, Alfa Aesar) and washed with deionised water. The drop cast area was then masked off using tape (3M Polyimide film tape) to leave an approximately 2 mm diameter exposed area. This allowed for substrate currents to be monitored as the bipotentiostat used had an upper current limit of 1 μA . A CV of this substrate in 0.1 M HClO_4 is shown in Figure 3.3 where a sharp increase in current to 100 nA is seen at negative potentials which is attributed to the generation of H_2 via the HER. The magnitude of the current change is relatively small compared with the exposed area, this is due to the low coverage of Au nanocrystals on the GC surface, verified via SEM imaging. In addition to the nanocrystals, large Au clusters (on the scale of several microns) are also deposited, these clusters are visible in the optical microscope when approaching the probe. A coarse scan was done first to locate the same cluster using the topographic mapping, the higher resolution C-SECM scans were then taken on individual crystals. Due to knowing the location of a large cluster, this was used as reference point for locating the same crystals in the SEM.

For ambient experiments AuNPs were deposited onto a GC support. First a solution of AuNPs (gold nanoparticles, 200 nm diameter, stabilised in citrate buffer, Sigma-Aldrich) was diluted 20 fold before sonicating for 20 minutes. 1 μL of this solution was then drop cast onto a GC support (as above). The GC was then washed with deionised water to remove any salt residue before experiments.

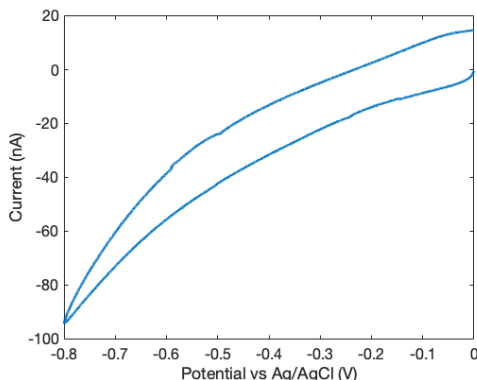


Figure 3.3: CV of GC substrate with Au nanocrystals drop cast. The substrate was masked to leave a ≈ 2 mm diameter circle uncovered to limit the overall currents measured. The potential was measured against a Ag/AgCl reference electrode in 0.1 M HClO_4 , scan rate 0.2 V s^{-1} .

3.2.3 SPM Instrumentation

All scanning probe experiments were carried out on an in-house constructed SPM system. Probe control is realised using vertical (P-753.1CD, Physik Instrumente) and lateral (P-733.2DD, Physik Instrumente) piezoelectric positioners with accompanying amplifiers for vertical (E665, Physik Instrumente) and lateral (E505, Physik Instrumente) positioners. Coarse lateral and vertical motion was carried out using Picomotor piezo linear actuators (Newport), which have been assessed for stability previously.⁵²

The tip in ambient (in air) experiments consisted of a mechanically cut Pt/Ir wire (70/30 %, 0.25 mm diameter, Sigma-Aldrich) which was connected to copper wire at the non-tip end and the substrate was connected to ground. All C-SECM experiments in solution were carried out in a three electrode system with the probe (PtNE), substrate (GC) and an Ag/AgCl reference electrode (Figure 3.5a). The potential was applied and the current measured on both the probe and substrate using separate in house built electrometers.

All parameters were then controlled using an FPGA card (PCIe-7825R, National Instruments) with home designed LabVIEW software (WEC-SPM).⁵³ Piezo-electric components, sample, tip and reference are kept inside a sealed Faraday cage on a vibration isolated table (Newport S-2000 series pneumatic vibration isolators). The electronics (controllers, amplifiers etc.) are all kept on a separate shelf in order to isolate the vibrations associated. To test the vibration isolation of the system a 3W speaker was used to generate noise at set frequencies (70 Hz, 85 Hz and 90

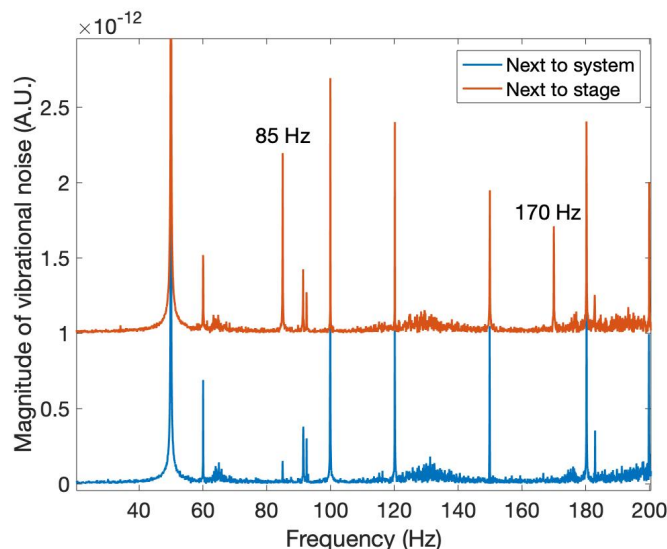


Figure 3.4: Fast Fourier transforms of measured tip current with a 3W speaker generating 85 Hz noise next to the instrument but outside the Faraday cage (blue) and directly next to the stage inside the cage (orange). 85 Hz and multiples thereof only become visible once the speaker is directly next to the stage. Peaks for multiples of 50 and 60 Hz are expected electrical noise.

Hz) to see if the associated frequency would show in measured currents. Figure 3.4 shows fast Fourier transforms of measured currents with the speaker inside and outside the Faraday cage for a 85 Hz generated noise (the results for 70 Hz and 90 Hz are very similar). Vibrations were only observed in the current response once the speaker was placed directly next to the imaging stage, which gives confidence that external vibration sources did not affect the instrumentation.

3.2.4 C-SECM Measurements

To the best of our knowledge, no other reports of C-SECM experiments have been published. However, the C-SECM studies were carried out in a “hopping pulse” methodology, which is similar to a previously reported method for SICM¹² and SECM⁴¹ described in Figure 3.5b,c. The tip potential is kept constant at a value where no electrochemical reaction is happening, but is appropriate to detect the hydrogen generated at the surface (0.4 V for HClO_4) throughout the scan. At each pixel (Figure 3.5b,c), the tip is (A) approached until a set current threshold is met (tunnelling or contact), recording the tip position whilst the substrate potential is kept at 0 V, the tip is then retracted a set amount (B) followed by a pause in this position, the substrate potential is switched to generate HER (-0.7 V for HClO_4)

and the hydrogen generated measured at the tip (C). Finally, the substrate potential is switched back to 0 V and the tip is retracted back to a bulk position (D), before repeating for each pixel in the scan in a raster type pattern to generate the maps. This methodology creates a simultaneous topographical and electrochemical map using the tunnelling/ contact position and electrochemical current respectively. This method also gives an absolute distance from the surface for electrochemical measurements, so that there is no need to deconvolute electrochemical and topographical data.

It is important to consider the approach rate during hopping scans; the approach must be sufficiently slow so that the electronics can “react” quickly enough to stop the approach before contacting the surface. Each electronic component will have a delay associated with it. The summation of delays should be small enough that, with a set approach rate, the probe will not contact the sample. For example, assuming the onset of tunnelling current happens within ≈ 2 nm and that a total delay of the electronics is 1 ms, then the approach velocity should be limited to $2 \mu\text{m s}^{-1}$. Unfortunately this is not the only factor that influences the system stability: whilst factors such as vibration were minimised, factors such as piezoelectric hysteresis and reaction speed are much harder to elucidate and are discussed further throughout. Here the following electronic components were considered for the delay: FPGA card ($1 \mu\text{s}$),⁵⁴ piezoelectric amplifier ($10 \mu\text{s}$),⁵⁵ electrometer filter ($200 \mu\text{s}$, instrument constructed in-house), data was acquired every $768 \mu\text{s}$ and the resonant frequency of the piezoelectric actuator ≈ 4.8 kHz, \approx ms scale⁵⁶. This gives a total delay of a couple of ms, therefore with an onset for tunnelling current of a couple of nm the approach rate should be limited to a couple of microns per second.

3.3 Results and Discussion

3.3.1 Piezoelectric Actuators Stability

As described in Section 1.2, electron tunnelling between the tip and substrate occurs only on a distance scale of a couple of nanometres.³⁵ For this reason, commercial STM instruments utilise extremely high resolution, stability and low noise piezoelectric actuators and controllers (Section 1.2.2). The system will then also be isolated thermally and from vibrations that can cause extra noise and instrument drift. Positioning systems like these have a very high spatial resolution but often a very small overall range of motion ($< 1 \mu\text{m}$ vertically and $< 5 \mu\text{m}$ laterally),^{57,58} limiting the applications to small scan areas, which may limit SECM experiments due to their typically larger scale. Given the piezoelectric actuators used here are

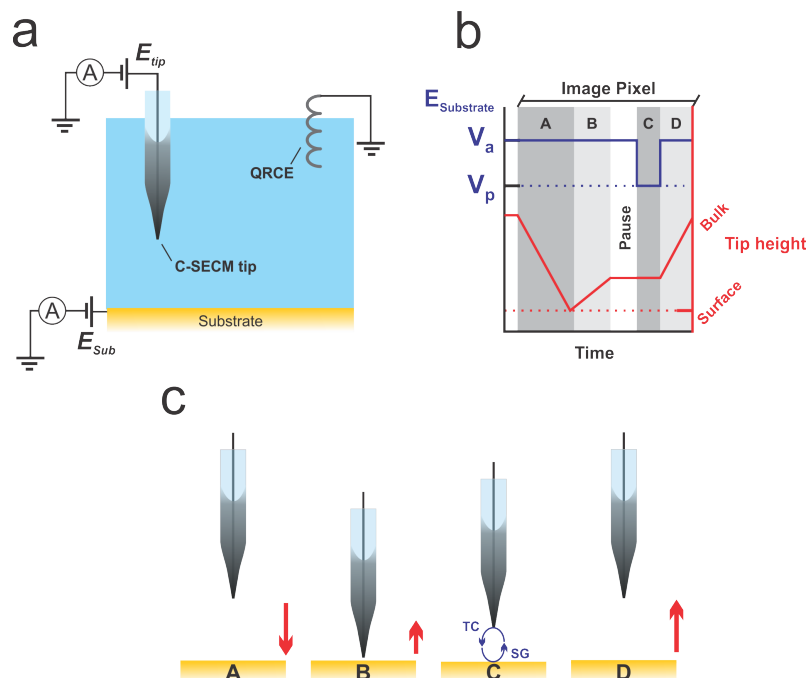


Figure 3.5: (a) Schematic representation of electrode configuration for C-SECM experiments with the tip and substrate potentials controlled relative to a QRCE at ground. (b,c) Representation of the hopping pulse scheme used for each pixel in C-SECM images. V_a is the substrate potential avoiding electrochemical activity and V_p is the substrate pulse potential. The tip is approached until a specific current feedback value is reached (conductance mode, A) where the position is used for topography, the tip is retracted a short distance (B) before a short pause, followed by the substrate pulse (C) which is used for electrochemical activity.

normally applied to electrochemical imaging, it is important that their stability and suitability for very high resolution studies such as C-SECM or STM is addressed. In addition to the vertical P-753.1CD piezoelectric used in the following experiments, a P-621.ZCD piezoelectric was also tested, as this model or similar models from the same range have been used in recent studies that involved tunnelling currents.^{7,38,39} Both models have a capacitance based sensor built-in that measures the current extension of the piezoelectric and can also be used to compensate for the drift of the extension. These piezoelectrics have a drift compensation operating mode known as “servo mode”. In this mode the desired extension of the piezoelectric is kept constant by adjusting the output voltage for the amplifier in a closed loop scenario. The manufacturer states resolution in the closed loop of 0.4 nm and 0.1 nm for the P-621.ZCD and P-753.1CD respectively.^{56,59} The open loop resolution for the P-621.ZCD is stated as 0.2 nm but this value is not stated for the P-753.1CD.

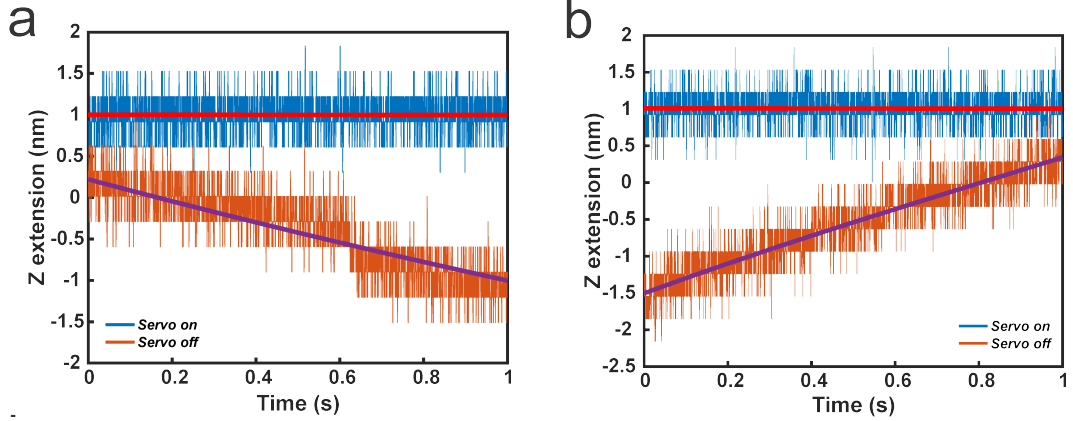


Figure 3.6: Readings from in-built sensor over 1 s with “servo mode” on (blue) and off (orange) for the P-621.ZCD (a) and P-753.1CD (b). A noise of ≈ 1 nm is shown for both piezoelectrics with the servo on or off and without the servo a drift of ≈ 1 nm s^{-1} is seen, this would make constant height or current imaging impossible in the tunnelling regime.

Figure 3.6a and Figure 3.6b show the output from the capacitance sensor (piezoelectric extension) for the P-621.ZCD and P-752.1CD respectively when a non-zero extension is set on the actuator (this was tested with and without a tip mounted with the same results). Both models show a discrete response corresponding to a positional change of at least 1 nm. This data was recorded with varied sample rates up to a maximum of one data point every $5 \mu s$ using a 16-bit FPGA card, with the same discrete behaviour noted. This would suggest that the sensitivity of the extension sensor is not high enough to measure the actual piezo extension to a greater precision than ≈ 1 nm, this makes it difficult to maintain tunnelling currents using the close loop feedback of the system. However, without the use of “servo mode” (open loop) drifts on the 1 nm s^{-1} scale can be observed (Figure 3.6), again showing that staying within a couple of nm of the surface for a significant length of time without other positional feedback methods is not possible. One study also demonstrated that minimal drift can only be achieved with a drift compensation mode even if the instruments thermal isolation is extremely well constructed.⁶⁰ Whilst limitations have been described here, the P-753.1CD is stated as higher resolution and has a much shorter overall extension range ($15 \mu m$ compared to $100 \mu m$) than the P-621.ZCD. Due to the decreased overall range, the smallest unit of motion is also greatly reduced. The FPGA card here is a 16-bit card, hence it has 2^{16} possible values to use. The piezoelectric amplifier takes a 0 to 10 V input which is then converted to a -30 to 160 V output, hence the smallest change the amplifier can output is 2.9 mV. Given a total piezo range of $15 \mu m$ (for the P-753.1CD) then

a change of 1 V corresponds to 79 nm of extension change. Therefore the smallest unit that the piezoelectric can theoretically be moved is 0.2 nm, the same calculation for the P-621.ZCD gives 1.5 nm. The resonant frequency of piezoelectrics also has an effect on their latency; higher resonant frequency piezoelectrics have been shown to have less of a tip overshoot in SICM approach measurements, even though no difference was observed in the piezoelectric monitors.^{11,61} The P-753.1CD has a resonant frequency of ≈ 4.8 kHz vs the P-621.ZCD at ≈ 500 Hz,^{56,59} therefore the P-753.1CD is the better choice regardless of the other issues stated. Also, when compared to previous studies, the hopping methodology employed here (see Section 3.2.3) bypasses some issues as the tip is not required to be held steady for longer than the length of substrate electrochemical pulses (< 0.2 s here), therefore the tip drift on this timescale is less than a nm. Constant separation methods, however, would require the tip to be in close proximity to the surface through the entire scan which would not be possible given the results above.

3.3.2 Ambient Measurements

Given the noise in piezoelectric monitors discussed above, slow approach curves ($\lesssim 5$ nm s⁻¹) were obtained to investigate the capability of the instrumentation to carry out tunnelling type experiments. The ambient approach curve in Figure 3.7 demonstrates this with an approach rate of 2 nm s⁻¹ and a feedback threshold of 30 pA. There is no significant overshoot above the threshold current and the exponential profile expected for a tunnelling current is obtained over the last 0.1 nm of the approach. Additionally the logarithm of the current is plotted in the inset of Figure 3.7 and shows the expected linear response.³⁵ Whilst the tunnelling response can be detected at these approach rates, carrying out topographical mapping in a hopping format requires faster rates so that scans can be obtained over a sensible range (> 100 nm) without thermal drift or sample and tip contamination becoming a significant issue in the timescale of the acquisition. Hence faster rates are investigated below for topographic imaging.

As mentioned above, the stability of the actuators used here was not sufficient for constant current or height mode STM imaging and hence a hopping protocol was utilised (Section 3.2.4). To demonstrate the capability of an electrochemical imaging instrument to carry out topographical experiments, two sample systems were studied under ambient conditions using a conventional STM probe (mechanically cut Pt/Ir wire) in a hopping methodology similar to described in Section 3.2.3 but without the pulse phase and with the substrate held at ground. The tip was approached towards the surface until the current feedback threshold is met (which should be sensed as

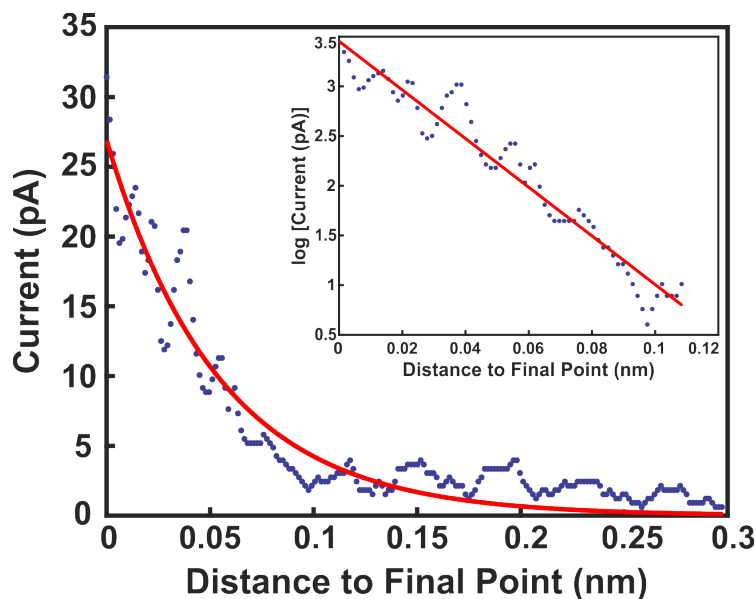


Figure 3.7: Approach curve with 30 pA current threshold and 2 nm s^{-1} approach rate to a clean GC substrate using a Pt/Ir wire tip in ambient conditions. The same data with the logarithm of the current is displayed in the inset.

a tunnelling current without surface contact), at each point before retracting back and moving onto the next pixel. In addition the hopping methodology has the advantage that it can potentially scan substrates with a much larger heterogeneity in topography than typical constant separation modes of operation. The first sample studied was 2D Au nanocrystals which have been shown previously using SECCM and AFM to have a thickness of $\approx 15 \text{ nm}$ and lateral dimensions varying from 100s of nm to a μm .^{42,62} Distinguishing 15 nm topographical features would typically prove challenging to electrochemical imaging techniques. The second system studied was $\approx 200 \text{ nm}$ diameter AuNPs also supported on GC. Typically operating in a constant current or height mode STM here would cause the tip to contact the side of the particle whilst scanning rather than moving over it.

Figure 3.8a shows a topographic scan of a Au nanocrystal along with a topographic line profile in Figure 3.8b. The crystal is easily distinguished from the GC support, with a height of 10 – 20 nm in accordance with the previous measurements.^{42,62} In addition, a non-uniform topography is observed across the surface of the crystal, demonstrating the capabilities of the piezoelectric actuators in terms of high resolution studies if a smart scanning protocol is employed. An SEM image of the AuNPs is shown in Figure 3.8c and the ambient hopping scans of the same sample (not the same particles) is shown in Figure 3.8d. Individual particles within

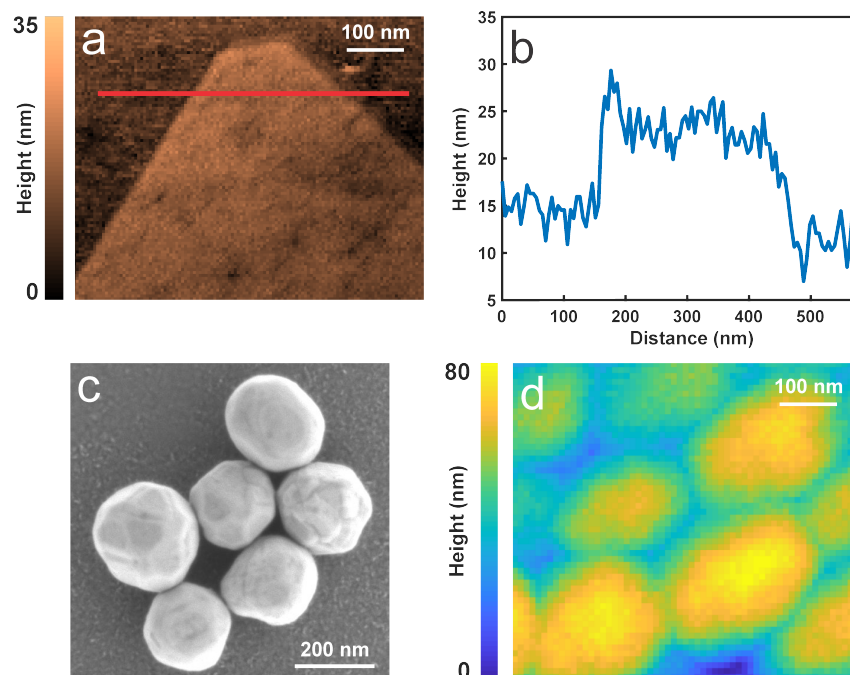


Figure 3.8: (a) Hopping ambient topographic scan of a Au nanocrystal with a mechanically cut Pt/Ir wire tip. Approach velocity: $1.1 \mu\text{m s}^{-1}$, tip bias: 0.4 V, pixel separation: 5 nm, current set point: 50 pA, retract distance: 60 nm. (b) Topographic line profile taken from red region in image (a), with dimensions in agreement with previous literature.^{42,62} (c) SEM image of drop cast 200 nm AuNPs on a GC substrate. (d) Ambient hopping topographic scan of AuNPs, larger topographical features than would normally be studied with STM are resolved. Approach velocity: $1.8 \mu\text{m s}^{-1}$, tip bias: 0.5 V, pixel separation: 10 nm, current set point: 100 pA, retract distance: 250 nm.

the cluster are distinguished which would not be possible with most electrochemical imaging techniques (due to diffusional broadening)³³ and the particles are not moved by the tip. The resolution presented here is still not as high as traditional STM but it is far better than any SEPM and the use of larger range actuators allows for the scale of this image to be much larger than traditional STM experiments in both lateral and vertical dimensions.

These scans show an excellent topographic resolution, however, an overshoot in the approaches in the hopping scan was observed. A typical approach curve during the scan in Figure 3.8a is displayed in Figure 3.9a, showing that despite a threshold current of 50 pA the system recorded up to ≈ 3200 pA before stopping and retracting the tip away. Due to the fast approach rate used here ($1.1 \mu\text{m s}^{-1}$) the onset of tunnelling current is only observed for one or two data points. Approach curves were plotted using the approach velocity ($1.1 \mu\text{m s}^{-1}$) and the time to avoid

using the piezoelectric monitors (which were shown in Section 3.3.1 to have a noise of 1 – 2 nm). An exponential fit (expected for the onset of tunnelling current)³⁵ was then plotted and the difference in distance between the last recorded data point and the expected distance for the threshold current was used to measure the overshoot (Figure 3.9a). The overshoot values for all approaches in the scan were then collected in Figure 3.9b showing that the overshoot is in the region of 0 – 2.25 nm (similar to the stated noise in Figure 3.6b), with the majority in the 1 – 1.5 nm range. Once the approach has overshoot by more than 2 nm it is almost certain that the tip has contacted the sample, in which case the measured tip current can no longer be used to give a sensible value for tip overshoot as the current becomes limited by the sample conductance rather than the tunnelling current, additionally at this point the tip could be overshooting further but no increase in the measured tip current would be observed.

The value of the current at the final data point in the approach curve was plotted for each pixel in the scan in Figure 3.9c with the data also summarised in a histogram in Figure 3.9d. Most of the approaches stop within a couple hundred pA of the threshold value (50pA), however, there is a large number of current values, that are much higher. Interestingly, the current values are higher over the Au nanocrystal compared to the GC support; given the overshoot is often a couple of nm or more it is suggested that the larger current values are due to the increased conductivity of Au compared to GC which suggests that this data set is actually more akin to conductive AFM,^{63,64} hence the term C-SECM is used for measurements herein.

3.3.3 C-SECM in Electrolyte Solution

The HER at Au 2D nanocrystals was used to investigate the possibilities of C-SECM with the SEPM instrumentation here. The Au crystals supported on GC (same substrate as for ambient scans) provide an ideal demonstration of the lateral resolution achievable due to their sharp well defined edges, also they present electrochemical contrast due to the lower onset potential for HER on Au compared to GC.^{43,44} The protocol described in Figure 3.5 was applied to the substrate with 0.1 M HClO₄, $V_a = 0$ V and $V_p = -0.7$ V. This setup drives HER at the substrate (see Figure 3.3) and the hydrogen is collected at the tip (by oxidation of protons). The tip current is monitored throughout all stages of the C-SECM scan and the response during a single pixel is shown in Figure 3.10. Whilst the tip is in bulk and sufficiently far from the substrate surface, the tip current is close to zero. Once the tip is approached sufficiently close, a sharp increase in cathodic current is observed (tunneling and/or contact). When this current reaches the threshold value (A) the tip is immediately

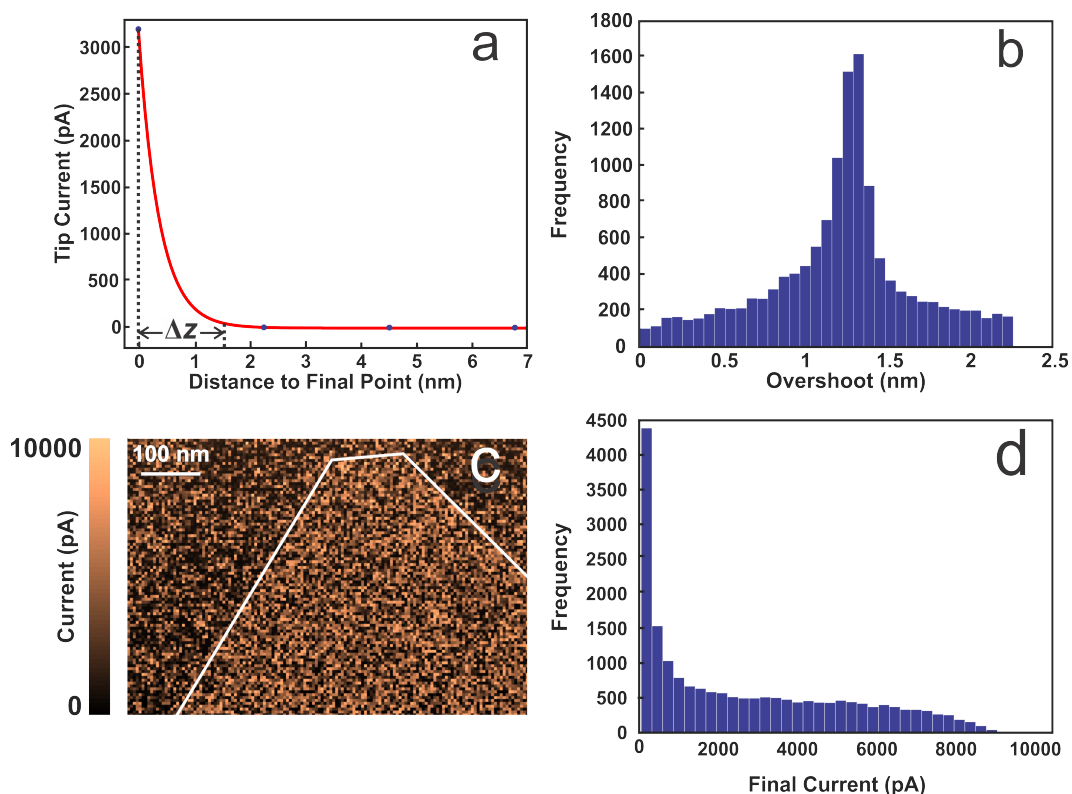


Figure 3.9: (a) Typical approach curve from scan in Figure 3.8a, with distance taken from approach rate ($1.1 \mu\text{m s}^{-1}$) and time. Calculated overshoot from exponential fit labelled as Δz . Current set point: 50 pA. (b) Histogram summarising all calculated overshoots for data from scan in Figure 3.8a, the majority being in the 1 – 1.5 nm range. (c) Scan data from Figure 3.8a using the current value of the final data point in the approach curve, displaying higher currents over the Au nanocrystal, highlighted within the white borders (transferred from Figure 3.8a). (d) Histogram summary of data from (c), whilst most pixels have currents within a few 100 pA of the threshold (50 pA), many are much larger.

withdrawn by a set amount and the current returns to zero (B). The system is held here for a short pause before the substrate potential is then jumped to drive the HER, and after a cathodic spike in the tip current, attributed to coupling between the tip and substrate through the interelectrode capacitance and resistance, REF, an anodic tip current is observed as expected for detection of H_2 from the HER (C). At the start and end of the substrate pulse a cathodic and anodic spike respectively are observed in the tip current, indicating an electronic coupling between the tip and the substrate. Electrochemical images are taken by averaging the last 30 ms of the tip current during the substrate pulse. After the pulse the current returns to zero and the tip is translated laterally to the next pixel (D).

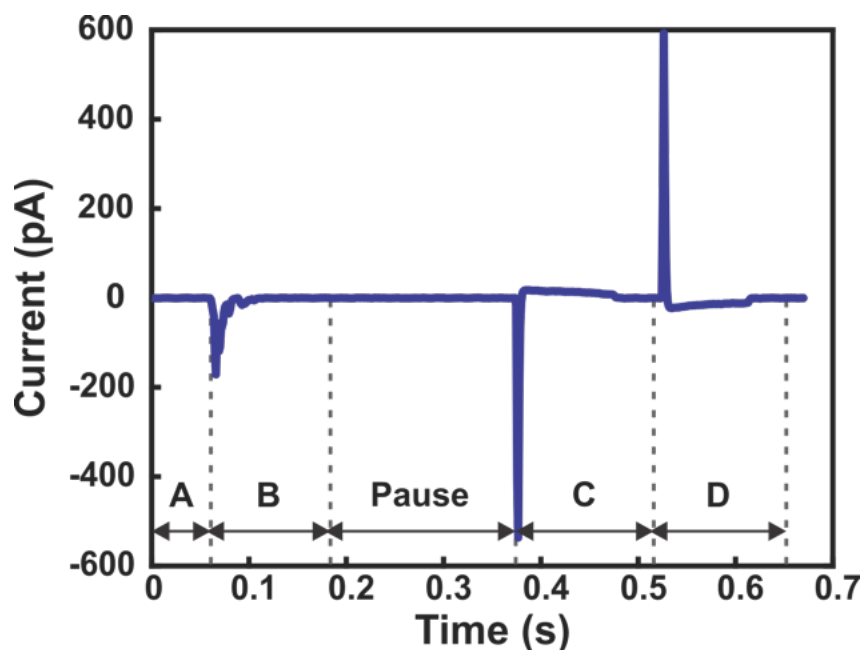


Figure 3.10: Measured tip current during a single pixel of a C-SECM scan. As in Figure 3.5b,c, the tip is approached towards the surface until tunnelling and/or contact is sensed (A), a short tip retract is then done (B), a pause is held in this position, the substrate potential is switched to drive the HER (and the electrochemical maps are made with the last 30 ms of the pulse, C), finally the tip is retracted and moved laterally to the next pixel (D). Tip potential: 0.4 V, substrate potential: -0.7 V.

Figure 3.11 displays simultaneous topography (b,c) and SECM scans (d,f) of a Au nanocrystal, compared with an SEM image (a) of the same crystal using the “hopping pulse” scanning method previously mentioned (Section 3.2.3). The crystals on the GC are kept immersed in 0.1 M HClO_4 throughout experiments. The CV of the substrate shown in Figure 3.3 was used to pick an appropriate potential for substrate pulses to generate hydrogen (-0.7 V). The topographic maps (Figure 3.11b,c) are in good agreement with the SEM image (Figure 3.11a) for the size of the crystals and the electrochemical maps (Figure 3.11d,e,f) show an increased activity over the crystal which is not visible over the GC support. In addition, the electrochemical currents measured here are on the pA scale which is much lower than the leakage current of most previous in-situ STM studies which are typically on the 10s to 100s of pA scale,^{30,65} highlighting an advantage of using a NE tip sealed in quartz.^{28,37} There are some key issues demonstrated here. In the SECM images several pixels with negative values are observed (seen as zero on the displayed scale) this is especially obvious in Figure 3.11f compared to 3.11d, where the abundance

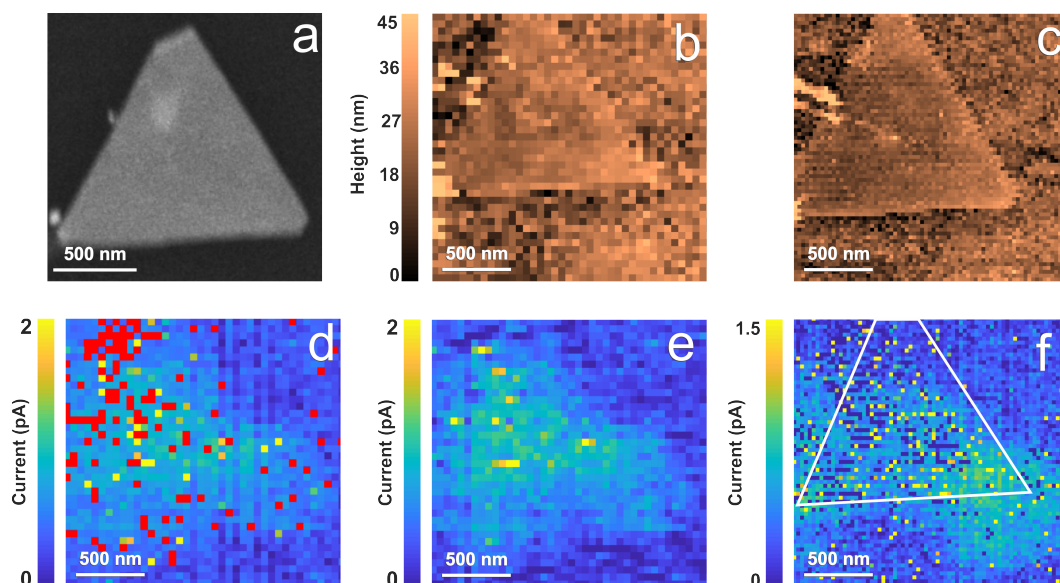


Figure 3.11: (a) An SEM image of a Au nanocrystal. Simultaneous topography(b,c) and unfiltered SECM (d,f) scans of the same crystal in 0.1 M HClO_4 . Topography and electrochemical maps were obtained simultaneously, such that, maps b and d were obtained together and the higher lateral resolution maps c and f were obtained together. Electrochemical maps were obtained by averaging the tip current for the last 30 ms of the pulse phase (Figure 3.5b,c, C). Pixels with tip-substrate contact exhibit large cathodic currents and hence appear as zero in (f). In (d) pixels with contact have been highlighted in red. (e) same data as presented in (d) where contact pixels are replaced with an average of the previous and subsequent pixels. White outline in (f) is taken from topography in (b,c). Approach velocity: 400 nm s^{-1} , tip bias: 0.4 V, first retract: 16 nm, pause: 0.15 s, substrate potential: pulsed from 0 V to -0.7 V for 0.15 s with final 30 ms of pulse used for electrochemical maps, second retract: 70 nm, tunnelling set point: 50 pA, pixel separation: 50 nm (b,d,e), 25 nm (c,e).

of these pixels reduces the SECM contrast considerably. These pixels are due to an intermittent re-entering of the tip into the tunnelling regime or contacting the surface during the pulse step of the scan and are discussed further below (Figure 3.5b,c, step C). Figure 3.11e, shows the result of some 1D, line-by-line image interpolation, the pixels where tip-substrate contact occurred were replaced with an average of the previous and subsequent pixels. This interpolation is valid as these crystals have been shown to have a homogeneous electrochemical activity⁴² with similar methods being used previously.⁶⁶

The slower approach and higher data acquisition rate here (compared to the ambient scans) allows for more data points for approach curves in the C-SECM scans. Figure 3.12a shows an approach curve from the scan in Figure 3.11c,e with

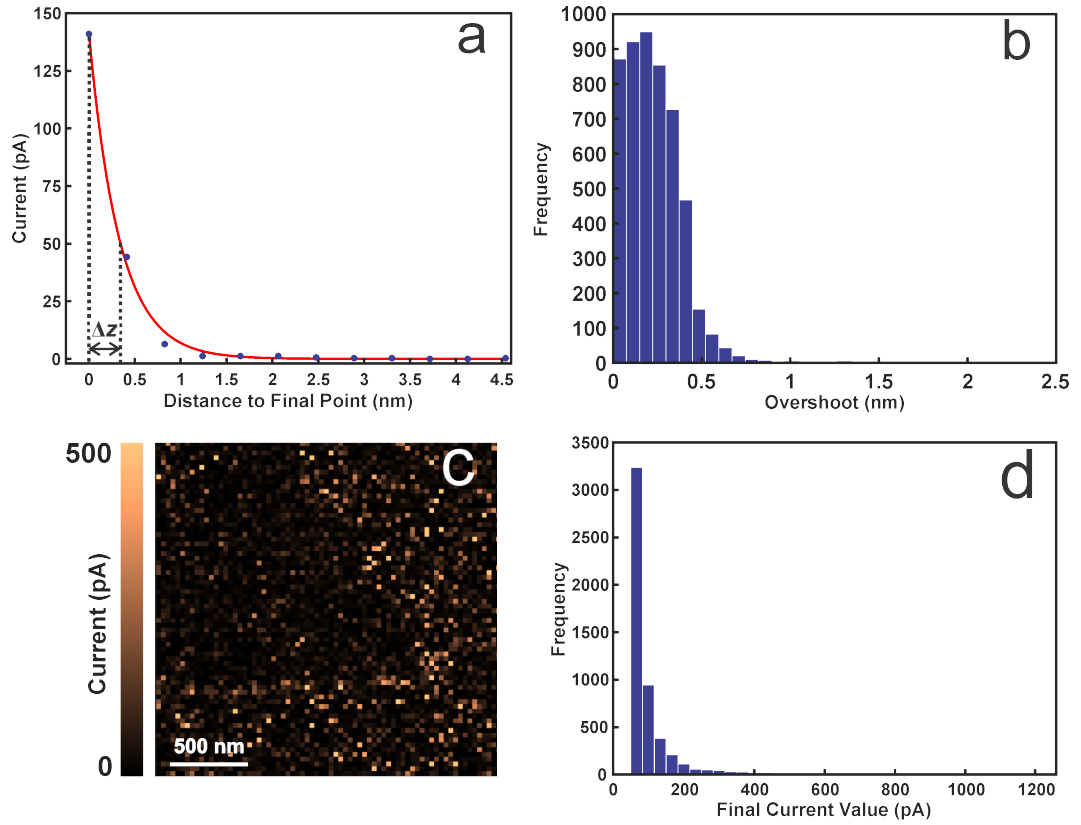


Figure 3.12: (a) Approach curve taken from scan in Figure 3.11c. Approach rate (400 nm s^{-1}) used with time to plot distance, Δz is the measured overshoot. (b) Histogram of calculated overshoot values for every approach curve in Figure 3.11c, the majority of which are now below 0.5 nm. (c) The same scan as Figure 3.11c but using the final current in the approach curve rather than the final piezoelectric position. Higher currents observed over nanocrystal. (d) Histogram of data from (c), the slower approach rate shows much lower final currents than those in Figure 3.9d.

an overshoot much like in Figure 3.9a but with a much smaller magnitude ($\approx 90 \text{ pA}$ over). The approach curves were plotted using the same method as for Figure 3.9a using the approach rate and time to avoid the uncertainty in the piezoelectric monitor, the overshoot Δz , is displayed on the exponential fit in Figure 3.12a. The summary of overshoots for the scan in Figure 3.11c,e are summarised in Figure 3.12b, showing that the reduced approach rate means that the majority of the overshoots are now within 0.5 nm however several pixels are still beyond this and as mentioned above (for ambient scans) the tip likely contacts the surface in this case and once in contact, the tip current can no longer be used as an accurate measure of overshoot and the tip may have a greater overshoot than is observed in the fitting.

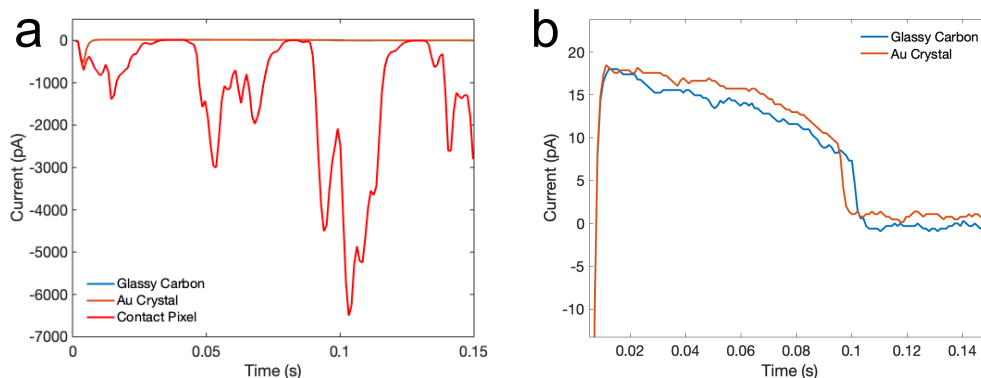


Figure 3.13: (a) Tip current traces during pulse phase over GC (blue), Au crystal (orange), tunnelling response (red). (b) Shows the GC and Au crystal response in a smaller scale range. An average over the last 30 ms was used to plot electrochemical maps.

A combination of the previously mentioned factors; resonant frequency, instrument delays and measured overshoot, could explain a greater overshoot than expected, causing the 16 nm short retract (as used in Figure 3.11 & 3.12) to not be sufficient to exit contact with the surface. The tip current during several electrochemical pixels are shown in Figure 3.13, the nature of the current response during a saturated pixel (red trace, Figure 3.13a) shows that it is a dynamic effect and not a consistent contact with the surface. The monitor response during the pulses showed no deviation and was the same as that in Figure 3.6b (servo-on). The traces for the tip response over the GC (blue trace) compared to the Au crystal (orange trace, Figure 3.13b) show the difference in current is small and show an impressive detection limit. It was suggested that the large cathodic currents could be the result of an electrochemical effect, however, this was dismissed due to the same methodology being applied to a clean GC substrate in ambient conditions showing the same cathodic signals.

The observation of a greater number of contact pixels over the Au nanocrystals is interesting (Figure 3.11d,e): one suggestion is that it could be due to the difference in work function for the Au and GC. Given the tunnelling current depends on the average of the work function between the tip and the substrate (equation 1.3) and that GC has a smaller work function (≈ 4.6 eV)⁶⁷ than that of Au (≈ 5.4 eV)⁶⁸, means that the tunnelling profile would be shallower for the GC hence giving the system more time to “react” to the current increase.

One significant difference with the ambient topographic scans is the plot using the final currents in the approach curves (Figure 3.12c, with data summarised

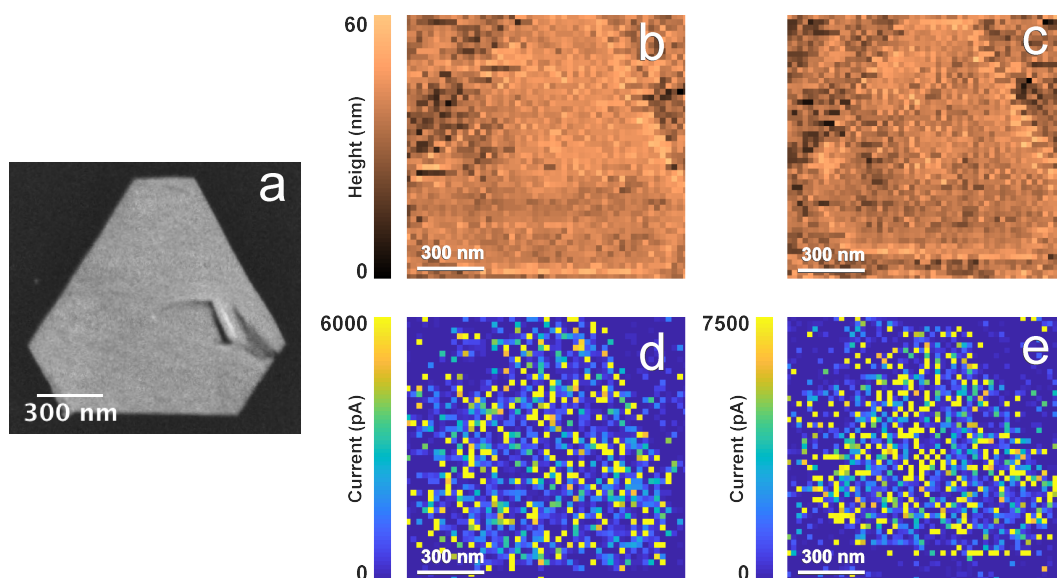


Figure 3.14: (a) SEM image of a Au nanocrystal. Simultaneous topography (b,c) and SECM (d,e) scans of the same crystal in 0.1 M HClO_4 . Approach velocity: 400 nm s^{-1} , tip bias: 0.4 V, first retract: 12 nm (b,d), 10 nm (c,e) pause: 0.15 s, substrate potential: pulsed from 0 V to -0.7 V for 0.15 s, second retract: 70 nm, tunnelling set point: 50 pA, pixel separation: 25 nm.

in Figure 3.12d) actually shows decreased currents on the Au plate rather than the GC support, the opposite of the observation in ambient conditions, even with the same potentials used (Figure 3.9c). The reason for this is still unknown. However, the occurrence of saturated pixels is more common over the Au nanocrystal than the GC support; the approaches preceding saturated pixels are likely ones that make contact with the sample.

Another example of C-SECM is demonstrated in Figure 3.14 with a different crystal and even shorter retract distances (10 & 12 nm), where the frequency of these contact pixels over the plates is greatly increased. Here the absolute value of the average pulse response was used to plot electrochemical maps, such that contact pixels show as bright yellow. This highlights more obviously that the contact is more prevalent over the crystals compared to the GC. SEM images of the crystals before and after scanning (Figure 3.15) do not show any noticeable damage to the sample meaning that the contact cannot be too destructive (hence the overshoot cannot be extreme). The frequency of these contact pixels can be greatly reduced (at the expense of lateral SECM resolution) by setting the short retract distance (step B in Figure 3.5b,c) to a larger value. Both the short retract distance and the approach velocity have a significant impact on the number of these contact pixels. Increasing

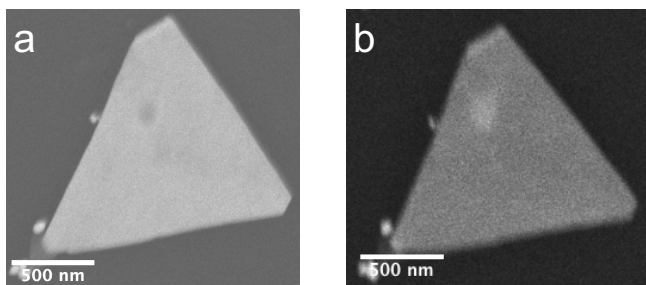


Figure 3.15: Au nanocrystal before (a) and after (b) C-SECM experiments. The same crystal was located using the method set out in Section 3.2.2. No discernible structural change is observed suggesting only minimal contact with the crystal. The resolution here is fairly poor however, due to the plastic bath used for solution partially blocking the electron detector.

the short retract distance past 20 nm shows a large reduction in the contact pixel count during a scan and reducing the approach rate below $\approx 40 \text{ nm s}^{-1}$ also brings the count to a minimum (Figure 3.16), but does not remove the problem entirely. The issues with reducing the approach rate, however, are that the length of time taken to complete scans is greatly increased which can lead to issues such as thermal drift and contamination of the substrate and tip.

The results above highlight how the positioning systems used here do not possess the necessary stability and precision required to do pure STM experiments without at least some sample contact. It is important to note that the issues here are greatly reduced by the application of the hopping protocol and these experiments are likely impossible with constant distance or current modes of operation. This would be of great concern for some previously reported constant distance experiments where it is highly unlikely that the probe and tip separation is kept constant over the full length of the electrochemical scan (on the scale of minutes).^{7,38,39} Additionally, as previously mentioned, the piezoelectrics in these studies had larger overall scan ranges and reduced stability compared to the ones here, they also had much slower resonant frequencies (790 Hz without load and 500 Hz with 30 g load)⁵⁹ which would also increase the “reaction” time of the system.

3.3.4 Future C-SECM and STM-SECM

To take C-SECM forward and potentially towards STM-SECM, implementation of purpose built STM instrumentation into an electrochemical imaging system would be ideal. The trouble here, as previously mentioned, is that STM piezoelectrics typically have a very small overall range and also mounting tips like NEs proves

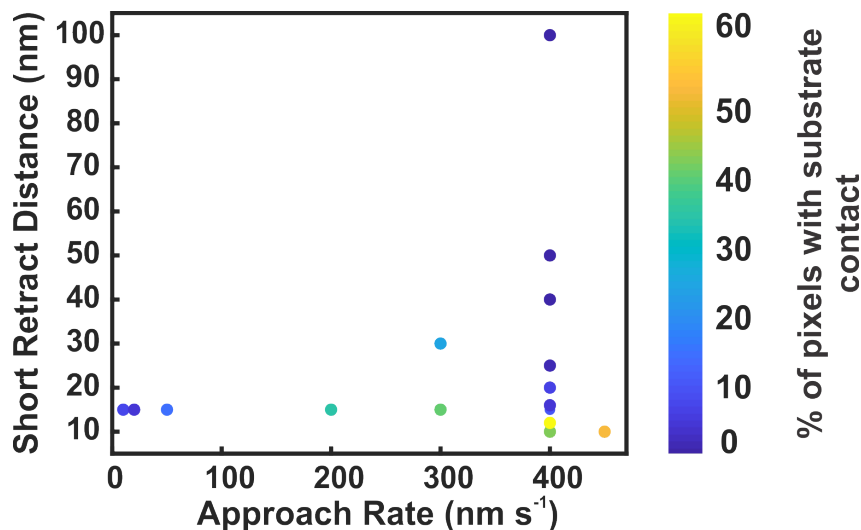


Figure 3.16: Percentage of pixels in a C-SECM scan that exhibit tip-substrate contact during the electrochemical pulse, depending on the short retract distance and initial approach rate. The percentage drops below 10 % for approach rates slower than 40 nm s^{-1} and drops to 0 % for short retract distances greater than $\approx 20 \text{ nm}$. 32 C-SECM scans were taken for this dataset, where scans had the same approach rate and short retract distance the contact pixel count was averaged.

challenging. It would be of interest to investigate the possibility of combining instrumentation to have the best of both. If an STM piezo (described in Section 1.2.2) could be mounted on a piezo used here then the STM piezo could carry out the extremely high resolution topography before switching to the other to do electrochemical imaging. This would require a form of switching between piezos as otherwise the instabilities of the larger actuator would simply translate across the smaller one. Another option is to use a STM actuator for topography and to use the electric stepper motors (in this case Newport Picomotors) for the electrochemical mapping. The motors here actually have a stated resolution of 30 nm ,⁶⁹ (although we have not tested this precisely) and these types of motor typically have backlash issues when changing directions and do not possess a monitoring sensor. They also generate a lot of electronic noise whilst moving, this could potentially be overcome by implementing a hopping style protocol where the motors are paused long enough to gather the electrochemical information before moving onto the next point, albeit at the expense of scanning speed. The advantage of this approach is that when the stepper motors are not moving they are fixed solidly in place and therefore would not add any issues to the STM piezoelectric. We are currently in the process of installing such a system, currently the main issues being addressed are the effective

shielding of the tip electrode from the piezoelectric electrodes, whilst still being able to mount NEs effectively.

3.4 Conclusions

Here we have shown that piezoelectric actuators used in SEPM can be used for high resolution C-SECM and tunnelling type experiments if the limitations of the instrumentation are understood and accounted for. We have used a hopping scanning protocol to overcome some of the limitations in stability of SEPM piezoelectrics to allow for the study of larger topographic features than typically available to STM, at a much higher resolution than possible with SEPM. The use of large extension actuators is also much more convenient for mounting of the probe and substrate due to their larger overall size compared to typical STM piezoelectrics.

There are many applications for this technique, from study of heterogeneous catalysts to detection of reaction intermediates at the nanoscale. The hopping protocol employed here allowed for synchronous topography and electrochemical activity to be acquired with an absolute tip to substrate separation and drift eliminated, whereas previous studies have used constant separation operating modes leaving themselves open to drift and possible sample contact issues. With the advancements here, using existing instrumentation, C-SECM and STM-SECM will hopefully find broad applications in the wider SEPM community.

3.5 Acknowledgements

This results from this chapter are in preparation to be published with the assistance of Dr. Gabriel Meloni, Prof. Patrick R. Unwin and Prof. Giovanni Costantini. All data collection and analysis was carried out by myself. Figure 3.5 was created by Dr. Gabriel Meloni, who also made minor formatting changes to Figures 3.6, 3.7, 3.8, 3.9, 3.10, 3.11, 3.12, 3.14 & 3.16.

3.6 References

- [1] Kranz, C. *Analyst*, 139(2), 336–352, **2013**.
- [2] Kang, M., Momotenko, D., Page, A., Perry, D. & Unwin, P. R. *Langmuir*, 32(32), 7993–8008, **2016**.
- [3] Takahashi, Y., Kumatani, A., Shiku, H. & Matsue, T. *Anal. Chem.*, 89(1), 342–357, **2017**.
- [4] Bard, A. J., Fan, F. R. F., Kwak, J. & Lev, O. *Anal. Chem.*, 61(2), 132–138, **1989**.
- [5] Zoski, C. G. *J. Electrochem. Soc.*, 163(4), H3088–H3100, **2016**.
- [6] Cannan, S., Cervera, J., Steliaros, R. J., Bitziou, E., Whitworth, A. L. & Unwin, P. R. *Phys. Chem. Chem. Phys.*, 13(12), 5403–5412, **2011**.
- [7] Mirkin, M. V., Sun, T., Yu, Y. & Zhou, M. *Acc. Chem. Res.*, 49(10), 2328–2335, **2016**.
- [8] Kim, J., Renault, C., Nioradze, N., Arroyo-Currás, N., Leonard, K. C. & Bard, A. J. *J. Am. Chem. Soc.*, 138(27), 8560–8568, **2016**.
- [9] Kim, J., Renault, C., Nioradze, N., Arroyo, N., Leonard, K. C. & Bard, A. J. *Anal. Chem.*, 88(20), 10284–10289, **2016**.
- [10] O’Connell, M. A., Lewis, J. R. & Wain, A. J. *Chem. Commun.*, 51(51), 10314–10317, **2015**.
- [11] Kang, M., Perry, D., Bentley, C. L., West, G., Page, A. & Unwin, P. R. *ACS Nano*, 11(9), 9525–9535, **2017**.
- [12] Page, A., Perry, D., Young, P., Mitchell, D., Frenguelli, B. G. & Unwin, P. R. *Anal. Chem.*, 88(22), 10854–10859, **2016**.
- [13] Ebejer, N., Güell, A. G., Lai, S. C., McKelvey, K., Snowden, M. E. & Unwin, P. R. *Annu. Rev. Anal. Chem.*, 6(1), 329–351, **2013**.
- [14] Snowden, M. E., Güell, A. G., Lai, S. C. S., McKelvey, K., Ebejer, N., Oconnell, M. A., Colburn, A. W. & Unwin, P. R. *Anal. Chem.*, 84(5), 2483–2491, **2012**.
- [15] Bentley, C. L., Kang, M., Maddar, F. M., Li, F., Walker, M., Zhang, J. & Unwin, P. R. *Chem. Sci.*, 8(9), 6583–6593, **2017**.

- [16] Amemiya, S., Bard, A. J., Fan, F.-R. F., Mirkin, M. V. & Unwin, P. R. *Annu. Rev. Anal. Chem.*, 1(1), 95–131, **2008**.
- [17] Bergner, S., Vatsyayan, P. & Matysik, F. M. *Anal. Chim. Acta*, 775, 1–13, **2013**.
- [18] Page, A., Perry, D. & Unwin, P. R. *Proc. R. Soc. A Math. Phys. Eng. Sci.*, 473(2200), **2017**.
- [19] Sen, M., Takahashi, Y., Matsumae, Y., Horiguchi, Y., Kumatani, A., Ino, K., Shiku, H. & Matsue, T. *Anal. Chem.*, 87(6), 3484–3489, **2015**.
- [20] O’Connell, M. A. & Wain, A. J. *Anal. Methods*, 7(17), 6983–6999, **2015**.
- [21] McKelvey, K., Nadappuram, B. P., Actis, P., Takahashi, Y., Korchev, Y. E., Matsue, T., Robinson, C. & Unwin, P. R. *Anal. Chem.*, 85(15), 7519–7526, **2013**.
- [22] Huang, Z., De Wolf, P., Poddar, R., Li, C., Mark, A., Nellist, M. R., Chen, Y., Jiang, J., Papastavrou, G., Boettcher, S. W., Xiang, C. & Brunschwig, B. S. *Microsc. Today*, 24(06), 18–25, **2016**.
- [23] Nellist, M. R., Chen, Y., Mark, A., Gödrich, S., Stelling, C., Jiang, J., Poddar, R., Li, C., Kumar, R., Papastavrou, G., Retsch, M., Brunschwig, B. S., Huang, Z., Xiang, C. & Boettcher, S. W. *Nanotechnology*, 28(9), 95711, **2017**.
- [24] Macpherson, J. V., Unwin, P. R., Hillier, A. C. & Bard, A. J. *J. Am. Chem. Soc.*, 118(27), 6445–6452, **1996**.
- [25] Velmurugan, J., Agrawal, A., An, S., Choudhary, E. & Szalai, V. A. *Anal. Chem.*, 89(5), 2687–2691, **2017**.
- [26] Kranz, C., Friedbacher, G., Mizaikoff, B., Lugstein, A., Smoliner, J. & Bertagnolli, E. *Anal. Chem.*, 73(11), 2491–2500, **2001**.
- [27] Eifert, A., Mizaikoff, B. & Kranz, C. *Micron*, 68, 27–35, **2015**.
- [28] Meier, J., Friedrich, K. A. & Stimming, U. *Faraday Discuss.*, pages 365–372; discussion 441–462, **2002**.
- [29] Nagahara, L. A., Thundat, T. & Lindsay, S. M. *Rev. Sci. Instrum.*, 60(10), 3128–3130, **1989**.

- [30] Bach, C. E., Nichols, R. J., Beckmann, W. & Meyer, H. *J. Electrochem. Soc.*, 140(5), 1281, **1993**.
- [31] Schulte, A. *Proc. SPIE*, 3512, 353–357, **1998**.
- [32] Polcari, D., Dauphin-Ducharme, P. & Mauzeroll, J. *Chem. Rev.*, 116(22), 13234–13278, **2016**.
- [33] Bard, A. J. & Mirkin, M. V. *Scanning Electrochemical Microscopy*. Wiley-VCH, 2nd edition, **2012**.
- [34] Tersoff, J. & Hamann, D. R. *Phys. Rev. B*, 31(2), 805–813, **1985**.
- [35] Della Pia, A. & Costantini, G. In G. Bracco & B. Holst, editors, *Surf. Sci. Tech.*, pages 565–597. Wiley-VCH, Berlin, Heidelberg, **2013**.
- [36] Ramachandra Rao, M. S. & Margaritondo, G. *J. Phys. D: Appl. Phys.*, 44(46), 460301, **2011**.
- [37] Treutler, T. H. & Wittstock, G. *Electrochim. Acta*, 48(20-22), 2923–2932, **2003**.
- [38] Sun, T., Wang, D. & Mirkin, M. V. *Faraday Discuss.*, 210, 173–188, **2018**.
- [39] Sun, T., Wang, D. & Mirkin, M. V. *Angew. Chemie - Int. Ed.*, 57(25), 7463–7467, **2018**.
- [40] Sun, T., Yu, Y., Zacher, B. J. & Mirkin, M. V. *Angew. Chemie - Int. Ed.*, 53(51), 14120–14123, **2014**.
- [41] Takahashi, Y., Shevchuk, A. I., Novak, P., Babakinejad, B., Macpherson, J., Unwin, P. R., Shiku, H., Gorelik, J., Klenerman, D., Korchev, Y. E. & Matsue, T. *Proc. Natl. Acad. Sci.*, 109(29), 11540 LP – 11545, **2012**.
- [42] Bentley, C. L. & Unwin, P. R. *Faraday Discuss.*, 210, 365–379, **2018**.
- [43] Perez, J., Gonzalez, E. R. & Villullas, H. M. *J. Phys. Chem. B*, 102(52), 10931–10935, **1998**.
- [44] Zhang, L., Xiao, J., Wang, H. & Shao, M. *ACS Catal.*, 7(11), 7855–7865, **2017**.
- [45] Facci, P. In P. B. T. B. E. Facci, editor, *Micro Nano Technol.*, chapter 4, pages 99–157. William Andrew Publishing, Oxford, **2014**.
- [46] Danilov, A. I. *Russ. Chem. Rev.*, 64(8), 767–781, **1995**.

- [47] Takahashi, Y., Shevchuk, A. I., Novak, P., Zhang, Y., Ebejer, N., Macpherson, J. V., Unwin, P. R., Pollard, A. J., Roy, D., Clifford, C. A., Shiku, H., Matsue, T., Klenerman, D. & Korchev, Y. E. *Angew. Chemie - Int. Ed.*, 50(41), 9638–9642, **2011**.
- [48] Wilde, P., Quast, T., Aiyappa, H. B., Chen, Y. T., Botz, A., Tarnev, T., Marquitan, M., Feldhege, S., Lindner, A., Andronescu, C. & Schuhmann, W. *ChemElectroChem*, 5(20), 3083–3088, **2018**.
- [49] Aoki, K. *Electroanalysis*, 5(8), 627–639, **1993**.
- [50] Andoy, N. M., Zhou, X., Choudhary, E., Shen, H., Liu, G. & Chen, P. *J. Am. Chem. Soc.*, 135(5), 1845–1852, **2013**.
- [51] Sastry, M. & Rai, A. *Nat. Mater.*, 3(July), 482, **2004**.
- [52] Güell, A. G., Cuharuc, A. S., Kim, Y.-R., Zhang, G., Tan, S.-y., Ebejer, N. & Unwin, P. R. *ACS Nano*, 9(4), 3558–3571, **2015**.
- [53] <https://warwick.ac.uk/fac/sci/chemistry/research/unwin/electrochemistry/wec-spm/> Warwick Electrochemistry and Interfaces Group. *WEC-SPM*, **2019**.
- [54] National Instruments. *NI R Series Multifunction RIO Specifications*, www.ni.com/pdf/manuals/372492c.pdf, **2020**.
- [55] Physik Instrumente LTD UK. *E-665 Piezo Amplifier / Servo Controller*, www.physikinstrumente.co.uk/en/products/controllers-and-drivers/nanopositioning-piezo-controllers/e-665-piezo-amplifier-servo-controller-600901/#specification, **2020**.
- [56] Physik Instrumente LTD UK. *P-753 LISA Linear Actuator and Stage*, www.physikinstrumente.co.uk/en/products/nanopositioning-piezo-flexure-stages/linear-piezo-flexure-stages/p-753-lisa-linear-actuator-stage-200900/, **2019**.
- [57] Kalkan, F., Zaum, C. & Morgenstern, K. *Rev. Sci. Instrum.*, 83(10), 103903, **2012**.
- [58] Petersen, L., Schunack, M., Schaefer, B., Linderoth, T. R., Rasmussen, P. B., Sprunger, P. T., Laegsgaard, E., Stensgaard, I. & Besenbacher, F. *Rev. Sci. Instrum.*, 72(2), 1438–1444, **2001**.

- [59] Physik Instrumente LTD UK. *P-620.Z - P-622.Z PIHera Vertical Precision Z Positioner*, www.physikinstrumente.com/en/products/nanopositioning-piezo-flexure-stages/linear-piezo-flexure-stages/p-620z-p-622z-pihera-precision-z-stage-202501/, **2019**.
- [60] Kim, J., Shen, M., Nioradze, N. & Amemiya, S. *Anal. Chem.*, 84(8), 3489–3492, **2012**.
- [61] Novak, P., Shevchuk, A., Ruenraroengsak, P., Miragoli, M., Thorley, A. J., Klenerman, D., Lab, M. J., Tetley, T. D., Gorelik, J. & Korchev, Y. E. *Nano Lett.*, 14(3), 1202–1207, **2014**.
- [62] Shankar, S. S., Rai, A., Ankamwar, B., Singh, A., Ahmad, A. & Sastry, M. *Nat. Mater.*, 3(7), 482–488, **2004**.
- [63] Avila, A. & Bhushan, B. *Crit. Rev. Solid State Mater. Sci.*, 35(1), 38–51, **2010**.
- [64] Lanza, M. *Conductive Atomic Force Microscopy: Applications in Nanomaterials*. Wiley-VCH, **2017**.
- [65] Chen, Z. F. & Wang, E. *Electroanalysis*, 6(8), 672–676, **1994**.
- [66] Chen, C.-H., Jacobse, L., McKelvey, K., Lai, S. C. S., Koper, M. T. M. & Unwin, P. R. *Anal. Chem.*, 87(11), 5782–5789, **2015**.
- [67] Ivey, H. F. *Phys. Rev.*, 76(4), 567, **1949**.
- [68] Sachtler, W. M. H., Dorgelo, G. J. H. & Holscher, A. A. *Surf. Sci.*, 5(2), 221–229, **1966**.
- [69] Newport. *Picomotor Piezo Linear Actuators*, www.newport.com/f/picomotor-piezo-linear-actuators, **2019**.

Chapter 4

Bipolar Nanoelectrodes: Fabrication and Characterisation

Typically the fabrication of nanoelectrodes (NEs) can be extremely challenging and potentially very time consuming and/or expensive. Low reproducibility combined with the fragility of NEs also creates challenges in their application and longevity.

This chapter will focus on the fabrication and characterisation of Pt and primarily AuNEs fabricated using a recently developed method utilising a chemical reduction followed by bipolar electrodeposition at the end of a nanopipette. These electrodes have been shown to be extremely reproducible, very easy to fabricate and very low cost (aside from some initial equipment purchases). However, some issues still arise over their longevity and the same method for Pt electrodes has been less successful. The application of these electrodes for scanning electrochemical probe microscopy will be investigated further in Chapter 5.

4.1 Introduction

4.1.1 Fabrication

The methodology most closely followed henceforth for the fabrication of bipolar nanoelectrodes (BPNEs) was set out by Gao *et al.* in 2018.¹ This study used the final electrodes for NP collision studies (much like a couple of other recent articles)^{2,3} rather than SEPM but the method is still potentially effective for SEPM probes.

The method starts with a laser pulled nanopipette with a diameter of 30 nm, which is then filled with a solution of 10 mM HAuCl₄ and 10 mM KCl. The pipette

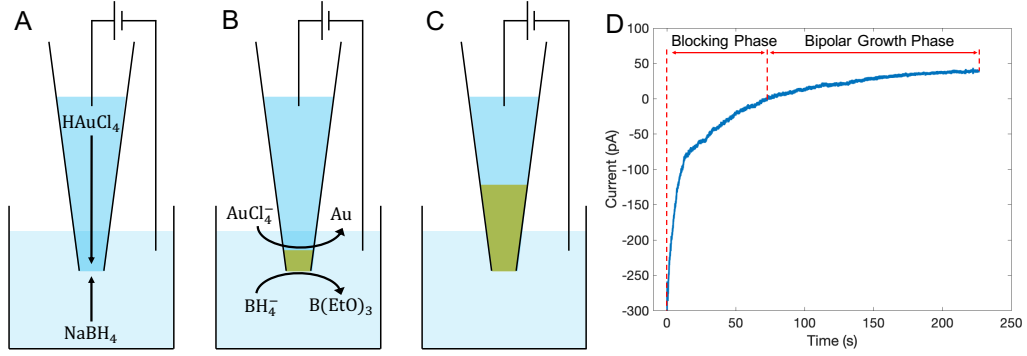
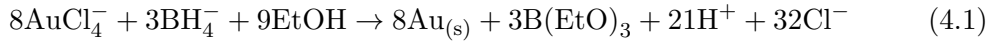


Figure 4.1: (A) Chemical reduction of HAuCl_4 by NaBH_4 to form a Au plug. (B) The Au plug acts as a closed bipolar electrode and electrochemical reduction of AuCl_4^- continues to grow the Au to form a longer plug (C). (D) Current measured at internal electrode of nanopipette during fabrication. A very fast blocking phase is observed as the chemical reduction occurs, followed by a steady electrochemical growth phase.

is then inserted into a solution of 10 mM NaBH_4 in ethanol. At the boundary of the tip opening a spontaneous chemical reaction takes place involving the reduction of the AuCl_4^- by the BH_4^- to generate a Au plug at the opening of the nanopipette (following equation 4.1, Figure 4.1A). Ethanol is used as it slows down the chemical reduction, in water the process is faster and H_2 bubble formation can cause deformation. Once this Au plug is formed no more chemical reaction takes place. Next a bias is applied between the solution inside and outside the pipette to form a closed bipolar electrochemical cell. A bias of 300 mV inside the pipette is sufficient to further reduce AuCl_4^- inside the tip and continue the growth of the Au plug (Figure 4.1B). Increasing the length of the plug results in a more stable Au solid for SEPM and means that the surface at the back of the plug is much larger than the surface exposed at the end which proves useful as discussed later (Figure 4.1C).^{1,4}



Current traces can be recorded during the deposition process to give information about the progress of Au formation. No current flows if the nanopipette is inserted into ethanol (without NaBH_4) as there is no electrolyte. On addition of NaBH_4 there is a large negative current resulting from the ionic flow, however, the magnitude of this current quickly decreases as the Au plug forms and blocks the nanopipette. After this, a small non zero current is observed which corresponds to the electrochemical deposition of Au on the inside of the formed plug (Figure 4.1D).

In the bipolar electrodeposition phase, a reduction at one side of the plug is coupled with an oxidation at the other side. So the reduction of AuCl_4^- is coupled with oxidation of Ag at the Ag/AgCl electrode inside the pipette, whilst outside, reduction of AgCl at the Ag/AgCl reference electrode is coupled with oxidation of BH_4^- at the external face of the Au plug.

The Au deposition rate can be calculated by considering Faraday's law and the total charge passed (Q) in equation 4.2:

$$Q = nFN \quad (4.2)$$

where n is the number of electrons transferred, N is the number of moles of Au and F is the Faraday constant. Integrating the deposition current with respect to time yields the total charge (Q), hence N can be calculated.⁴ For the BPNEs presented here the average growth rate in length of Au plug corresponds to deposition on the order of 10s of nm per second. This amount obviously varies throughout the process, being quicker at the start where the pipette is narrower and slower as the internal radius of the plug increases.

4.1.2 Characterisation

BPNEs have been characterised by optical microscopy,⁴ SEM,^{1,4,5} plasmonic scattering spectra¹ and by voltammetry.⁴⁻⁷ One group managed to make a physical connection to the Au plug so that it can be used like a conventional nanoelectrode.⁵ However, the length of plug is generally small ($\lesssim 3 \mu\text{m}$) and also the narrow taper (100s nm) of the nanopipette can make a physical connection impractical. Hence back filling the pipette with a new electrolyte solution is easier. However, this does affect the electrochemical behaviour of the electrode.^{4,6,7}

The electrochemical response of BPNEs can be derived from the microelectrode response in a two electrode cell (Figure 4.2):

$$E = E^{\circ'} + \frac{RT}{nF} \ln \left(\frac{D_{\text{O}}}{D_{\text{R}}} \right) - \frac{RT}{nF} \ln \left(\frac{i_{\text{ss}} - i}{i} \right) \quad (4.3)$$

where E is the applied potential, $E^{\circ'}$ is the formal potential for the reaction $\text{R}_{\text{ed}} \rightarrow \text{O}_{\text{x}} + ne^-$, R is the gas constant, T is the temperature in Kelvin, n is the number of electrons transferred, F is the Faraday constant, D_{O} and D_{R} are the diffusion coefficients for O_{x} and R_{ed} respectively, i_{ss} is the steady state limiting current and i is the current measured at potential E .⁸

If it is assumed that the diffusion constants are approximately equal for O_{x}

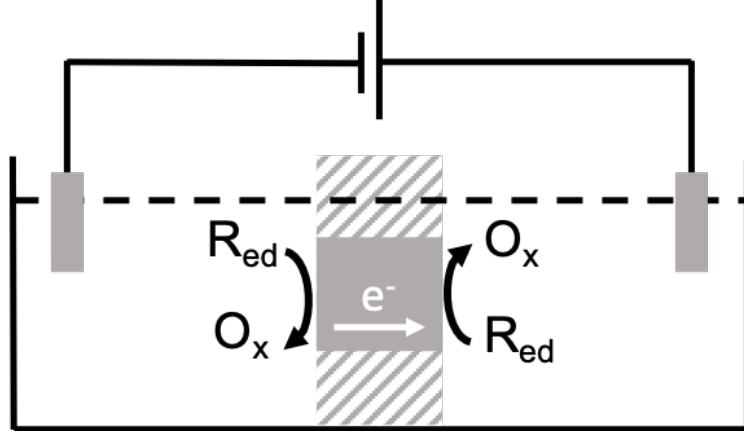


Figure 4.2: Schematic of a closed bipolar electrochemical cell used for derivation of voltammetric response of BPNEs.⁷ Oxidation at one side of the cell is coupled to reduction at the other.

and R_{ed} ($D_O \approx D_R$) then equation 4.3 becomes:

$$E = E^{\circ'} - \frac{RT}{nF} \ln \left(\frac{i_{ss} - i}{i} \right) \quad (4.4)$$

In a closed bipolar system the bias across the bipolar electrode is given by the difference between the bias at the anodic (E_a) and cathodic poles (E_c). So the potential of the whole system is given by:

$$E = E_a - E_c = (E_a^{\circ'} - E_c^{\circ'}) - \frac{RT}{F} \left(\frac{1}{n_a} \ln \left(\frac{i_{ss}^a - i_a}{i_a} \right) + \frac{1}{n_c} \ln \left(\frac{i_{ss}^c - i_c}{i_c} \right) \right) \quad (4.5)$$

where E_a° and E_c° are the formal potentials for the anodic and cathodic processes respectively, n_a and n_c are the number of electrons transferred for the anodic and cathodic processes respectively, i_{ss}^a and i_{ss}^c are the steady state limited currents at the anodic and cathodic poles respectively. The current at the anodic pole (i_a) is equal but opposite to the current at the cathodic pole (i_c) such that $i_a = -i_c$. In addition, if both anodic and cathodic processes transfer the same amount of electrons ($n_a = n_c = n$), then equation 4.5 becomes:

$$E = (E_a^{\circ'} - E_c^{\circ'}) + \frac{RT}{nF} \left(\ln \left(\frac{i}{i_{ss}^a - i} \right) + \ln \left(\frac{-i}{i_{ss}^c + i} \right) \right) \quad (4.6)$$

This equation governs the voltammetric response for a closed bipolar micro-electrode.⁷ The measured current will be limited by whichever pole has the smaller steady state limiting current. In the case of electrodes here, that current is the

cathodic pole such that the steady state current in a voltammogram will be given by i_{ss}^c and the current at the half wave potential ($E_{\frac{1}{2}}$) will be given by $i = -\frac{1}{2}i_{ss}^c$, substituting this into equation 4.6 results in:

$$E_{\frac{1}{2}} = (E_a^{o'} - E_c^{o'}) - \frac{RT}{nF} \ln \left(-2 \left(\frac{i_{ss}^a}{i_{ss}^c} \right) - 1 \right) \quad (4.7)$$

Therefore the electrochemical response of BPNEs in this configuration can be predicted.^{4,7}

4.2 Methodology

The initial methodology followed closely resembles that from Gao *et. al.*¹ (as discussed in Section 4.1.1), however we found several factors to also influence the success rate of fabrication and characterisation so below the details of all the specifics and why they were carried out is discussed.

Firstly the nanopipettes are pulled from quartz capillaries (QF100-50-10, Sutter Instrument Co.) using a P-2000 laser pipette puller (Sutter Instrument Co.). A two line program was used: 1. *Heat* = 750, *Filament* = 4, *Velocity* = 30, *Delay* = 150, *Pull* = 80, 2. *Heat* = 650, *Filament* = 3, *Velocity* = 40, *Delay* = 135. This results in nanopipettes with an orifice between 30 – 50 nm diameter (described further in Section 2.2.1).

The nanopipette is then filled from the back with a solution of 10 mM KAuCl₄ (98 %, Sigma-Aldrich) and 10 mM HCl (37 %, Honeywell Fluka) in deionised water (Integra HP, Purite) using a MicroFil syringe (MF34G-5, World Precision Instruments). Filling nanopipettes with aqueous solutions using this method often results in bubbles or incomplete filling. To counter this, nanopipettes were held in Omnifit standard bore, two-way connectors and centrifuged (Eppendorf AG, 22331 Hamburg) at 8 krpm for 5 minutes. These conditions result in complete filling without bubbles, higher speeds often resulted in pipette breakages.

Ag/AgCl reference electrodes are prepared by anodising 0.125 mm annealed Ag wire (99.99 %, Goodfellow) in a saturated KCl (> 99 %, Sigma-Aldrich) solution. One of these references is inserted into the back of the filled nanopipette and another is submerged into a solution of 10 mM NaBH₄ (99.99 %, Sigma-Aldrich) in ethanol (99 %, Fisher Scientific).

The nanopipette is then submerged into the NaBH₄ solution where the chemical deposition of Au at the end of the nanopipette occurs to form a Au plug. Generally better results were obtained if the Ag/AgCl electrodes were connected prior

to submerging with a bias of 300 mV applied to the Ag/AgCl reference inside the pipette. Applying the bias before submerging means that as soon as the circuit is completed (by submerging) there is ion flow into the nanopipette which stops the deposition solution leaking out and forming larger poor geometry electrodes. The references were connected using in house built electrometers allowing the current to be measured at the same time as manipulating the potential. The measured current was then collected and bias manipulated using an FPGA card (7852R, National Instruments) coupled with an in house developed LabVIEW control system.⁹

The Au plug forms rapidly and from thereon the 300 mV bias serves as a suitable potential for subsequent electrochemical reduction of Au inside the NE. Electrodes were left for a minimum of 5 minutes, which was sufficient for a Au plug length of 1 – 2 μm .

After the electrochemical deposition phase, the bias was changed between 100 – 300 mV several times, observing the difference in current response gives an idea of the quality of the NE. Larger noisier current changes were often caused by poorly formed electrodes. This was then checked by STEM and voltammetry after fabrication too. Figure 4.3A,B shows typical responses from a good quality and poor quality electrode with the corresponding STEM images (Figure 4.3C,D). The poorer quality electrode shows a noisier current trace.

For characterisation and application it is generally required to refill electrodes with a new solution to avoid further effects to the Au plug and to allow for other studies. However, filling with aqueous solutions once again proves difficult however, centrifuging with the Au plug at the end is not very effective and can also damage the electrode. To overcome this, in our experiments acetonitrile (ACN, HPLC grade, Fisher) based electrolytes are used inside the tip. ACN is much less viscous than water and therefore fills the pipettes more effectively, in addition NEs were left for at least an hour to ensure that full filling had occurred. Specifically Ferrocene (Fc, 98 %, Sigma-Aldrich) and 0.2 M TBAPF₆ (99 %, Merck) were used. As mentioned previously (Section 2.2.1), an anti-static ankle bracelet was worn whilst handling nanoelectrodes in an attempt to reduce the risk of electrostatic damage to electrodes.

STEM images were acquired using a ZEISS GeminiSEM 500, using the STEM mode at 30 kV accelerating voltage with electrodes mounted on a multi-TEM sample holder. This instrument is also equipped with a large area silicon drift detector energy-dispersive X-ray spectroscopy (EDX) detector for elemental analysis. All STEM images in this chapter (unless otherwise stated) are taken using bright field imaging with the background set to black, in order to make the edges of the capillary more defined.

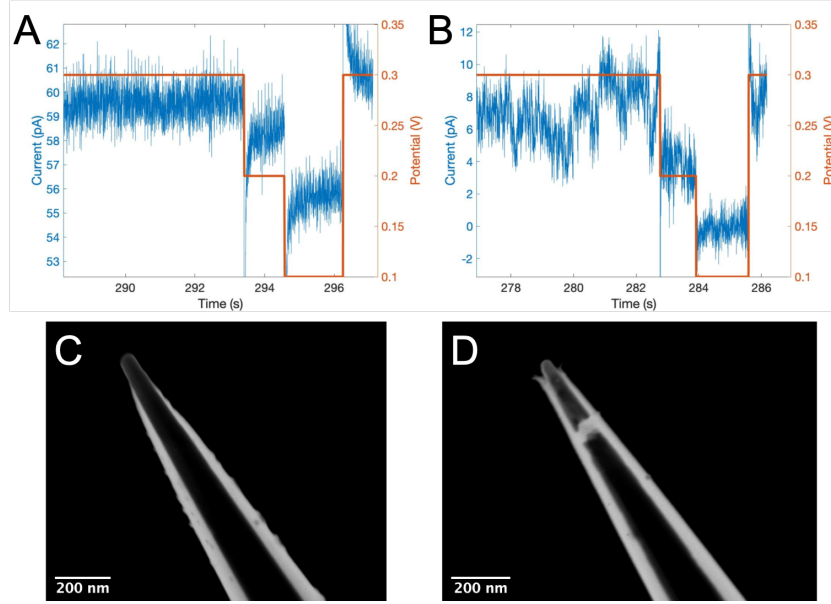


Figure 4.3: (A,B) Current traces with changing potential at the end of BPNE fabrication with corresponding dark field STEM images of electrodes (C,D). (A,C) Show a well formed BPNE with a lower noise level than a poorly formed electrode as in (B,D).

Finite element method (FEM) models were created using COMSOL Multiphysics software. The external geometry of electrodes was taken from STEM images (Figure 4.4), with the values for the electrode radius a , insulating sheath radius r_g , protruding height of electrode h and the angle of the sheath θ . This was then converted to a two dimensional format for the calculation of the expected steady state limiting current accounting for mass transport limited diffusion to the electrode. The resulting current was then integrated through 360° to give the expected steady state limited current for the three dimensional electrode. The internal redox process of the BPNE was not accounted for, so the half wave potential is not accurately predicted and the simulated CV was then shifted on the potential scale using equation 4.7 to calculate the expected half wave potential.

4.3 Results

A typical current trace during Au deposition is shown in Figure 4.5A along with a STEM image of the resulting BPNE (Figure 4.5B). After the initial blocking of the pipette a nearly constant non-zero current is observed. Using equation 4.2 the approximate Au deposition rate can be determined. Integrating the current

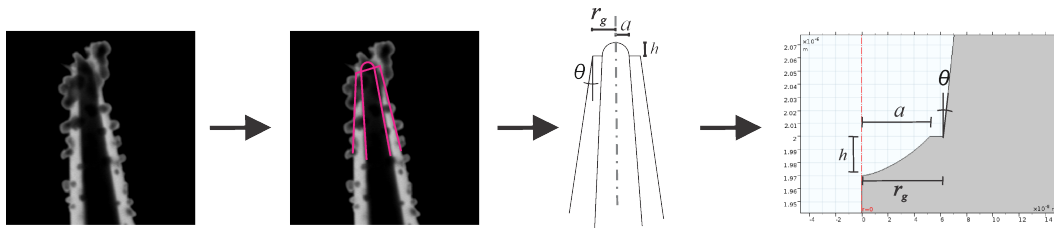


Figure 4.4: Geometry is taken from STEM images including the values for a , r_g , h and θ , this is then converted to a two dimensional representation for simulating mass transport limited diffusion to the electrode surface in COMSOL Multiphysics software.

(≈ 4 pA) over a region of 10 s gives a value of Q which in turn gives a value of N as 4.1×10^{-17} moles s^{-1} . This deposition rate can be converted to the rate at which the plug grows in length. The value does, however, change as the plug grows along the pipette as the diameter of the pipette increases. If it is assumed that the inside of the pipette is a cylinder, at the start the radius is ≈ 45 nm which corresponds to a deposition rate of ≈ 60 nm s^{-1} whereas at the final state shown in Figure 4.5B where the radius is ≈ 130 nm then the rate is ≈ 10 nm s^{-1} . This means that there is a diminishing rate of deposition in terms of the Au plug length. Given the total length of deposition here (≈ 300 s) and the total length of plug (≈ 1.8 μm) would suggest an average of ≈ 6 nm s^{-1} . This diminishing rate of growth for the Au plug length means depositing for longer timescales at this potential would not result in a significant increase in Au plug length.

To confirm the BPNE composition, EDX mapping was used to show the contrast between the Au of the plug and the Si of the pipette (Figure 4.6A). In addition EDX spectra were taken in a region of empty nanopipette and in a region filled with a Au plug (Figure 4.6B). There is a clear distinction in both the mapping and spectra between the empty nanopipette which is mostly Si and O compared to the plug where Au is obvious.

Values for formal potentials required to use equations 4.6 & 4.7 have some variability in the literature and can be difficult to match with different reference electrodes. Therefore, here a CV was taken using a 10 μm Au UME for both the cathodic (5 mM $[\text{Ru}(\text{NH}_3)_6]^{3+}$ (hexaamineruthenium(III) chloride, 98 %, Sigma-Aldrich), 0.1 M KNO_3 (≥ 99.0 %, Sigma-Aldrich) in water against Ag/AgCl) and anodic (50 mM Fc, 0.2 M TBAPF₆ in ACN against Ag wire) processes used in BPNEs so that the conditions are exactly matched. These CVs are shown in Figure 4.7, the half wave potentials from these curves were used as the formal potentials such that $E_c^{\circ'} = -0.28$ V and $E_a^{\circ'} = 0.54$ V. STEM images were used to simulate the

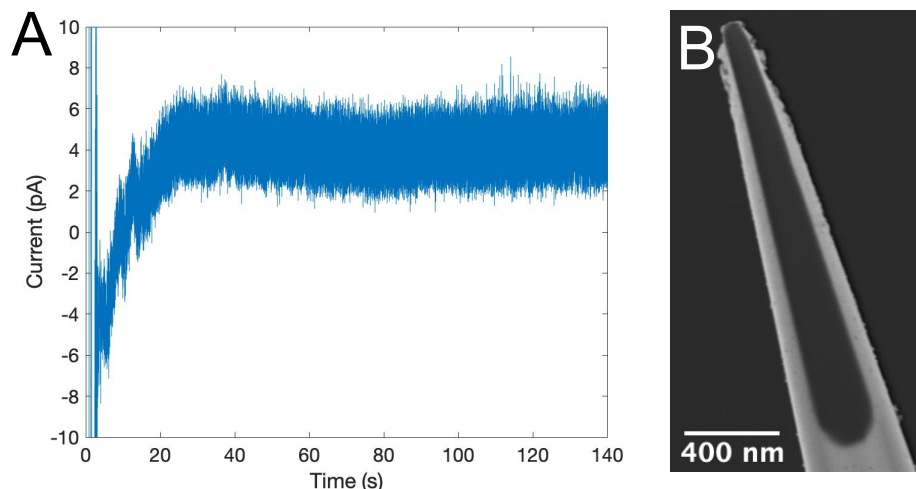


Figure 4.5: (A) Current trace recorded during BPNE formation, after initial blocking event, current drops to a steady value for the duration (≈ 300 s), time axis cropped to show initial blocking more clearly. (B) Corresponding STEM image of final BPNE.

CV response of BPNEs by measuring the dimensions of the Au plug and choosing the appropriate formula for i_{ss} at each pole from equations 1.8–1.11. This then gives the values for i_{ss}^a and i_{ss}^c which in turn can be used to plot the expected i vs E using equation 4.6.

Studying the AuNEs using STEM shows that several different geometries can be formed at the tip of the pipette. The observed geometries include (in order of prevalence) conical, hemispherical, disc and a sharp point (Figure 4.8A,C,E,G). It is also observed that in most cases the size of the glass opening is larger than that of the nanopipette before Au deposition (≈ 30 nm). This would lead us to believe that the process of Au deposition is quite aggressive and can damage the glass, resulting in a larger exposed area of electrode that protrudes from the glass sheath. This process in some cases could cause leakage of the internal solution around the Au. Potential issues with the electrochemical response of BPNEs will be discussed further through this chapter.

The measured CVs are shown in Figure 4.8B,D,F,H along with a theoretical CV calculated from equation 4.6 and a simulated CV using COMSOL (finite element model). The CVs calculated from equation 4.6 are done so by taking measurements of geometry from the STEM images and then picking the most relevant equations from equations 1.8–1.11 for both the external and internal face of the BPNE. All values for i_{ss}^a were calculated using hemispherical electrodes as in equation 1.9. All

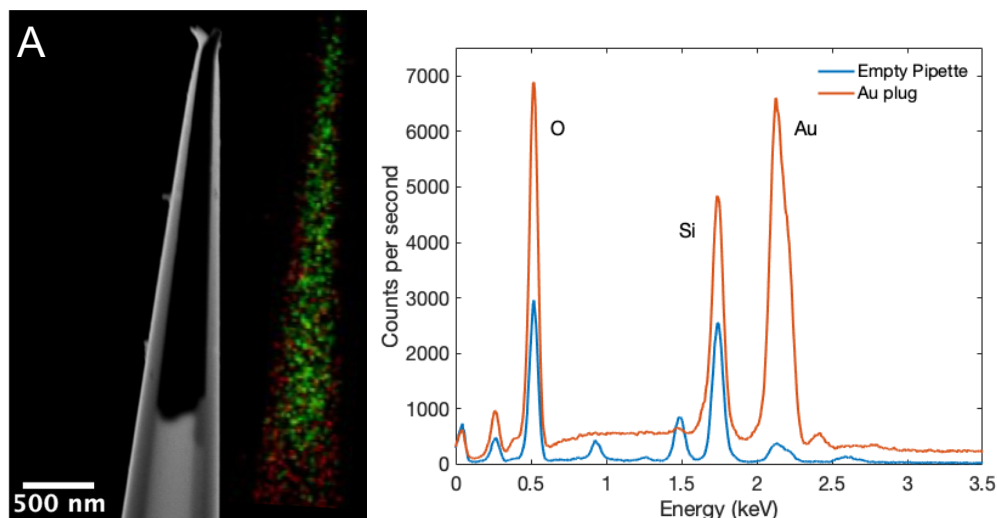


Figure 4.6: (A) Dark field STEM image a of NE with EDX map displayed offset to the right. Red and green correspond to Si and Au respectively. (B) Elemental spectra over an empty region of pipette (blue) and a Au filled region (orange).

i_{ss}^c for external faces of BPNEs were calculated using equation 1.11 for an insulated conical electrode. It can be seen that for the cases displayed here the value of $E_{\frac{1}{2}}$ is a good match with the measured values. However, as expected, these fully analytical solutions are less reliable when predicting the steady state current. For BPNEs in Figure 4.8F,H the CV is a good match whereas in Figure 4.8B,D the current is much less correlated. Equations 1.8–1.12 are analytical solutions and do not take account of the exact geometry and therefore should only be a guideline and COMSOL simulated responses are much more accurate.

COMSOL simulated CVs take the best approximation of true geometry that can be obtained from the STEM images to simulate the steady state current, whilst the half wave potential is picked from the experimental data. These show a much better match to experimental data. In the COMSOL modelled CVs, deviations in steady state current values are expected to arise firstly from difficulty in determining exactly which sections of the BPNE are coated in the insulating sheath and secondly STEM images are only a 2D cross section which means that the full 3D geometry is not fully accounted for.

The effect of internal and external concentrations on the electrochemical response of BPNEs was investigated further using three concentrations for the cathodic process ($[\text{Ru}(\text{NH}_3)_6]^{3+}$ reduction) and the anodic process (Fc oxidation). This was carried out with several different electrodes, washing internally and externally with deionised water between experiments. The measured CVs were then compared to

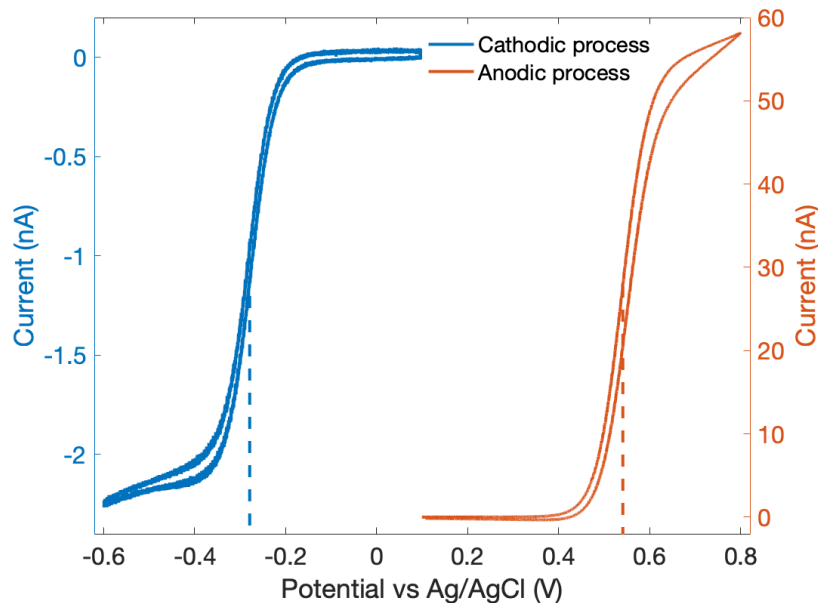


Figure 4.7: CVs with a 10 μm Au UME for the cathodic (blue) and anodic (orange) processes with a BPNE. The half wave potential ($E_{1/2}$) is measured as -0.28 V and 0.54 V for the cathodic and anodic processes respectively. Cathodic CV: reduction of 5 mM $[\text{Ru}(\text{NH}_3)_6]^{3+}$, 0.1 M KNO_3 in water against Ag/AgCl, 50 mV s^{-1} scan rate. Anodic CV: oxidation of 50 mM Fc, 0.2 M TBAPF₆ in ACN against Ag wire, 20 mV s^{-1} scan rate.

the expected half wave potential calculated from the STEM and equation 4.7. The steady state current was also predicted using the STEM and is given by the magnitude of whichever is smaller between the cathodic and anodic processes. Figure 4.9A displays an example electrode when the internal concentration is kept the same (100 mM Fc, 0.2 M TBAPF₆, ACN) and the external concentrations are altered (1.3 mM, 4.9 mM, 19.8 mM, $[\text{Ru}(\text{NH}_3)_6]^{3+}$ in 0.1 M KNO_3). As expected the steady state limiting current increases proportionally with the concentration of the external species as the internal concentration is high enough that it can be assumed it does not limit the overall current flow in any way. Figure 4.9B shows an example of three differing internal concentrations (4.6 mM, 25.4 mM, 50.4 mM, Fc, 0.2 M TBAPF₆ in ACN) with the same external concentration (24.5 mM $[\text{Ru}(\text{NH}_3)_6]^{3+}$ in 0.1 KNO_3). Here, due to the higher external concentration, it can be seen that the anodic process becomes the limiting factor at a certain internal concentration, as expected. However, these are two selected data sets. To summarise the electrodes and concentrations studied, the expected half wave potential (from STEM images and equation 4.7) was plotted against the measured half wave potential (Figure

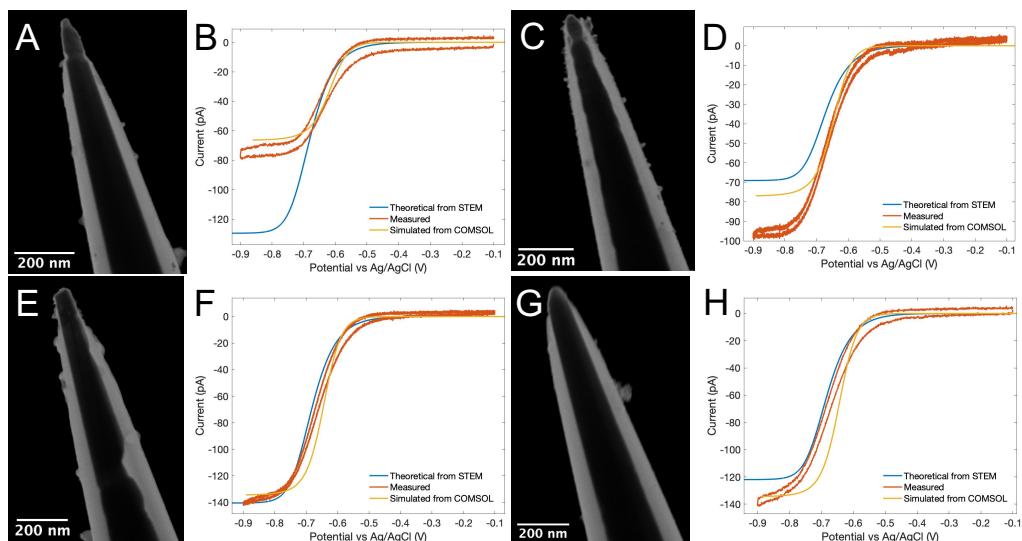


Figure 4.8: (A,C,E,G) Show STEM images of various Au BPNEs. (B,D,F,H) Give corresponding measured (orange), simulated with equation 4.6 and STEM dimensions (blue) and simulated using a COMSOL model (yellow). All CVs show the reduction of 5.2 mM $[\text{Ru}(\text{NH}_3)_6]^{3+}$ with 0.1 M KNO_3 in water against an Ag/AgCl reference, with a scan rate of 50 mV s^{-1} .

4.9C); here if predictions were accurate then the gradient should be 1. As it can be seen, there is a trend but it is not close to 1 (-0.3 ± 0.1) and the spread of data is rather large with a large error in the fit. The same can be said for the expected and measured steady state currents calculated from equation 4.6, where the prediction is very poor (Figure 4.9D). One trend that is noticed is that none of the measured steady state responses go above 250 pA despite there being expected values of up to 1100 pA.

The analytical solutions proposed assume that the internal electrode acts as a disc shaped or a hemispherical electrode, whereas diffusion of species to the electrode is actually occurring down a narrow channel and therefore diffusion is not radial and may actually become limited, like in the case of a highly recessed electrode (see Section 1.4.1.3). This could then limit the overall current measured and help explain why many of the expected values for steady state current are much larger than that observed. This would also affect the prediction of the half wave potential in that the value for i_{ss}^a would be lower than previously expected. For use in electrochemical studies (as discussed further in Chapter 5), if the internal concentration is kept much higher than the concentration used externally and the currents of interest are small then this should not be an issue.

A potential explanation for the irreproducibility is to do with the backfilling

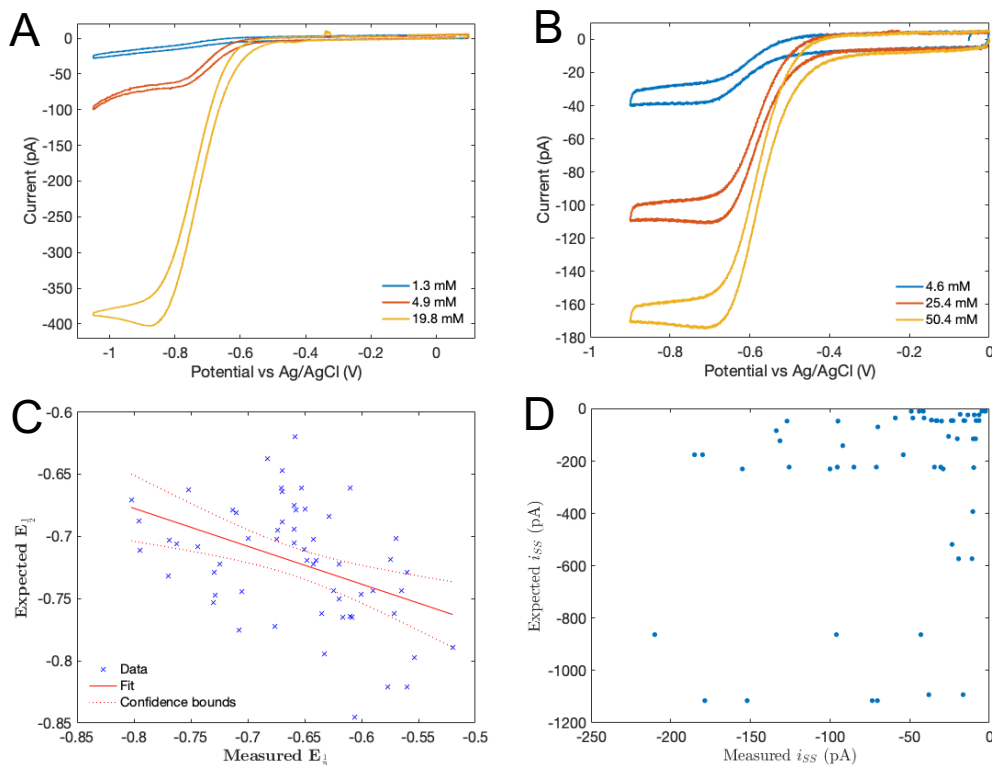


Figure 4.9: (A) CV of a BPNE with varied external concentrations of $[\text{Ru}(\text{NH}_3)_6]^{3+}$ with 0.1 M KNO_3 and the same internal concentration of 100 mM Fc, 0.2 M TBAPF_6 , ACN. (B) CV of a BPNE with differing internal concentrations of Fc with 0.2 M TBAPF_6 in ACN. (C) Summary of expected vs measured half wave potential ($E_{1/2}$) for several electrodes with varied internal and external concentrations. (D) Expected vs measured steady state limiting current for the same data as (C). All CVs used a scan rate of 50 mV s^{-1} .

of the electrodes. It is very difficult to remove all of the solution from inside of a capillary, this means that in the case of changing internal solutions there is likely some mixing of the solution that was used previously, especially in close proximity to the Au plug. In addition there is some likelihood that there may still be some of the initial Au deposition solution left inside the pipette after filling. Even if using a vacuum (as is done here) to evacuate the capillaries, some solid residue can remain that will redissolve upon backfilling the capillaries. Despite the drawbacks in fitting of the expected and measured data, it does at least give a reasonable “ball park” estimation for the half wave potential, as most of the measured and predicted data lie within 0.1 V of -0.7 V in this case and as shown in Figure 4.7 a standard Au electrode would see a half wave potential around -0.3 V. The issue in prediction

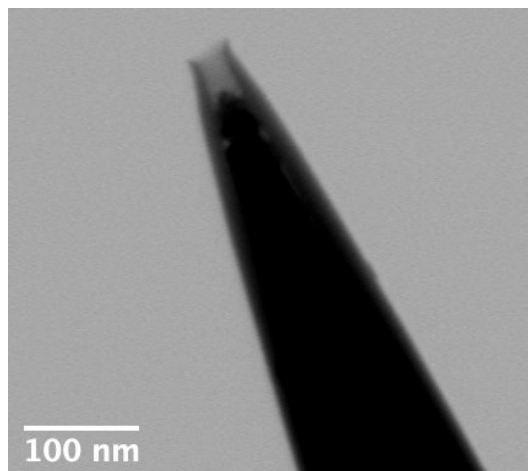


Figure 4.10: Bright field STEM image of a BPNE formed using Pt instead of Au. The capillary remains intact, however, the electrode is more recessed.

comes from distinguishing between different BPNEs with similar overall sizes and geometries with changing concentrations.

Pt BPNEs were also fabricated using the same method as for Au except for the use of 10 mM H_2PtCl_6 ($\geq 37.50\%$ Chloroplatinic acid hexahydrate, Sigma-Aldrich) with 0.1 M HClO_4 (70 %, Sigma-Aldrich) as the deposition solution inside the nanopipette. Generally this process is much less reproducible and the success rate was much lower than BPNEs formed using Au. As the STEM image shows (Figure 4.10), in the case of Pt the glass at the end of the capillary remains intact (unlike most of the Au electrodes) but the Pt plug is recessed inside the capillary (≈ 40 nm). In most cases under STEM investigation pipettes were found to be empty or very poorly filled with Pt. In an attempt to avoid H_2 gas formation, the deposition solution was adjusted to pH 10 (using NaOH dropwise). However, similar results of empty pipettes were observed. The exact reason for Pt being much more difficult to fabricate is unknown and further study is necessary. One possibility is that the generation of hydrogen gas during the formation of the Pt disrupts the deposition stability in the capillary, this gas formation is much less prevalent with Au formation, which could explain this discrepancy.¹⁰

Due to some of the issues presented with refilling electrodes, an attempt was made to electrodeposit a conductive polymer inside the electrode. A previous study was followed that electrodeposited a conductive polymer (polyaniline) from a meniscus in a SECCM style format. The study held 20 mM aniline hydrochloride in 75 μM HCl inside a nanopipette and used a potential on the substrate relative to a QRCE inside the nanopipette to carry out electropolymerisation, creating a

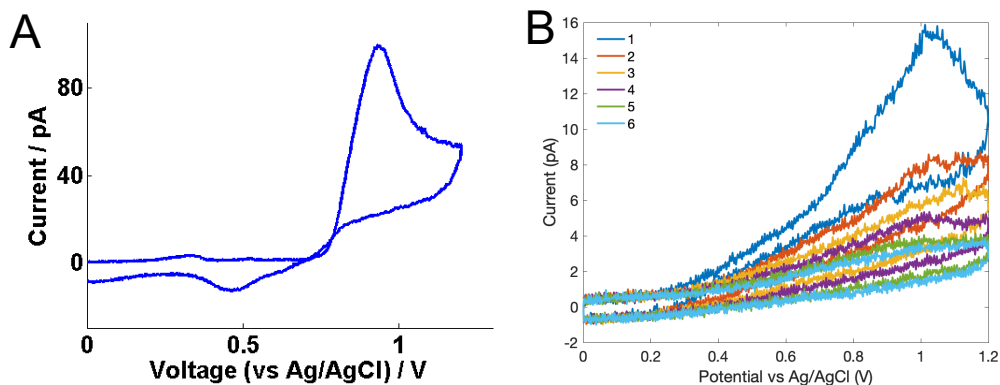


Figure 4.11: (A) CV of aniline electropolymerisation on a Au substrate taken from the previous study.¹¹ Scan rate of 200 mV s^{-1} in 20 mM aniline hydrochloride and 75 μM HCl with a 1 μm diameter SECCM probe. Reproduced from McKelvey, *et al.*, *Chem. Commun.*, 49(29), **2013**.¹¹ with permission from The Royal Society of Chemistry. (B) CV taken with aniline solution inside the BPNE, with each sweep (1 – 6) the observed current decreases. CVs were averaged every 10 data points to make overlaid differences obvious. Scan rate: 200 mV s^{-1} , data collected at one point every 1.29 ms.

conductive polymer on the substrate.¹¹ Attempts here using the 20 mM aniline hydrochloride ($\geq 99\%$ aniline hydrochloride, Sigma-Aldrich) and 75 μM HCl (37 % hydrochloric acid, Honeywell Fluka) did not show any results, so the concentration was increased to 0.1 M and was used to backfill the BPNE, which was then inserted into a bath of 5 mM $[\text{Ru}(\text{NH}_3)_6]^{3+}$ with 0.1 M KNO_3 . The potential was applied to a Ag/AgCl QRCE in the bath relative to another inside the BPNE. A CV was then carried out in the same potential range as the previous study and found a very similar response (Figure 4.11A,B), albeit with a lower current magnitude as expected for the reduced area of the internal face of the BPNE compared to the 1 μm SECCM probe used in the previous study. However, this response was only observed for the first cycle, after this the response quickly dropped in intensity, after 6 cycles no response was seen at all (Figure 4.11B). Attempting to do any further voltammetry after this point results in no electrochemical response. If the electropolymerisation had continued throughout the internal solution then this would have created a direct electrical connection to the Au plug, however, the lack of response suggests that this is not the case. There is the possibility that as deposition can only proceed on the back of the Au plug and not the glass walls, that layer of polymer is formed on the back of the Au plug which then stops any further electrodeposition.

4.4 Conclusions

Au BPNEs have been fabricated and it is shown that electrodes with a good voltammetric response and decent geometry are commonplace. Care should be taken when applying analytical solutions for the voltammetric response of any NE. Here the half wave potential can be predicted within a small region but determining differences between electrodes using the same configuration is not as reliable. Additionally prediction of steady state currents is also poor when comparing several BPNEs. Combining the experimental and COMSOL simulated CVs with STEM images gives a much better representation of the system as a whole and will be required for further studies of BPNEs in SEPM applications (Chapter 5). The fabrication of Pt BPNEs was also investigated with much less reproducible results and requires further study.

4.5 Acknowledgements

COMSOL simulations in this chapter were carried out by Dr Gabriel Meloni with the use of STEM images acquired by myself.

A PhD student, Yongxu Hu from the Ying group at the East China University of Science and Technology assisted in the fabrication and characterisation of BPNEs whilst visiting our group. Dr. Gabriel Meloni contributed to discussions and suggestions between myself and Yongxu relating to BPNE characterisation.

4.6 References

- [1] Gao, R., Ying, Y. L., Li, Y. J., Hu, Y. X., Yu, R. J., Lin, Y. & Long, Y. T. *Angew. Chemie - Int. Ed.*, 57(4), 1011–1015, **2018**.
- [2] Hao, R., Fan, Y. & Zhang, B. *J. Am. Chem. Soc.*, 139(35), 12274–12282, **2017**.
- [3] Hao, R., Fan, Y., Han, C. & Zhang, B. *Anal. Chem.*, 89(23), 12652–12658, **2017**.
- [4] Wood, M. & Zhang, B. *ACS Nano*, 9(3), 2454–2464, **2015**.
- [5] Wang, F. F., Wang, W., He, X., Han, L., Zhou, J. Z., Tian, Z. Q., Tian, Z. W. & Zhan, D. *Sci. China Chem.*, 60(5), 649–655, **2017**.
- [6] Guerrette, J. P., Oja, S. M. & Zhang, B. *Anal. Chem.*, 84(3), 1609–1616, **2012**.
- [7] Cox, J. T., Guerrette, J. P. & Zhang, B. *Anal. Chem.*, 84(20), 8797–8804, **2012**.
- [8] Bard, A. J. & Faulkner, L. R. *Electrochemical Methods: Fundamentals and Applications*. Wiley, New York, 2nd edition, **2001**.
- [9] Warwick Electrochemistry and Interfaces Group. *WEC-SPM*, **2019**.
- [10] Popov, K. I., Djokic, S. S., Nikolic, N. D. & Jovic, V. D. *Morphology of Electrochemical and Chemically Deposited Metals*. Springer International Publishing, **2016**.
- [11] McKelvey, K., O’Connell, M. A. & Unwin, P. R. *Chem. Commun.*, 49(29), 2986–2988, **2013**.

Chapter 5

Bipolar Nanoelectrodes: Applications in Scanning Electrochemical Probe Microscopy

The use of nanoelectrodes (NEs) for scanning electrochemical probe microscopy (SEPM) is an extremely challenging field. Many different methods for the fabrication, characterisation and application of NEs have been demonstrated with varied reproducibility and success. Here the electrodes fabricated and characterised in the previous chapter (Chapter 4) will be accessed for their application in SEPM, specifically in the use of in-situ scanning tunnelling microscopy (STM) and nanoscale scanning electrochemical microscopy (SECM) with the ultimate goal of STM-SECM studies. It is demonstrated that these electrodes show some early promise, however, issues regarding longevity and robustness will limit their application in the near future. But there could be opportunity for improvements to the method which would allow for further applications on a longer timescale.

5.1 Introduction

Nanoscale SECM studies have been summarised in a few review articles,¹⁻⁶ and the most recent studies have been summarised in Section 1.4.1.4, in light of this the introduction below will focus on BPNE publications rather than general nanoscale SECM. The method of BPNE fabrication detailed in Chapter 4 is relatively new and has not yet seen much application in SEPM, but has been used in a couple of studies

and a few nanoscale electrochemical applications outside of mapping techniques.

The methodology followed to fabricate BPNEs here closely follows a recent publication⁷ and the full details are discussed in Section 4.2. The same study also used the BPNEs to study NP collisions. It was possible to distinguish between collision events for two different sizes (13 nm and 60 nm) of AuNPs at the tip of the 30 nm BPNE by the magnitude of the current spike observed, upon NPs impacting the Au plug.⁷

Another group used a similar method to fabricate a Pt plug at the end of a nanopipette and the Pt face inside the nanopipette was used as the NE.⁸ Opposed to the work in Chapter 4, the external external face of the Pt was purposefully much larger than the internal face such that the processes inside the nanopipette would limit the Faradaic response. This “nanocell” then confines the motion of NPs inside the cell to effectively one dimension and reduces the background noise in the fluorescence signal. Individual AgNPs were studied by both the current response of the electrode and by fluorescence microscopy as they collided and were oxidised at the Pt electrode.⁸ The same group also created a BPNE using Pt to fill a FIB milled nanopore on a sealed glass capillary, a double barrel pipette and a thin membrane of silicon nitride.⁹

Specific to SEPM, one study previously conducted a form of STM-SECM using BPNEs as the tip. The study fabricated Au BPNEs in a similar fashion to results presented here (Chapter 4), however, $\text{Fe}(\text{CN})_6^{2-}$ was used instead of NaBH_4 and a larger voltage of 3 – 5 V was used for electrodeposition. This was then left to deposit until the Au plug reached a length where an etched Ag wire could be inserted into the pipette to make a physical connection. In this fashion the result is a more traditional NE without the need for further backfilling. The NE used for STM-SECM experiments was ≈ 110 nm in diameter with an $RG = 1.3$. The substrate used for scanning experiments was a Si surface with a AuNP array enclosed in an Au band. The tip was approached into tunnelling distance of the Au band before using this point to scan in a constant height SECM mode 200 nm above the AuNP array. The SECM was carried out with FcCH_2OH being oxidised at the AuNE and regenerated at the AuNP.¹⁰

To date only one study has been published on the use of BPNEs in SEPM.¹⁰ This chapter focusses on the application of Au BPNEs for use with in-situ STM and nanoscale SECM, making use of a commercial STM instrument and a high end SEPM setup respectively.

5.2 Methodology

Two separate instruments were used for SPM measurements here. A home constructed SEPM system (as in Chapter 3) and a commercial ambient STM system. The SEPM system consists of the following: vertical (P-753.1CD, PhysikInstrumente) and lateral (P-733.2DD, PhysikInstrumente) piezoelectric positioners with accompanying amplifiers for vertical (E665, PhysikInstrumente) and lateral (E505, PhysikInstrumente) positioners. Picomotor piezo linear actuators (Newport) were used for coarse vertical and lateral motion. SEPM experiments used a three electrode system with the probe (BPNE), substrate and an Ag/AgCl QRCE (see Figure 3.5). The potential was applied and the current measured on both the probe and substrate using separate in house built electrometers. All parameters were then controlled using an FPGA card (PCIe-7825R, National Instruments) with home designed LabVIEW software.¹¹ Piezoelectric components, sample, tip and reference were kept inside a sealed Faraday cage on a vibration isolated table (Newport S-2000 series pneumatic vibration isolators). The electronics (controllers, amplifiers etc.) were all kept on a separate shelf in order to isolate the vibrations associated. The commercial STM consists of a Veeco STM with Nanoscope E controller and an A-type scanner. The scanner and sample are held inside a Faraday cage on bungee cords to isolate the system from electrical noise and vibrations respectively. The potentials are applied to the substrate with the tip held at ground. Typically the instrument would use a 0.25 mm Pt/Ir wire which is mechanically cut to a sharp point and inserted by the other end directly into the STM head.

In experiments using BPNEs in a commercial STM, mounting the electrode becomes challenging, as usually capillaries are several cm long, filled with solution and fairly fragile. The STM instrument in question normally uses a 0.25 mm Pt/Ir wire that can simply be inserted into the STM head. BPNEs were fabricated as in Section 4.2 using 10 mM KAuCl_4 (98 %, Sigma-Aldrich) and 10 mM HCl (37 %, Honeywell Fluka) inside a nanopipette (30 nm aperture, laser pulled from quartz capillaries, QF100-50-10, Sutter Instrument Co.) and submerged in 10 mM NaBH_4 (99.99 %, Sigma-Aldrich) in ethanol (99 %, Fisher Scientific). BPNEs were then back-filled with Ferrocene (Fc, 98 %, Sigma-Aldrich) and 0.2 M TBAPF_6 (99 %, Merck) in acetonitrile (ACN, HPLC grade, Fisher) for characterisation with $[\text{Ru}(\text{NH}_3)_6]^{3+}$ (hexaamineruthenium(III) chloride, 98 %, Sigma-Aldrich) and 0.1 M KNO_3 (≥ 99.0 %, Sigma-Aldrich) in deionised water. The length of pipettes used is normally on the scale of 10 cm. However, to fit these electrodes into the commercial STM instrument the total length of pipette has to be ≈ 1 cm, with another cm of wire

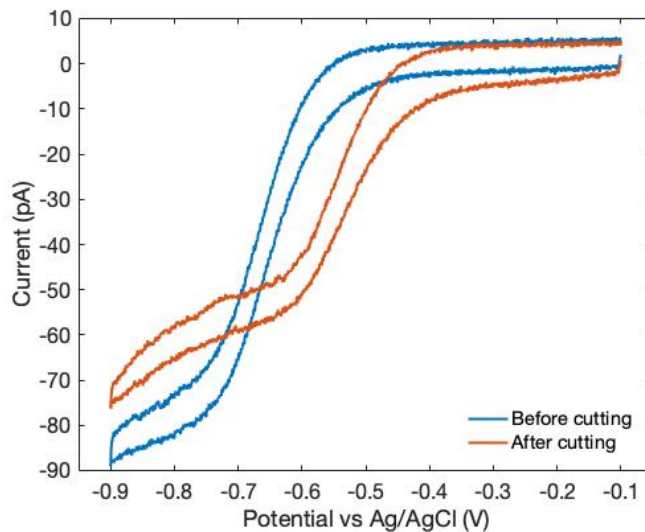


Figure 5.1: CVs taken before (blue) and after (orange) breaking to fit in STM system. The change in half wave potential is due to the Pt/Ir opposed to Ag wire used internally. Outside BPNE: 4.5 mM $[\text{Ru}(\text{NH}_3)_6]^{3+}$, 0.1 M KNO_3 in water against Ag/AgCl. Inside BPNE: 50 mM Fc, 0.2 M TBAPF₆ in ACN with Ag wire (blue) and Pt/Ir wire (orange). 200 mV s⁻¹ scan rate.

for connection. To do this, the fabricated BPNE was cut using a glass pen before inserting a 2 cm length of Pt/Ir wire (70/30 &, 0.25 mm, Sigma-Aldrich). Epoxy (Super Glue, Loctite) was then used to seal the wire and ACN electrolyte in the back of the pipette. The use of Pt/Ir wire internally does shift the half wave potential of the BPNE as discussed previously (Section 4.1.2). Figure 5.1 shows the CV of an electrode before and after the breaking and sealing process. This shift can be accounted for using equations 4.6 and 4.7 using the new formal potential ($E_a^{\circ'}$) for a Pt/Ir wire as a reference instead of a Ag wire. The new $E_a^{\circ'}$ is given by 0.44 V opposed to 0.55 V which gives an expected half wave potential of -0.57 V opposed to -0.68 V before the cutting, which is in good agreement with the CVs measured.

HOPG substrates were prepared by exfoliation of graphite using scotch tape to remove a thin layer which was then placed onto the STM stage. Glass substrates were simply microscope slides (Super Premium Microscope Slides, VWR) with a solution bath attached (Araldite Rapid, RS PRO). Au substrates were prepared by sputtering Au onto Ti on glass, the sample was then insulated, bar a small area (≈ 100 μm), using tape (3M Polyimide film tape) and a small solution bath was secured using araldite (Araldite Rapid, RS PRO).

STEM images were obtained using a Zeiss Gemini SEM, using 30 kV accel-

erating voltage in a STEM mode, with electrodes mounted on a multi-TEM sample holder. FIB milling was realised using a Jeol 4500 FIB/SEM: This system has two columns, the first is a 30 kV with a LaB6 electron gun used for SEM imaging and the second is a 30kV ion column with a Ga⁺ ion source for FIB milling.

COMSOL Multiphysics software was used to create FEM models for SECM type approach curves. This model does not take into account the internal solution of the BPNE and only takes the geometry of the external face of the electrode into account, including the insulating sheath (Figure 4.4). The model works by taking the geometry and making it into a two dimensional problem, then simulating the expected steady state current assuming mass transport limited diffusion to the electrode surface. The same steady state current calculation is then carried out with varied distances for the electrode from the surface to generate an approach curve. The range of values calculated is from 0 distance (electrode touching surface) to five tip radii over 50 steps.

In addition to COMSOL models, SECM approach curves were also calculated using analytical solutions from the literature. One useful feature of SECM approach curves is that they are independent of redox species concentration and are only related to the geometry of the probe and the kinetic constant (k) of the substrate. If the substrate is an insulator then k can be set to 0 and the approach then only depends on electrode geometry allowing for another level of electrode characterisation. The expected response of an insulated microdisc electrode approached to an insulating surface (negative feedback) is given by:

$$Ni_T^{\text{ins}}(L, RG) = \frac{\frac{2.08}{RG^{0.358}} \left(L - \frac{0.145}{RG} \right) + 1.585}{\frac{2.08}{RG^{0.358}} (L + 0.0023RG) + 1.57 + \frac{\ln(RG)}{L} + \frac{2}{\pi RG} \ln \left(1 + \frac{\pi RG}{2L} \right)} \quad (5.1)$$

where Ni_T^{ins} is the normalised tip current (i_T/i_∞), L is the normalised surface to tip separation (d/a) and RG is the dimensionless constant r_g/a .¹² The expected response to a conducting substrate (positive feedback) is governed by:

$$Ni_T^{\text{cond}}(L, RG) = \alpha(RG) + \frac{\pi}{4\beta(RG) \arctan(L)} + \left(1 - \alpha(RG) - \frac{1}{2\beta(RG)} \right) \frac{2}{\pi} \arctan(L) \quad (5.2)$$

where α and β are functions of RG and are given by equation 5.3 and 5.4 respectively.¹²

$$\alpha(RG) = \ln(2) + \ln(2) \left(1 - \frac{2}{\pi} \arccos \left(\frac{1}{RG} \right) \right) - \ln(2) \left(1 - \left(\frac{2}{\pi} \arccos \left(\frac{1}{RG} \right) \right)^2 \right) \quad (5.3)$$

$$\beta(RG) = 1 + 0.639 \left(1 - \frac{2}{\pi} \arccos \left(\frac{1}{RG} \right) \right) - 0.186 \left(1 - \left(\frac{2}{\pi} \arccos \left(\frac{1}{RG} \right) \right)^2 \right) \quad (5.4)$$

The full response of an electrode approaching a substrate can then be written as a combination of the insulating and conducting terms such that:

$$Ni_T(L, \Lambda, RG) = Ni_T^{\text{cond}} \left(L + \frac{1}{\Lambda}, RG \right) + \frac{Ni_T^{\text{ins}}(L, RG) - 1}{(1 + 2.47RG^{0.31}L\Lambda)(1 + L^{0.006RG+0.113}\Lambda^{-0.0236RG+0.91})} \quad (5.5)$$

which is a function of L , Λ and RG , where $\Lambda = ka/D$ and hence also depends on the kinetic constant.¹²

5.3 Results

5.3.1 In-situ STM

STM was attempted using BPNEs as the STM tip in order to assess the robustness and longevity of BPNEs for STM imaging. The radius of curvature for typical STM tips can be quite poor (Figure 1.1) and hence these BPNEs could actually be a good improvement in that regard. Conventionally electrons will tunnel directly from the sample to tip or vice versa depending on the bias. However, the situation is different when using a BPNE. In the setup used here, no redox process is happening outside of the BPNE and the oxidation of Fc at the internal face of the Au plug is used to complete the circuit. The STM instrument used applies the bias to the sample and the current is measured at the internal Pt/Ir electrode. So once the tip comes within tunnelling distance of the sample, the bias of the plug should then be the same as the sample, this will then drive the oxidation of the Fc inside the tip, resulting in a measured current at the Pt/Ir electrode (Figure 5.2). This setup will also limit the potentials available, as the potential has to be sufficient to drive the oxidation. Negative sample potentials, for instance, would not oxidise the Fc and hence no

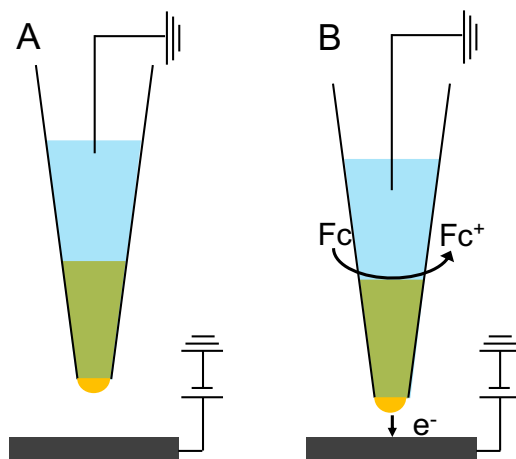


Figure 5.2: (A) With the tip far from the surface no electrochemical reaction is happening inside the electrode and no tunnelling is occurring. (B) Once the electrode is within tunnelling distance, the bias at the substrate can drive the oxidation of Fc inside the tip resulting in a measured current at the electrode inside the BPNE.

current would be measured.

Figure 5.3A displays a constant current STM scan of HOPG using a commercial STM instrument with a BPNE as the tip. Step edges of the HOPG are easily visible and a linescan over several steps is shown in Figure 5.3B. The step features have an easily discernible height of ≈ 0.3 nm in agreement with the literature.¹³ Difficulties in this specific setup arise when attempting to achieve atomic resolution; normally the conditions required involve a low bias ($\lesssim 100$ mV) with a high tunnelling current ($\gtrsim 800$ pA). However, with BPNEs in this format, a low bias does not provide a sufficient current for shuttling of the redox species, plus the overall current is limited by the redox process at the internal face of the plug, hence the tip crashes into the surface before reaching the desired current.

Normally in ambient STM the system is left scanning for a period of at least 15 minutes before acquiring data to allow for thermal drift within the system to minimise. In this case we found that drift in the z-piezo required to maintain tunnelling current was more significant than with a conventional Pt/Ir wire tip. This meant that the time available for scanning was reduced as the vertical piezoelectric runs out of extension over the course of approximately 5 minutes whilst trying to keep the tunnelling current constant. The exact cause of this drift is not obvious, however, one possibility is that there is a depletion of redox species at the internal face of the Au plug due to the narrow channel for the internal solution, this would cause a reduction in current and hence a further extension of the z-piezo. However,

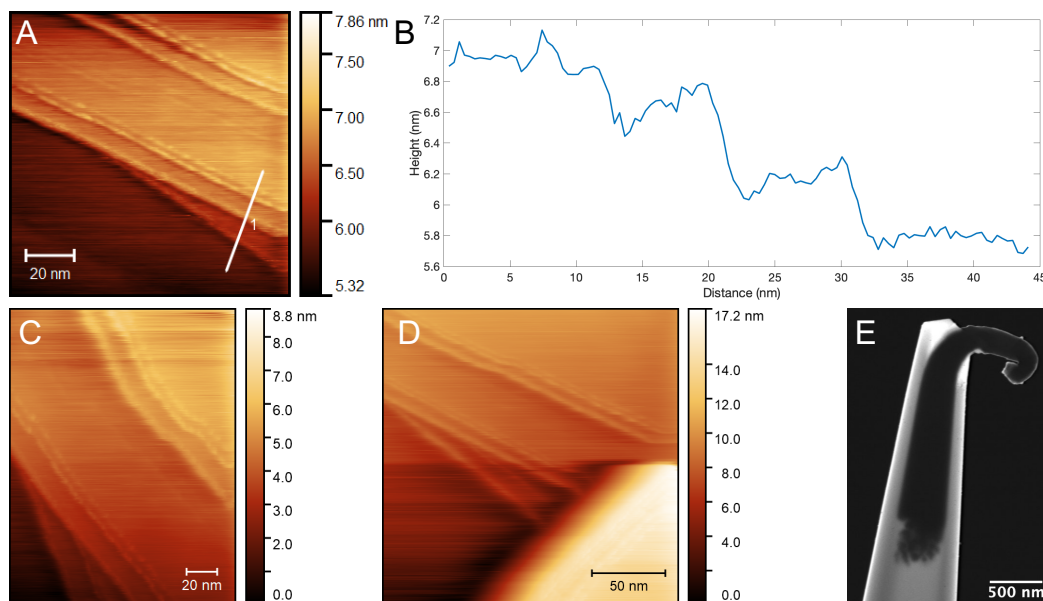


Figure 5.3: (A) STM scan of HOPG immersed in water, using a BPNE as the STM tip. Step edges are observed. Line 1 is a linescan displayed in (B) showing step feature height of ≈ 0.3 nm. (C,D) STM images of a HOPG surface immediately after the BPNE was approached to the surface, showing an increased drift. Sample bias: 0.5 V, current set point: 50 pA, scan rate: 4 nm s^{-1} . Internal BPNE solution: 50 mM Fc, 0.2 M TBAPF₆ in ACN. (E) STEM image of a BPNE after use in the STM, showing the deformation of the Au plug without fully breaking the electrode.

due to the high concentration of Fc and the fairly large area of the internal face, it is highly unlikely that depletion is the cause. Another possibility is that there is a leakage of the ACN past the Au plug which could cause the formation of insulating debris as the internal solution reacts with the atmosphere potentially blocking the electrode (see Section 5.3.2).

Some other examples of STM images are shown in Figure 5.3C,D. These scans were obtained very soon (≈ 10 s) after approaching the surface which is the reason for the large amount of drift. In this case the tunnelling current was fairly stable for a short while (≈ 1 minute), before dropping extremely rapidly, resulting in the tip impacting the surface (Figure 5.3E). As the full range of the piezo on this system is fairly low ($\approx 1 \mu\text{m}$) the damage to the electrode is limited, meaning that the subsequent STEM images can actually show the physical deformation of the Au plug without breaking the glass fully.

Scans shown here were done inside a water droplet which was more successful than attempts without water. This improvement was attributed to water stopping the formation of salt crystals on the end of the tip and possibly reducing any issues

from leakage of the electrode.

5.3.2 Nanoscale SECM

Using the SEPM system, both negative and positive feedback approach curves were obtained using a BPNE on insulating and conducting substrates respectively.

Negative feedback approach curves were created by approaching a BPNE to an insulating glass substrate. Figure 5.4A displays a STEM image of the BPNE taken after the SECM scans were complete. This was used to check for damage and to map the geometry for COMSOL simulations. CVs were recorded before (Figure 5.4B), during and after SECM use to check for major differences indicating damage or degradation. The COMSOL simulated CV is in reasonable agreement with the measured CV, the fully analytical simulation (using equation 4.6 for an insulated conical electrode) is not as close but that is to be expected given the assumptions made; it is unlikely for fully idealised geometries to produce results as good as FEM simulations. The raw data for a negative feedback approach curve are shown in Figure 5.4C which shows a 5 % decrease in the current over the last ≈ 2 tip radii of the approach. Given the small radius ($r = 25$ nm), the relatively small change in current is expected. Figure 5.4D shows the same data with the addition of the analytically calculated from equation 5.5 (orange) and COMSOL simulated (yellow) approach curves. Both the analytical and COMSOL solutions suggest the approach was stopped ≈ 2.5 tip radii away from the surface. This feedback set point was used initially as a precaution not to contact the surface, however, further attempts with similar sized electrodes and larger feedback thresholds often resulted in damage to the electrode over longer timescales as will be further discussed later. The COMSOL simulated approach appears to be a better fit to the experimental data, which is expected as it takes into account the geometric factors from the STEM imaging which the analytical approximation does not. It can also be seen that the analytical approximation will result in zero current at zero distance which is definitely not the case for an electrode with a protruding geometry. So, whilst the analytical approximation can give a reasonable estimate of the tip to surface separation, the COMSOL model will always be a more effective method.

In order to enhance the response measured during approach curves, a larger BPNE was used to obtain positive feedback data. This was done by taking a BPNE with a radius of ≈ 50 nm and FIB milling to a flat geometry with an approximate electrode radius of 340 nm (Figure 5.5A). A positive feedback approach curve obtained with this electrode is shown in Figure 5.5B, where an increase in tip current of 5 % over 0.5 tip radii is observed. One notable issue found with FIB milling

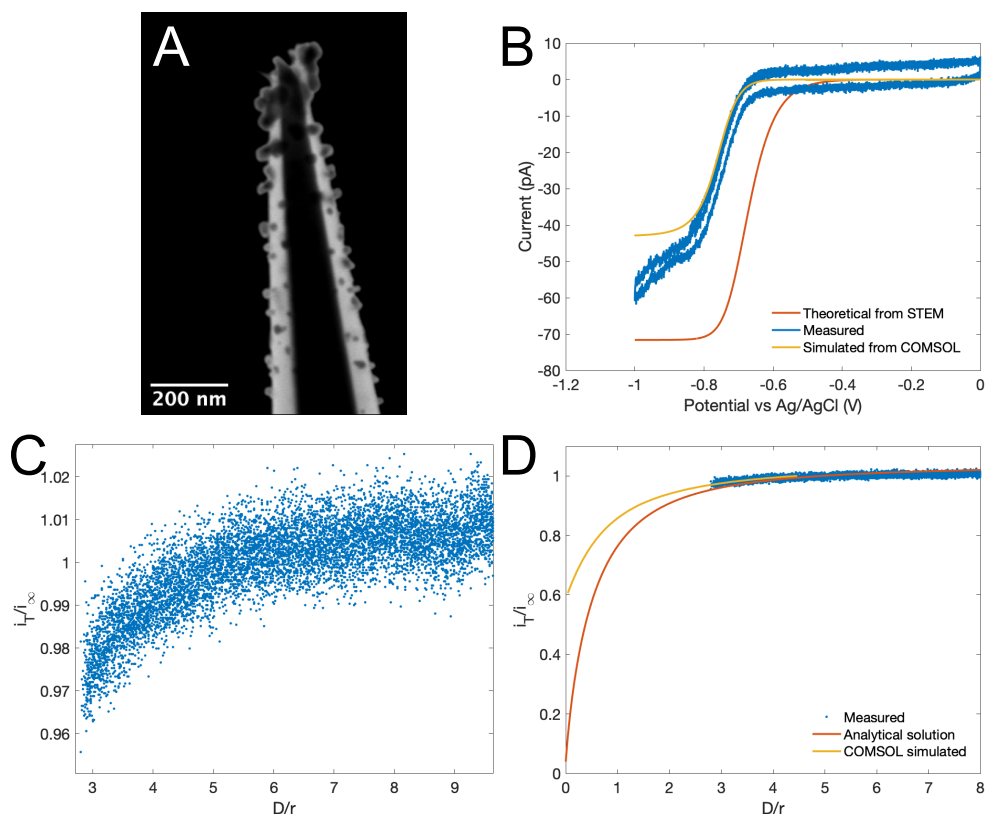


Figure 5.4: (A) STEM of BPNE used after scanning showing a radius $r = 25$ nm. (B) Measured CV (blue) of BPNE with simulated CV using equation 4.6 (orange) and simulated with COMSOL (yellow). 200 mV s^{-1} scan rate used for measured CV. (C) SECM negative feedback approach curve to current set point (5 pA) with approach velocity of 40 nm s^{-1} and tip bias of -0.9 V . (D) COMSOL simulated (yellow) and analytical solution from equation 5.5 (orange) negative feedback approach curve with measured approach from (C). The same tip, simulated COMSOL geometry and solution is used for all data in this figure. Solution bath: $4.9 \text{ mM } [\text{Ru}(\text{NH}_3)_6]^{3+}$, 0.1 M KNO_3 in water against Ag/AgCl. Inside BPNE: 50 mM Fc , 0.2 M TBAPF_6 in ACN with Ag wire.

BPNEs is that whilst the Au formed at the end of the electrode forms a good seal with the glass, the seal is not necessarily as effective further along the pipette, therefore FIB milling can expose these flaws at the surface of the newly FIB milled electrode. Sometimes this becomes evident in the CV response of these electrodes (Figure 5.5C). A slightly strange response is observed in the steady state region of the voltammogram before use (blue trace), the half wave potential is also less negative than expected, although the steady state response is well matched. In addition after several approach curves (10 repetitions) were measured the CV was

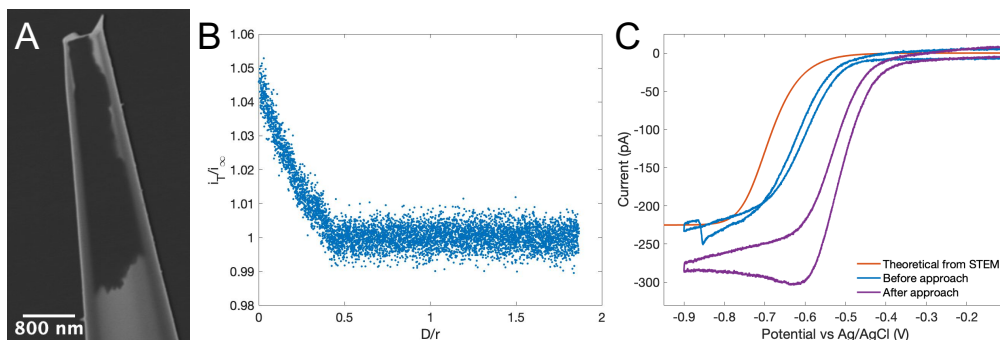


Figure 5.5: (A) STEM image of FIB milled BPNE. (B) Positive feedback approach curve to a Au surface, 100 nm s^{-1} approach rate, -0.9 V tip bias and 260 pA feedback threshold. (C) Theoretical CV (orange), BPNE CV before (blue) and after (purple) use for SECM approach curves, with scan rate of 200 mV s^{-1} . (B,C) solution bath: $4.84 \text{ mM } [\text{Ru}(\text{NH}_3)_6]^{3+}$, 0.1 M KNO_3 in water against Ag/AgCl. Inside BPNE: 50 mM Fc , 0.2 M TBAPF_6 in ACN with Ag wire.

taken again (purple trace) where the steady state current, half wave potential and shape of the CV have changed significantly. This is likely due to a conformational change after contact with the surface caused by a reduction in steady state current due to leakage forming features on the tip and blocking the electrode surface (as discussed at the end of this section).

After the positive and negative feedback approach curves were obtained, hopping type SECM scans were attempted on several substrates. As the process inside the BPNE is oxidation of Fc (as in Section 4.2), the processes studied outside are limited to reductions. For these scans a CV is taken in the bulk solution to show the steady state reduction of the species ($[\text{Ru}(\text{NH}_3)_6]^{3+}$), then the probe is left biased at a suitable potential to continue to reduce the species (-0.9 V). The probe is then approached towards the surface (approach rate: 80 nms^{-1}) until the current changes (positively or negatively) by a set threshold (6 pA), once the threshold is reached the probe is retracted (500 nm), moved laterally (200 nm) and then re-approached at the next pixel. Repeating this process then generates a map of the surface. What was generally found is that reproducible approach curves are obtained for a certain period of time before a large change in the current response is observed (Figure 5.6B). It is likely that some cases where a very large increase in the current is observed is due to the tip contacting the surface and damaging the electrode in some way. However, the reason for this contact is unknown. As shown in the approach curves previously (Figure 5.4C and Figure 5.5B) the tip position at the current threshold is generally a couple of tip radii away from the surface and, with the sizes of electrode used here, this is well within the range of precision of the

positioning instrumentation used (see Chapter 3). In addition, the CV response of the electrode is checked in between each scan attempt. In some cases the response stays fairly consistent over some time before the rapid change, in other cases the CV response can change fairly dramatically between each check even if the scan completes without any drastic changes.

STEM images were also taken before and after scanning attempts to check the electrode for damage and geometrical changes. It can be seen that in some cases a build up of small features is observed around the tip (Figure 5.6A). The formation and possibly detachment of these may be the cause of the change in CV response, as the formations block the electrode this will cause a reduction in the measured current, subsequent detachment would then cause a relative increase. The blocking would then also cause the tip to approach closer to the surface and potentially contact it (depending on the severity of the blocking). Upon contact with a conductor a large sharp spike in the current is seen and the tip will retract and approach again, contacting an insulator will likely continue until enough damage is caused that new electrode material is exposed, increasing the current response again (Figure 5.6C). These formations are most likely due to the internal solution leaking out of the electrode and reacting with the external solution, which could be a result of poor sealing of the the Au to the glass.

5.3.3 Future Possibilities

Whilst some issues have been presented above, it would be a shame to completely abandon BPNEs for SEPM as the reproducibility of the geometry in a very simple and cheap method is a very attractive feature.

The main issues appear to relate to the composition of the internal solution and leakage around the Au plug. It has been suggested that the electrodes could be filled with a conductive polymer solution which would then allow for a “direct” connection to the Au plug and hence the half wave potential would not be changed and as it is more viscous than ACN it should not have the same issues with leakage. A previous study has shown the fabrication of nanostructures with one such polymer in an SECCM format.¹⁴ However, as mentioned in Section 4.2, filling with ACN is carried out due to its reduced viscosity (0.39 mPa·s vs 0.89 mPa·s for dynamic viscosity compared to water)¹⁵ and hence the same problems arise with refilling pipettes with solutions as the solution often does not reach down to the Au plug. In addition, full polymerisation of the alinine to polyalinine may also prove difficult as only the plug or inserted electrode can be polarised and not the glass walls. This is still an avenue that may be worth exploring (see end of Section 4.3).

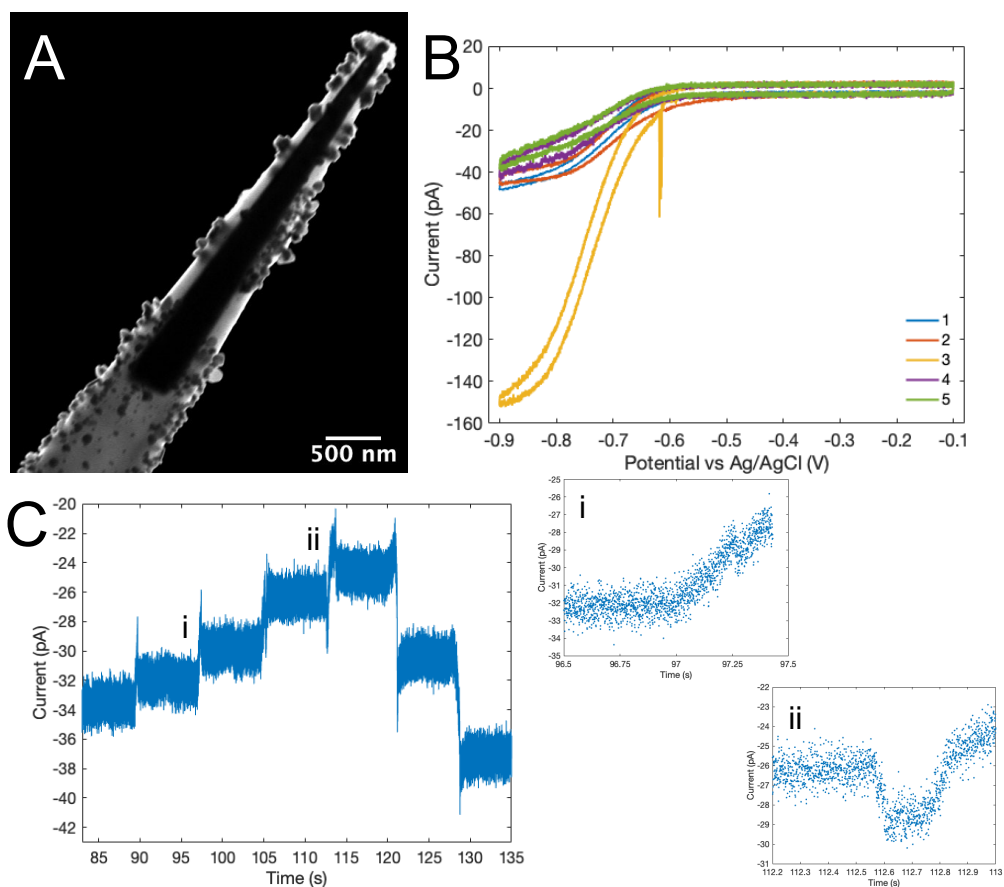


Figure 5.6: (A) STEM image of BPNE after SECM scans, showing small formations along the sides and end of the electrode. (B) CVs of the same electrode, before scanning in bulk (1,2), after the first SECM scan (3), after the second SECM scan (4) and after the third and final SECM scan (5). (C) Current response measured at the BPNE during an SECM scan. Several expected negative approach curves (an example is enlarged in i) are observed but with a decrease in response after each approach. At ii a sharp increase in current is seen and subsequent approaches result in enhanced current responses. 5.7 mM $[\text{Ru}(\text{NH}_3)_6]^{3+}$, 0.1 M KNO_3 in water against Ag/AgCl. The scan rate for CVs was 200 mV s^{-1} . SECM parameters: $1 \mu\text{m s}^{-1}$ lateral scan rate, 80 nm s^{-1} approach velocity, -0.9 V approach tip bias, 6 pA feedback set point, $0.5 \mu\text{m}$ retract distance, $1 \mu\text{m s}^{-1}$ retract rate and 200 nm pixel separation.

As mentioned in Chapter 4 in many cases the very end of the glass sheath breaks away leaving the Au exposed. It is possible that this breaking process leads to a poorer seal around the Au. More time could be spent in attempting to optimise the initial Au deposition parameters. It is likely that this damage occurs very early in the deposition process, therefore it is unlikely that the bias applied has a

great effect. The initial concentrations of NaBH_4 and KAuCl_4 may have an effect on the vigorousness of the deposition, in addition it is possible that reducing the temperature of the ethanol solution could slow the deposition process down and cause less disruption to the glass. Another method of slowing down the reaction could be to experiment with the temperature of the NaBH_4 solution: at lower temperatures the reaction rate will be slower and potentially less vigorous.

5.4 Conclusions

The suitability of BPNEs fabricated in Chapter 4 for use in SEPM studies has been investigated. BPNEs were applied to a HOPG surface under water in a commercial STM instrument with impressive resolution achieved. BPNEs have also been applied to SECM style approach curves for both conductive and insulating substrates also showing good detection limits and positioning at nanoscale separations. Unfortunately BPNEs in this format have issues with longevity and performing STM or SECM experiments for a long enough time to be effective does not appear to be possible. The reasons for this are likely due to issues with plug stability and the back filling of capillaries: if the solution is too viscous then proper filling does not occur, in the opposite case, electrode leakage appears to be much more of an issue. BPNEs have presented a method for easy and reproducible fabrication of NEs with ideal geometries, with further study and modifications to the fabrication and characterisation process it is possible that these electrodes could become a very popular alternative to the current methods used.

5.5 Acknowledgements

COMSOL simulations in this chapter were carried out by Dr Gabriel Meloni with the use of STEM images acquired by myself.

5.6 References

- [1] Kai, T., Zoski, C. G. & Bard, A. J. *Chem. Commun.*, 54(16), 1934–1947, **2018**.
- [2] Kim, J., Renault, C., Nioradze, N., Arroyo, N., Leonard, K. C. & Bard, A. J. *Anal. Chem.*, 88(20), 10284–10289, **2016**.
- [3] Izquierdo, J., Knittel, P. & Kranz, C. *Anal. Bioanal. Chem.*, 410(2), 307–324, **2018**.
- [4] Bentley, C. L., Edmondson, J., Meloni, G. N., Perry, D., Shkirskiy, V. & Unwin, P. R. *Anal. Chem.*, 91(1), 84–108, **2019**.
- [5] Zoski, C. G. *J. Electrochem. Soc.*, 163(4), H3088–H3100, **2016**.
- [6] Oja, S. M., Fan, Y., Armstrong, C. M., Defnet, P. & Zhang, B. *Anal. Chem.*, 88(1), 414–430, **2016**.
- [7] Gao, R., Ying, Y. L., Li, Y. J., Hu, Y. X., Yu, R. J., Lin, Y. & Long, Y. T. *Angew. Chemie - Int. Ed.*, 57(4), 1011–1015, **2018**.
- [8] Hao, R., Fan, Y. & Zhang, B. *J. Am. Chem. Soc.*, 139(35), 12274–12282, **2017**.
- [9] Hao, R., Fan, Y., Han, C. & Zhang, B. *Anal. Chem.*, 89(23), 12652–12658, **2017**.
- [10] Wang, F. F., Wang, W., He, X., Han, L., Zhou, J. Z., Tian, Z. Q., Tian, Z. W. & Zhan, D. *Sci. China Chem.*, 60(5), 649–655, **2017**.
- [11] <https://warwick.ac.uk/fac/sci/chemistry/research/unwin/electrochemistry/wec-spm/> Warwick Electrochemistry and Interfaces Group. *WEC-SPM*, **2019**.
- [12] Cornut, R. & Lefrou, C. *J. Electroanal. Chem.*, 621(2), 178–184, **2008**.
- [13] Chang, H. & Bard, A. J. *Langmuir*, 7(6), 1143–1153, **1991**.
- [14] McKelvey, K., O’Connell, M. A. & Unwin, P. R. *Chem. Commun.*, 49(29), 2986–2988, **2013**.
- [15] www.ddbst.com/en/EED/PCP/VIS-C3.php Dortmund Data Bank. *Dortmund Data Bank*, **2019**.

Chapter 6

Characterisation of Benzotriazole Adsorption on the Cu(110) Surface

Molecular assembly on ideal substrates is one of the most fundamental studies possible in materials characterisation. Understanding how the first layer or two of individual molecules arrange and deposit on a substrate can lead to a new understanding of the system of interest. This level of information can be routinely obtained using an ultra-high vacuum (UHV) scanning tunnelling microscopy (STM). This chapter illustrates the capability of STM to characterise materials at the nanoscale and show what can be achieved in ideal conditions.

Benzotriazole (BTAH) is a molecule that has been used as a corrosion inhibitor for copper surfaces since the mid 1900s.¹ The mechanism of how BTAH interacts with the copper surface is actually quite poorly understood despite its fairly wide industrial application.²⁻⁴ Some previous research has studied BTAH adsorption on the Cu(111) surface in vacuum,^{5,6} and the Cu(100) surface in-situ,⁷ but very little has been reported about the Cu(110) surface and the role of oxygen in the process, hence the study here looks at the adsorption of BTAH onto a Cu(110) single crystal in UHV conditions using STM and high resolution electron energy loss spectroscopy (HREELS). The role of oxygen in the adsorption process is also briefly investigated.

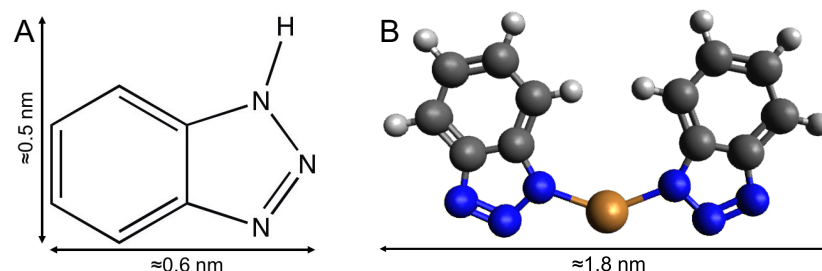


Figure 6.1: (A) Structure of BTAH with approximate dimensions.^{5,6} (B) Suggested structure for $\text{Cu}(\text{BTA})_2$ dimers formed with Cu adatoms.^{5,6} The grey, blue, white and gold colours represent carbon, nitrogen, hydrogen and copper respectively.

6.1 Introduction

Industrial companies have used BTAH as a corrosion inhibitor for copper (Cu) since the 1950s.¹ Despite the wide application in corrosion, debate still exists in regards to its molecular adsorption and orientation on the Cu surface.^{2–4} There has been some more recent literature which attempts to resolve this debate,^{5,6} however, there are still many gaps in this understanding when it comes to specific crystallographic orientations and the role of oxygen.

6.1.1 Benzotriazole (BTAH)

BTAH is a colourless, polar, heterocyclic compound with the structure described in Figure 6.1A. Ultraviolet, infra-red and nuclear magnetic resonance (NMR) studies have confirmed that this is the predominant tautomeric configuration at room temperature.^{8–11} BTAH also has applications in photographic emulsions and as a drug precursor but is most commonly used as a corrosion inhibitor for Cu due to a long history in Cu protection and its high solubility in several basic solutions.¹²

It has been shown that the protective function of BTAH is related to the formation of a layer at the surface which is a complex between the BTAH and Cu.¹³ The industry typically forms this layer via either simple immersion of the Cu into aqueous BTAH or via vapour transport from impregnated paper, the difference this makes at the molecular level is still debated.¹³ The bond between Cu and BTAH is thought to occur through the lone pairs on the N molecules but upright (from an ultraviolet photoelectron spectroscopy, UPS in UHV study¹⁴), flat (from NMR studies¹⁵) and tilted (from studies with x-ray photoelectron spectroscopy, XPS, UPS and infrared reflectance spectra in UHV¹⁶) adsorption geometries have been reported.¹³ The upright configuration (Figure 6.2A) has the molecule sit perpendicular to the

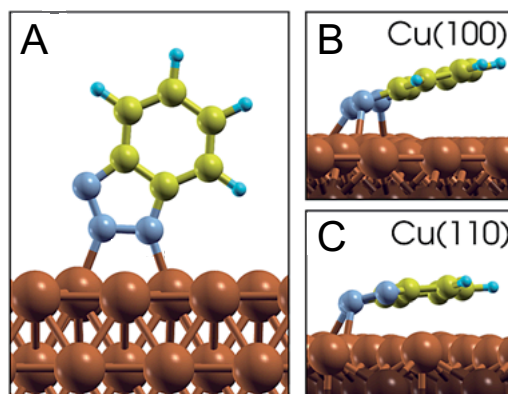


Figure 6.2: Deprotonated BTAH adsorption geometries determined from DFT.²¹ (A) Upright configuration seen on all crystallographic orientations in the DFT study. Flat adsorption geometry observed on the Cu(100) surface (B) and on the Cu(110) (C). Figure adapted from Kokalj., *Faraday Discuss.*, 180(0), 415-438, **2003**.²¹ with permission from The Royal Society of Chemistry.

surface, bonding by only the N lone pairs. The flat (parallel to the surface, Figure 6.2B,C) configuration uses both the N lone pairs and π orbitals.¹⁷

There is still debate on the role of oxygen too, some have even suggested that BTAH does not readily bond to clean Cu and have suggested that oxygen must be present to form Cu-BTA.^{14,18,19} Other reports have stated that oxygen is not needed for the initial stages of adsorption, suggesting [Cu(I)-BTA] films can form on clean Cu.^{14,20} This discrepancy alone highlights the debate that currently exists in the adsorption mechanism.

6.1.2 BTAH on Cu(111)

More recent STM work on Cu(111) observed several structures for BTAH adsorbed onto the Cu surface.^{5,6} One is the physisorbed flat lying case where the molecule remains neutral, parallel to the surface and highly mobile. In addition, upright chemisorbed BTAH commonly form via the deprotonation of BTAH to BTA before combining with free Cu atoms at surface defects and step edges. The structures observed were also attributed to Cu(BTA)₂ dimers at step edges and CuBTA monomers at defects surrounded by the dimers. The suggested dimer structure is displayed in Figure 6.1B, where the exact orientation of the BTA molecules can vary.²² Lastly this work reported Cu(BTA)₂ arranging parallel to each other on defective terraces which are weakly chemisorbed, determined by a high mobility under the STM tip.⁶

An adsorption mechanism has been suggested for the low coverage situation:

BTAH deprotonates to BTA forming both $\text{Cu}(\text{BTA})_2$ dimers and CuBTA monomers. The dimers then undergo a substrate mediated interaction to form chains of 3 – 5 dimer units in length. This contradicts some older work which proposed a continuous organometallic polymer stabilised by hydrogen bonds.²³ Further stabilisation is then through the induced extended (2×1) surface reconstruction.⁵

At a higher coverage (multilayered), STM data showed a regular but incommensurate pseudohexagonal pattern which is also observed in the monolayer regime. Many structures are present in the multilayers with a coverage dependence, however, multilayers are only physisorbed compared to the first chemisorbed layer.⁶

The effect of annealing the system has also been investigated. When a multilayer system is annealed a metastable structure of dimers and flat lying polymeric species is observed, with the pseudohexagonal phase still present. Between 350–375 K desorption of the weakly bound species occurs, above 550 K the chemisorbed layer also desorbs. An increase in ordering is also observed at approximately 420 K and complete desorption is reported above 600 K.⁶

To support the experimental data, density functional theory (DFT) calculations have been carried out for BTAH on $\text{Cu}(111)$.²⁴ It has been shown that BTAH adsorbs intact under acidic conditions, but in alkaline solutions or UHV, BTAH deprotonates during adsorption.²⁴ The DFT calculations conclude that the two lowest energy configurations are stacked $\text{Cu}(\text{BTA})_2$ dimers or organometallic chains formed with the Cu adatoms, which species depends on whether the energy of formation for Cu adatoms is taken into account.²⁴ This agrees well with the UHV experiments reporting a nearly upright configuration.⁶ The stacked dimers were also observed for the reconstructed $\text{Cu}(111)$ surface where the adatoms require a lot of energy to form, there was also suggestion of both BTAH and BTA forming in close packed layers to create a physical barrier to corrosive molecules or elements.²⁴ Another study also corroborated the experimental observation of $\text{Cu}(\text{BTA})_2$ using DFT, showing that the $\text{Cu}(\text{BTA})_2^-$ configuration is most stable on $\text{Cu}(111)$ as all the N atoms can bond to the Cu surface.²² There has, however, been a contradictory DFT study where it was suggested that the $[\text{BTA-Cu}]_n$ complex is the most favourable configuration due to the formation of three bonds, two of which are with low-coordinated adatoms.²⁵ It was also shown that in the case of single BTA units, an upright geometry was most favourable compared to more tilted or flat adsorption.²⁵

A recent study worth discussing, investigated the effect of pH in the growth of BTAH using STM and XPS. The study took a $\text{Au}(111)$ /mica substrate and deposited $\text{Cu}(111)$ monolayers by underpotential deposition, resulting in a (5×5) Cl terminated Cu layer on the $\text{Au}(111)$ /mica substrate. XPS results showed Cu(I)BTA

formation upon immersion of the sample in BTAH solutions (Cu(I) being the +1 oxidation state of Cu), with the interaction being more favourable at lower pH.²⁶ The STM measurements concluded that BTAH adsorbs upright in a parallel packing, with a $\pi - \pi$ interaction being the suggested mechanism. Metalorganic compounds are formed upon adsorption of BTAH, however, they are formed in discrete units not an extended polymer. This was independent of immersion time and pH.²⁶ This study was in-situ and therefore cannot be directly compared with the UHV results in this chapter, but remains a very interesting investigation which has started to describe the BTAH adsorption process on Cu in more realistic conditions.

6.1.3 BTAH on Cu(100)

Less information has been published for the Cu(100) surface, one study using in-situ STM and Fourier transform infra-red spectroscopy reported the molecular plane being parallel to the surface (flat configuration).⁷ Another used near edge x-ray absorption fine structure and found that the molecular plane was within 15° of the surface normal (upright configuration), this study went on to show that with multilayered coverages the molecular plane was tilted by 40° from the substrate (flat/tilted configuration).²⁷ One DFT study on the Cu(100) surface showed either a flat or upright configuration having the most energetically favourable geometry depending on which functional was used for calculation and whether a semiempirical correction is used to describe the van der Waals dispersion.²⁵

6.1.4 BTAH on Cu(110)

This chapter will focus on the Cu(110) surface, as this crystal surface has much less information available than for the Cu(111). There has been one study which showed that BTAH on clean Cu(110) presents a rectangular $c(4 \times 2)$ structure, the same study looked at oxygen reconstructed Cu(110)- $(2 \times 1)\text{O}$ and found a completely disordered adsorption structure, a flat adsorption orientation was suggested for both the clean and oxygen reconstructed surface.¹³ DFT calculations (similarly to the Cu(100) case) found that either flat or upright geometries could be the lowest energy state depending on whether a semiempirical correction for van der Waals dispersion is included in the functional.²⁵

One in-situ study in acidic conditions also exists where flat lying fully protonated BTAH molecules were seen. However, it is already known the BTAH does not deprotonate in acidic conditions compared to the case in vacuum and hence would be expected to behave differently.²⁸

6.1.5 High Resolution Electron Energy Loss Spectroscopy

Whilst STM shows incredible lateral resolution, the “height” in STM images is actually a convolution of topography and the local density of states and hence can also be influenced by the bias applied (Section 1.2). Therefore for accurate information on the exact orientation of molecules on a surface, other analytical techniques are required, such as HREELS.

High resolution electron energy loss spectroscopy (HREELS) is a surface sensitive analytical technique utilising inelastic scattering of electrons to study vibrational modes of a surface or molecules adsorbed on a surface. EELS in general relies on the electronic structure of a surface being excited by the scattering of incident electrons, in this case the scattered electron loses a specific amount of energy, from measuring this energy a spectrum of intensity vs energy loss can be created (often plotted in eV or cm^{-1}).²⁹ HREELS spectra specifically deal with only small energy losses and the peaks are very close to the elastic scattering peak, hence a high energy resolution is needed and the term HREELS is used. To attain this high resolution, incident electrons must have a very well defined energy (achieved with an electron monochromator) and a high quality analyser is required (Figure 6.3A). In addition, the energy of the incident electrons cannot be significantly larger than the losses which are trying to be measured, in HREELS electron energies are significantly smaller than 100 eV. The mean free path of electrons at this energy corresponds to ≈ 1 nm, hence HREELS is a surface specific technique. This is also the reason that HREELS can only be operated in UHV conditions (to avoid electrons colliding with ambient gas particles) compared to other EELS techniques which can be found in TEM instruments.²⁹

There are two mechanisms of energy loss in HREELS experiments, dipole and impact scattering. With dipole scattering the incident electron interacts at long range with oscillating dipoles created from vibrations of surface species, this leads to selection rules which are key to interpreting HREELS spectra. The first is that only fundamental transitions are allowed, second, vibrations are only observed if they also have a change in dipole moment. For metal surfaces (like Cu used here) there are also another two selection rules: firstly, and most crucially to our work, is that only vibrations perpendicular to the surface are observed. Secondly, oscillators vibrating parallel to the surface will have their dipole moment cancelled out by their image dipole, resulting in a net zero dipole moment. Perpendicular to the surface dipoles will actually have a reinforcement from the image dipole (Figure 6.3B). Impact scattering peaks are only observed if detection is carried out away from the direction of specular reflection (off centre collection).²⁹ As all the HREELS

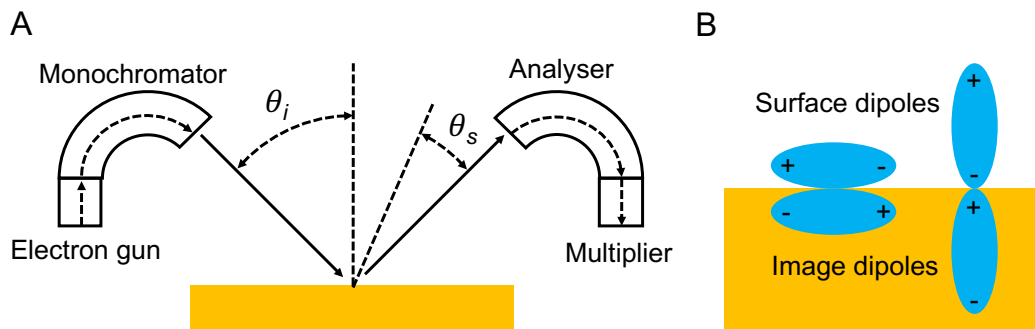


Figure 6.3: (A) Schematic of HREELS experiment for a first generation spectrometer.²⁹ Incident beam angle (θ_i) is at 45° to the surface and the off specular angle of detection (θ_s) in experiments here is zero. (B) Schematic representation of dipole effects in adsorbed molecules. The dipole parallel to the surface has its moment cancelled out by the image dipole, whereas the perpendicular dipole has a reinforcement.²⁹

data presented here is in the specular direction the impact scattering effects can be essentially ignored (Figure 6.3A).

6.2 Methodology

BTAH (99 %, Sigma Aldrich) STM measurements were carried out using an in house constructed variable temperature UHV STM in constant current mode with an electrochemically etched tungsten tip. The majority of the instrument is within two chambers which we refer to as the STM and preparation chambers. The STM chamber houses the STM scanner itself and is separated by a gate valve from the preparation chamber where annealing, sputtering, molecular deposition and some other functions are carried out. For more information on the operational principles of STM, see Section 1.2.

BTAH has a relatively low mass ($119.13 \text{ g mol}^{-1}$) and starts to sublime immediately upon entering vacuum, this means that generally it coats the inside of the preparation chamber extremely quickly if the deposition is not controlled effectively. Advice was taken from Dr. Federico Grillo (School of Chemistry, University of St. Andrews) in order to create a new system for a more reproducible deposition method for BTAH in vacuum. A setup as shown in Figure 6.4 was constructed. This consists of a cross piece which is attached to the preparation chamber by an angle valve (Figure 6.4B), a crucible containing the BTAH powder is on the bottom of the cross (Figure 6.4D) and an individual vacuum pump is used to pump just the cross (Figure 6.4A). The crucible sits in a water bath (Figure 6.4C) to allow

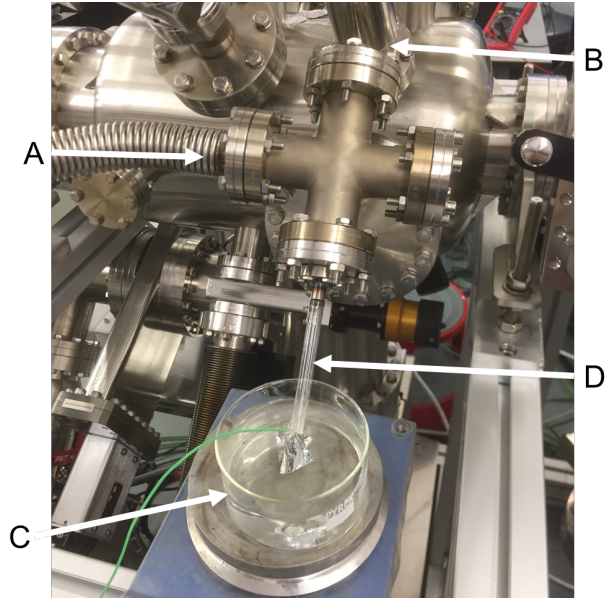


Figure 6.4: Experimental setup attached to preparation chamber of vacuum system. System consists of a cross piece with (A) a vacuum pump, (B) an angle valve to control deposition, (C) a water bath for temperature control and (D) a crucible to house the BTAAH powder.

for temperature control of the BTAAH powder and the amount at which the angle valve is opened controls the quantity of BTAAH deposited. The pump used also has a pressure gauge built-in which was used as a reference point for the pressure in the cross (P_c). After being left for several hours P_c drops to 4.3×10^{-7} mbar at room temperature. However, using an ice and CaCl bath at 268 K resulted in P_c dropping to 3.8×10^{-8} mbar, allowing for better control of deposition.

Unfortunately opening the angle valve did not see the pressure in the preparation chamber (P_p) increase as much as would be expected for the pressure differential, we attribute this to the gauge reading P_c not being entirely accurate. Therefore for consistent deposition, the increase in P_p was used as the reference point for BTAAH quantity. To give a quantitative value for deposition the unit of Langmuir (L) was used, which is defined as the surface being exposed to 10^{-6} torr for one second. In theory (assuming every molecule that hits the surface sticks) then 1 L is enough to have one monolayer on the surface. For our system using this method with the P_p difference it was found that 0.038 L deposited much greater than a monolayer, 0.012 L was less than a monolayer and 0.024 L was just over one monolayer. Whilst these values do not agree with the expected quantities (as 1 L or more is expected for a monolayer) it did give us a relative measure and some control within our own

system of the amount of BTAH deposited.

All STM measurements were taken with an STM chamber pressure in the range of $(7 - 10) \times 10^{-11}$ mbar and P_p was in the range of $(6 - 10) \times 10^{-10}$ mbar before carrying out cleaning or deposition processes.

Keeping a Cu surface clean can be extremely difficult, even a small amount of oxygen will have a large effect on a Cu surface, hence the need for operating in UHV. Even in UHV the Cu surface needs cleaning regularly and between subsequent depositions of molecules. Here, this was done with a series of annealing and sputtering cycles: the single Cu(110) crystal was annealed at 500 °C for 5 minutes and then sputtered with Ar at a sample current measured of 6 μ A for 30 minutes, this was repeated 3 times before the sample was transferred to the STM where imaging was used to check for any contaminants or unexpected surface reconstructions. In order to calibrate the STM measurements, a clean single Cu(110) crystal was imaged with atomic resolution (Figure 6.5A) to show the atomic rows in the $[1\bar{1}0]$ direction. This allows for the crystallographic orientation to be obtained and as the spacing between rows is known (3.6 Å, Figure 6.5B)³⁰, can therefore be compared to the measured value of (3.77 ± 0.02) Å to find the error in the instrumental measurement and hence correct further measurements. Here the correction factors were found to be 0.96 and 1 for the $[001]$ and $[1\bar{1}0]$ directions respectively at room temperature, while for 125 K these were found to be 0.88 and 0.87 for the $[001]$ and $[1\bar{1}0]$ directions respectively. All biases stated here are applied to the sample with respect to the tip (which is held at ground). All STM images are plane corrected using a third order polynomial. Unless otherwise stated measurements taken from STM images are averaged over at least 30 measurements and the error is given by the standard error of the mean.

When Cu interacts with oxygen it is well known that the oxygen reconstructs the Cu(110) surface to form a Cu(110)-(2 \times 1)O reconstruction. It is also known that when the quantity of oxygen is not sufficient to fully cover the Cu surface then it forms in stripes that follow the $[001]$ surface direction (see Figure 6.5C).^{13,31–33} A partially oxygen reconstructed Cu(110) surface was fabricated using controlled deposition of oxygen; the Cu(110) was cleaned using the previously described method, a leak valve with an oxygen cylinder was then used to deposit 20 L of oxygen by controlling the pressure rise in the preparation chamber. 20 L allowed for a mixture of both clean and oxygen reconstructed regions. The sample was then annealed at 600 K, as suggested by previous literature, to form the (2 \times 1) reconstruction.³² The reconstruction with atomic resolution is shown in Figure 6.5D with the corresponding model of the atomic structure shown in Figure 6.5E. It should also be noted that

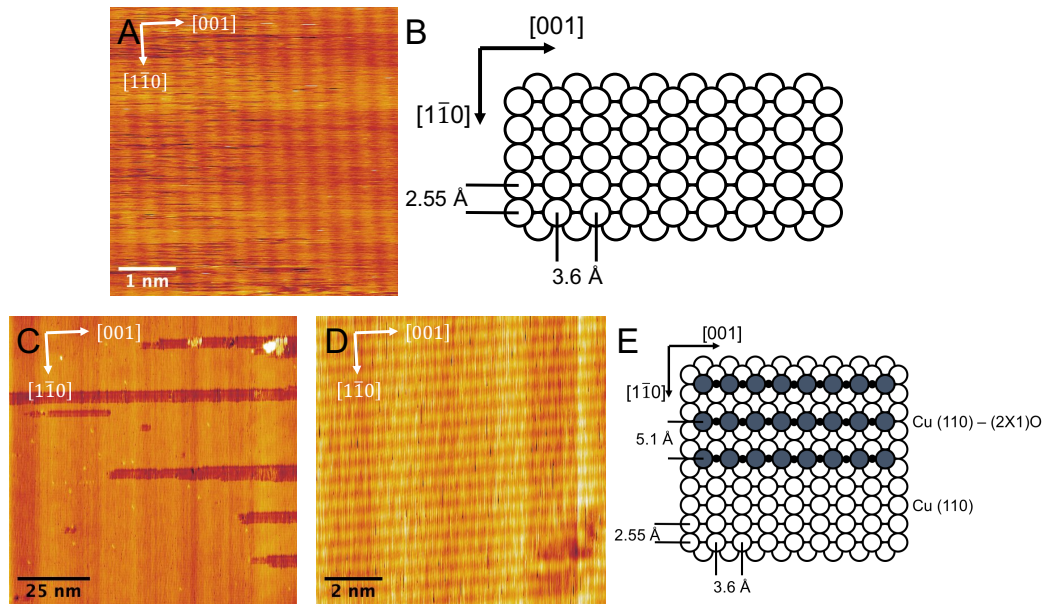


Figure 6.5: (A) STM image of clean Cu(110) surface, used for calibration of future measurements and alignment of crystallographic orientation. Scan size: $5 \times 5 \text{ nm}^2$, sample bias: 0.5 V, tunnelling current threshold: 800 pA. (B) Model of the Cu(110) surface with atomic separations and crystallographic orientations labelled.³¹ (C) STM image of a partially oxygen reconstructed Cu(110) surface. The darker stripes are the clean regions of the Cu surface. $100 \times 100 \text{ nm}^2$, 1.4 V, 700 pA. (D) Higher resolution image of the (2×1) oxygen reconstructed Cu(110) surface. $10 \times 10 \text{ nm}^2$, 1.4 V, 500 pA. (E) Structural model of the Cu(110)- (2×1) O surface reconstruction, alongside the clean Cu(110) surface. White shows Cu atoms, grey are the Cu atoms involved in the reconstruction and black are the oxygen atoms.³¹

all STM scans on the oxygen reconstructed surface had the scan direction rotated by 90° , as otherwise the quick scan direction aligned with the oxygen reconstruction in the $[001]$ direction for our crystal and made imaging oxygen much more difficult. This also means that the calibration carried out for the left to right direction on clean Cu corresponds to the top to bottom in these images.

In some cases (as will be stated) the STM instrument was cooled to $\approx 125 \text{ K}$ by flowing liquid nitrogen through the STM body, cooling the sample and STM mount. Operating at 125 K decreases the surface diffusion of adsorbed species and allows for easier imaging (less noise) and imaging in circumstances where it would not be possible at room temperature (highly mobile adsorbed species).

HREELS data were obtained by a collaborator (Federico Grillo, Department of Chemistry, University of St Andrews), using a VSW HIB 1000 double pass spectrometer. Measurements were done in the specular direction (45°) with 8 eV

incident beam energy and a $\approx 50 \text{ cm}^{-1}$ resolution at the elastic peak (6.2 meV at full width half maximum, FWHM). Spectra were recovered from instrumental broadening using a maximum likelihood based resolution enhancement,^{34,35} which gives an improved resolution of $\approx 40 \text{ cm}^{-1}$ FWHM. All spectra are normalised to the intensity of the elastic peak.

6.3 Results

6.3.1 Low Coverage

The first regime considered is that of much less than a monolayer of BTAH deposited on clean Cu(110). Initially it is very obvious that imaging BTAH at room temperature is extremely difficult due to its high mobility and is only possible at higher surface coverages (around 0.038 L in our measurements). This has been previously reported.⁶ A reconstruction of the Cu step edges is observed but no BTAH molecules are visible, hence for the lower coverage here (0.012 L), imaging was carried out at 125 K. Figure 6.6 displays these images of the lowest coverage regime studied. The Cu step edges have been reconstructed to follow two specific orientations, $(45.5 \pm 0.3)^\circ$ and $(65 \pm 4)^\circ$, whilst these angles are separated by $\approx 110^\circ$ as expected for opposite diagonals of the Cu(110) surface, the orientations do not appear to align with the underlying Cu atoms. It is also observed that the BTAH molecules congregate along these reconstructed step edges. Between the steps, small clusters of BTAH molecules are observed with no particular ordering visible. The previous Cu(111) study that observed high mobility at low coverage also showed BTAH to form chains aligned with the Cu(111) crystallographic orientations, whereas the only structure observed here is at the step edges, the previous Cu(111) study also observed a large reconstruction of step edges via the deprotonation and coordination with Cu atoms at the steps.⁶ One key difference here is the lack of Cu(BTA)₂ dimers observed, the previous study observed dimers which have a width of $\approx 18 \text{ \AA}$, which was not observed here.

6.3.2 Monolayer Coverage

A larger surface coverage of slightly more than a monolayer was obtained using a 0.024 L deposition (Figure 6.7A). At this coverage, species were still quite mobile and hence in all images in this section the system was cooled to 125 K. In the monolayer regime a centered rectangular cell with dimensions of $((10.2 \pm 0.1) \times (7.2 \pm 0.1)) \text{ \AA}^2$ was observed (Figure 6.7B), the short side of the rectangle aligns with the [001]

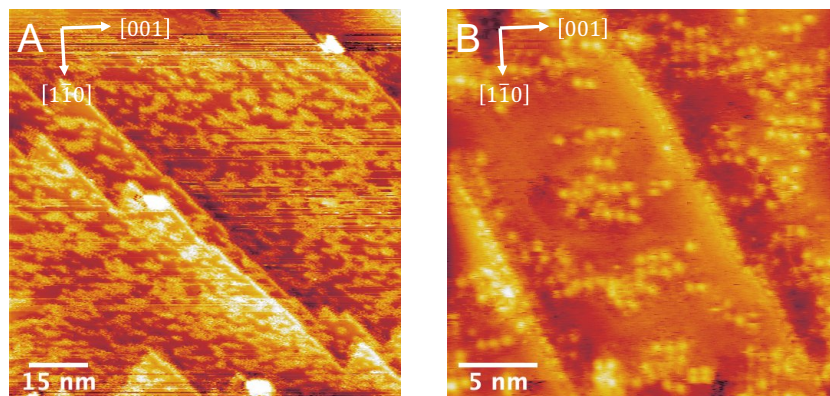


Figure 6.6: (A) Less than a monolayer of BTAAH deposited on Cu(110). Disordered clusters of BTAAH are shown on the terraces, highly restructured step edges are also observed. $100 \times 100 \text{ nm}^2$, 1 V, 50 pA, 125 K. (B) Higher resolution STM image where small clusters are seen on terraces and BTAAH molecules are observed along the reconstructed step edges. $25 \times 25 \text{ nm}^2$, -1 V, 30 pA, 125 K.

crystallographic orientation of the Cu(110) surface and the long edge aligns with the $[1\bar{1}0]$. These dimensions correspond with the expected $c(4 \times 2)$ cell dimensions of $10.2 \times 7.2 \text{ \AA}^2$ which is in agreement with the only previous UHV STM study on the Cu(110) surface.¹³ Figure 6.7C shows a suggested structure for the $c(4 \times 2)$ arranged BTAAH on the Cu(110) surface. Although this STM data does not tell us anything about whether the molecules are flat or upright on the surface, this is discussed later with HREELS data (Section 6.3.4). Lying on top of the monolayer are chains that tend to form in either quite a long straight pattern or in shorter zigzag patterns (Figure 6.7A). It is observed that the monolayer $c(4 \times 2)$ structure exists in regions which are separated by lines which appear lower than the rest of the monolayer. This is shown more clearly in Figure 6.7D which is the result of annealing to 373 K and cooling back down to 125 K. A representative line scan is shown in Figure 6.7E displaying the molecular spacing and height difference of the lower regions. The average trough depth between molecules is $(19 \pm 2) \text{ pm}$ whereas at the lower regions the trough is $(41 \pm 1) \text{ pm}$ deep, also the distance between the molecules on each side of the lower region is $(1.36 \pm 0.03) \text{ nm}$, which corresponds to approximately two molecules (the spacing of molecules in the monolayer perpendicular to the low regions is $(0.81 \pm 0.01) \text{ nm}$). The lower lines are also consistent in their orientation, preferentially following the diagonal through the $c(4 \times 2)$, $(53.7 \pm 0.5)^\circ$ from the $[001]$ surface direction and less commonly follow the opposite diagonal with the same angle (within error) of $(54.2 \pm 0.5)^\circ$. The height difference suggests less than a BTAAH molecule's length in difference and hence these deviations from the monolayer

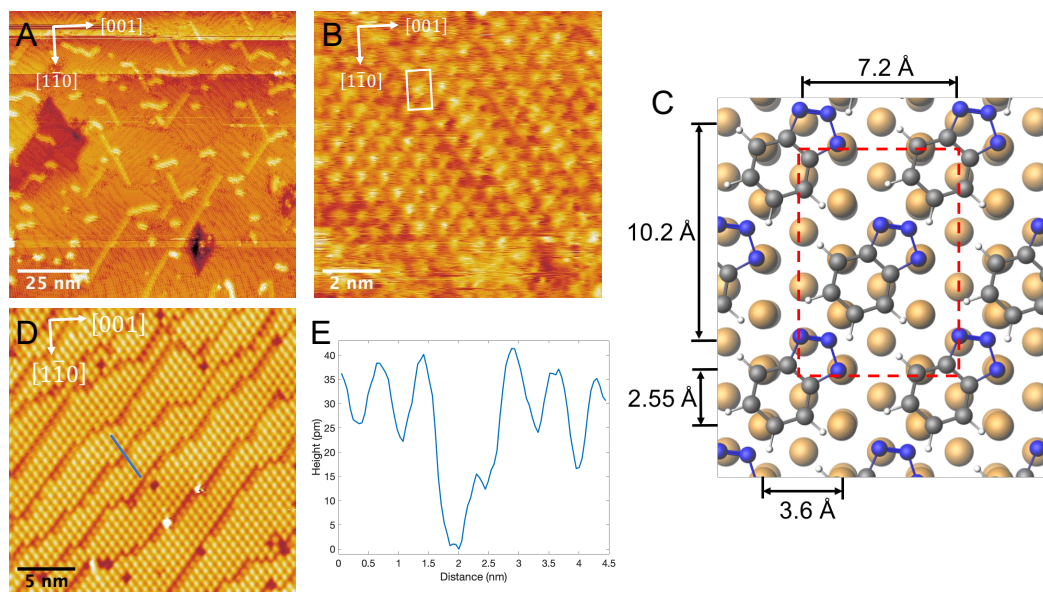


Figure 6.7: (A) Slightly greater than a monolayer coverage (0.024 L) of BTAH deposited, short more disordered chains are observed with longer straight chains also visible. $100 \times 100 \text{ nm}^2$, 1 V, 30 pA, 125 K. (B) High resolution image of monolayer structure with $c(4 \times 2)$ labelled (white rectangle). $10 \times 10 \text{ nm}^2$, 1 V, 30 pA, 125 K. (C) Model schematic of BTAH on Cu(110) with the $c(4 \times 2)$ highlighted in red, the exact orientation of which is discussed later (Section 6.3.4). (D) BTAH monolayer on Cu(110) after annealing to 373 K, the $c(4 \times 2)$ rectangular cell is clearly visible with dislocations separating regions of the monolayer. $25 \times 25 \text{ nm}^2$, 1V, 100 pA, 125 K. (E) Line profile taken from blue region in (D) with the base of the dislocation taken to be zero.

structure are likely the result of dislocations in the formation of the monolayer rather than Cu adatoms. It is also found that post annealing in this case, most of the chains on top of the monolayer have desorbed.

6.3.3 Multilayer Coverage

Once a high enough coverage is reached (0.038 L deposition in our case) then imaging of BTAH on Cu(110) at room temperature becomes possible. We suggest that once enough BTAH is deposited the formation of a full monolayer has a stabilising effect so that surface diffusion of the BTAH molecules is not so prevalent. When investigated as deposited, the same $c(4 \times 2)$ rectangular structure is observed ($(10.2 \pm 0.1) \times (7.2 \pm 0.1) \text{ \AA}^2$) in the monolayer with dislocations between regions much like in the monolayer coverage results. On top of the monolayer occasionally ordered chains are observed similar to before but the more disordered, shorter zigzag type chains

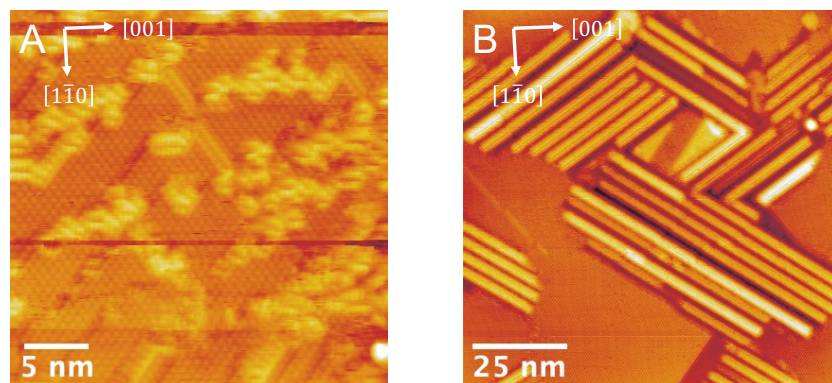


Figure 6.8: (A) Highest coverage studied (0.038 L) as deposited, the $c(4 \times 2)$ monolayer structure is still present, with small disordered clusters and some longer straight chains observed on top of the monolayer. $30 \times 30 \text{ nm}^2$, 1 V, 20 pA. (B) After annealing to 373 K, disordered structures are no longer observed instead large ridges are formed, with the small chains and monolayer structure preserved. $100 \times 100 \text{ nm}^2$, 1 V, 15 pA.

are much more prevalent (Figure 6.8A).

Upon annealing this deposition, two new structures are observed above the monolayer and the absence of the disordered chains from before is also noted (Figure 6.8B). The first structure consists of large ridges and the second of smaller chains. Figure 6.9A shows a high resolution image of one of these ridges, molecules can be seen to be adsorbed along these ridges with a spacing of $(4.4 \pm 0.1) \text{ \AA}$. Along the top of the ridge the molecules appear to be in pairs with a width of $(15 \pm 1) \text{ \AA}$. These dimensions are not exactly consistent with expected values for $\text{Cu}(\text{BTA})_2$ dimers ($\approx 18 \text{ \AA}$)^{5,6} created with Cu adatoms but are larger than the normal spacing in the $c(4 \times 2)$, so may still be dimers in a slightly different configuration. BTAH molecules also appear to be bonded down the sides of these ridges. The line profile displayed in Figure 6.9B shows the height of the ridges that corresponds to the Cu adatom height of 1.8 \AA with the “bumps” down the side due to extra BTAH molecules bonded. The ridges have an angle of $(35.0 \pm 0.3)^\circ$ relative to the $[001]$ direction and therefore combining this with the measurements of spacing would suggest a structure like the one displayed in Figure 6.9C where each Cu adatom in the dimer is one atom along the $[001]$ direction and one atom along the $[1\bar{1}0]$ direction. The expected spacing and angle for this suggested model would be 4.4 \AA and 35.3° respectively which is in good agreement with the measured values. Once again whether the BTAH is upright or flat cannot be determined precisely from the data here, however, there does not appear to be enough space for the molecules to lie completely flat between the Cu adatoms.

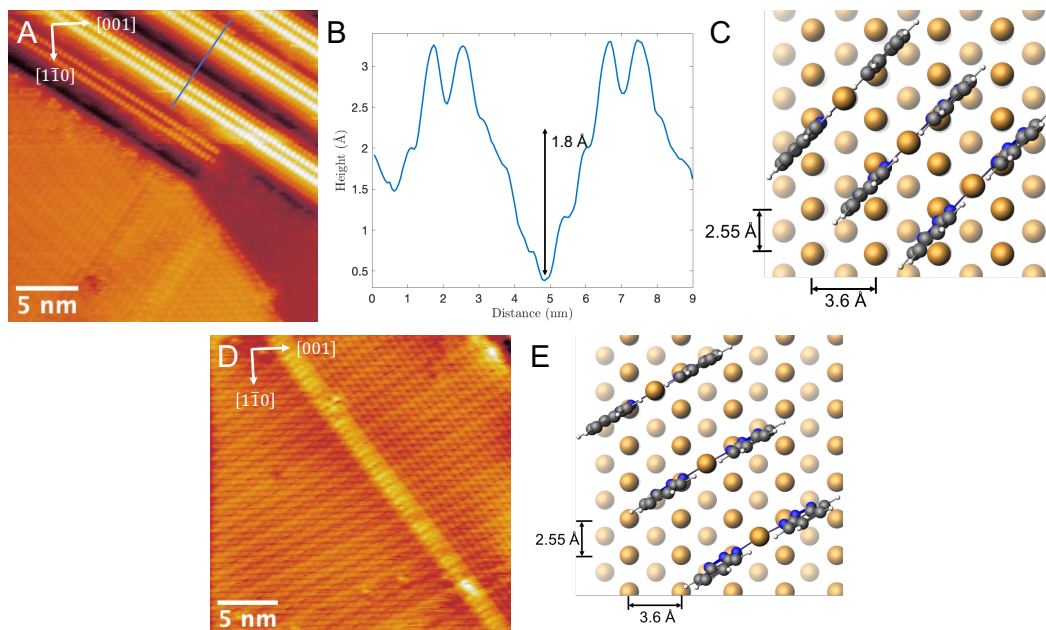


Figure 6.9: (A) High resolution image of large ridge structure, suggesting dimers along the top with molecules adsorbed down the side. $25 \times 25 \text{ nm}^2$, -0.5 V , 80 pA . (B) Line profile taken from blue region in (A), Cu adatom height of 1.8 \AA labelled. (C) Suggested structure with $\text{Cu}(\text{BTA})_2$ dimers adsorbed on each atom along the diagonal of the $\text{Cu}(110)$ surface. (D) STM image of smaller chain structure observed in higher coverages after annealing (and also in some lower coverage examples). $25 \times 25 \text{ nm}^2$, -1 V , 30 pA . (E) Suggested structure with each $\text{Cu}(\text{BTA})_2$ dimer centred on every atom in the $[001]$ and every other atom in the $[1\bar{1}0]$ direction.

The second smaller chain structure (Figure 6.9D) is less common but is similar in dimensions to the top of the large ridges with a width of $(17.7 \pm 0.1) \text{ \AA}$. However, the orientation is different and the apparent height much lower. The orientation here is $(55.3 \pm 0.3)^\circ$ to the $[001]$, also the spacing between molecules is larger at $(6.3 \pm 0.1) \text{ \AA}$. These dimensions are once again consistent with the $\text{Cu}(\text{BTA})_2$ dimer structure but without such a significant reconstruction of the Cu surface, the model in Figure 6.9E shows that having the centre of the dimer placed on every Cu atom in the $[001]$ direction and every other Cu atom in the $[1\bar{1}0]$ direction matches well, where the expected spacing and angle to the $[001]$ would be 6.2 \AA and 54.8° respectively. The larger spacing and much lower apparent height $(28 \pm 1) \text{ pm}$ compared to the large ridge suggests that these molecules may have much less of an angle away from the surface and exist in a flatter structure than the dimers on top of the large ridges.

For both the large ridges and smaller chains the dimers are stacked along

their short axis, whereas previous literature on the Cu(111) showed dimers joining end to end.^{5,6}

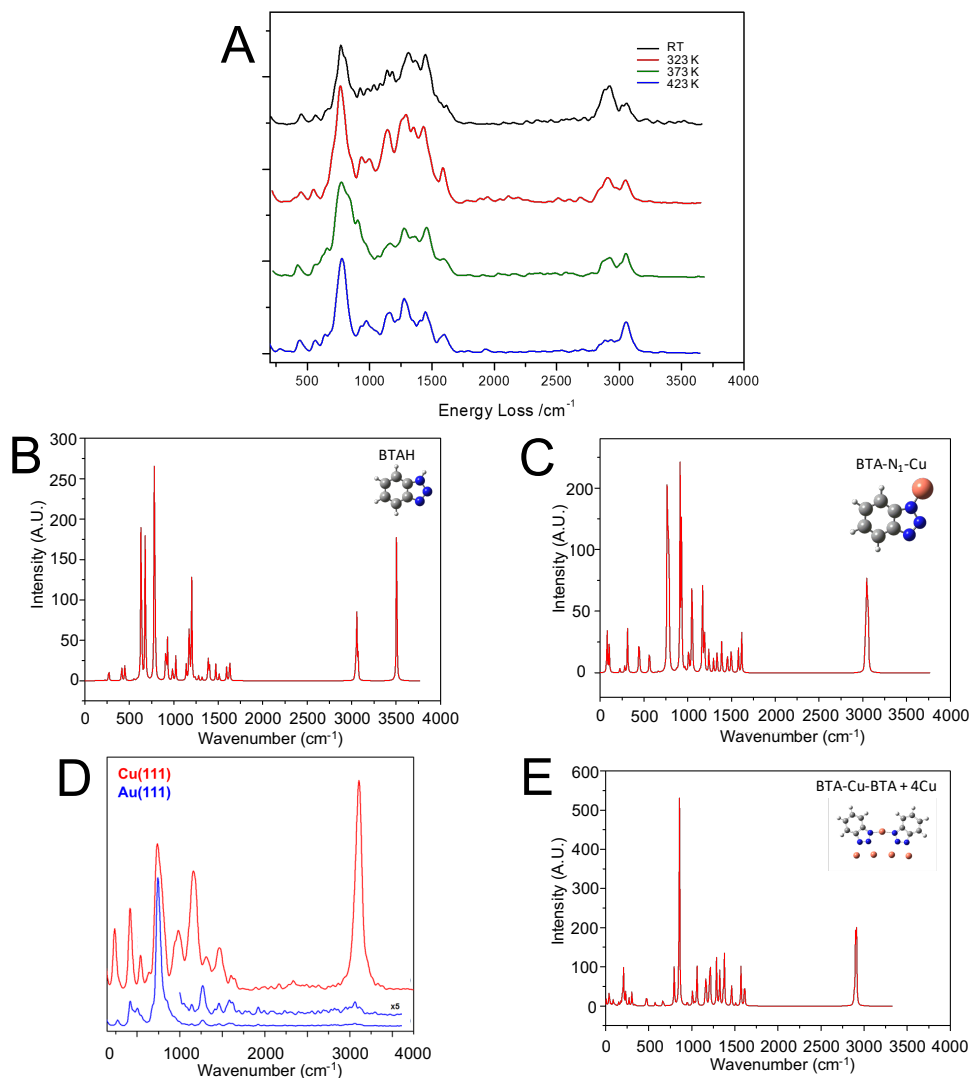


Figure 6.10: (A) Experimentally obtained HREELS spectra for multilayer coverage of BTAA on Cu(111) with several annealing temperatures. Peaks at 2900 cm^{-1} and 3100 cm^{-1} are the main features of interest. Simulated HREELS spectra for protonated (B) and deprotonated (C) BTAA on Cu, the main difference being the presence of the 3500 cm^{-1} for the protonated case. (D) Previous experimental HREELS spectra for BTAA on Cu(111) (red) and Au(111) (blue) where BTAA is known to be upright and flat respectively.^{5,6,36} Au(111) data previously published.³⁶ (E) Simulated HREELS spectrum for $\text{Cu}(\text{BTA})_2$ dimers on Cu, with a peak at 2900 cm^{-1} .

6.3.4 HREELS

Several simulated HREELS spectra were used to compare to experimentally obtained spectra in order to gain information about the orientation of BTAH with regards to annealing temperature in the highest coverage regime. As mentioned earlier (Section 6.1.5) the key here to analysis is that only vibrations which are not parallel to the surface will be observed. The experimentally obtained spectra for a multilayer coverage of BTAH on Cu(110) is shown in Figure 6.10A, with different annealing temperatures. The main features of interest are the peaks at 2900 cm^{-1} and 3100 cm^{-1} , as the annealing temperature increases, the 2900 cm^{-1} peak intensity decreases while the 3100 cm^{-1} intensity increases. However, both peaks have a relatively low intensity compared to the rest of the spectra.

The first simulated spectra to consider are Figures 6.10B,C. These demonstrate the comparison between the protonated and deprotonated spectra for BTAH on Cu. The experimentally observed peak at 3100 cm^{-1} is shown in both cases, but a peak at 3500 cm^{-1} is also seen in the protonated case which is definitely not observed experimentally. This is a good confirmation that BTAH does indeed deprotonate in UHV conditions when adsorbing on Cu, as shown previously.^{5,6,23,24}

Two previous experimental spectra were also used for comparison (Figure 6.10D), in this case the two spectra represent BTAH adsorbed on Cu(111) and Au(111) where much more is known about the BTAH adsorption geometry. For Au(111) BTAH in this regime is essentially flat lying³⁶ whereas on the Cu(111) it is upright and dimeric.^{5,6} The obvious difference in these spectra is the presence of the peak at 3100 cm^{-1} which is only present significantly in the upright case. The experimental spectra for the Cu(110) does indeed show a peak at 3100 cm^{-1} , however, its intensity is much smaller compared to the rest of the spectra which would suggest a mostly flat adsorption geometry or with a slight tilt away from the surface. It can also be seen that as the annealing temperature increases the intensity of this peak also increases which means that more of the BTAH becomes upright at higher annealing temperatures.

Finally the simulated spectrum for $\text{Cu}(\text{BTA})_2$ dimers on Cu (Figure 6.10E) show a distinct peak at 2900 cm^{-1} which is also observed in the experimental spectra. However, once again the intensity of this peak is much less than the rest of the spectrum suggesting that only a minority of species are in this form.

To conclude the HREELS observations, it appears that in the high coverage case that most of the BTAH on the surface is flat lying or with only a small angle away from the surface, with a minor contribution from upright and dimeric species. As the sample is annealed more of the BTAH transfers to upright but non-dimeric

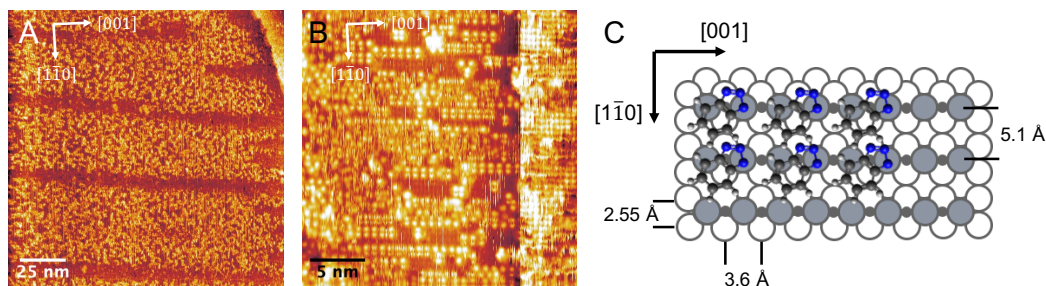


Figure 6.11: (A) BTAH deposited on the oxygen reconstructed Cu(110) surface, darker regions are the clean Cu. At this scale disordered clusters of BTAH are present on the oxygen reconstructed surface, with much less visible in the clean regions. $150 \times 150 \text{ nm}^2$, 1.4 V, 400 pA. (B) A higher resolution image of an oxygen reconstructed region. Between disordered clusters a pattern with pairs of molecules is seen that corresponds to a (1×2) structure on the Cu(110)- (2×1) O reconstruction. (C) Suggested model of BTAH adsorption on the Cu(110)- (2×1) O reconstruction, as before the STM alone cannot tell us about the precise orientation of the molecules in this case.

species. This would agree with the formation of the large ridges observed in the STM data (Section 6.3.3) as BTAH is seen to bond along the sides of these large ridges with only the molecules running along the top being dimeric in nature.

6.3.5 Oxygen Reconstructed Cu(110)

In order to bring the studies here more towards a realistic system, oxygen was deposited onto the Cu surface in a quantity which led to both clean and oxygen reconstructed regions of the Cu(110) surface being visible (Figure 6.5C). After observation of the partially reconstructed surface, 0.014 L of BTAH was deposited. The first observation was that BTAH bonds preferentially to the oxygen covered regions as opposed to the clean Cu surface (Figure 6.11A). This is contrary to what might be expected due to the reactivity of clean Cu, but is in agreement with some previous studies.^{14,18,19} However, it was also stated that oxygen was required for the bonding of BTAH which has been shown here and elsewhere not to be the case.^{5,6} In most cases the BTAH forms disordered clusters on the oxygen reconstructed surface much like previously observed.¹³ In the measurements here, however, between the disordered clusters, chains are formed where BTAH sits in pairs that lie along the $[001]$ direction like the oxygen reconstruction (Figure 6.11B). The spacing along the $[001]$ is given by $(7.3 \pm 0.3) \text{ \AA}$ and $(5.1 \pm 0.1) \text{ \AA}$ in the $[1\bar{1}0]$ direction, which corresponds to double (7.2 \AA) in the $[001]$ and equal to (5.1 \AA) in the $[1\bar{1}0]$ Cu atom spacing respectively, hence a (1×2) structure on the Cu(110)- (2×1) O re-

construction. Figure 6.11C shows a suggested (1×2) pattern, the apparent height of the BTAH is (94 ± 3) pm which would suggest a fairly flat adsorption but the STM data cannot give us any information about the orientation laterally and the measured vertical dimension should not be taken as a confirmation of orientation without other analytical techniques. It is possible that this structure is only observed at lower coverages which would explain why it is not seen universally on the surface and why previous studies did not observe this pattern.

6.4 Conclusions

This chapter demonstrates some of the capabilities of STM in a UHV system for materials characterisation at the molecular level. BTAH was deposited on a clean and partially oxygen reconstructed single crystal Cu(110) surface to highlight the adsorption structure with varying coverage and annealing regimes, HREELS was also used to assist in the analysis of STM data.

In the low coverage regime on clean Cu(110), BTAH is observed in disordered clusters with a likely flat lying geometry, in addition, BTAH molecules are seen to congregate along reconstructed Cu step edges.

The monolayer of BTAH forms in a $c(4 \times 2)$ structure. Combination of STM and HREELS data suggests that the majority of BTAH sits with a small angle to the surface with a minority sitting upright. When only a small amount more than a monolayer is deposited, on top of the monolayer elongated chains are observed, annealing this regime to 373 K sees either the desorption of these chains or the formation of long straight $\text{Cu}(\text{BTA})_2$ chains. These $\text{Cu}(\text{BTA})_2$ dimers likely account for the minority of the total molecules.

At higher coverages the monolayer retains its $c(4 \times 2)$ structure but the chains on top become more clustered and disordered. Upon annealing to 373 K these disordered chains are no longer visible, but large ridge structures of Cu adatoms topped with $\text{Cu}(\text{BTA})_2$ dimers are observed. Single layer $\text{Cu}(\text{BTA})_2$ dimer chains are also seen here but in much smaller quantities and with a different orientation to the large ridges.

When BTAH is deposited on a partially $(2 \times 1)\text{O}$ reconstructed Cu(110) surface, BTAH preferentially bonds to the oxide regions over the clean Cu(110). Generally, disordered clusters of BTAH are observed (which agrees with previous literature), but in many cases a previously unobserved (1×2) structure is seen on top of the oxygen reconstruction.

Combining the work here with more recent previous literature on the Cu(111)

surface starts to fill in the gaps in the adsorption process of BTAH on the Cu surface. Some further study on the Cu(100) would then go some way to a complete adsorption model, at least for the three main crystallographic orientations. Here we have also started to consider the role that oxygen plays in the adsorption process but this area requires further study with multiple crystallographic orientations of Cu, varying coverages of oxygen and several annealing temperatures.

6.5 Acknowledgements

The work in this chapter started in a project carried out during the MSc year of my centre for doctoral training scheme. The work was then carried on by another PhD student, Marco Turano throughout my other PhD studies. However, all STM data presented here were collected and analysed by myself. This work is in preparation to be published, co-authored between myself, Marco, Dr. F. Grillo and Prof. G. Costantini.

Dr. Federico Grillo is acknowledged as he was responsible for all HREELS data presented here, he has also carried out high coverage STM experiments on the Cu(110) which agreed with our results shown here. He also contributed to discussions relating to BTAH deposition in UHV and to analysis of results.

Dr. Dan Warr is also acknowledged for training and advice with the STM instrumentation.

6.6 References

- [1] Proctor and Gamble, Ltd. *Compositions for Inhibiting Metal Tarnish*, British Patent 625339, 1947.
- [2] Finšgar, M. & Milošev, I. *Corros. Sci.*, 52(9), 2737–2749, **2010**.
- [3] Kokalj, A. & Peljhan, S. *Langmuir*, 26(18), 14582–14593, **2010**.
- [4] Kokalj, A., Peljhan, S., Finšgar, M. & Milošev, I. *J. Am. Chem. Soc.*, 132(46), 16657–16668, **2010**.
- [5] Grillo, F., Tee, D. W., Francis, S. M., Früchtl, H. & Richardson, N. V. *Nanoscale*, 5(12), 5269–5273, **2013**.
- [6] Grillo, F., Tee, D. W., Francis, S. M., Früchtl, H. A. & Richardson, N. V. *J. Phys. Chem. C*, 118(16), 8667–8675, **2014**.
- [7] Vogt, M. R., Nichols, R. J., Magnussen, O. M. & Behm, R. J. *J. Phys. Chem. B*, 102(30), 5859–5865, **1998**.
- [8] O’Sullivan, D. G. *J. Chem. Soc.*, pages 3653–3658, **1960**.
- [9] Roberts, J. E. *Comm. Math. Phys.*, 37(4), 273–286, **1974**.
- [10] Nesmeyanov, A. N., Babin, V. N., Fedorov, L. A., Rybinskaya, M. L. & Fedin, E. I. *Tetrahedron*, 25(19), 4667–4670, **1969**.
- [11] Sease, C. *Stud. Conserv.*, 23(2), 76–85, **1978**.
- [12] Cadien, K. C. & Nolan, L. In K. B. T. H. o. T. F. D. T. E. Seshan, editor, *Handb. Thin Film Depos.*, pages 179–219. Wiley-VCH, Oxford, **2012**.
- [13] Cho, K., Kishimoto, J., Hashizume, T. & Sakurai, T. *Japanese J. Appl. Phys.*, 33(1), L125–L128, **1994**.
- [14] Fang, B. S., Olson, C. G. & Lynch, D. W. *Surf. Sci.*, 176(3), 476–490, **1986**.
- [15] Hollander, O. & May, R. C. *Corrosion*, 41(1), 39–45, **1985**.
- [16] Nilsson, J.-O., Törnkvist, C. & Liedberg, B. *Appl. Surf. Sci.*, 37(3), 306–326, **1989**.
- [17] Mansikkamaki, K., Ahonen, P., Fabricius, G., Murtomaki, L. & Kontturi, K. *J. Electrochemical Soc.*, 152(1), B12–B16, **2005**.

- [18] Ling, Y., Guan, Y. & Han, K. N. *Corrosion*, 51(5), 367–375, **1995**.
- [19] Sutter, E. M., Ammeloot, F., Pouet, M. J., Fiaud, C. & Couffignal, R. *Corros. Sci.*, 41(1), 105–115, **1999**.
- [20] Cho, K., Kishimoto, J., Hashizume, T., Pickering, H. W. & Sakurai, T. *Appl. Surf. Sci.*, 87-88(C), 380–385, **1995**.
- [21] Kokalj, A. *Faraday Discuss.*, 180(0), 415–438, **2015**.
- [22] Chen, X. & Häkkinen, H. *J. Phys. Chem. C*, 116(42), 22346–22349, **2012**.
- [23] Jiang, Y. & Adams, J. B. *Surf. Sci.*, 529(3), 428–442, **2003**.
- [24] Gattinoni, C. & Michaelides, A. *Faraday Discuss.*, 180, 439–458, **2015**.
- [25] Peljhan, S., Koller, J. & Kokalj, A. *J. Phys. Chem. C*, 118(2), 933–943, **2014**.
- [26] Mirarco, A., Francis, S. M., Baddeley, C. J., Glisenti, A. & Grillo, F. *Corros. Sci.*, 143, 107–115, **2018**.
- [27] Walsh, J., Dhariwal, H., Gutiérrez-Sosa, A., Finetti, P., Muryn, C., Brookes, N., Oldman, R. & Thornton, G. *Surf. Sci.*, 415(3), 423–432, **1998**.
- [28] Sugimasa, M., Wan, L.-J., Inukai, J. & Itaya, K. *J. Electrochem. Soc.*, 149(10), E367–E373, **2002**.
- [29] Soriaga, M. P., Chen, X., Li, D. & Stickney, J. L. *High Resolution Electron Energy-Loss Spectroscopy*, **2005**.
- [30] Davey, W. P. *Phys. Rev.*, 25(6), 753–761, **1925**.
- [31] Novák, J., Oehzelt, M., Berkebile, S., Koini, M., Ules, T., Koller, G., Haber, T., Resel, R. & Ramsey, M. G. *Phys. Chem. Chem. Phys.*, 13(32), 14675–14684, **2011**.
- [32] Eren, B., Liu, Z., Stacchiola, D., Somorjai, G. A. & Salmeron, M. *J. Phys. Chem. C*, 120(15), 8227–8231, **2016**.
- [33] Guo, X. C. & Madix, R. J. *Surf. Sci.*, 367(3), L95–L101, **1996**.
- [34] Frederick, B. G., Nyberg, G. L. & Richardson, N. V. *J. Electron Spectrosc. Relat. Phenom.*, 64-65, 825–834, **1993**.
- [35] Frederick, B. G. & Richardson, N. V. *Phys. Rev. Lett.*, 73(5), 772, **1994**.

- [36] Grillo, F., Garrido Torres, J. A., Treanor, M.-J., Larrea, C. R., Götze, J. P., Lacovig, P., Früchtl, H. A., Schaub, R. & Richardson, N. V. *Nanoscale*, 8(17), 9167–9177, **2016**.

Chapter 7

Summary and Outlook

Throughout this thesis nanoelectrode (NE) fabrication and characterisation has been emphasised with a focus towards applications in scanning electrochemical probe microscopy (SEPM). Electrode characterisation with multiple techniques is of great importance and is often overlooked in the literature. Here two classifications of NEs have been investigated and their application to nanoscale electrochemical mapping has been demonstrated. Additionally a study using ultra-high vacuum scanning tunnelling microscopy (STM) has found new information about the adsorption of a specific molecule (benzotriazole) on a copper (Cu(110)) surface, highlighting the ability of STM to characterise materials at the molecular level.

Chapter 2 addresses a long used method of NE fabrication, involving the pyrolysis of hydrocarbons inside a quartz nanopipette to form a carbon nanoelectrode (CNE). Despite the methods historic use, CNEs are often quite poorly characterised. Recently more thoroughly engineered approaches to CNE fabrication have been attempted. Chapter 2 undertakes an investigation on the historically used method, and our own take on a newer method, to show the issues relating to the reproducibility of CNE fabrication and the dangers of characterising with voltammetry alone. The chapter then goes on to study the electrodeposition of Pt onto these CNEs for use as PtNEs using three different methods of deposition. The advantages and disadvantages of each method are highlighted, but the key factor is the need for perfect CNEs as a base support, otherwise it is unlikely that the formed PtNE will have the desired geometry.

Whilst Chapter 2 highlights the issues with CNEs, due to their cheap and quick nature of fabrication, statistically, good quality CNEs can be fabricated in a reasonable time frame and electrodeposition of Pt on these CNEs can be carried out to form PtNEs. These PtNEs were then applied in Chapter 3 to a technique

termed conductance - scanning electrochemical microscopy (C-SECM), capable to mapping topography and electrochemistry simultaneously. The combination of these NEs with modern SEPM instrumentation and a novel scanning protocol allowed for nanoscale electrochemical mapping with a topographic resolution impossible with traditional SECM and with substrates that would typically have too much surface heterogeneity to be imaged in traditional STM. Limitations of using typical SEPM instrumentation for tunnelling type experiments are detailed in reference to previous studies with similar regimes. The advances made here could allow for more research groups to pick up C-SECM as a technique due to the use of more widely available instrumentation and the obtainable topographic resolution.

A newer method of NE fabrication involving chemical and bipolar electrochemical deposition of Au in a nanopipette, labelled bipolar nanoelectrodes (BPNEs) has been investigated in Chapter 4. BPNEs fabricated with the methodology used here represent a very quick, cheap and easy way of fabricating NEs with ideal geometries. Due to the size of the Au plug, however, refilling the pipette with another solution is often utilised and hence bipolar electrochemistry has to be considered when characterising or using these electrodes. Previously formulated relationships, in combination with COMSOL models, go some way to predicting the electrochemical response of BPNEs. Whilst different solution and electrode combinations can be predicted, accurately predicting the difference in response between similar electrodes with multiple solutions is much less reliable. Nevertheless this method represents a potential future standard for NE fabrication due to the ease, low cost and short timescale of fabrication.

The BPNEs fabricated in Chapter 4 are applied to SEPM techniques in Chapter 5. The first application is to in-situ STM measurements and the second is to SECM style approach curves. SECM was carried out on previously used SEPM instrumentation (Chapter 3) whereas the STM data was acquired using a commercial STM instrument. Both applications showed early promise with both positive and negative feedback observed in SECM and individual graphite step edges observed in the STM. Unfortunately BPNEs (at least in our configuration) appear to have issues regarding longevity when applied to SEPM, with drops in measured current and an inconsistent electrochemical response being commonplace after a short while. Hopefully these issues can be addressed in the future by adaptations to the current configuration as methods that can generate ideal NE geometries with this simplicity are few and far between.

The ability of STM to study surfaces with atomic resolution has been demonstrated repeatedly for some time, especially when considering systems in ultra-high

vacuum (UHV). The adsorption of the molecule benzotriazole (BTAH) onto the copper surface is widely used in industry but quite poorly understood at the molecular level. In Chapter 6 BTAH is deposited onto a single crystal Cu(110) surface, in order to address this puzzle piece of the complete adsorption mechanism. Several different adsorption structures are seen depending on the coverage, annealing temperature and if the role of oxygen is considered. With the addition of data from high resolution electron energy loss spectroscopy (HREELS), this chapter goes some way to completing the model for the adsorption mechanism of BTAH on the Cu(110) surface, with most findings being consistent with previous literature, but with some (especially with the role of oxygen) being contradictory to previous studies.

In summary, this thesis has demonstrated and investigated the fabrication and characterisation of two types of nanoelectrode with several methodological approaches for each, emphasising the limitations of individual characterisation techniques. Additionally the application of these electrodes to nanoscale electrochemical mapping has been approached utilising modern instrumentation with novel approaches to scanning. Finally a study of a well known industrial corrosion inhibitor has been carried out using UHV-STM to elucidate several features of the adsorption mechanism on a copper surface.